

Molecular Modelling Particulate Interactions in Metered Dose Inhaler Suspension Formulations

Vivian Gerard Walter Barron

Submitted in accordance with the requirements
for the degree of

Doctor of Philosophy
(Chemical Engineering)

The University of Leeds

Centre for Doctoral Training in Complex
Particulate Products and Processes

School of Chemical and Process Engineering

March 2023

The candidate confirms that the work submitted is his own, except where work which has formed part of jointly authored publications has been included. The contribution of the candidate and the other authors to this work has been explicitly indicated below. The candidate confirms that appropriate credit has been given within the thesis where reference has been made to the work of others.

Research work from Chapters 3 and 4, and sections of Chapter 2 describing the method appeared in two joint authored publications. Vivian W. Barron was the lead author and completed all research in the first publication. The other authors supervised with discussions and with using the modelling software. Details are:

Vivian W. Barron, Chin W. Yong, Alex Slowey, Ilian T. Todorov, Kevin J. Roberts, Robert B. Hammond. 2023. Comparison between the Intermolecular Interactions in the Liquid and Solid forms of Propellant 1,1,1,2 – Tetrafluoroethane. *Journal of Molecular Liquids*, 383, pp 121993.

In the second publication, Vivian W. Barron was the secondary author and produced the simulations that were analysed. Chin W. Yong was the lead author and generated analysis algorithms. The other authors supervised with discussions. Details are:

Chin W. Yong, Vivian W. Barron, Alex Slowey, Ilian T. Todorov, Kevin J. Roberts, Robert B. Hammond. 2023. Data on the intermolecular interactions of 1,1,1,2-tetrafluoroethane liquids from molecular dynamics simulations. *Data in Brief*, 50, pp 109485.

This copy has been supplied on the understanding that it is copyright material and that no quotation from the thesis may be published without proper acknowledgement.

The right of Vivian Gerard Walter Barron to be identified as Author of this work has been asserted by him in accordance with the Copyright, Designs and Patents Act 1988.

Abstract

In this study, predominantly molecular modelling was employed to investigate intermolecular interactions affecting a metered dose inhaler (MDI) suspension formulations two core ingredients, its liquid propellant and solid drug particle. Taking a first principles approach has potential to help explain the cause of formulation issues at a molecular scale. In turn, it could be a valuable tool during development and contribute to a digital drug design approach.

A previously determined solid-state structure of propellant 1,1,1,2-Tetrafluoroethane, known commercially as HFA-134a, provided a reference point of favoured interactions at low temperatures. Its intermolecular interaction strength was predicted using molecular mechanics techniques. This identified that its dipole moment, caused by the asymmetric distribution of fluorine atoms, was responsible for the formation of 'weak hydrogen bonds' in the low temperature structure. These were believed to promote structural change from the higher temperature cubic phase.

The disordered liquid propellant structure was modelled at different temperatures using molecular dynamics. Structural resemblance to the solid-state increased as liquid temperature was reduced. For instance, the liquid's local density arranged in a similar manner to the body centred cubic phase. Plus, weak hydrogen bond interactions appeared in the liquid, like those seen in the solid-state. However, steric repulsions were the largest influence on the liquid packing.

Two polymorphs of corticosteroid fluticasone propionate (FP) had previously been determined, these were visualised, and empirical force fields were applied to predict the strength of their intermolecular interactions. There was very little difference between molecular conformations in both polymorphs due to the rigidity of its the molecular structure. Intermolecular interactions were mostly non-polar in nature in both polymorphs. However, Form I showed better stability due to its favoured interactions.

FP's external morphology was predicted through the attachment energy model. It partially resembled the needle shaped, experimentally recrystallized samples, and the strongest synthon grew along the length of the crystal. Surface analysis showed mostly non-polar functional groups were exposed on the capping faces. A grid-based search tool predicted the interaction energies with probes. It was hypothesised polar solvents preferably adsorbed to the crystal's side faces, which left the non-polar capping faces as a favourable growth environment. Also, particle morphologies with a smaller proportion of capping faces were shown to have lower cohesive energies.

Acknowledgements

I would like to thank Dr Robert Hammond and Professor Kevin Roberts for their supervision and valuable discussions that have helped me navigate the challenges of this project. I would also like to thank my industrial supervisor Alex Slowey for his interest, advice, and help with selecting chemicals of interest.

I would like to acknowledge Kindeva Drug Delivery and the Engineering and Physical Sciences Research Council for providing project funding through the Centre for Doctoral Training in Complex Particulate Products and Processes (CDT-CP³) at the University of Leeds. This provided me with research facilities and supported my professional development.

Thank you to Dr Hien Nguyen and Dr Ian Rosbottom for their guidance and technical assistance, this was invaluable in the early stages of my project. Also, I would like to thank Dr Chin Yong and Professor Sarah Harris for helpful discussions and aiding my molecular dynamics studies. Likewise, thank you to Professor Darragh Murnane for his useful input regarding inhalation devices.

This is dedicated to my parents and family for constantly supporting me in both academic and non-academic pursuits. Thank you to all close friends who made this scholarly journey more enjoyable, and a special shout out to everyone on the first floor of the Energy building who kept me sane!

Contents

Abstract.....	3
Acknowledgements	4
Contents.....	5
List of Figures	8
List of Tables.....	20
Nomenclature.....	23
Abbreviations	25
Chapter 1: Introduction to Intermolecular Interactions of Metered Dose Inhaler Formulations	
1.1.1 Introduction to Research Context	2
1.1.2 Research Question and Objectives	6
1.1.3 Selection of Methods.....	7
1.1.4 Selection of Materials.....	7
1.1.5 Project Management	8
1.1.6 Thesis Layout.....	9
1.2.1 Introduction Intermolecular Interactions of Metered Dose Inhaler Formulations	10
1.2.2 Formulation Factors Influencing Performance	10
1.2.3 Crystalline Properties of Fluticasone Propionate	17
1.2.4 Structuring of Liquid Propellants.....	24
1.2.5 Conclusion	28
Chapter 2: Intermolecular Interactions, Molecular Modelling Background and Method & Materials.....	
2.1.1 Introduction to Intermolecular Interactions, Molecular Modelling	31
2.1.2 Fundamental Intermolecular Science	31
2.1.3 Basic Crystallography of APIs	37
2.1.4 Morphology Prediction and Molecular Modelling	49
2.2.1 Methods and Materials.....	58
2.2.2 Materials for Experiments.....	58
2.2.3 Experimental Method	58

2.2.4	Computational Methods	60
2.2.5	Conclusion	75
Chapter 3: Intermolecular Packing of Hydrofluoroalkane's Solid-State.....		77
3.1	Introduction.....	77
Chapter Flowchart Overview		78
3.2	Hydrofluoroalkane Propellants.....	79
3.3	HFA-134a Intermolecular Structure Analysis	82
3.4	Relationship between Monoclinic and Cubic Phase.....	87
3.5	Conclusion.....	90
Chapter 4: Structuring of Pure Liquid Propellant HFA-134a Across Temperature Range		93
4.1	Introduction.....	93
Chapter Flowchart Overview		94
4.2	Local Density of Liquid Structure	95
4.3	Frequency of Three Carbon Intermolecular Interaction	102
4.4	Non-Bonded Dihedral Angle between C-C axes	104
4.5	Liquid Structure Discussion and Comparison with Solid-State	106
4.6	Conclusion.....	109
Chapter 5: Comparing Molecular and Crystal Structure of Form I and II Fluticasone Propionate		111
5.1	Introduction.....	111
Chapter Flowchart Overview		112
5.2	Fluticasone Propionate and its Polymorphs	113
5.3	Lattice Energy Calculation	118
5.4	Synthon Strength Analysis.....	119
5.5	Comparing Different Crystal Packing Arrangements.....	128
5.6	Conclusion.....	128
Chapter 6: Morphology Prediction of Fluticasone Propionate and Particulate Surface Interactions with Formulation		131
6.1	Introduction.....	131
Chapter Flowchart Overview		132

6.2	Morphology Prediction of FP.....	133
6.3	Surface Chemistry	142
6.4	FP Molecule – Solvent Interactions.....	151
6.5	Grid-Based Search of FP Surfaces.....	156
6.6	Summary and Discussion	170
6.7	Conclusion.....	172
Chapter 7: Conclusions and Future Work.....		174
7.1	Introduction.....	174
7.2	Conclusions of this study	174
7.3	Review of Original Research Objectives	175
7.4	Suggestions for Future Work	177
7.5	Closing Remarks	181
Appendix Chapter		183
A.1	Predicted Partial Charges	183
A.2	Force Field Comparison: Lattice Energy of FP.....	188
A.3	MD Simulation Settings: Liquid HFA-134a	189
A.4	Morphology Effect on Particle Interactions.....	193
References		194

List of Figures

Figure 1-1 Images of three main types of inhalers, MDI (KindevaDrugDelivery, 2015), DPI (ShutterStock, 2022), Nebuliser (PrimaryCareSupplies, 2022). 3

Figure 1-2 Labelled schematic of a typical metered dose inhaler device's contents. An actuator houses the formulation filled canister, when activated an aerosol is emitted. 5

Figure 1-3 Molecular structures of propellant 1,1,1,2-tetrafluoroethane, HFA-134a. And active pharmaceutical ingredient fluticasone propionate, C₂₅H₃₁F₃O₅S. 8

Figure 1-4 Graphical thesis workflow. FP's solid-state profile from molecule to morphology and shows HFA's intermolecular packing across different phases. Combining to examine FP's particulate interactions of surfaces with solvents. 9

Figure 1-5 Overview of three main stages of developing an MDI suspension formulation: Pre-formulation, Formulation and Stability. Adapted from (Vervaet and Byron, 1999). 11

Figure 1-6 Illustration showing how the deposition behaviour of particles depends on size, with smaller particles reaching the lower airways (Carvalho et al., 2011). 12

Figure 1-7 Example of APSD measured through an NGI showing the distribution of particle sizes collected at different stages (Kamiya et al., 2004). 13

Figure 1-8 Illustration of calcium chloride particles; (A) inflated spray dried particle with smooth surface, (B) solid micronized particle with wrinkled surface (D'Sa et al., 2014) 15

Figure 1-9 AFM images of different cannister walls; (A) borosilicate glass (B) aluminium canister (C) PTFE-coated aluminium (Young et al., 2003) 16

Figure 1-10 SEM images of particles formed by different methods: micronized FP particles (a) (Murnane et al., 2008b) and (b) (Moura et al., 2016), spray dried FP (Louey et al., 2004) and in-situ micronized FP (Murnane et al., 2008a). 18

Figure 1-11 (A) AFM image of FP particle surface formed during anti-solvent crystallisation shows a visibly terraced structure. (B) SEM image of same FP particles (Bártová et al., 2022). 19

Figure 1-12 FP's powder x-ray diffraction patterns. Form I crystallised with water as anti-solvent and then milled, peaks at 15.9° and 16.3° are highlighted. Form II produced with supercritical CO₂ as anti-solvent, peak at 19.0° is highlighted (Steckel et al., 1997). 20

Figure 1-13 FP morphologies, dissolved in Acetone (A) and Methanol (B). Water used as anti-solvent (Murnane et al., 2008a) 21

Figure 1-14 SEM images of different shaped particles formed when FP was dissolved in acetone, then different solvents were added to initiate anti-solvent crystallisation: water, ethyl acetate, n-hexane, iso-propanol (Kubavat et al., 2012). 21

Figure 1-15 SEM images of FP-SX mixtures particle morphologies, spray dried from different solvents: acetone, methanol, ethanol (Westmeier and Steckel, 2008). 22

Figure 1-16 Previous FP morphology predictions, (a) using attachment energy method (Ramachandran et al., 2015). and (b) fitted to match experimental morphology via 'crystal modelling' (Kubavat et al., 2012). 23

Figure 1-17 Structural diagrams of CFC and HFA propellants that are suitable for use in MDI formulations. 25

Figure 1-18 Different phases of HFA-134a across a range of temperatures, all conditions were recorded at 1 atm pressure apart from the critical conditions. 25

Figure 2-1 (a) Tetragonal geometry of methane with labelled angles and bond lengths. (b) Flat geometry of ethylene molecule with labelled angles and bond lengths. (c) Butane molecule showing staggered conformation to minimise steric repulsions. 32

Figure 2-2 (a) Chair conformation of cyclohexane with labelled C-C-C bond angle. (b) Flat geometry of benzene molecule with labelled bond angles. (c) Structure of polycyclic molecule, steroid fluticasone propionate. 33

Figure 2-3 Potential energy for a point charge interacting with a dipole as function of both distance and dipole angle (Israelachvili, 2011). 35

Figure 2-4 Potential energy for dipole-dipole interactions as function of both distance and dipole orientation (Israelachvili, 2011). 36

Figure 2-5 Example solubility curve and super-solubility diagram. The solid and dashed black lines represent equilibrium solubility and super solubility line, respectively. The red lines represent different crystallisation methods. Adapted from (Mullin, 2001). 39

Figure 2-6 Free energy diagram for nucleation. The dashed line is total free energy, ΔG , equal to the sum of bulk volume energy, ΔG_V , and surface energy, ΔG_S . Nuclei must reach a critical radius, r_c , to crystallise (Mullin, 2001). 40

Figure 2-7 Different nucleation mechanisms of nucleation. (a) BCF, growth by screw dislocations. (b) B&S, growth from surface nucleation. (c) Relationship between

mechanisms and supersaturation levels. (d) and (e) RIG, growth on a smooth surface transitioning to presence of a kink (Clydesdale et al., 1997a). 42

Figure 2-8 2-D growth planes of a crystal showing the variation in growth rate means some faces of the initial 3-D nucleus are not present once growth has finished (Clydesdale et al., 1997a). 43

Figure 2-9 (a) Shows the cell axes and respective angles. (b) Atom positions defined with the unit cell. (c) Lattice structure consists of multiple unit cells (Clegg, 1998). 44

Figure 2-10 Examples of unit cells, (a) is a body-centred cubic cell where all edge lengths and angles are equal. (b) Is a Primitive monoclinic structure with non-90° β angle (Tilley, 2006). 44

Figure 2-11 Example synthon of fluticasone propionate showing the distance between the centres of geometry. Direction defined with respect to the unit cell. 45

Figure 2-12 Varied molecular conformations in Ritonavir's polymorphs, Form I (a) and Form II (b). The torsional angle change is highlighted by an asterisk (Wang et al., 2021). 46

Figure 2-13 Examples of Miller Indices planes relative to a unit cell. (a) shows the (100) plane dissects the a-axis. (b) Shows the (110) plane dissects a and b-axis (Tilley, 2006). 47

Figure 2-14 Examples of external morphologies with faces defined by Miller Indices (hkl) (Docherty et al., 1991). 48

Figure 2-15 Examples of different crystal habits. (a) High aspect ratio needles of Lovastatin crystals produced through cooling crystallisation from methanol, and (b) more prismatic crystals from hexane (Turner et al., 2019). (c) Shows small FP particles crystallised through the addition of an anti-solvent (Bártová et al., 2022). 48

Figure 2-16 Wulff plot illustrating the different growth directions and distances of surfaces relative to the nucleation centre (Docherty et al., 1991). 49

Figure 2-17 Process of deciding if interacting molecule is within the same slice as central molecule, A. e.g., Molecule B is outside the slice and D is within the slice (Clydesdale et al., 1991). 51

Figure 2-18 (a) Examples of bond-stretch and angle bend mechanisms, with Harmonic and Morse energy profiles as a function of bond length. (b) Example of torsion stretch mechanism, with Cosine energy profile as a function of torsion angle. 54

Figure 2-19 (a) Energy profile of 12-6 Lennard-Jones potential, representative of van der Waals interactions between two atoms. Total energy is the sum of attractive and repulsive terms (Maghfiroh et al., 2020). (b) Example of attractive and repulsive coulombic interactions. 55

Figure 2-20 Summary of procedure for MD simulations numerically solving the equations of motion. After step 1, simulations cycle through steps 2 through 4. 57

Figure 2-21 An image of the experimental set up and a labelled diagram of vial used for slow evaporation. 59

Figure 2-22 (A) Shows the Olympus BX51 Optical Microscope and (B) shows Keyence VHX1000 Optical Microscope when linked to a computer. 59

Figure 2-23 Image of the Malvern PANalytical Empyrean XRD machine used to characterise recrystallised FP. 60

Figure 2-24 Spherical polar coordinates with respect to a stationary target molecule and mobile probe molecule (Hammond et al., 2003). 65

Figure 2-25 Molecule-molecule grid-based search. A probe molecule occupies each of the orange points surrounding the target molecule and interaction energy is measured. 66

Figure 2-26 Molecule-surface grid-based search. A 3-D grid over crystal surface, probe molecule occupies each cell. Surface embedded in a matrix. Interaction energy between molecule and crystal slab below then predicted (Ramachandran et al., 2015). 67

Figure 2-27 Overview of the DL Suite. A series of packages that combined to build, perform, and analyse molecular dynamics simulations. 69

Figure 2 28 Example RDF for a liquid with 1st and 2nd coordination shells highlighted. 73

Figure 2-29 HFA-134a molecule categorised into two halves based on its induced dipole. Group A refers to the carbon atom of the tri-fluoroalkane, (C)F₃, and group B refers to the carbon in the mono-fluoroalkane, (C)H₂F. 73

Figure 2-30 Example of a linear interaction with critical distance of 5 Å between three A groups. The 1st and 3rd atoms are further than the critical distance, so it is linear. 74

Figure 2-31 Four atoms are defined: h, i, j and k. The non-bonded interaction between atoms i and j have a separation distance ≤ 7 Å. The dihedral angle, ϕ , is equivalent to

the angle between the green and blue planes in the diagram. When viewed along the non-bonded interaction between atoms i and j , the dihedral angle, ϕ , represents the twist between the bonded axes. 74

Figure 3-1 Melting and boiling points of fluoro-ethanes; molecules with an ethane skeleton and different numbers of fluorine atoms. Ordered based on molecular mass and varying number of fluorine atoms. (van Nes and Vos, 1978). (Lide, 2005). (Meyer and Morrison, 1991). (Brunelli and Fitch, 2002). (Pace. and Aston., 1948). 80

Figure 3-2 Polarizability of different fluorinated ethane molecules. Atomic partial charges showing the effect of additional fluorine atoms. 80

Figure 3-3 Lattice energy of HFA-134a as a function of the limiting radius, predicted using the Dreiding potential. Total lattice energy (black) is broken up into its constituent parts, van der Waals (red) and coulombic (blue). 81

Figure 3-4 (A) Unit cell of monoclinic HFA-134a, the carbon of (C)F₃ is blue whereas the carbon of (C)FH₂ is red. Fluorine atoms are lime green and hydrogen atoms are white. (B) The packing of 2x2x2 unit cells viewed down the a-axis. 83

Figure 3-5 Images of synthons A - F with their separation distance labelled and which molecule of the asymmetric unit they belong to. Carbon atoms are coloured based on their group, the carbon of (C)F₃ is blue whereas the carbon of (C)FH₂ is red. Fluorine atoms are lime green and hydrogen atoms are white. 84

Figure 3-6 (A) Position of the top six strongest synthons relative to each other. The carbon of (C)F₃ is blue and the carbon of (C)FH₂ is red. Fluorine is fluorescent yellow and hydrogen white. (B) Spacefill model of the monoclinic phase. The foreground shows a layer connected by the strong synthons, A, B, C, and D, shown by black lines. 86

Figure 3-7 (A) Diagram of equivalent pseudo cubic structure within monoclinic structure. Each molecule's central point (centroid) is coloured navy blue, distances are measured between these points. (B) Shows HFA-134a's BCC cell with edge length dimensions. 88

Figure 3-8 (A) The (040) plane in HFA-134a's monoclinic phase unit cell. (B) The BCC phase unit cell with the (110) plane highlighted. These planes are equivalent and dissect the same five centroids, which are represented by navy-coloured spheres. 88

Figure 3-9 Looking down the equivalent (001) face of the psuedo cubic shape in the monoclinic phase. Each molecule's centre point is coloured navy blue. The closest interactions, synthons A and D, travel diagonally in the equivalent cell. 89

Figure 3-10 A proposed BCC layout for HFA-134a, based on the previously proposed structure of ethane (van Nes and Vos, 1978), where molecules occupy the $Im\bar{3}m$ space group positions. Within each molecule the carbon of (C)F₃ is blue and the carbon of (C)FH₂ is red. The central point represents the possible orientations as molecules rotate about their centres of mass on each lattice point. 90

Figure 4-1 Molecular RDF plot for different temperature simulations of liquid HFA-134a. The inset graph shows the first peak. The coordination number of the 203 K simulation is shown in the upper x-axis. 95

Figure 4-2 (a) Molecular RDF patterns of liquid simulation at 203 K, blue, and BCC solid phase, black. Both were normalised by the same number density. (b) Closest contacts of a BCC solid relative to a central point, black, 8 nearest, red, 6 second nearest, green, 12 third nearest, blue. Fifth nearest, purple. 97

Figure 4-3 Atom pair RDF graphs for simulations at 203 K. These grouped into their different variations: carbon-carbon, carbon-hydrogen, carbon-fluorine, fluorine-fluorine, fluorine-hydrogen, and hydrogen-hydrogen. The notations include atoms in brackets, these represent the atoms involved in the RDF, e.g., C(H₂)F represents the hydrogens of that group. 99

Figure 4-4 Atom pair RDF graphs for simulations at 263 K. These grouped into their different variations: carbon-carbon, carbon-hydrogen, carbon-fluorine, fluorine-fluorine, fluorine-hydrogen, and hydrogen-hydrogen. The notations include atoms in brackets, these represent the atoms involved in the RDF, e.g. C(H₂)F represents the hydrogens of that group. 100

Figure 4-5 Atom pair RDF graphs for simulations at 323 K. These grouped into their different variations: carbon-carbon, carbon-hydrogen, carbon-fluorine, fluorine-fluorine, fluorine-hydrogen, and hydrogen-hydrogen. The notations include atoms in brackets, these represent the atoms involved in the RDF, e.g., C(H₂)F represents the hydrogens of that group 101

Figure 4-6 Example three carbon interaction with critical distance of 5 Å between three A groups [i.e., the (C)F₃ carbon atoms], the first and third atoms are further than the critical distance, so the interaction is referred to as linear rather than a ring. Snapshot of 323 K trajectory file showing example 'linear interactions'. Distances and angles between three group B, (C)FH₂ carbon atoms, (red) have been labelled. The group B, (C)F₃ atoms, are coloured blue, fluorine is fluorescent yellow, and hydrogen is white. 102

Figure 4-7 Distribution of three-body intermolecular interaction within a critical distance of 5 Å, between three A groups [A-A-A] and three B groups [B-B-B]. Distributions are coloured based on their temperature. Each graph shows an example interaction diagram. The mean number of interactions for each simulation temperature is shown as an inset graph with standard deviation included. 103

Figure 4-8 (A) Probability of the 1--2--3 vector angle between three A groups, including a diagram highlighting the angle, θ . Two temperatures, 203 K is blue, and 323 K is red. (B) Proposed BCC layout for HFA-134a with a highlighted angle between molecules centres of geometry. Each molecule represented by the two carbons; group A is the blue carbon atom of (C)F₃, whereas group B is the red carbon atom of (C)FH₂. 103

Figure 4-9 Distribution of three-body intermolecular interaction between three alternating carbon atom groups within a critical distance of 5 Å. [A-B-A] Shows the A...B...A interaction and [B-A-B] is the B...A...B interaction. Distributions are coloured based on their temperature. The mean number of interactions for each simulation temperature is also shown with standard deviation included. 104

Figure 4-10 The dihedral angle, ϕ , is equivalent to the angle between the green and blue planes. Atoms i and j must have a separation distance ≤ 7 Å. The angle, ϕ , can be seen when viewed along the non-bonded interaction between atoms i and j. 105

Figure 4-11 Probability of non-bonded dihedral angle distribution between the different carbon-carbon axes. Showing when the two A groups are closest (A---A), two B groups are closest (B---B), and an A and B group are close (A---B). All graphs show three different simulation temperatures, 203 K is blue, 293 K is green, and 323 K is red. 105

Figure 4-12 Non-bonded vector angle distribution between different carbon-carbon axes, at two different simulation temperatures, 203 K is blue, and 323 K is red. Showing when group A to A [A-A], B to B [B-B], and A to B [A-B]. 106

Figure 5 1 Fluticasone Propionate molecule with possible H-bond donator and acceptor atoms labelled green and red, respectively. S and R enantiomers are highlighted orange and purple, respectively. The molecule is divided into three sections: α , β , γ . 113

Figure 5-2 Form I, DAXYUX unit cell, the right-hand image is viewed down the b-axis. This shows the non-90° angle present in the monoclinic unit cell. 115

Figure 5-3 Form II, DAXYUX01 unit cell, the right-hand image is viewed down the b-axis. This shows all angles in the orthorhombic unit cell are 90°. 115

Figure 5-4 (a) Overlay of molecular conformations, DAXYUX structure (Form I) is coloured with grey carbon atoms, and DAXYUX01 (Form II) structure is pink. (b) The γ section's two parts: fluoro-methyl-sulfanyl-carbonyl and propionate. 116

Figure 5-5 Space-fill representation of FP molecule in structures of Form I DAXYUX and Form II DAXYUX01. Atoms coloured relative to partial charge calculated through MOPAC method. Deeper blue or red coloured atoms represent stronger negative or positive partial charges, respectively, while white atoms are closer to neutral. 117

Figure 5-6 Lattice energy of form I and II fluticasone propionate, predicted using the Dreiding force field at different limiting radii. Total lattice energy and its electrostatic contribution are shown. 118

Figure 5-7 Synthon A in the Form I structure relative to the unit cell. (A) is viewed down the b-axis and (B) is viewed down the a-axis. Intermolecular distance between centres of geometry is 7.65 Å. 119

Figure 5-8 Synthon B in the Form I structure, (A) relative to the unit cell, (B) is viewed down the a-axis. Intermolecular distance between centres of geometry is 9.04 Å. 120

Figure 5-9 Synthon C in the Form I structure, (A) relative to the unit cell, (B) is viewed down the c-axis. Intermolecular distance between centres of geometry is 10.78 Å. 121

Figure 5-10 Synthon D in the Form I structure, (A) relative to the unit cell, (B) is viewed down the a-axis. Intermolecular distance between centres of geometry is 9.21 Å. 121

Figure 5-11 Synthon E in the Form I structure, (A) relative to the unit cell. It passes in the direction of the c-axis. (B) is viewed down the c-axis. Intermolecular distance between centres of geometry is 10.98 Å. 122

Figure 5-12 Synthon A in the Form II structure, (A) relative to the unit cell, intermolecular distance between centres of geometry is 9.21 Å. (B) is viewed down the c-axis with an inset of F---HC interaction. (C) shows the F---HC and F---HO interactions. 123

Figure 5-13 Synthon B in the Form II structure, (A) relative to the unit cell, it points in the c-axis direction. (B) is viewed down the c-axis and this shows the molecules are super imposed on top of each other. Intermolecular distance between centres of geometry is 7.65 Å. 124

Figure 5-14 Synthon C in the Form II structure, (A) relative to the unit cell, intermolecular distance between centres of geometry is 8.26 Å. (B) is viewed down the c-axis. 125

Figure 5-15 Synthon D in the Form II structure, (A) relative to the unit cell, intermolecular distance between centres of geometry is 11.57 Å. (B) is viewed down the c-axis. Inset shows a Space-fill representation of the closest interatomic distances between the two molecules interacting in synthon D. 126

Figure 5-16 Synthon E in Form II structure, (A) relative to the unit cell. (B) Viewed down the c-axis, synthon points in the a-axis direction, with intermolecular distance of 11.5 Å. (C) Shows the H-bond between hydroxyl and carbonyl group. 127

Figure 6-1 (A) Predicted morphology predicted, all faces are labelled. (B) Viewed down the a-axis, and (C) viewed down the b-axis. 134

Figure 6-2 FP recrystallised via slow evaporation from methanol over 24 hours. Optical microscope image taken using 5x zoom (A) and taken with 10x zoom (B). 136

Figure 6-3 FP recrystallised via slow evaporation from methanol over 4 weeks. Collection of images captured using an optical microscope with 5x zoom. 137

Figure 6-4 FP recrystallized via slow evaporation from methanol over 4 weeks. Captured using an optical microscope, the lens was tilted at an angle of 35° relative to the sample. 137

Figure 6-5 FP recrystallized from ethanol over 4 weeks. Captured using an optical microscope. 138

Figure 6-6 FP recrystallised via slow evaporation from ethanol and 10 wt% water over 4 weeks. Optical microscope images taken using 5x zoom. 138

Figure 6-7 PXRD patterns of FP recrystallised from methanol, ethanol, and original micronized sample. Compared with previously measured patterns of Form I (Čejka et al., 2005) and Form II (Kariuki et al., 1999). 140

Figure 6-8 Original attachment energy morphology was modified to resemble experimental crystals. New morphology is more elongated and the (020) and (0-20) faces are no longer present. Capping faces have an angle of 28°, matching experimental observations. 141

Figure 6-9 (A) Surface chemistry of (100) when viewed down the c-axis, important groups are circled. (B) Topology of (100) surface, coloured by rugosity, higher parts are yellow and lower parts are blue. (C) Coloured by polar interaction proclivity, H-bond acceptor groups are red and donor groups blue. 142

Figure 6-10 Surface chemistry of (110) with important groups circled, (A) is viewed down the c-axis and (B) is perpendicular to that view. (C) Topology of (110), coloured

on rugosity, higher parts are yellow and lower parts are blue. (D) Coloured by polar interaction proclivity, H-bond acceptor groups are red and donor groups blue. 143

Figure 6-11 (A) Surface chemistry of (1-10) when viewed down the c-axis with unit cell and important groups labelled. Topology of (1-10) surface, (B) colours the surface based on rugosity, higher parts are yellow and lower parts are blue. (C) H-bond acceptor groups are coloured red and donor groups coloured blue. 144

Figure 6-12 (A) Surface chemistry of (020) when viewed down the a-axis with unit cell and important groups labelled. Topology of (020) surface. (B) Colours the surface based on rugosity, higher parts are yellow and lower parts are blue. (C) Shows H-bond acceptor groups are coloured red and donor groups coloured blue. 145

Figure 6-13 (A) Surface chemistry of (0-20) when viewed down the a-axis with unit cell and important groups labelled. Topology of (0-20) surface. (B) Colours the surface based on rugosity, higher parts are yellow and lower parts are blue. (C) Shows H-bond acceptor groups are coloured red and donor groups coloured blue. 146

Figure 6-14 (A) Surface chemistry of (001) when viewed down the a-axis with unit cell and important groups labelled. Topology of (001) surface. (B) Colours the surface based on rugosity, higher parts are yellow and lower parts are blue. (C) Shows H-bond acceptor groups are coloured red and donor groups coloured blue. 147

Figure 6-15 (A) Surface chemistry of (011) when viewed down the a-axis with unit cell and important groups labelled. Topology of (011) surface. (B) Colours the surface based on rugosity, higher parts are yellow and lower parts are blue. (C) Shows H-bond acceptor groups are coloured red and donor groups coloured blue. 148

Figure 6-16 (A) Surface chemistry of (0-11) when viewed down the a-axis with unit cell and important groups labelled. Topology of (0-11) surface. (B) Colours the surface based on rugosity, higher parts are yellow and lower parts are blue. (C) Shows H-bond acceptor groups are coloured red and donor groups coloured blue. 149

Figure 6-17 Predicted morphology of FP with faces classified as either polar or non-polar based on the observed surface chemistry. The symbol Rg represents surface roughness from measured rugosity. Note some surface properties are labelled by their form, i.e., {100} represents (100) & (-100) as both faces have the same properties. 150

Figure 6-18 Top six strongest interactions of FP interacting with FP. Each interaction is from a unique grid point. 151

Figure 6-19 Grid point positions with interaction energies greater than -1 kcal/mol, ethanol with green grid points and water with blue grid points. 152

Figure 6-20 (A + B) Two different angles showing examples of the strongest interactions between FP and methanol, grid points of interactions <-3 kcal/mol are also visualised. (C) Partial charges of methanol probe. 153

Figure 6-21 (A + B) Two different angles showing examples of the strongest interactions between FP and ethanol, grid points of interactions <-3 kcal/mol are also visualised. (C) Partial charges of ethanol probe. 154

Figure 6-22 (A + B) Two different angles showing examples of the strongest interactions between FP and water, grid points of interactions <-3 kcal/mol are also visualised. (C) Partial charges of water probe. 155

Figure 6-23 (A + B) Two different angles showing examples of the strongest interactions between FP and HFA-134a, grid points of interactions <-3 kcal/mol are also visualised. (C) Partial charges of HFA-134a probe. 155

Figure 6-24 Visualisation of the strongest interaction between methanol and the (001) surface. The methanol probe has been circled. 156

Figure 6-25 Interaction energies of methanol probing FP's surfaces, side faces are outlined with a dashed line. Contribution to total interaction energy % is represented red squares for vdW, green circles for H-bonds, blue triangles for electrostatic. 157

Figure 6-26 Visualisation of the strongest interaction between ethanol and the (011) surface. The ethanol probe has been circled. 158

Figure 6-27 Interaction energies of ethanol probing FP's surfaces, side faces are outlined with a dashed line. Contribution to total interaction energy % is represented by red squares for vdW, green circles for H-bonds, blue triangles for electrostatic. 159

Figure 6-28 Visualisation of the strongest interaction between water and the (001) surface. The water probe has been circled. 160

Figure 6-29 Interaction energies of water probing FP's surfaces, side faces are outlined with a dashed line. Contribution to total interaction energy % is represented by red squares for vdW, green circles for H-bonds, blue triangles for electrostatic. 129

Figure 6-30 Visualisation of strongest interaction between HFA-134a and (110) surface. The probe has been circled. 162

Figure 6-31 Interaction energies of HFA-134a probing FP's surfaces, side faces are outlined with a dashed line. Contribution to total interaction energy % is represented by red squares for vdW, green circles for H-bonds, blue triangles for electrostatic. 163

Figure 6-32 Visualisation of the strongest interaction between FP and the (110) surface. The two molecules with similar orientations have been circled. 164

Figure 6-33 Interaction energies of FP molecule probing FP's surfaces, side faces are outlined with a dashed line. Contribution to total interaction energy % is represented by red squares for vdW, green circles for H-bonds, blue triangles for electrostatic. 165

Figure 6-34 Attachment energy morphology modified by incorporating ethanol probe interaction energies, Model 1. Model 2 also accounted for surface roughness. 166

Figure 6-35 Attachment energy morphology modified by incorporating methanol probe interaction energies, Model 1. Model 2 also accounted for surface roughness. 167

Figure 6-36 Attachment energy morphology modified by incorporating water probe interaction energies, Model 1. Model 2 also accounted for surface roughness. 167

Figure 6-37 Varied surface area % of particle morphologies: Original attachment energy model, experimentally fitted needle shaped modification, and Platelet modification fitted to SEM images of micronized particles. 169

Figure 7-1 Proposed workflow on how to continue from this thesis and implement molecular modelling into the development of inhalation devices. 179

Figure A-1 Labelled atoms of fluticasone propionate. First, letter corresponds to its element, second, the number is the repetition of that element. 183

Figure A-2 Predicted lattice energy of Form I fluticasone propionate, DAXYUX. Predicted using the Dreiding and Tripos 5.2 force field potentials with identical charges. 188

Figure A-3 Molecular RDF for simulation size test. A cubic box filled with different number of HFA-134a molecules was simulated using the PCFF potential, for 1 ns at 293 K, at 20 atm pressure in the NPT ensemble. 189

Figure A-4 Thermal expansion of HFA-134a, average density from molecular dynamics simulations using different force fields is compared to physical measurements by Padua et al, 1996, illustrated by red points. 191

Figure A-5 Molecular RDF of simulations testing production run length. A cubic box filled with 1000 HFA 134a molecules simulated using the Peguin potential, for 5 and 100 ns. At 293 K 20 atm pressure in the NVT ensemble. 192

List of Tables

Table 1-1 Maximum solubility of FP in different solvents, measured at 20 °C (Westmeier and Steckel, 2008). Also, water ^a (Magee et al., 2003).	20
Table 1-2 Physical properties of CFC and HFA based propellants, values from (Vervaeet and Byron, 1999) & ^a (Smyth, 2003).	24
Table 2-1 Typical functional forms of energy terms used in force field potentials. Where, l is bond length. θ is bond-angle. r is non-bonded distance. q is charge. D_e is dissociation energy. n is an integer. α , k , ϵ and σ are parameterised constants for atom types (Young, 2001).	53
Table 2-2 Details of micronized FP powder used in recrystallisation experiments.	58
Table 2-3 Details of different solvents used in recrystallisation experiments.	58
Table 3-1 Chemical structures and physical properties of ethane, difluoro, tetrafluoro, and hexafluoro ethanes. a (van Nes and Vos, 1978). b (Lide, 2005). c (Meyer and Morrison, 1991). d (Brunelli and Fitch, 2002). e (Pace. and Aston., 1948).	79
Table 3-2 Summary of the crystal properties of HFA-134a's two solid forms, previously measured using powder x-ray diffraction (Brunelli and Fitch, 2002).	82
Table 3-3 Top six strongest synthons are ordered on total interaction strength (Eng), with their van der Waals (vdW) and coulombic (Coul) components included. Multiplicity (Mult) represents frequency per unit cell. Distance (Dist) was measured between centres of geometry. Synthon symmetry was detailed (Symm Op) and which molecule of the asymmetric unit (AU). Also, percentage contribution to lattice energy (Latt %).	84
Table 3-4 Non-bonded vector angles of the different solid-state synthons. This is the equivalent dot product angle between the two vectors of a C-C axis. Group A are the (C)F3 carbon atoms and group B are the (C)H2F carbon atoms.	85
Table 3-5 Non-bonded dihedral angles of the different solid-state synthons. This represents the twist between the two C-C axes in the synthon. Group A are the (C)F3 carbon atoms and group B are the (C)H2F carbon atoms.	86
Table 4-1 Number of molecules in the first shell and sum of first and second co-ordination shells at a range of simulation temperatures.	96
Table 4-2 Closest contacts in a BCC formation with distance as a function of cell edge and as actual distance for BCC phase of HFA-134a.	97

Table 5-1 Crystal properties and experimental conditions for fluticasone propionate's two polymorphs. DAXYUX and DAXYUX01 refers to the reference codes used in the structural database for form I and II, respectively. 114

Table 5-2 Attributes of the top five strongest synthons of Form I, DAXYUX. Including: Interaction type, Which molecule of the asymmetric unit, Z, Distance between centres of geometry, Interactions strengths. 119

Table 5-3 Attributes of the top five strongest synthons of Form II, DAXYUX01. Including: Interaction type, Which molecule of the asymmetric unit, Z, Distance between centres of geometry, Interactions strengths. 123

Table 6-1 BFDH identified forms belonging to FP, ordered descending from the largest d-spacing. Each form represents two equivalent faces. 133

Table 6-2 Slice, attachment, and surface energy of each form, predicted at a radius when lattice energy was fully converged. D-spacing and surface area % also listed. Note, labels refer to equivalent morphological faces: (100) represents (100) & (-100). 135

Table 6-3 Growth directions Form I FP synthons relative to morphology faces. If directed outside the growth slice, the interaction was categorised as contributing to face growth via attachment energy (Att), and if it was within the growth slice it contributed to slice energy (Slice). 136

Table 6-4 Number of unique grid points per solvent with energies greater than the specified values for interactions between FP-solvent. 152

Table 6-5 Average interaction energy of FP and HFA-134a probing different FP crystal surfaces. Weighted based on surface area % of different morphologies. 169

Table A-1 Atomic partial charges for DAXYUX Form I, calculated using semi empirical AM1 method within MOPAC 184

Table A-2 Atomic partial charges for DAXYUX01 Form II, calculated using semi empirical AM1 method within MOPAC 185

Table A-3 Atomic charges for solid-state HFA-134a assigned using the MOPAC method. The VUZQIQ structure contains two molecules in the asymmetric unit. 186

Table A-4 Atomic charges for relaxed ethanol probe assigned using the MOPAC method. 186

Table A-5 Atomic charges for relaxed methanol probe assigned using the MOPAC method. 187

Table A-6 Atomic charges for relaxed water probe assigned using the MOPAC method.	
187	
Table A-7 Intramolecular parameters for HFA-134a for Peguin force field	190
Table A-8 Partial charges for HFA-134a assigned by Peguin's optimised force field	190
Table A-9 Average cohesion interaction energy of FP probing different FP crystal surfaces. Weighted based on surface area % of different morphologies.	193
Table A-10 Average wetting interaction energy of HFA-134a probing different FP crystal surfaces. Weighted based on surface area % of different	193

Nomenclature

α	- Molecule Polarizabilities
ϵ_0	- Permittivity of Free Space
θ	- The Bragg Angle
λ	- Wavelength
ρ	- Number Density
ΔH_{sub}	- Sublimation Energy
μ	- Dipole Moment
a	- Acceleration
$a, b, c,$	- Unit Cell Axis Dimensions
$d(\varphi)$	- Non-Bonded Dihedral Angle
d_{hkl}	- Inter-Planar Spacing
E	- Energy
E_{att}	- Attachment Energy
E_{Bend}	- Angle Bending Energy
E_{Elec}	- Electrostatic Interaction Energy
E_{latt}	- Crystal Lattice Energy
E_{sl}	- Slice Energy
E_{Stretch}	- Bond Stretch Energy
E_{Torsion}	- Torsional Angle Energy
E_{vdW}	- van-der-Waals Energy
F	- Force of Interaction
$G(r)$	- Radial Distribution Function
I_1 and I_2	- Ionisation Energies
k	- Boltzmann's Constant
m	- Atom Mass
n_r	- Number of atoms in bin of spherical distance r
$n(\varphi)$	- Number of samples with angle φ
N	- Coordination number or Total number of samples
ρ	- Number density
q	- Point Charge
R	- Ideal Gas Constant
r	- Separation Distance or Spherical Radial Distance
R_g	- Surface Rugosity
T	- Temperature
t	- Time
Δt	- Timestep

u	- Point Dipole
U_{hkl}	- Surface Growth Rate
U_{solute}	- Solute Interaction Energy
U_{solvent}	- Solvent Probe Interaction Energy
V_r	- Volume bin at spherical distance r
x	- Atom Position
$X, Y, Z,$	- Where the Plane Intercepts Cell Edge Length

Abbreviations

ADDOPT	- Advanced Digital Design of Pharmaceutical Therapeutics
AFM	- Atomic Force Microscopy
AM1	- Austin Model 1
AMBER	- Assisted Model Building with Energy Refinement
API	- Active Pharmaceutical Ingredient
ASPD	- Aerosolised Particle Distribution
AU	- Asymmetric Unit
BCC	- Body Centred Cubic
BFDH	- Bravais-Friedel-Donnay-Hakker
CAB	- Cohesive Adhesive Balance
CFC	- Chloro-Fluoro-Carbon
COPD	- Chronic Obstructive Pulmonary Disease
CSD	- Cambridge Structural Database
DL	- Daresbury Laboratory
DLVO	- Derjaguin, Landau, Verwey and Overbeek
DPI	- Dry Powder Inhaler
e.g.	- For example
EPSRC	- Engineering and Physical Sciences Research Council
FDA	- Food and Drug Administration
FP	- Fluticasone Propionate
FPF	- Fine Particle Fraction
GWP	- Global Warming Potential
H-Bond	- Hydrogen Bond
HFA	- Fluorinated Hydrocarbon
HPC	- High Performance Computer
HPMC	- Hydroxypropyl Methylcellulose
ICS	- Inhaled Corticosteroids
i.e.	- That is, That is to say
IPA	- Isopropyl Alcohol
LABA	- Long-Acting Beta ₂ Agonists
LJ	- Lennard-Jones
MC	- Monte Carlo
MD	- Molecular Dynamics
MDI	- Metered Dose Inhaler
MMAD	- Mass Median Aerodynamic Diameter
MNDO	- Modified Neglect of Differential Overlap

NDDO	- Neglect of Diatomic Differential Overlap
NGI	- Next Generation Impactor
NICE	- National Institute for Health and Care Excellence
NPT	- Moles (N), Pressure (P), And Temperature (T)
NVE	- Moles (N), Volume (V), And Energy (E)
NVT	- Moles (N), Volume (V), And Temperature (T)
OPLS	- Optimised Potentials for Liquid Simulations
PCFF	- Polymer Consistent Force Field
PEG	- Poly Ethylene Glycol
PET	- Pentaerythritol
PM3	- Parameterisation Model 3
PSD	- Particle Size Distribution
PTFE	- Polytetrafluoroethylene
PXRD	- Powder X-Ray Diffraction
RDF	- Radial Distribution Function
SABA	- Short-Acting Beta ₂ Agonists
SCA	- Surface Component Analysis
SEM	- Scanning Electron Microscope
STFC	- Science and Technology Facilities Council
SX	- Salmeterol Xinafoate
vdW	- van der Waals
XRD	- X-Ray Diffraction

Chapter 1: Introduction to Intermolecular Interactions of Metered Dose Inhaler Formulations

Summary: The wider research context is introduced, specifically the importance of metered dose inhalers and difficulties associated with designing them. From this, the research question and objectives for the study are proposed.

Then, an overview of previous studies on the performance of MDI formulations is provided. Focusing on how intermolecular interactions affect the cohesion and adhesion of solid drug particulates suspended in liquid propellant.

Chapter 1: Introduction to Intermolecular Interactions of Metered Dose Inhaler Formulations

1.1.1 Introduction to Research Context

1.1.1.1 Background of Inhaler Devices

There are many different drug delivery routes and they each have their own advantages. Fundamentally, they all aim to transport active pharmaceutical ingredients (API) to a patient's bloodstream for them to take effect. Apart from intravenous injections, drugs delivery routes must pass through different parts of the body before entering the bloodstream. Formulations are designed to account for this variation, where an API is combined with excipient ingredients to target a specific route. For example, they can be formulated as tablets, capsules, or liquids. These must pass through the gastrointestinal tract which can be a relatively slow process, so excipients are included to help speed it up. Other routes include respiratory, topical, rectal, eye and parenteral. Each delivery method has their own advantages and may be chosen to target specific areas of a body. For instance, a respiratory route can deliver drugs to a patient's lungs and enter the bloodstream quickly due to their highly permeable membranes. Therefore, it is a common route used to treat patients suffering from respiratory illnesses.

Asthma and chronic obstructive pulmonary disease (COPD) are widespread. It is estimated that 1 in every 12 people of the UK suffer from asthma (AsthmaUK, 2022), and the term COPD describes two diseases, emphysema and chronic bronchitis. Inhalers help to provide treatment for these respiratory illnesses and can be categorised into three main types: pressurised metered dose inhalers (commonly referred to as MDI), dry powder inhalers (DPI) and nebulisers. All devices have the same basic mechanism of generating a medicinal aerosol which the patient inhales. This has the advantage of being a non-invasive, and pain-free route which can directly target the site requiring attention. Also, compared to oral delivery, the lungs have low enzymatic drug deactivation, which minimises the dosage needed and lowers side-effects (Sosnowski, 2018). This form of administration is considered very effective, so it has been used to treat diabetes via inhaled insulin with the DPI branded as Afrezza (Afrezza, 2022).

The vapour pressure of a liquid propellant is utilised to generate aerosols in MDIs. When activated, the drug formulation is atomised for the patient to inhale and the metering valves ensure the same volume is emitted each time (Stein et al., 2014). MDIs are beneficial as they are portable and do not require a power source to generate the spray. Although, some patients struggle with the correct inhalation technique, resulting in poor

lung deposition (Clark, 1995). DPIs house capsules containing a consistent dose of the API in powder form. When actuated by the patient, the capsules are opened and the powder can be inhaled, this powder typically consists of coarse carrier particles that transport finer drug powder. DPIs have the advantage of being portable and breath-actuated, so particle movement is always synchronised with a patient's breath. However, this can also be counteractive as it requires a minimum flow rate to move the particles which some people may struggle to produce (Clark, 1995). Nebulisers produce an aerosol by atomising a medicinal solution and they can be classified into two types: jet small volume and ultrasonic. Jet nebulisers use compressed air to pump the solution into a larger cup so that pressure lowers and the liquid vaporises (Ali, 2010). Ultrasonic nebulisers use piezoelectric crystals that generate high frequencies to produce respirable droplets (Clark, 1995). The downside of nebulisers is that some designs contain a dead volume which reduces efficiency as some formulation remains in the device. Also, nebulisers require a power source which is an added complication. Some nebulisers are large and must be plugged into mains power source, whereas smaller devices can be battery operated and therefore portable (Clark, 1995).

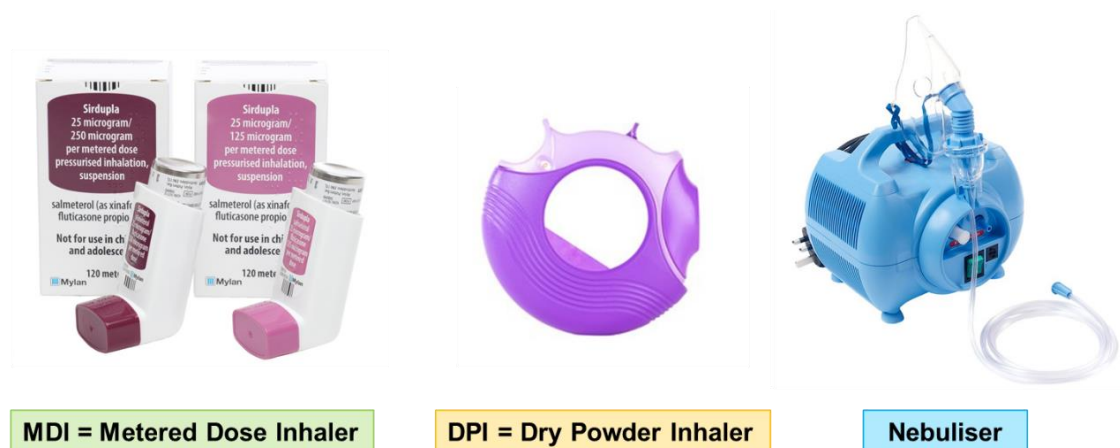


Figure 1-1 Images of three main types of inhalers, MDI (KindevaDrugDelivery, 2015), DPI (Shutterstock, 2022), Nebuliser (PrimaryCareSupplies, 2022).

Devices are prescribed based on the patient's personal preference and their ability to use them correctly (Dolovich et al., 2005). For example, if patients struggle using their device it introduces uncertainty in the amount of drug deposited to the target area in the lungs. MDIs are the most popular type of inhaler, estimated to represent 53% of total portable inhalers (excluding nebulisers) sold in Europe between 2019 and 2020 (IQIVA, 2020). The advantage of MDIs over DPIs is they do not require a minimum flow rate to release the API (Newman, 2005). The following section describes the mechanism behind MDIs and details how material selection impacts performance.

1.1.1.2 Description of Metered Dose Inhalers

From a user's perspective, MDI devices comprise of two separate pieces: an aluminium canister and a plastic actuator. The canister is filled with a liquid formulation, and this slots into the actuator, which is designed to guide the generated aerosol. A detailed diagram of the MDI contents is labelled in Figure 1-2 below. Liquid formulations consist of a pressurised propellant, one or more APIs, and dispersants such as surfactants. APIs can be dissolved as solutions, suspended as solid particulates (Newman, 2005), or a combination of both (Stein et al., 2015). Typically, canisters are pressurised at 300-500 kPa (approx. 3-5 times atmospheric pressure) to ensure the propellant is in dynamic equilibrium as a liquid and gas phase. The gas phase's vapour pressure must remain constant throughout the canister's lifetime, irrespective of how much formulation is present (Myrdal et al., 2014). It is responsible for pushing the liquid phase into the metering chamber, providing impetus for vaporisation and causing the same dosage to be emitted with each actuation. When a canister is pressed into the actuator it activates the valve, this shuts off the chamber to the container of liquid and releases a measured volume from the metering chamber to atmospheric pressure. The formulation vaporises inside the actuator nozzle and atomises a high velocity spray of inhalable aerosol (Newman, 2005).

The pressurised canister filled liquid propellant is a defining feature that distinguishes MDIs from other inhaler devices. The vapour pressure of the propellant's gas phase stores the potential energy which enables a high velocity aerosol to be produced while still being portable. The canister is a closed system, so after each actuation and the liquid levels decrease, more molecules join the gas phase to fill the increased volume and thus keeping vapor pressure constant. In earlier version of MDIs, chlorofluorocarbons (CFCs) were used as liquid propellants. They matched the key requirements of being non-flammable, non-toxic and offering a constant vapour pressure which is independent of the mass present (Smyth, 2003). However, ozone depleting CFCs have been banned from use in MDIs since 2009 due to the Montreal agreement (EPA, 2022). Fluorinated hydrocarbons (HFAs) have been popular replacements, (Sicard and Baker, 2020) used as propellants and over a range of other industrial applications (Sicard and Baker, 2020). They offer similar density and vapour pressures and are non-ozone depleting which brings a lower global warming potential (GWP) compared to their CFC counterparts. Nevertheless, there have been calls for them to be phased out in favour of alternatives with even lower GWPs (Pritchard, 2020).

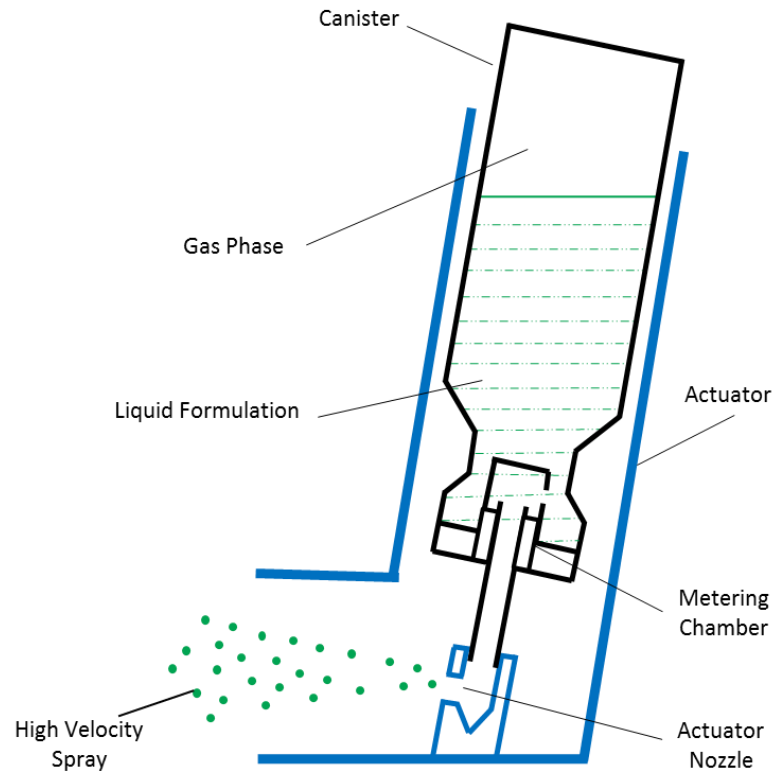


Figure 1-2 Labelled schematic of a typical metered dose inhaler device's contents. An actuator houses the formulation filled canister, when activated an aerosol is emitted.

Low API lung deposition can arise from poor timing, inhaling too quickly and not exhaling fully before using the device (Levy et al., 2013) (van Holsbeke et al., 2018). Breath actuated MDIs have been developed which overcome synchronisation problems as they only spray when the patient inhales (Smith et al., 1998). Also, mouthpiece spacers can be fitted to improve efficiency by reducing spray velocity and thus reducing throat deposition (van Holsbeke et al., 2018).

According to the national institute for health and care excellence (NICE), the three most commonly prescribed treatments for asthma and COPD are; inhaled corticosteroids (ICS), Long-acting β_2 agonists (LABA) and Short-acting β_2 agonists (SABA) (NICE, 2021). Corticosteroids act as anti-inflammatories to prevent asthma attacks in patients and β_2 agonists are classed as bronchodilators which provide relief by widening airways. It has been found that excessive exposure to LABAs, e.g. salmeterol xinafoate, can actually increase asthma related breathing problems, to reduce the chances of these problems they are often combined with corticosteroids, e.g. fluticasone propionate (Daley-Yates et al., 2014). These APIs can be formulated as either solutions or suspensions. Solutions have the advantage of uniform API distribution, but generally drugs have limited solubility in HFAs which means co-solvent excipients are required, consequentially these additional ingredients in the inhaled particles can have undesired pharmacological effects on the patient (Myrdal et al., 2014). Therefore, suspension

formulations tend to be a more popular choice. It is important these mixtures are formulated to minimise non-uniform drug particle dispersion, which can impact performance (Myrdal et al., 2014).

1.1.1.3 MDI Suspension Formulation Requirements and Challenges

For effective drug delivery, inhalers must consistently generate an aerosol within a desired particle size distribution (PSD) over the device's entire shelf life. It is generally recognised that particles must have diameters between 1-5 microns ($1-5 \times 10^{-6}$ m) so they deposit in the lungs rather than the throat (Carvalho et al., 2011) (Myrdal et al., 2014) (O'Donnell and Williams, 2013). Other formulation ingredients must be combined in way to optimise performance and ensure the size distribution of the generated aerosol remains in the desired region. For instance, propellants can be chosen to reduce the likelihood of solid phase separation from liquid, stabilising agents can also be included to minimise permanent particle growth caused by aggregation of suspended drug particles. Further disruption may be caused by loss of drug particles sticking to canister materials which could impact the dosage of drugs delivered. Also, materials such as gasket seals may leach into the formulation over time. Therefore, device hardware must be also designed to keep their impact on the formulation to a safe standard.

The performance of MDIs is rooted in their complex formulations and previous studies have shown how interactions within these formulations relate to physio-chemical properties of the materials. It is possible for molecular modelling to be implemented further and investigate these interactions from a different perspective using a first principles approach. Such as understanding how particle surface chemistry affects cohesion and adhesion. This has the potential of benefitting formulation development by aiding a quality by design approach and being a step in the direction of digital design for MDI formulations. Due to the variety in materials used in MDIs, there are wide selection of possible case-studies which a first principles investigation can be implemented. The following sections will outline the scope of this report and the materials selected.

1.1.2 Research Question and Objectives

Research Question

How can molecular modelling techniques examine the inter-molecular interactions influencing particle cohesion and adhesion, which may disrupt the performance of MDI suspension formulations?

Research Aims & Objectives

- Establish favoured structuring of pure propellant and evaluate strength of inter-molecular interactions. Forms foundation to investigate wetting and dissolution when other suspension ingredients are included.
- Generate a solid-state profile of an inhalation drug. From a first principles approach, determine the strength of intermolecular interactions in its crystal structure and predict particulate external morphology.
- Investigate the wetting of particle surfaces with liquid propellant and determine how the propellants structuring is affected by different chemistries of crystal faces.
- Develop a workflow for investigating the effect formulation ingredients and device materials have on particle interactions, including cohesion and adhesion.

1.1.3 Selection of Methods

Predominantly molecular modelling will be employed to investigate inter-particulate interactions of these materials, it has the advantage of being able to examine specific crystal surfaces which is difficult through experiments. A molecular dynamics approach is used to model the disordered liquid propellant structure, it is capable of modelling molecular movement with time at different temperatures. Empirical force fields are also applied to predict the strength of intermolecular interactions within a crystal structure, and subsequently predict the shape of drug particulates. One advantage to this approach is being able to understand the molecular scale properties of each surface, and then testing how they would have different interactions with formulation ingredients.

1.1.4 Selection of Materials

Materials used in this study were chosen to represent the two core ingredients of an MDI suspension formulation: liquid propellant and solid API particle. 1,1,1,2-Tetrafluoroethane, known commercially as HFA-134a, was selected for study as it is one of the standard propellants used in MDI formulations. The corticosteroid fluticasone propionate (FP) was chosen as the API particle of interest. In 2020, it was the 23rd most prescribed drug in the United States (ClinCalc, 2023), and is commonly delivered via MDIs.

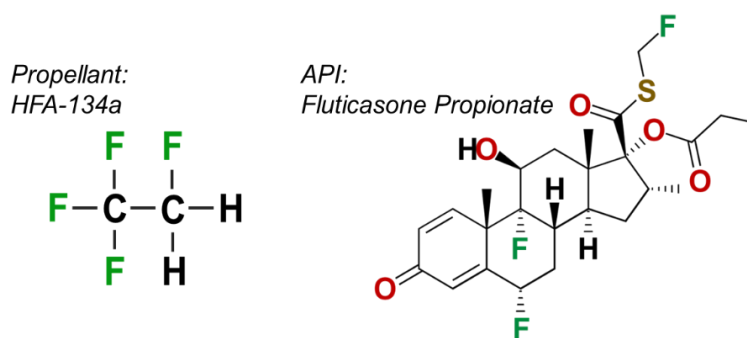


Figure 1-3 Molecular structures of propellant 1,1,1,2-tetrafluoroethane, HFA-134a. And active pharmaceutical ingredient fluticasone propionate, $C_{25}H_{31}F_3O_5S$.

1.1.5 Project Management

Work in this project was funded by the EPSRC Centre for Doctoral Training in Complex Particulate Products and Processes (cP3), EPSRC Grant EP/L015285/1. Also, additional funding came from Kindeva Drug Delivery with guidance from Alex Slowey. This project was also in collaboration with INFORM 2020 - Molecules to manufacture: processing and formulation engineering of inhalable nano-aggregates and micro-particles, EPSRC grant EP/N025075/1, which was led by Professor Darragh Murnane from the University of Hertfordshire.

My main project supervisor was Dr Robert Hammond, who aided me with choosing the research direction of this project. I also had similar help from co-supervisors Professor Kevin Roberts and Alex Slowey of Kindeva Drug Delivery.

Technical assistance with molecular modelling tools such as Habiti98 and Systematic Search was provided by Dr Hien Nguyen at the University of Leeds, who was part of the INFORM 2020 project.

Assistance with the DL suite of molecular dynamics packages came from Dr Ian Rosbottom, who was part of the advanced manufacturing supply chain initiative 'Advanced Digital Design of Pharmaceutical Therapeutics' (ADDoPT) project Grant No. 14060.

Further help with the DL suite of molecular dynamics package was provided by both Dr Chin Yong and Professor Ilian Todorov of science and technology facilities council (STFC) at the Daresbury Laboratory.

Figure 1-4 Graphical thesis workflow. FP's solid-state profile from molecule to morphology and shows HFA's intermolecular packing across different phases. Combining to examine FP's particulate interactions of surfaces with solvents.

1.2.1 Introduction Intermolecular Interactions of Metered Dose Inhaler Formulations

The following sections outline the science behind MDI suspension formulations and explains how intermolecular interactions can impact device performance. First, an overview of the formulation development process will show where the main challenges are. It is important to understand particulate properties, such as size, shape, and surface chemistry, as they can impact performance. It is also important to know the liquid propellant intermolecular structuring as things could affect surfactant solubility. Therefore, recent work looking at intermolecular structuring of the materials of interest, HFA-134a and FP, is summarised. Other relevant studies are also discussed, such as organic crystal particulate morphology formation and molecular modelling approaches that can advantageously looking at specific crystal faces.

1.2.2 Formulation Factors Influencing Performance

1.2.2.1 MDI Formulation Science

It is important that MDI devices consistently produce the same dosage of aerosol over their entire shelf life, this means each formulation must be carefully designed to meet all required performance and safety specifications. The journey of MDI formulation creation begins with a drug and then other ingredients are combined. As the inherent physical properties of each drug can vary, it is important the other ingredients are carefully chosen to optimise performance. HFA propellants are usually selected, these are non-toxic, non-flammable and have a suitable density. The propellant is pressurised into the liquid phase within the cannister, and this provides the driving force for atomisation. Stabilising agents, such as surfactants, can also be included in the formulation. Steric forces prevent irreversible particle agglomeration and adhesion to canister components. The nature of HFA propellants means ethanol must be used as a co-solvent to dissolve some surfactants. Care must be taken as ethanol can affect evaporation rates (Myrdal et al., 2014) (O'Donnell and Williams, 2013).

Formulation development can be complex due to the inter-linking relationship between different physical characteristics. The procedure has been categorised into three main steps: *Pre-Formulation*, *Formulation* and *Stability*. These are shown in Figure 1-5, with sub-steps included. During the *Pre-Formulation* stage, current models are used to develop a suspension that does not permanently separate and assess ingredient compatibility. Then, the *Formulation* stage judges how successful this design is based on different performance metrics, the output aerosol should be in desired range. Finally, *Stability* tests the formulations shelf life. For example, identify if permanent phase

separation or excessive material leaching has occurred over an extended period of time.

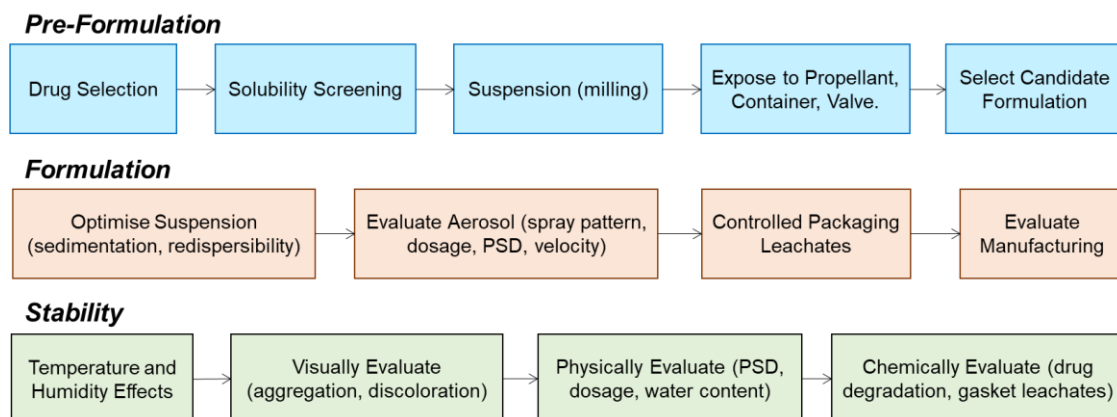


Figure 1-5 Overview of three main stages of developing an MDI suspension formulation: Pre-formulation, Formulation and Stability. Adapted from (Vervaet and Byron, 1999).

Formulations containing APIs with a slight solubility in the propellant can lead to Ostwald ripening through particle surface re-crystallisation, resulting in an increase in particle size (Myrdal et al., 2014). Water may enter the formulation during manufacturing as it has a higher solubility in HFA than CFCs. This can be detrimental with water degrading the compound, changing density, aerosol evaporation rate and causing surfactant precipitation (Myrdal et al., 2014).

Phase separation may occur in the suspension due to gravity. Particles denser than the liquid may settle to the bottom, those which are less dense can rise and cream out of the liquid. Smaller diameter particles have slower velocities so are less likely to settle or cream. Also, particles with similar densities to the formulation have lower settling velocities. Therefore, separation by settling or creaming can be minimised by matching the liquid propellant density to the solid particles (O'Donnell and Williams, 2013) (Myrdal et al., 2014). Reducing below 0.5µm can bring about Brownian motion if the particle density is not too high. Furthermore, it is possible to reduce settling with hollow particles produced by spray drying (O'Donnell and Williams, 2013). Some lightly flocculated suspensions can be re-dispersed and then still perform as required by being shaken before use or de-agglomerated from the shearing forces of atomisation (Vervaet and Byron, 1999) (O'Donnell and Williams, 2013).

Particles have an affinity to stick to the canister walls or to other components of the canister, this reduces dosage and wastes valuable API. Low-energy fluoropolymer coatings for the canister and components have been developed to minimise their interaction with the formulation (Stein et al., 2014). Also, metering valves must be

selected to minimise moisture ingress and leaching into the formulation, strict guidelines are in place by the U.S. food and drug administration (FDA) regarding acceptable levels of leachates delivered to the patient (O'Donnell and Williams, 2013).

1.2.2.2 Emitted Particle Size Importance

Aerosols can also vary based on density, to help with comparisons one can standardise to spheres of the same density. The aerodynamic diameter, is the diameter required for an equivalent particle of unit density 1 to produce the same terminal settling velocity when falling through still air (De Boer et al., 2002). It is described for spherical particles by Equation 1-1, where d_a is the aerodynamic diameter, d is the geometric diameter, ρ is particle density, ρ_o is unit density. Non-spherical particles can include a shape factor.

$$d_a = d \cdot \sqrt{\frac{\rho}{\rho_o}} \quad \text{Equation 1-1}$$

It is generally considered that particles must have aerodynamic diameters less than $5\mu\text{m}$ to be inhaled effectively by the lungs. Smaller particles travel further and deposit deeper within lungs compared to larger particles. The size of emitted particles may vary compared to the size of particles in the canister. This is because each aerosol droplet can contain many particles, therefore the aerosol particles will be larger than those in the canister. Larger particles may also break due to the shear force inflicted by actuation (Carvalho et al., 2011).

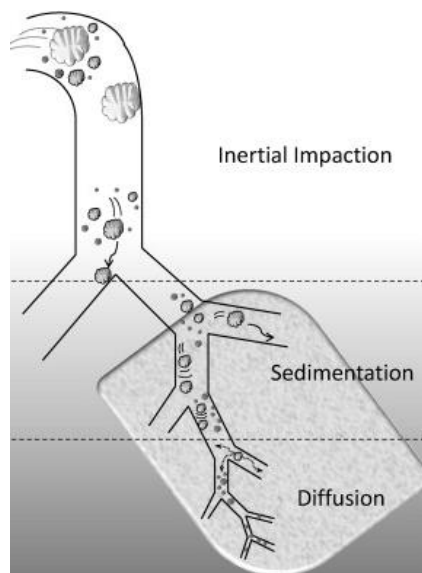


Figure 1-6 Illustration showing how the deposition behaviour of particles depends on size, with smaller particles reaching the lower airways (Carvalho et al., 2011).

One important performance attribute is the aerodynamic particle size distribution (APSD), this describes the size range of particles emitted as an aerosol by the MDI device. APSD can be measured with next generation impactors (NGI), these devices

filter aerosolised particles based on size and calculate their distribution. It is possible to calculate the mass median aerodynamic diameter (MMAD), a particle aerodynamic diameter at which 50% of the total mass is smaller than this value. Also, fine particle fraction (FPF) is the fraction of total mass of particles with an aerodynamic diameter less than 5 μ m (Rowland et al., 2018).

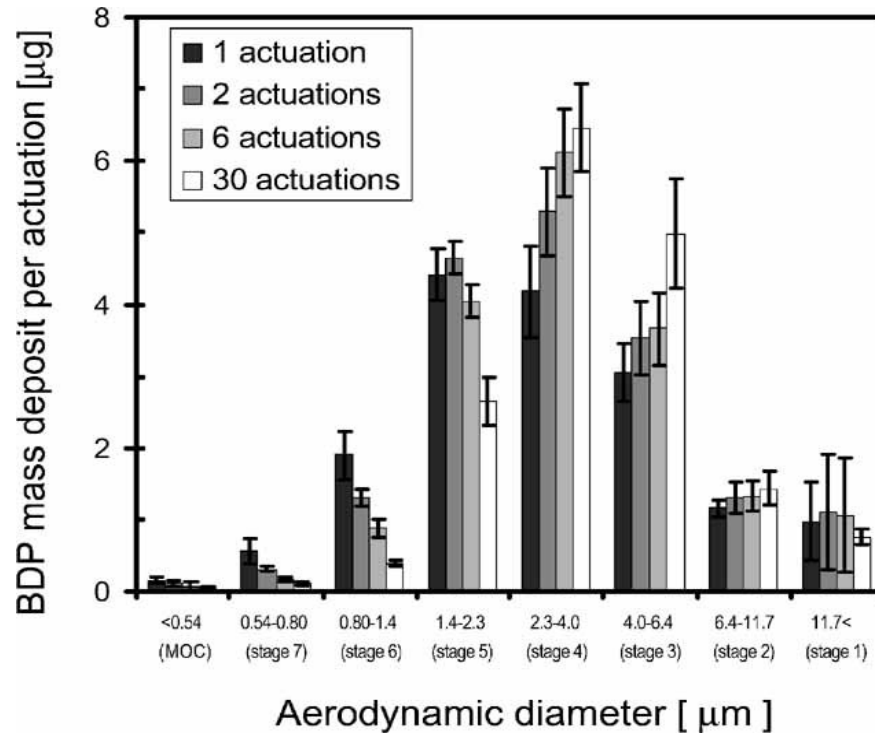


Figure 1-7 Example of APSD measured through an NGI showing the distribution of particle sizes collected at different stages (Kamiya et al., 2004).

1.2.2.3 Physio-Chemical Properties Affecting Aerosolization

Apart from device hardware aspects, such as actuator orifice, the APSD is mostly effected by formulation characteristic, including drug PSD, suspension density and its ability to redisperse (Smyth, 2003). Previous investigations into how these formulation characteristics impact MDI performance helped with development of new products through a quality-by-design approach. It was generally found that increasing the drug PSD caused the emitted APSD to become larger, spreading over a wider range and the MMAD increased (Myrdal et al., 2014) (Pu et al., 2015), and also decreased the emitted FPF (Louey et al., 2004) (Sheth et al., 2017). This shows how the smallest particle size is limited by the input PSD, it does not tend to decrease in size after being in the canister.

Ethanol is often included as a co-solvent to help dissolve surfactant stabilising agents into HFA propellant. The presence of both these excipients can influence the emitted aerosol. Higher ethanol concentrations have been noted to lower the mean emitted FPF (Zhu et al., 2014) (Pu et al., 2015) (Saleem and Smyth, 2013) (Sheth et al., 2017). This is most likely due to ethanol reducing the pressurised propellants vapor pressure which would reduce the atomisation ability and thus lead to larger particle sizes. When surfactant concentrations surpass a certain level, they can also become a hinderance to performance. Studies have shown the MMAD increases which results in lower FPF (Saleem and Smyth, 2013) (Williams III and Liu, 1999). It is believed the low volatility of surfactants reduce the evaporation rate of emitted aerosol particles, resulting in a larger MMAD. Atomic force microscopy (AFM) measurements of particle to canister interactions, observed bridging interactions, where a single surfactant molecule adheres to multiple particles (Ashayer et al., 2004). This may also increase MMAD and lead to formulation instability.

The dosage emitted from a device is also influenced by its surrounding environment. A study found more drug was released at lower temperatures, but smaller particles were achieved at higher temperatures, which lead to deeper more effective deposition. This behaviour was attributed to larger vapour pressures at higher temperatures (Wilson et al., 1991). It was also observed that less drug was delivered at higher temperatures due to the lowering of density (Hoye et al., 2005). Other investigations looked into the effect of humidity on drug particle suspensions depositing onto different canister coatings (Skemperi et al in 2016) (Skemperi et al in 2017). At low humidity deposition was highly dependent on the surface energy, lower surface energy correlated with low drug deposition and vice versa (Skemperi et al in 2016). At higher humidity deposition was dependent on surface roughness, smoother surfaces showed less deposition. It was hypothesised the rougher surfaces entrapped water which increased the adhesive potential (Skemperi et al in 2017). Similarly, drug deposition was also dependent on the surface energy of the coating (Skemperi et al in 2017).

Micronized particles form agglomerates, these must be dispersed when emitted so a suitable aerosol can be inhaled and flow through airways. An investigation into performance of dry powder inhalers found that as interparticle force and agglomerate strength increased, the performance of the emitted FPF decreased due to reduced dispersion (Adi et al., 2011). Atomic force microscopy (AFM) was used to look at the effect of particle surface area on interparticle forces (D'Sa et al., 2014). Micronized particles were found to settle to a smaller volume compared to the spray dried particles with a larger surface area. It was hypothesised this was due to increased contact area. It can be seen in Figure 1-8 that the solid micronized particles have grooves which

interlink to form a larger contact area and increases the cohesion force (D'Sa et al., 2014).

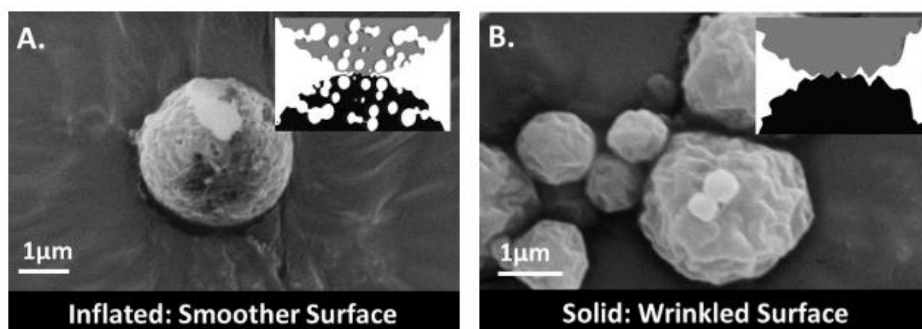


Figure 1-8 Illustration of calcium chloride particles; (A) inflated spray dried particle with smooth surface, (B) solid micronized particle with wrinkled surface (D'Sa et al., 2014)

Other investigations have used AFM to measure the force of interaction between API particles, and with canister wall materials. Studies were performed in the presence of a model fluorinated liquid to represent the propellant in a suspension formulation (Traini et al., 2006c, Traini et al., 2005, Young et al., 2003) (Traini et al., 2007). These resulted in cohesive adhesive balances (CAB) between particles to see the effect on ease of redispersion, aerosol generation and potential wastage (Traini et al., 2005) (Traini et al., 2006a) (Traini et al., 2006b, Traini et al., 2006c, Young et al., 2003). Aqueous suspensions typically follow the DLVO theory, which describes how colloidal stability is a balance of attractive van der Waals and repulsive electrostatic forces. Counterions form an electric double layer around particles and these provide repulsive forces when they overlap at close distances (Verwey, 1947, Derjaguin, 1941). The stability of a suspension can be judged based on the systems zeta potential, a measure of the strength of double layers strength. Unlike aqueous systems, the DLVO theory cannot adequately describe suspensions of relatively non-polar liquids, such as HFAs, because they do not form an electric double layer around particles (Traini et al., 2006b, Traini et al., 2006c, Young et al., 2003). Particle polar surface energy calculations were used to predict work of adhesion, these showed good correlation with experimental measurements and the energy differences were attributed to particle surface roughness not being accounted for in the model (Traini et al., 2006c, Traini et al., 2005). Performance evaluation showed that a particularly hydrophilic API had cohesive particles which resulted in formulations of poor stability, sedimentation occurred rapidly and then agglomerated. This also led to poor lung deposition, as poor re-dispersion ability increased particle size (Traini et al., 2007). Generally, it was found that APIs and canister materials with lower polar surface energy had lower adhesion properties, (Traini

et al., 2006c, Traini et al., 2005, Young et al., 2003) and that longer chained surfactants provided more repulsion forces (Traini et al., 2006b).

A different AFM study highlights the importance of contact area in particle adhesion to canister materials. Figure 1-9 shows surfaces produced using AFM in its traditional imaging mode of three different canister materials: borosilicate glass, aluminium, and polytetrafluoroethylene (PTFE) coated aluminium. Elongated shaped particles formed large areas of contact with planar canister materials, such as the glass, and experienced high adhesive forces. Separation energy between particles and the PTFE coated aluminium was lower compared to interactions with pure aluminium, this was attributed to reduced contact area and lower energy surface (Young et al., 2003).

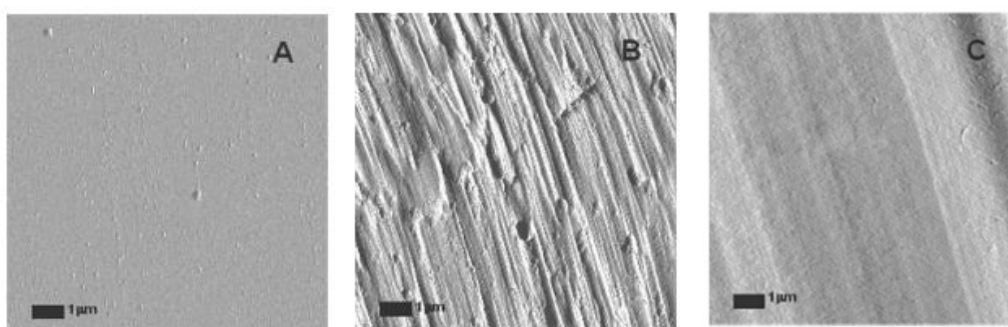


Figure 1-9 AFM images of different cannister walls; (A) borosilicate glass (B) aluminium canister (C) PTFE-coated aluminium (Young et al., 2003)

AFM offers a good opportunity to measure particle cohesion and adhesion forces, the resulting CAB provides a useful indicator of the interparticle forces present. The technique can potentially help formulation design, but standardisation is required as AFM measurements can vary due to differences in particle size, contact area, and length of contact time between substrates (James et al., 2008). Additionally, measurements typically look at the largest face of the particle, thus, interactions of the smaller faces are neglected.

In summary, it has been shown how MDI performance is affected by formulation properties such as environment conditions, canister coating, concentrations of stabilising agents and co-solvent. Furthermore, it was highlighted how the emitted aerosolised PSD can be affected by interactions between micronized particles which are influenced by particle surface polarity and surface roughness. The next section will look at how inherent crystal characteristics can govern particle properties, specifically of the drug fluticasone propionate.

1.2.3 Crystalline Properties of Fluticasone Propionate

1.2.3.1 Particle Size Reduction

Manufacturing steps ensure drug particles are small enough within the desired PSD. The majority of inhalation powder particle size reduction is prepared through milling (Shoyele and Cawthorne, 2006), and spray drying is also popular. Both techniques affect the particle morphology, and in turn this affects aerosolization performance. Therefore, one must understand the impacts of different particle size reduction techniques when formulating. This sub-section will focus on the API of interest, fluticasone propionate.

In general, due to high nucleation rates, anti-solvent crystallisation tends to produce many small drug particles. These are micronized to make the PSD within the desired range. Jet milling reduces particle size by passing through a high velocity jet of air which causes them to rotate at high speeds, the impact of one particle to another can lead to particle attrition through shearing at different faces (Shoyele and Cawthorne, 2006). It tends to produce more angular particles, higher levels of amorphous content, higher surface area and higher rugosity (Moura et al., 2016) (Louey et al., 2004) (Steckel et al., 2003). Micronized FP powder readily sticks to itself, with it being reported to flow as aggregates (Louey et al., 2004), and not flow at all (Steckel et al., 2003).

Fundamentally, particles crystallised via spray drying form when a solution containing the drug is atomised over a counter flowing current of air. Different parameters of the process can be tuned to control the particle size and morphology (Shoyele and Cawthorne, 2006). The resulting PSD tends to be narrower when produced through spray drying, whereas milling produces a high population of smaller particles so the PSD is usually a wider range (Shoyele and Cawthorne, 2006). It is possible to produce rounder and smoother FP (Louey et al., 2004) hollow particles (O'Donnell and Williams, 2013), also elongated and jagged shaped particles (Vatanara et al., 2009) (Westmeier and Steckel, 2008).

In-situ micronization is an alternative way of preparing particles without the need for milling. For example, smaller crystals formed due to a greater degree of increased nucleation rate when using poly ethylene glycol (PEG) as the main solvent and water as the anti-solvent (Murnane et al., 2008a). Separately, hydroxypropyl methylcellulose (HPMC) was included in the anti-solvent solution, this impeded growth and reduced particle size (Steckel et al., 2003). Another alternative is wet polishing, particles are suspended in an anti-solvent, micro fluidisation reduces particle size, and then spray dried to removes the solvent. This produces very smooth and spherical particles (Moura et al., 2016).

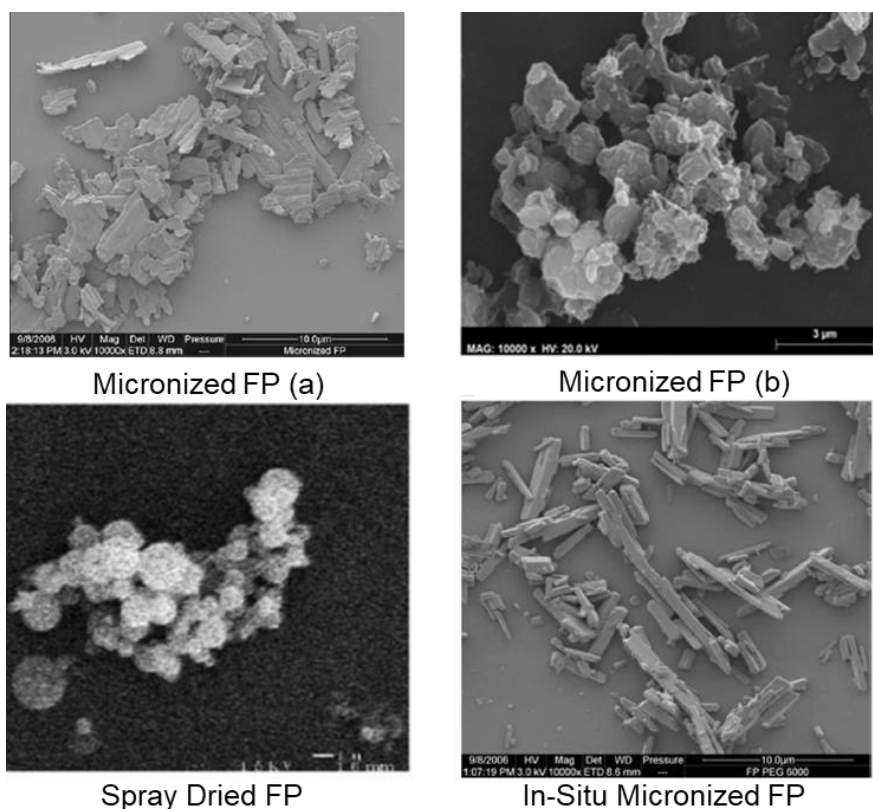


Figure 1-10 SEM images of particles formed by different methods: micronized FP particles (a) (Murnane et al., 2008b) and (b) (Moura et al., 2016), spray dried FP (Louey et al., 2004) and in-situ micronized FP (Murnane et al., 2008a).

The size reduction method alters the particle interaction forces. For instance, jet-milled FP tends to agglomerate and have poor powder flowability, in comparison in-situ micronized FP had better flow properties. This was attributed to the lower interparticle forces, possibly due to coating FP with the polymer, and hence improving flowability (Steckel et al., 2003) (Murnane et al., 2008a). This also affects aerosolization performance. Generally, in-situ micronized powder was better than jet-milled, showing higher FPF (Steckel et al., 2003). When comparing the aerosolization performance of formulations prepared using milled and spray dried particles, milled particles showed stronger cohesive forces and this was hypothesised to be due to differences in particle surface properties (Louey et al., 2004). An AFM study of FP particles produced using anti-solvent shows surfaces are not smooth, even before they are micronized. The AFM image in Figure 1-11 shows the surface has a terraced structure, which could show the inherent roughness of that crystal surface or could be due to the growth mechanism during crystallisation (Bártová et al., 2022). Interestingly, a different study found that changing the solvent used in anti-solvent crystallisation used would change FP's particle morphologies. When these particles were subsequently formulated, the aerosolization behaviour changed depending on the anti-solvent used. Results suggested the crystallisation method altered particle de-agglomeration and de-attachment (Kubavat et al., 2012).

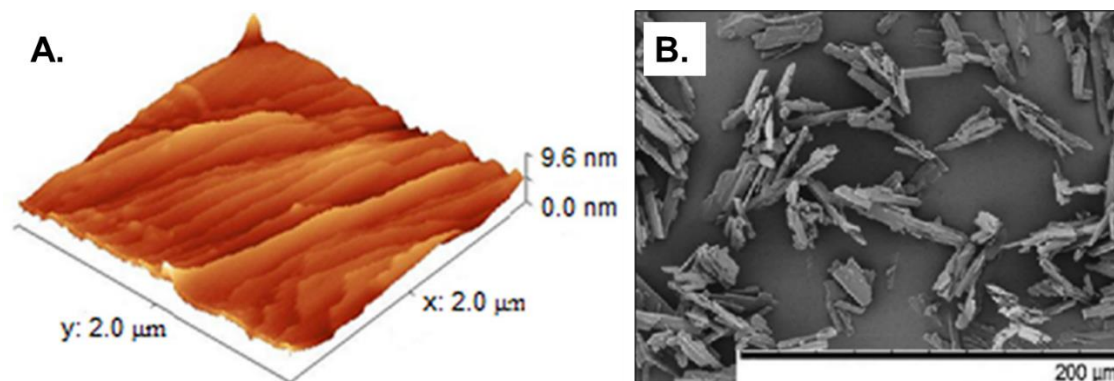


Figure 1-11 (A) AFM image of FP particle surface formed during anti-solvent crystallisation shows a visibly terraced structure. (B) SEM image of same FP particles (Bártová et al., 2022).

1.2.3.2 Crystal Structure and Morphology

Crystallisation conditions determine which crystal polymorph of FP is produced. It has two known polymorphs, Form I used most often in commercial application and it occurs through more common crystallisation techniques, such as anti-solvent (Louey et al., 2004) (Čejka et al., 2005) (Murnane et al., 2008a) (Kubavat et al., 2012). The meta-stable polymorph, Form II, has been reported when super critical carbon dioxide is used as the counter flowing fluid during spray drying (Steckel et al., 1997) (Steckel and Müller, 1998). The main difference in XRD patterns, seen in Figure 1-12, is that only Form II shows a peak at 19.0° , and Form I pattern shows peaks at 15.9° and 16.3° .

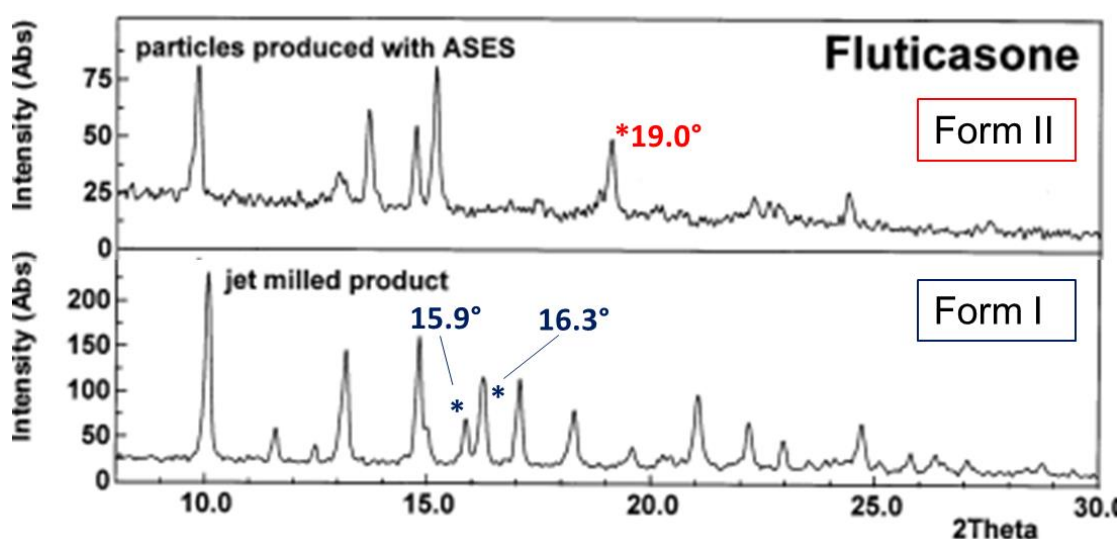


Figure 1-12 FP's powder x-ray diffraction patterns. Form I crystallised with water as anti-solvent and then milled, peaks at 15.9° and 16.3° are highlighted. Form II produced with supercritical CO₂ as anti-solvent, peak at 19.0° is highlighted (Steckel et al., 1997).

FP's large molecular structure affects its solubility, values are listed in Table 1-1. It tends to show better solvation in solutions exhibiting both polar and non-polar properties (Westmeier and Steckel, 2008). Whereas, very low solubility in the solely polar water (< 0.1 µg/ml) (Magee et al., 2003, Davies and Feddah, 2003) and the solely non-polar n-hexane, (Kubavat et al., 2012) both can be used as anti-solvents. The choice of growth solvent has also been found to influence morphology. Plate like crystals have been reported when FP is crystallised from acetone through slow evaporation (Čejka et al., 2005) and anti-solvent crystallisation with the addition of water (Murnane et al., 2008a) (El-Gendy et al., 2011) (Bártová et al., 2022). Plates also seen with anti-solvent crystallisation when FP is dissolved in methanol and water is added (Murnane et al., 2008a), shown in Figure 1-13.

Table 1-1 Maximum solubility of FP in different solvents, measured at 20 °C (Westmeier and Steckel, 2008). Also, water^a. (Magee et al., 2003).

Solvent	Solubility Fluticasone Propionate (mg/mL)
Acetone 100%	34.5
Methanol 100%	3.1
Ethanol 96%	1.7
Water ^a	0.0001

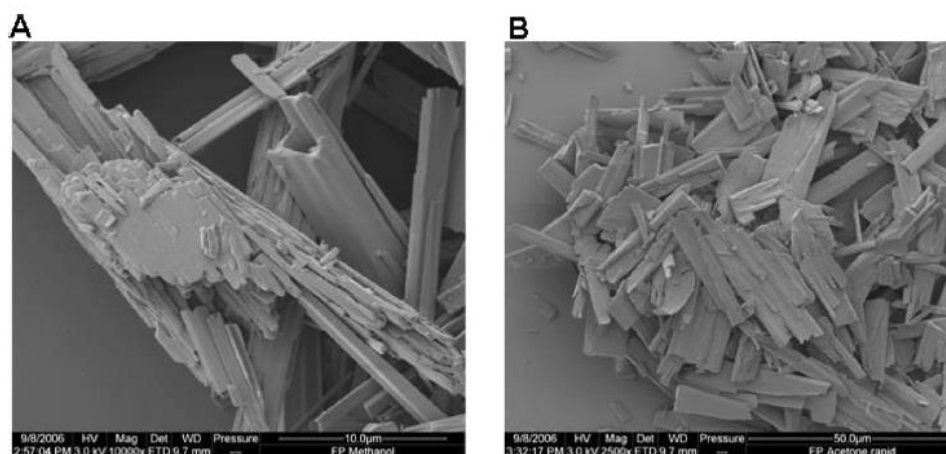


Figure 1-13 FP morphologies, dissolved in Acetone (A) and Methanol (B). Water used as anti-solvent (Murnane et al., 2008a)

Different morphologies were also seen when different anti-solvents were used. First FP was dissolved in acetone, then water, n-hexane, ethyl-acetate, and iso-propanol were added to induce crystallisation. It can be seen in Figure 1-14 that all particles were elongated in shape, those formed using n-hexane and iso-propanol looked more needle-like. Whereas, water and ethyl acetate produced flatter, more plate-like particles (Kubavat et al., 2012).

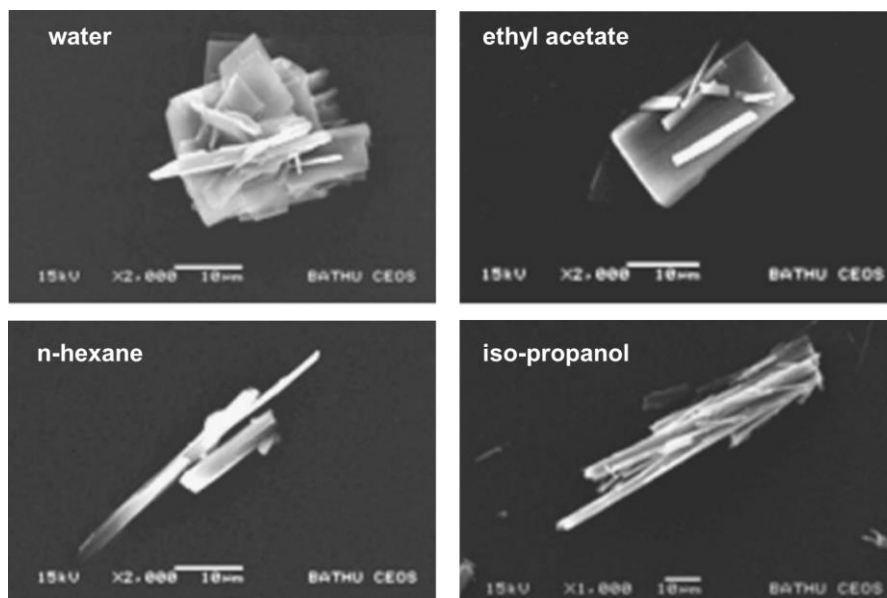


Figure 1-14 SEM images of different shaped particles formed when FP was dissolved in acetone, then different solvents were added to initiate anti-solvent crystallisation: water, ethyl acetate, n-hexane, iso-propanol (Kubavat et al., 2012).

Interestingly, particle morphology also changed when a combination of FP and salmeterol xinafoate (SX) mixtures were crystallised together. SEM of spray dried

particles shows Acetone make them close to needle like. Methanol shortens and flattens the needles. Ethanol also flattens the needles further (Westmeier and Steckel, 2008).

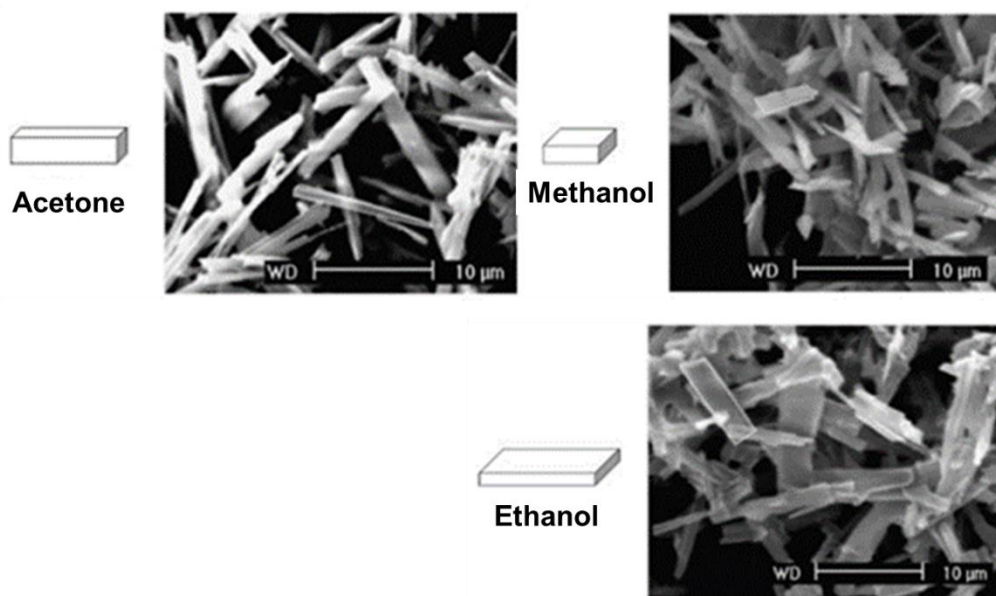


Figure 1-15 SEM images of FP-SX mixtures particle morphologies, spray dried from different solvents: acetone, methanol, ethanol (Westmeier and Steckel, 2008).

Previous attempts to predict FP's particle shape using molecular modelling, in Figure 1-16, are platelets and needles (Ramachandran et al., 2015, Kubavat et al., 2012). The crystallographic faces assigned to each surface differ with each. In one, the (200) crystal form was speculated to be most important and largest of the platelet morphology (Ramachandran et al., 2015). In the other, (010) was hypothesised to be the largest crystal form of both the platelet and needle shapes (Kubavat et al., 2012). No specification of modelling method was provided in this study, it only stated that morphologies made with 'crystal modeller' were compared to SEM images of crystals (Kubavat et al., 2012).

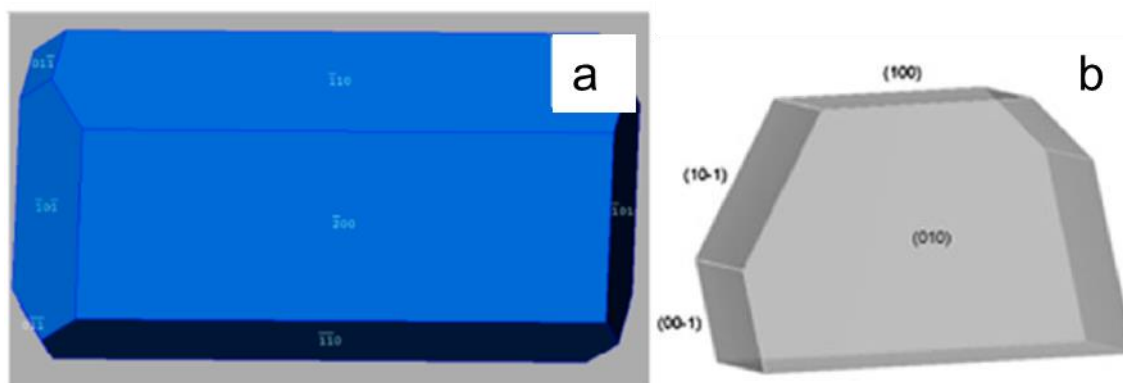


Figure 1-16 Previous FP morphology predictions, (a) using attachment energy method (Ramachandran et al., 2015). and (b) fitted to match experimental morphology via 'crystal modelling' (Kubavat et al., 2012).

Molecular modelling tools can help predict external crystal morphologies by using the solid structures determined through XRD, thus classifying the different surfaces shown. The attachment energy method has reliably predicted crystal morphologies of APIs other than FP (Taulelle et al., 2009) (Turner et al., 2019) (Rosbottom et al., 2015, Moldovan et al., 2017, Wang et al., 2021). This method understood how molecule-molecule interactions were responsible for crystal growth in certain directions. Generally, it is hypothesised that during crystallisation from solvents, certain surfaces are more soluble. As a result, crystal growth is more likely on the surfaces which are less soluble. Other molecular modelling tools were used in combination with the attachment energy morphology prediction to understand how solvation may have inhibited crystal growth in certain directions. These tools applied empirical force fields to systematically-search through the interaction energies between solvent-solute and solvent-crystal surface (Kaskiewicz et al., 2021) (Rosbottom et al., 2018, Rosbottom et al., 2017) (Moldovan et al., 2017) (Turner et al., 2019).

As it has been discussed that particles are usually micronized. It is important to understand which surfaces of these particles might form. This might help with trying to understand why the surfaces post micronization may be more likely to agglomerate. Previous hypothesis that the face with highest absolute attachment energy is more likely to act as a cleavage plane (Roberts et al., 1994). Other hypothesis is to look at the plane with the smoothest overlap between layers. Looking at crystal surface energy and intermolecular interactions. It was proposed that cleavage fracture of pentaerythritol (PET) along (001) was enabled by strong in-plane H-bonding in the $\langle 110 \rangle$ family of directions (Ibrahim et al., 2022).

1.2.4 Structuring of Liquid Propellants

1.2.4.1 Physical Properties of Propellants

HFAs were selected as replacements for CFCs, they could perform similar roles as they shared similar physical properties. Values are listed in Table 1-2. It shows that although they are not identical, important attributes such as density and vapor pressure are comparable. These were essential for controlling atomisation and minimising phase separation, respectively. Corresponding molecular structures are shown in Figure 1-17, the presence of chlorine increases the molecular mass of CFCs compared to their HFA counterparts with equivalent alkyl chain length.

An increased number of chlorine atoms on the CFCs means they have higher polarizability, suggesting stronger intermolecular interactions are formed between these propellants as there is a correlation between higher polarizability and higher liquid density. To compensate for differences in density, different combinations can be prepared in the formulation to match the particles (O'Donnell and Williams, 2013).

The dipole moments and dielectric constants of both HFA propellants are higher than CFCs. This is due to the presence of hydrogen atoms in HFA as electronegative fluorine atoms draw electrons from hydrogen and increase molecule polarity. As a result, HFA molecules can form H-bonds and is capable of a higher moisture capacity compared to CFCs. Furthermore, this causes oxygen containing hydrophilic surfactants to have a higher solubility in HFA, which is why ethanol is included in formulations to help dissolve methyl-based, hydrophobic surfactants (Vervaeet and Byron, 1999) (Blondino and Byron, 1998).

Table 1-2 Physical properties of CFC and HFA based propellants, values from (Vervaeet and Byron, 1999) & ^a(Smyth, 2003).

Propellant	CFC 11	CFC 12	CFC 114	HFA 134a	HFA 227ea
Condensed Formula	CCl ₃ F	CCl ₂ F ₂	C ₂ Cl ₂ F ₄	C ₂ F ₄ H ₂	C ₃ F ₇ H
Molecular mass (g/mol)	137.4	120.9	170.9	102.0	170.0
Density (g/cm³) at 293 K	1.49	1.33	1.47	1.23	1.41
Boiling Point (°C)	23.8	-29.8	3.6	-25.8	-17.3
Dipole Moment (Debye)	0.46	0.51	0.50	2.06	0.93
Dielectric Constant (ε)	2.3	2.13	2.26	9.51	4.07
Polarizability (cm³/molecule)	9.5	7.9	8.5	5.4	5.8
Moisture Content^a (ppm)	130	120	110	2200	610

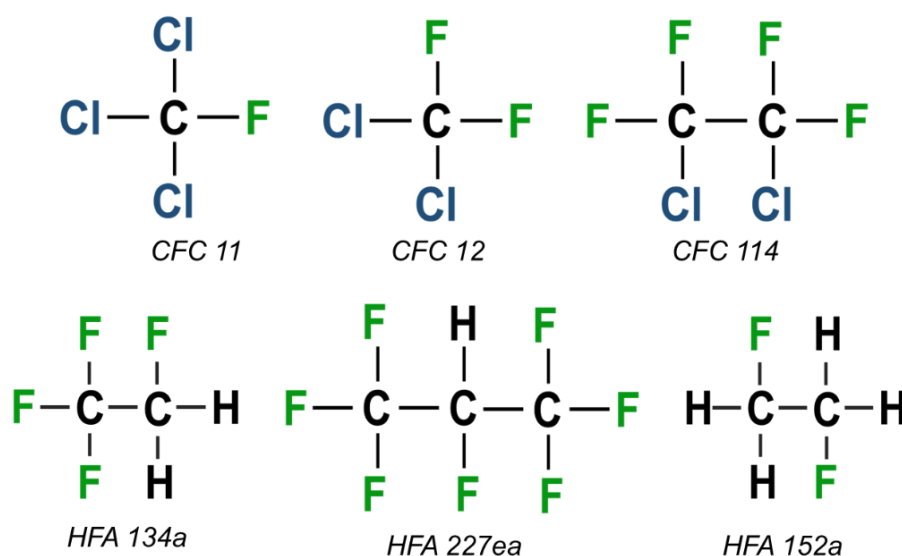


Figure 1-17 Structural diagrams of CFC and HFA propellants that are suitable for use in MDI formulations.

1.2.4.2 HFA Propellants

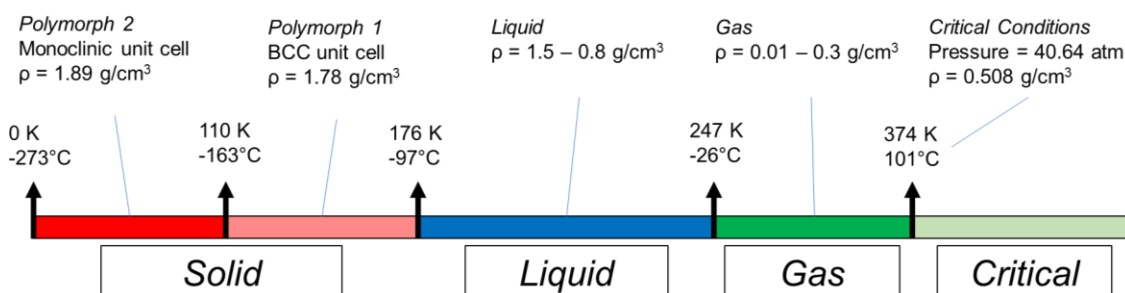


Figure 1-18 Different phases of HFA-134a across a range of temperatures, all conditions were recorded at 1 atm pressure apart from the critical conditions.

HFA-134a is the propellant of interest, it is commonly used in formulations. It has a vapor pressure of 5.6 atm at around 25 °C, MDI canisters are usually pressurised to match this. In its gas phase, the dipole moment was measured to be 2.06 D, it pointed from -ve to +ve towards the point between the hydrogen atoms in the CFH_2 group at angle of approximately 60° relative to the C-C axes (Meyer and Morrison, 1991). The liquid density of HFA-134a's was measured experimentally over different pressures and temperatures. At 1 atm pressure the liquid vaporises at -26 °C (Padua et al., 1996). This is illustrated in Figure 1-18. As temperature is lowered, the propellants HFA-134a initially crystallises into an orientationally-disordered body centred cubic (BCC) structure.(Brunelli and Fitch, 2002) Then, at even lower temperatures, the solid becomes ordered and resembles a monoclinic phase.(Brunelli and Fitch, 2002) This

behaviour was also observed in HFA-152a (Brunelli and Fitch, 2002), hexafluoroethane (Klimenko et al., 2010) and in ethane (van Nes and Vos, 1978).

Powder x-ray diffraction (PXRD) studies of both HFA 134a and 152a's monoclinic phases showed the molecular conformation varied from their staggered, low energy state. The torsion angle around the C-C axis showed a greater change in 152a compared to 134a (Brunelli and Fitch, 2002). It was hypothesised that these monoclinic phases formed due to intermolecular dipole-dipole interactions between its fluorine and hydrogen atoms, i.e. C-H...F (Brunelli and Fitch, 2002).

Molecular modelling has proven itself to be a valuable technique for investigating intermolecular structuring and interaction. A lot of work has gone into using molecular modelling to predict HFA-134a's thermodynamic properties, notably its free energy, vapour-liquid equilibrium behaviour and surface tension (Budinský et al., 2004, Do et al., 2010, Fermeglia et al., 2003, Lisal et al., 1999, Lísal and Vacek, 1996, Lisal and Vacek, 1997, Stoll et al., 2003)(Peguin et al in 2006). A generic force field potential (Jorgensen et al., 1996) was refined to reproduce HFA-134a's experimental vapour-liquid equilibrium (Peguín et al., 2009). It was then used in MD simulations to study the HFA-water interfacial tension (Peguín et al., 2009), and investigate HFA-134a's solvation in ionic liquids (Lepre et al., 2019). This potential was also used in Monte Carlo simulations to investigate HFA-134a's attraction to metal organic frameworks,(Barpaga et al., 2019) thermo-physical properties as part of HFA refrigerant mixtures (Yang et al., 2020), and to look at the liquid phase's microstructure (Do et al., 2010).

Previous liquid simulations have no consensus on how the molecules dipole prefer to align. Some predict the closest molecules tend to an anti-parallel arrangement between the dipoles (Lisal and Vacek, 1997, Lísal and Vacek, 1996), another showed dipoles preferred parallel arrangement, with some tolerance up to 30° (Do et al., 2010). This latter study also showed the molecule's C-C axis align perpendicular to each other and at short distances, with some preference for anti-parallel alignment (Do et al., 2010).

Longer chain fluorinated alkanes have been reported to deviate from typical alkyl linear chains and show helical structures (Zhang and Lerner, 1999, Liu et al., 2007, Jang et al., 2003), and was speculated to be caused by electrostatic repulsions of fluorine atoms or intra-molecular C-H...F hydrogen bonds. A conformational study into HFA-134a showed preference for the staggered conformation, likely due to the small scale of the molecule and minimisation of steric repulsions (Do et al., 2010). This implies that HFA-134a won't show helical structures due to its small scale and focus on minimising steric repulsions.

All liquid simulations showed evidence for C-H...F interaction, the F-H atom-atom RDF had a small peak in the region 2.4–3 Å (Lisal and Vacek, 1997, Lisal and Vacek, 1996), (Do et al., 2010). This is similar to distances seen for weak H-bonds, seen previously in fluoro-benzene crystals (Thalladi et al., 1998) and dimers between CHF₃ molecules (Tsuzuki et al., 2003). The presence of weak H-bonds corresponds to the hypothesis that C-H...F interactions prompt the formations of HFA's more ordered solid monoclinic phases (Brunelli and Fitch, 2002).

1.2.4.3 Weak Hydrogen Bonds in HFAs

Normal H-bonds are classified as types of van der Waals interactions, stronger versions of dipole-dipole interaction. Interaction strengths in the size range of -4 to -16 kcal/mol with distances typically shorter than 2.2 Å (Desiraju and Steiner, 1999). Typically arise due to dipole formed by a hydrogen covalently bonded to highly electronegative atom, such as fluorine, oxygen, and nitrogen. Subsequently, the positive hydrogen atom is donated to an electronegative atom on a separate molecule, which is labelled an acceptor. 'Weak hydrogen bonds' are also dipole-dipole interactions, but the hydrogen is not covalently bonded to a highly electronegative atom and so the dipole is not as strong. Hence, why these are classed as weak H-bonds and are typically weaker than -4 kcal/mol, positioned at distances between 2.2 – 3.0 Å (Desiraju and Steiner, 1999).

Examples of C-H...F interactions have been seen in solid state crystals containing fluorine (Thalladi et al., 1998) (Singla et al., 2020). A study of the Cambridge structural database (CSD) found that fluorine rarely accepted traditional H-bonds with distances shorter than 2.2 Å, weak H-bonds were more common (Dunitz and Taylor, 1997). The C-H...F interactions were believed to stabilise structures and ab-initio techniques predicted interaction energies of -14 kcal/mol (Singla et al., 2020). Other, ab-initio calculations predicted interactions between fluoro-benzene and benzene were as strong as -4 kcal/mol (DerHovanessian et al., 1999), whereas HFA-134a dimers linked by C-H...F were predicted to be -2.4 kcal/mol (Brunelli and Fitch, 2002). Also, ab-initio predictions of C-H...O weak H-bonds had a strength of -3.8 kcal/mol (Alonso et al., 2004).

These weak H-bonds were believed to complement normal H-bonds in liquid systems. C-H...F interactions were hypothesised to promote desired molecular ordering in a spin coated organic solid film (Li et al., 2006). In a separate study, the RDF graphs from MD simulations of fluorinated alcohol hexafluoro-isopropanol in the liquid phase inferred both weak and strong interactions occurred in the same system. Atom-atom interactions showed C-H...F had peaks in the region of 2.7 – 2.9 Å. Whereas, normal H-bonds of

O-H---O interactions had comparatively higher RDF peaks positioned around 1.9 Å (Mondal et al., 2017).

Biomolecules can also be delivered via MDIs and as these APIs are often water soluble, their formulations must be designed to form stable micro-emulsions in liquid HFAs. Investigations into the suitability of a surfactant molecule using MD and ab-initio chemical modelling predicted the interfacial interactions and surface energies associated with these propellant and surfactant molecules, these also speculated the formation of weak H-bonds with HFA propellants (Peguín and da Rocha, 2008, Peguín et al., 2006, Peguín et al., 2007, Selvam et al., 2006, Wu et al., 2007). Weak H-Bonds forming between C-H---F had bond distances 2.7-3 Å with angles ranging between 140-160°. Surfactants with fluorine and with oxygen formed stronger interactions compared to pure methyl chains. The presence of oxygen helped to increase the strength of interactions, these formed stronger (closer and straighter) interactions. Considered to be as strong as normal H-bonds. i.e. this backs up the claim that the H-bonds fluorine forms are weaker compared to oxygen (Peguín and da Rocha, 2008, Peguín et al., 2006, Peguín et al., 2007, Selvam et al., 2006, Wu et al., 2007).

1.2.5 Conclusion

This chapter provided an overview of intermolecular interactions in an MDI formulation, and thus the important role it plays in the device's performance. The development process usually starts with an API and other ingredients are formulated to produce a suitable aerosol in the desired PSD. This an important metric used to differentiate the eligibility of different formulation designs. Therefore, in suspension formulations, the drug's particle properties, such as shape, surface energy and surface roughness play an important role as they can influence permanent particle growth. Propellants also influence formulations, density matching with the drug reduces phase separation and solubility of surfactants can affect stability. It is discussed how HFA propellant's molecular composition affect macro scale properties.

Particle properties varied per API, FP crystalised into elongated, mostly needle shaped morphologies. Particle properties were also affected by size reduction methods, micronized FP easily agglomerated. Previous attempts to predict FP's external morphology and identify its crystal surfaces did not explain how it was caused by inherent intermolecular interactions. There is potential to build upon previous predictions by using the attachment energy method. When complemented with other grid-based search molecular modelling methods, these have proven to be valuable techniques capable of predicting API particulate morphologies from a first principles

approach. Understanding the fundamental intermolecular interactions would help speculate what drives FP's natural needle shape to form. Also, once a morphology is predicted, this could help investigate the different hypotheses proposed of why FP particle agglomerates form.

The presence of hydrogen atoms sets HFAs apart from their CFC predecessors, this provides the ability to form a class of H-bonds known as 'weak H-bonds'. As the name suggests, these are not as strong as conventional H-bonds. But have still been reported to influence molecular orientations in solid and liquid phases of HFA-134a. These were also found to influence the solubility of surfactants in propellants, HFA-134a preferred to dissolve more hydrophilic surfactants due to stronger H-bonds. Molecular dynamics has proven itself as a useful method to understand intermolecular structuring of liquid HFA-134a. Previous hypothesised preferred interactions between pure propellant molecules. But it doesn't show how they vary with temperature. Ultimately, there is potential to investigate the wetting of particulate crystal surfaces and find out which forms stronger interactions with the propellant. However, one must first establish the structures of the ingredients individually before comparing how they change at a solid-liquid interface.

In summary, previous molecular modelling techniques have distinguished surfactant solubility in liquid propellants. This can potentially be implemented as digital drug design tool and streamline formulation development. It would be interesting if a similar approach be used to look at API particulates. Areas where molecular modelling can be further applied have been identified.

Chapter 2: Intermolecular Interactions, Molecular Modelling Background and Method & Materials

Summary: Background is provided on the fundamental science relevant to this thesis. Including details on intermolecular interactions, crystallisation science, and how these can be represented through molecular modelling.

Then, a description of the method followed which correlates to the results shown in chapters 3, 4, 5 and 6. It includes a description of the computational and experimental procedure, with details of the materials used.

Chapter 2: Intermolecular Interactions, Molecular Modelling Background and Method & Materials

2.1.1 Introduction to Intermolecular Interactions, Molecular Modelling

One must understand important fundamental science relative to MDI suspensions before looking at specific cases. Therefore, established background theory is detailed in this chapter, everything which is needed prior to conducting my own investigation. Initially, the theory focuses on the intermolecular interactions which define the molecular scale. These fundamental interactions are defined as atom-atom interactions and collectively are responsible for macro scale behaviour. Then, an introduction to appropriate crystallisation science provides a brief background of how API crystals are formed and how understanding the structure can help control particle properties. It also details how structures are defined with respect to unit cell and miller indices. Finally, an outline of computational chemistry theory explains how molecular interactions are represented as force field potentials. Also, how to predict an external crystal morphology formation, and how force fields are incorporated with Newtonian laws of motion with molecular dynamics approaches.

2.1.2 Fundamental Intermolecular Science

2.1.2.1 Intermolecular Structure Relationship with Material Properties

A molecule's three-dimensional conformational arrangement is fundamentally affected by the bonds connecting different atoms and intramolecular interactions. Thermal energy causes molecular conformations to constantly fluctuate, but some thermodynamically favourable arrangements are seen more frequently and are known as conformers. The molecule's bond lengths, bond angles and torsional angles are optimally arranged to minimise the total potential energy by reducing the bond, angle, torsional, and steric strain energy.

An optimal bond length distance between a pair of covalently bonded atoms must balance attractive and repulsive forces. Initially when atoms are close enough, an attraction is formed between the oppositely charged nuclei and electron clouds, this draws atoms closer together into an optimal bond length. Atoms tend to stay at this point of strongest attraction as the bond energy is at its most negative. When they become too close, positively charged nuclei repel each other, causing a highly positive and repulsive bond energy (McMurry, 1992). Typical bond lengths depend on the

elements involved and their atomic orbitals, for instance an optimal C-C bond length is around 1.54 Å for ethane and 1.34 Å for ethylene, whereas C-H is around 1.09 Å (McMurry, 1992).

The electron orbitals of covalently bonded atoms also influence the angle strain energy. For example, Figure 2-1 (a) shows the tetrahedral shape of methane, CH_4 , arises from sp^3 hybridisation of the central carbon atom which causes H-C-H bond angles to favour an average of 109.5° . This pattern is continued when the alkane chain length increases, an angle of roughly 109.5° for the H-C-H and H-C-C bonds is favoured as chains grow. In contrast, alkenes like an ethylene molecule, C_2H_4 , feature a double bond between carbon atoms in sp^2 orbitals, these bonds do not rotate as freely as those between sp^3 orbitals and this results in a flat shape rather than tetrahedral, with Figure 2-1 (b) showing H-C-H and H-C-C bond angles are 120° (McMurry, 1992).

One must also be aware of the favoured torsion angle when there is free rotation between two carbon sp^3 orbitals, in chemically uniform molecules staggered conformations are typically lower in energy than their eclipsed counterparts. For example, ethane, C_2H_6 , shows energy minima when the H-C-C-H torsion angle is 60° , 180° or 300° , and energy maxima at angles of 0° , 120° or 240° . When alkyl chains increase in length, the arrangements with lowest potential energy tend to be staggered conformations where the large groups are positioned as far away as possible, thus minimising steric repulsions from groups occupying the same positions (McMurry, 1992). This is showcased by butanes structure in Figure 2-1 (c) where the larger methyl groups are bonded to opposing positions of the central ethane molecule. When alternative functional groups are bonded, the favoured angles may differ from those seen in standard alkyl chains, for example, attractive intramolecular interactions via hydrogen bond (H-bonds) may contort the lowest energy conformation.

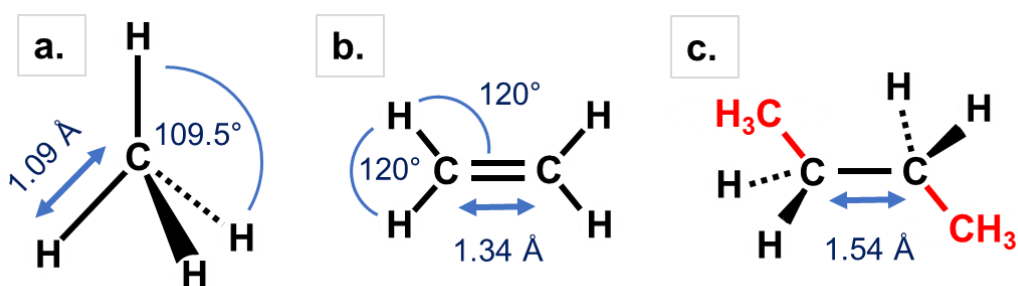


Figure 2-1 (a) Tetragonal geometry of methane with labelled angles and bond lengths. (b) Flat geometry of ethylene molecule with labelled angles and bond lengths. (c) Butane molecule showing staggered conformation to minimise steric repulsions.

The favoured conformations of ringed carbon structures can vary due to the number of carbons present. There are six carbons in the ring of cyclohexane, C_6H_{12} , and it is an interesting example due to the different conformational shapes possible, such as chair, half-chair, twist-boat, and boat. The chair conformation has the lowest energy state so will most likely be seen at equilibrium room temperature conditions (McMurry, 1992). Figure 2-2 (a) shows this conformation is not flat, carbon atoms have sp^3 hybridisation so also follow tetrahedral shapes, with typical C-C-C bond angles of $\sim 111.4^\circ$. Other ringed cycloalkane structures favour this tetrahedral arrangement when only single bonds are present. However, when compared cyclohexane, they are seen less frequently in nature due to the geometrical restraints introducing angle strain energy. The tetrahedral shape is not seen in benzene with the presence of carbon atoms bonded through sp^2 hybridisation making it relatively flat compared to cyclohexane. Figure 2-2 (b) shows the double bonds cause angles to differ from the tetrahedral shape, with C-C-C bond angles of 120° (Levine, 2009). Many active pharmaceutical ingredients are polycyclic molecules consisting of a combination of ringed structures, this includes the corticosteroid fluticasone propionate (FP). Figure 2-2 (c) shows FP's steroid structural skeleton consists of three cyclo-hexane and a single cyclo-pentane ring. These molecules follow the same principles as the simple rings, with angles close to tetrahedral shapes and chair conformations for the cyclo-hexane. They can show both sp^2 and sp^3 hybridised carbon atoms, meaning these molecules show both C-C-C bond angles of $\sim 109.5^\circ$ and 120° .

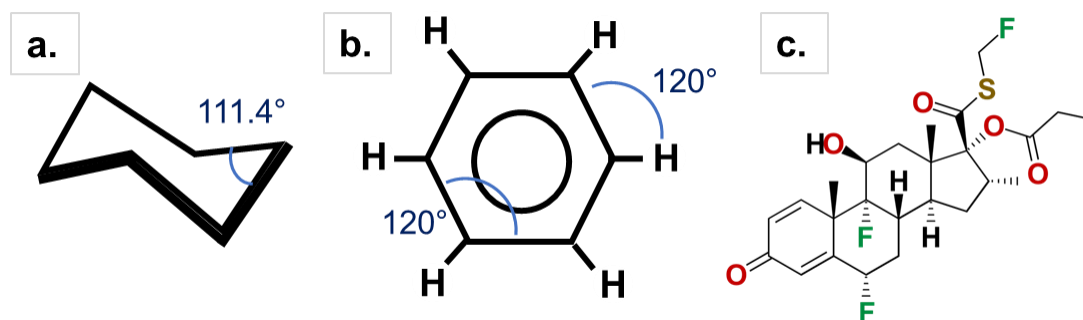


Figure 2-2 (a) Chair conformation of cyclohexane with labelled C-C-C bond angle. (b) Flat geometry of benzene molecule with labelled bond angles. (c) Structure of polycyclic molecule, steroid fluticasone propionate.

The impact of molecular conformation variation can influence intermolecular interactions, which in turn can change a system's state of matter and physical properties. For example, alkenes tend to have lower melting points compared to equivalent alkanes. The introduction of a double bond reduces the uniformity of the chain so molecules can't pack together as tightly, which reduces intermolecular interaction strength (Israelachvili, 2011).

A molecule's conformation may leave its lowest energy state to maximise certain intermolecular interactions. This depends on the system, for example in crystalline solids, this stronger interaction could increase the overall stability and thus be more favourable. Crystalline solids are highly structured phases, a pattern between molecules is repeated throughout and they show long-range ordering. In contrast, gas phase is disordered so molecules are relatively free to move and typically exist in their low energy conformation. Liquid structure is in between a gas and a solid with some short-range ordering. This means that although molecules move and are randomly positioned, they can show a preference of being in certain positions. Amorphous solids do not exhibit long-range ordering, instead their structure resembles a super-cooled liquid (Levine, 2009).

2.1.2.2 Intermolecular Interactions

Considering a medium, such as gas or liquid, each individual molecule experiences an energy which is the total interaction energy from all its surrounding molecules. Interactions can be intra-molecular and occur within molecules, or inter-molecular and occur between separate molecules. Intermolecular interactions can be categorised into different types, this section describes how their energy experienced can vary depending on the interaction distances and orientation.

Thermodynamic and statistical evaluation produced mathematical forms to describe the potential energy of these interactions. Finding the derivative of an interaction potential, $w(r)$, with respect to interaction distance, r , is the force between two particles, F , as shown in Equation 2-1. Therefore, the following interaction potentials in this sub-section form the basis of force fields, which are discussed later in section 2.1.4. Note that the equations show similarities but are not exactly the same as those used in force fields.

$$F = -\frac{dw(r)}{dr} \quad \text{Equation 2-1}$$

Electrostatic Interaction (Charge-Charge)

Electrostatic interactions arise between two charged points, it can be attractive or repulsive. Coulomb's inverse square law in Equation 2-2 defines how the force is affected by the charge magnitude and how it reduces at further separation distances. Where F is the force of interaction, q is a point charge, and r is separation distance.

$$w(r)_{\text{electrostatic}} = \frac{q_i q_j}{4\pi\epsilon_0 r_{ij}^2} \quad \text{Equation 2-2}$$

Charge-Dipole

This interaction describes a charged point interacting with a polar molecule, it can be attractive or repulsive. The charge magnitude, and angle of the dipole relative to the charge dictates the interaction strength. It is described by Equation 2-3, where v is intermolecular potential, q is a point charge, u is a point dipole, θ is the angle of the dipole, ϵ_0 is permittivity of free space, r is separation distance. Figure 2-3 shows the interaction energy, both repulsive and attractive, is maximised at closer distances when the dipole is angled to point directly at the point charge. The force fields explained in section 2.1.4. don't include this equation as the dipole is not explicitly included, rather it is represented through atomic point charges.

$$w(r)_{\text{charge-dipole}} = -\frac{q u \cos\theta}{4\pi\epsilon_0 r^2}$$

Equation 2-3

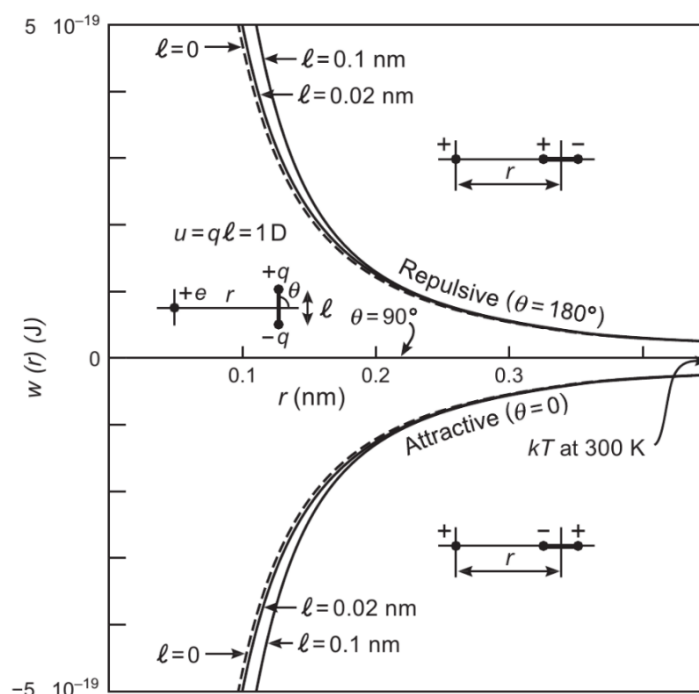


Figure 2-3 Potential energy for a point charge interacting with a dipole as function of both distance and dipole angle (Israelachvili, 2011).

Van der Waals: Dipole-Dipole (Including Hydrogen bonds)

Van der Waals interactions are categorised into three different types: dipole-dipole, induced dipole-dipole, induced dipole-induced dipole. It should be noted that each of the van der Waals terms are proportional to $1/r^6$.

Dipole-dipole interactions arise between two polar molecules and are also known as Keesom interactions, the relationship between potential energy and dipole orientation is shown in Figure 2-4. At further separation distances, it can be seen the interaction is

stronger when dipoles moments are in line with each other, i.e. the positive end of one is pointing to the negative end of another pole. At closer distances, interactions are stronger with anti-parallel arrangement where the two dipole moments are parallel to each other but pointing in opposite directions. This interaction is not considered as strong as electrostatic interactions, ion-ion or ion-dipole, but not as strong as intramolecular covalent bonds (Israelachvili, 2011). It can be described by Equation 2-4. Where k is Boltzmann's constant, T is temperature, μ is dipole moment.

$$w(r)_{\text{dipole-dipole}} = -\frac{2}{3kT} \frac{\mu_1^2 \mu_2^2}{(4\pi\epsilon_0)^2 r^6} \quad \text{Equation 2-4}$$

Hydrogen bonds are a stronger sub-set of dipole-dipole interactions, occurring between A-H---B, where A and B are highly electronegative atoms, such as F, O, or N, but not strictly limited to those three elements. The electronegative atoms draw in the electron of covalently bonded to hydrogen, this brings the proton in closer and effectively reduces its radius. As a result, electronegative atoms in other molecules can get closer and form a strong electric field which can dictate their directionality (Israelachvili, 2011).

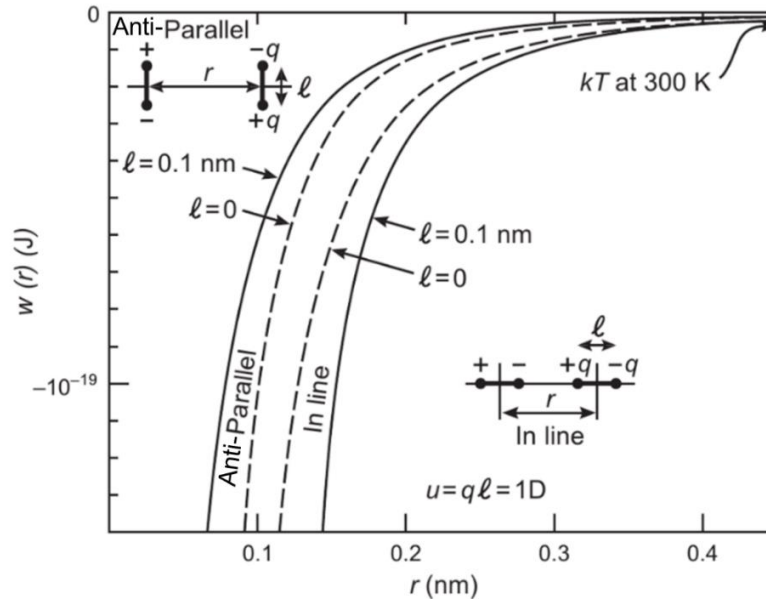


Figure 2-4 Potential energy for dipole-dipole interactions as function of both distance and dipole orientation (Israelachvili, 2011).

Van der Waals: Induced dipole-dipole

Induced dipole-dipole interactions occur when one molecule's permanent dipole induces an instantaneous dipole in a secondary molecule, even if it does not have a permanent dipole. It is defined by Equation 2-5, where α are the molecule polarizabilities.

$$w(r)_{\text{induced dipole-dipole}} = -\frac{\mu_1^2 \alpha_2 + \mu_2^2 \alpha_1}{(4\pi\epsilon_0)^2 r^6} \quad \text{Equation 2-5}$$

Van der Waals: Induced dipole-induced dipole

Induced dipole-induced dipole interactions are also known as London Dispersion forces, these are present in molecules without permanent dipoles. Electrons are always moving, even in neutral molecules, and at a single moment in time they may all be positioned on one side. This resulting instantaneous dipole can induce other instantaneous dipoles in surrounding molecules, and form interactions. Their strength is proportional to the molecule's polarizability and therefore molecule size. These are not as stronger as dipole-dipole interactions and are long range forces, effective interactions range between 2 – 20 Å. Equation 2-6 approximates induced dipole-induced dipole interactions, where I_1 and I_2 are the ionisation energies.

$$w(r)_{\text{induced dipole-induced dipole}} \approx -\frac{3I_1I_2}{2(I_1+I_2)} \frac{\alpha_1\alpha_2}{(4\pi\epsilon_0)^2 r^6} \quad \text{Equation 2-6}$$

Steric Repulsion

Steric repulsion, also known as steric hindrance, describes the repulsive force caused by the overlap of electron clouds in different atoms. Efficient packing of the solid state is often determined by the minimisation of steric repulsions between molecules, more so than maximisation of attractive forces (Israelachvili, 2011).

2.1.3 Basic Crystallography of APIs

2.1.3.1 Introduction to Crystallisation from Solution

Crystallisation generally describes the act of a solid-state forming out of a liquid, with either the liquid itself solidifying, or precipitation of solute that was dissolved in the liquid. It can be sub-categorised into two distinct kinetic steps, nucleation and growth, both are described in this chapter. When manufacturing APIs, crystallisation helps to produce a desired particle size and to purify the compound by removing impurities that may be left over from synthesis stages. Because APIs, such as the one discussed in this thesis, are typically recrystallised from solution, the rest of this sub-chapter refers to crystallisation from solution.

Solubility

When crystallising from solution, one must first understand solvation and the formation of a homogeneous solution. An energy change occurs as a solution is formed, known as the enthalpy of solution formation. It is equal to the difference in energy input required to separate solute-solute and solvent-solvent interactions, and the energy released

when solvent-solute interactions form. It must be thermodynamically favourable for a certain concentration of solute to dissolve in the liquid and the energy of interactions between solute and solvent molecules is influenced by temperature.

Solubility is defined as the amount of solute that can be dissolved to form a saturated solution at a certain temperature and pressure. When creating a solution, excess solid is dissolved until the solution becomes saturated, this is known as the equilibrium solubility. Usually, an increase in temperature increases a systems solubility and when liquid temperature is too low this may be unfavourable, the solute is forced to precipitate out, hence leading to crystallisation. This relationship is expressed through solubility curves which show the concentration of dissolved solute as a function of temperature (Mullin, 2001). An example solubility curve is shown in Figure 2-5, the solid black line represents equilibrium solubility. Reducing the temperature can cause a solution to hold onto more solid than its equilibrium solubility, this is known as a *Meta-Stable* super-saturated solution. Precipitation of solids may not occur straight away as there is an energy barrier that must be overcome for nucleation, the time frame can vary from occurring instantly to taking several years. The temperature can only be reduced to a certain point until crystallisation occurs spontaneously, when it is so energetically unfavourable for solute molecules to be surrounded by the solvent that solids are forced to precipitate. This is shown in Figure 2-5 by a dashed black line, when the solution enters the *Labile* zone. The temperature gap between that point of entering Labile zone and the equilibrium solubility line is known as the meta-stable zone width, the distance between B>C in Figure 2-5, it is useful to know when designing a crystallisation process.

Super-saturation of a solution could be induced through different methods, such as cooling, evaporation or adding another solvent which reduces solute solubility. The red lines in Figure 2-5 showing A>B>C exhibit the process of cooling crystallisation, with D representing crystallised particles in the labile zone. A'>B'>C' represents evaporation crystallisation, while A''>B''>C'' is a combination of the two (Mullin, 2001).

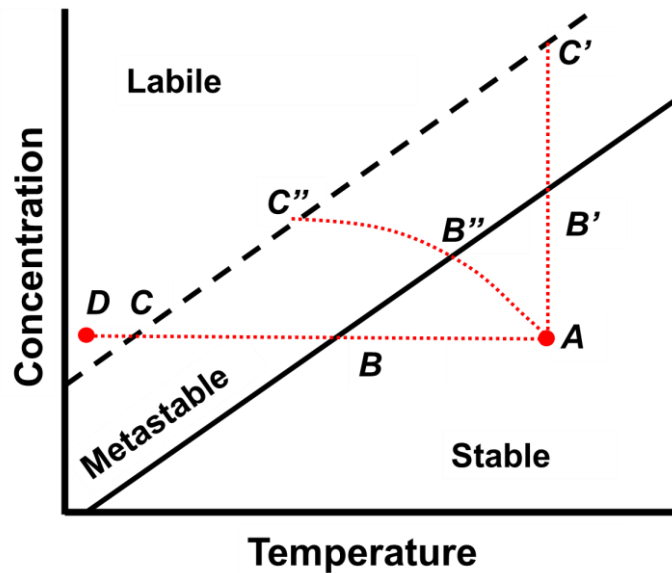


Figure 2-5 Example solubility curve and super-solubility diagram. The solid and dashed black lines represent equilibrium solubility and super solubility line, respectively. The red lines represent different crystallisation methods. Adapted from (Mullin, 2001).

Nucleation

During nucleation, an initial cluster of molecules forms in the solution, then it grows as more molecules are incorporated. The rate at which this occurs can affect physical properties, such as number of crystallised particles, size distribution, and their polymorph. Nucleation's stochastic nature makes it a challenging study, but different models help to control the process (Mullin, 2001).

Nucleation from solution encompasses two main types: primary and secondary. Primary nucleation is when crystallisation occurs when the solution does not contain any crystalline material. Primary can be further sub-categorised into homogenous nucleation when an assembly of molecules spontaneously forms and heterogenous nucleation is caused by the presence of foreign objects, such as suspended particles or impurities in the solution. Secondary nucleation is caused by the presence of other crystalline material, such as seeds.

During homogenous nucleation, molecules are moving around a homogenous fluid and randomly forming clusters. If they are to precipitate out of the solution, rather than continue to be dissolved and surrounded by solvent molecules, they must reach a certain size. Typical nuclei consist of ten to several thousand molecules. Furthermore, the complexity is increased as molecules must arrange into the lattice formation to form crystal (Mullin, 2001).

This is a three-dimensional process and can be described thermodynamically by looking at the system's free energy, ΔG , which is equal to the sum of volume energy,

ΔG_v , and surface energy contributions, ΔG_s , represented by Equation 2-7. Where, r is the nucleus radius, γ is interfacial tension, ΔG_v is the free energy change for transformation per unit volume (Mullin, 2001). Note that for simplicity is assumed the nucleus forms a sphere, this means surface energy is proportional to r^2 and bulk volume energy is proportional to r^3 .

$$\Delta G = \Delta G_s + \Delta G_v = 4\pi r^2 \gamma + \frac{4}{3}\pi r^3 \Delta G_v \quad \text{Equation 2-7}$$

Viable particles can only form when the cluster of molecules is large enough for the volume term to dominate over the surface term. Figure 2-6 shows this is when the nucleus has grown large enough to reach the critical radius, r_c , then as particle grows further the systems free energy is reduces. If a nucleus is smaller than r_c it will redissolve as this will reduce the free energy.

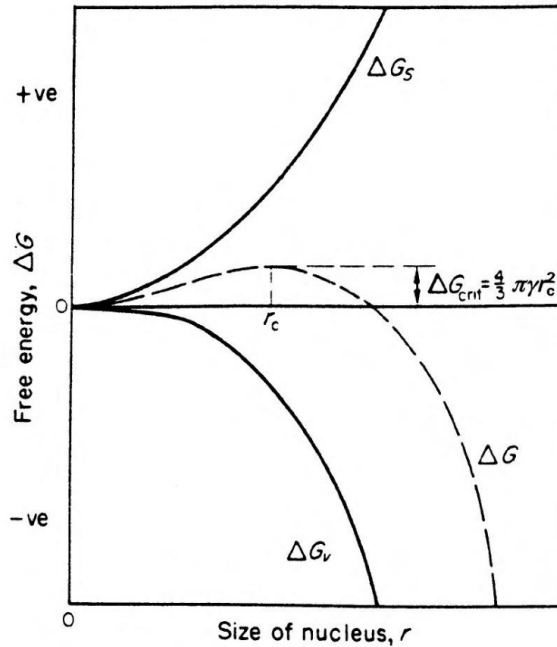


Figure 2-6 Free energy diagram for nucleation. The dashed line is total free energy, ΔG , equal to the sum of bulk volume energy, ΔG_v , and surface energy, ΔG_s . Nuclei must reach a critical radius, r_c , to crystallise (Mullin, 2001).

Depending on the application, one might want to control the size, shape and number of particles formed. Having rapid cooling rates usually causes higher rates of nucleation which typically reduce the ability for growth, thus resulting in a higher number of particles but with a smaller size. Conversely, if larger particles are desired, lower cooling rates can help to have lower levels of super-saturation and this typically promotes crystal growth over nucleation (Taguchi et al., 1996). Furthermore, seeded nucleation can help to control crystal size. This is when pre-prepared crystals are added to the

system when it is supersaturated. These act as favourable growth destinations with a lower energy barrier compared to nucleation. Hence, the 'seeds' grow into larger crystals. Then, keeping the system at a lower super-saturation helps to minimise nucleation so there is more control over the size range of particles formed. This is an example of secondary nucleation (Mullin, 2001).

Growth

Once a nucleus has formed it can begin to grow, although the nucleus formed is 3-D, growth is often represented as new molecules attaching to a series of 2-D interfaces. Different mechanisms have been proposed to describe how the kinetics and method which new molecules attach is influenced by the degree of supersaturation (Mullin, 2001). Furthermore, growth can be affected by solvent type, and impurity level (Sangwal, 2007)

Crystal surfaces can have varied topographies due to imperfections, such as defect in the crystal structure is referred to as a dislocations and screw dislocations are when there is part misalignment of a lattice layer. These can act as attachment sites and can ultimately lead to spiral growth, which was described by the Burton, Carberry, Frank (BCF) model. This is based on the idea that screw dislocations are the source of growth by offering viable binding sites at low rates of supersaturation, illustrated in Figure 2-7 (a). This typically occurs at lower levels of supersaturation and growth rate is proportional to supersaturation squared (Clydesdale et al., 1997a). The birth and spread model (B&S) occurs at moderate supersaturations on flat surfaces, as illustrated in Figure 2-7 (b). This does not require steps or kinks to be present so supersaturation must high enough to cause surface nucleation (Clydesdale et al., 1997a). Rough interface growth (RIG). A rough surface can form consisting of many monomer sites, this enables growth to take place at a higher rate and it does not need steps to have formed (Clydesdale et al., 1997a). Figure 2-7 (d) and (e) shows initially a monomer joins a smooth surface and it transitions to rough surface. Usually occurs at high levels of supersaturation and growth is considered to have a linear rate dependence with supersaturation.

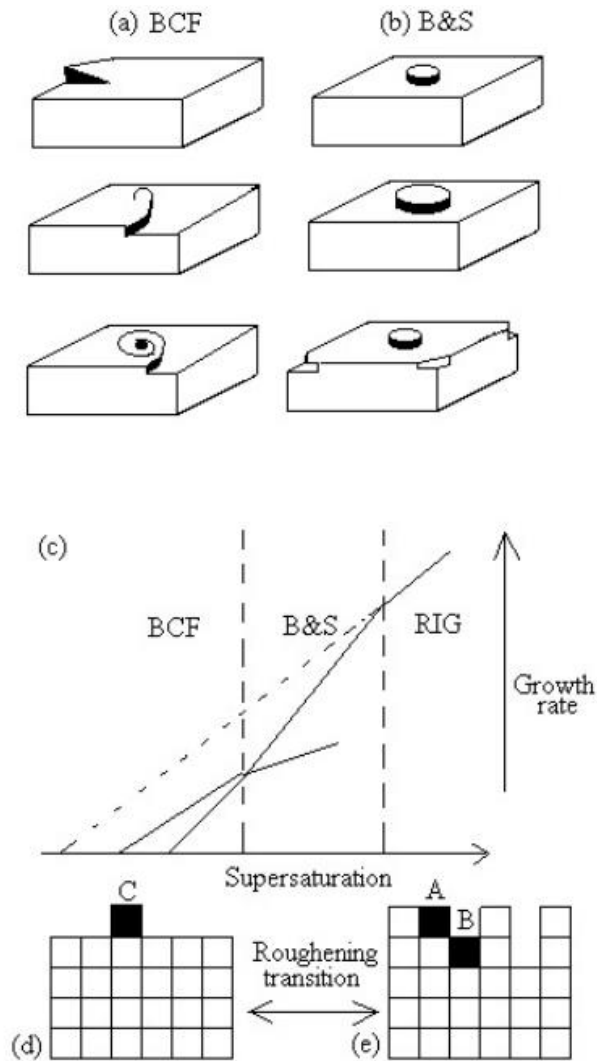


Figure 2-7 Different nucleation mechanisms of nucleation. (a) BCF, growth by screw dislocations. (b) B&S, growth from surface nucleation. (c) Relationship between mechanisms and supersaturation levels. (d) and (e) RIG, growth on a smooth surface transitioning to presence of a kink (Clydesdale et al., 1997a).

Crystal surfaces are different termination points of the bulk structure and therefore are anisotropic in nature, this can lead to anisotropic crystal morphologies. Crystals may not retain their initial geometry, as smaller faces with a faster growth rate are typically eliminated from the final morphology, having been 'facetted out'. Leaving slower growing surfaces to dominate the habit, as illustrated in Figure 2-8. In some extreme cases this can lead to needle morphologies, with one face growing at a considerably faster rate.

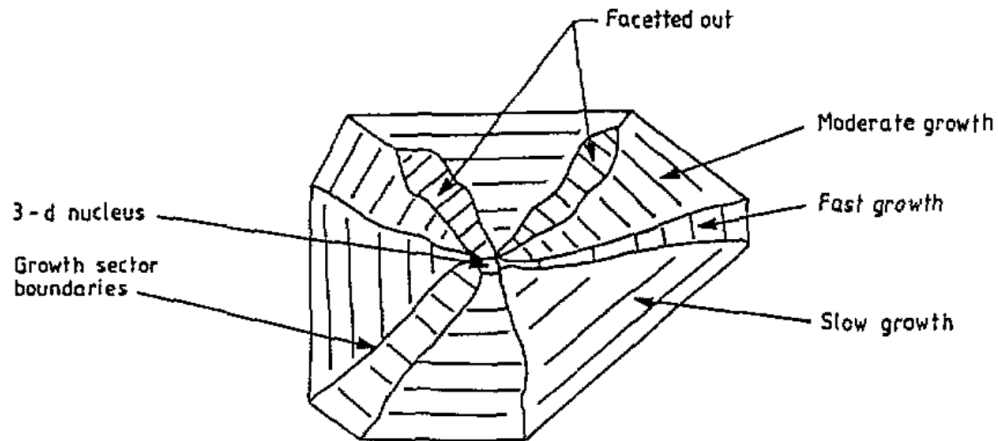


Figure 2-8 2-D growth planes of a crystal showing the variation in growth rate means some faces of the initial 3-D nucleus are not present once growth has finished (Clydesdale et al., 1997a).

2.1.3.2 X-ray Diffraction: Structure Determination

It is possible to interpret the atomic arrangement in a crystal by directing a beam of x-rays through a crystal and measuring the scattered beams. X-ray diffraction (XRD) occurs when the wavelength of the incident beam is similar size to inter-atomic spacing in the crystal. From this, a diffraction pattern of defined beams forms which can be interpreted using Bragg's law to deduct the interplanar spacing of a structure (Tilley, 2006). This is represented in Equation 2-8 where, n is an integer, λ is a wavelength, d_{hkl} is inter-planar spacing, θ is the Bragg angle.

$$n\lambda = 2d_{hkl}\sin\theta \quad \text{Equation 2-8}$$

2.1.3.3 Crystal Structure

A crystal is classified as a solid-state exhibiting long range order. Within this structure, the atom or molecule positions stay constant in a repeating structural unit, and this produces the long range order. The arrangement can be categorised as a three-dimensional array, also known as a lattice structure. Figure 2-9 illustrates this lattice consists of repeating unit cells, each cell specifies atom positions relative to the defined edge length and angle parameters (Mullin, 2001).

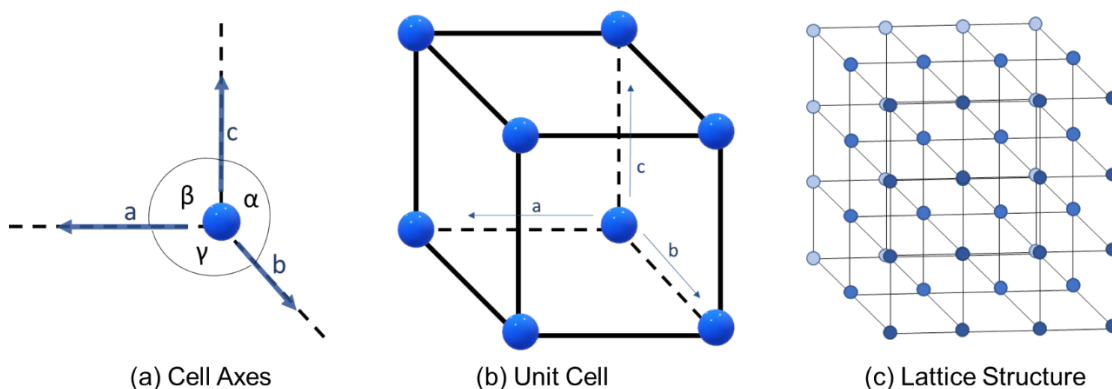


Figure 2-9 (a) Shows the cell axes and respective angles. (b) Atom positions defined with the unit cell. (c) Lattice structure consists of multiple unit cells (Clegg, 1998).

These unit cells can be categorised into seven different lattice groups: Triclinic, Monoclinic, Orthorhombic, Tetragonal, Rhombohedral, Hexagonal, Cubic. Furthermore, these can then be sub-divided into 14 different Bravais Lattices. For example, Figure 2-10 (a) below shows all edge lengths and angles are equal with a lattice point in the centre of the body-centred cubic cell. Whereas the primitive monoclinic cell in Figure 2-10 (b) shows cell edge lengths are not equal and the β angle is non- 90° .

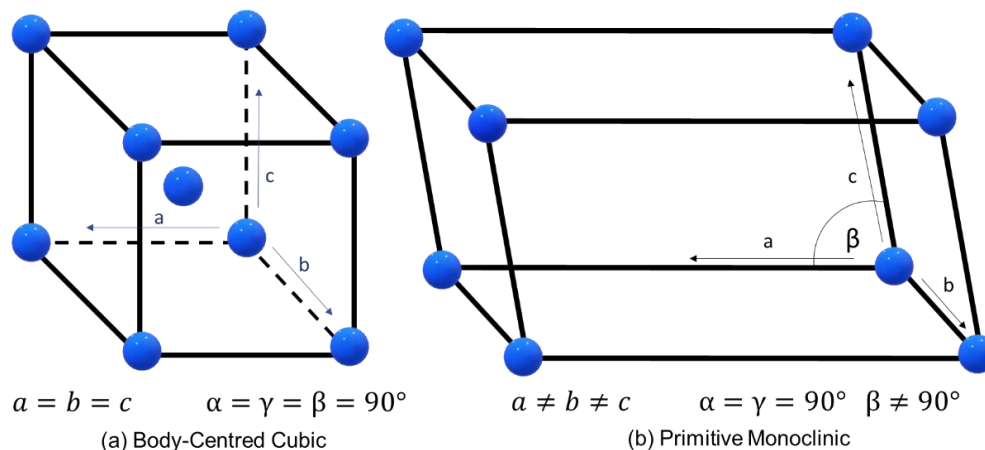


Figure 2-10 Examples of unit cells, (a) is a body-centred cubic cell where all edge lengths and angles are equal. (b) Is a Primitive monoclinic structure with non- 90° β angle (Tilley, 2006).

2.1.3.4 Synthons: Interactions in Crystal Structure

In the field of crystal engineering, the term 'synthon' refers to building blocks that form solid-state structures of crystalline material (Desiraju et al., 1989). Synthons represent the pairwise intermolecular interactions that connect molecules within a lattice.

Directionality is defined relative to the unit cell and the distance between molecules is measured between the centres of geometry. An example synthon is shown in Figure 2-11 with 10.80 Å between the pair of FP molecules. Identifying synthons in a structure can be useful for predicting crystal growth and external morphology. With ‘intrinsic synthons’ referring to the interactions within the bulk of the crystal structure, and ‘extrinsic synthons’ at crystal surfaces are undersaturated due to the termination of the crystal lattice.

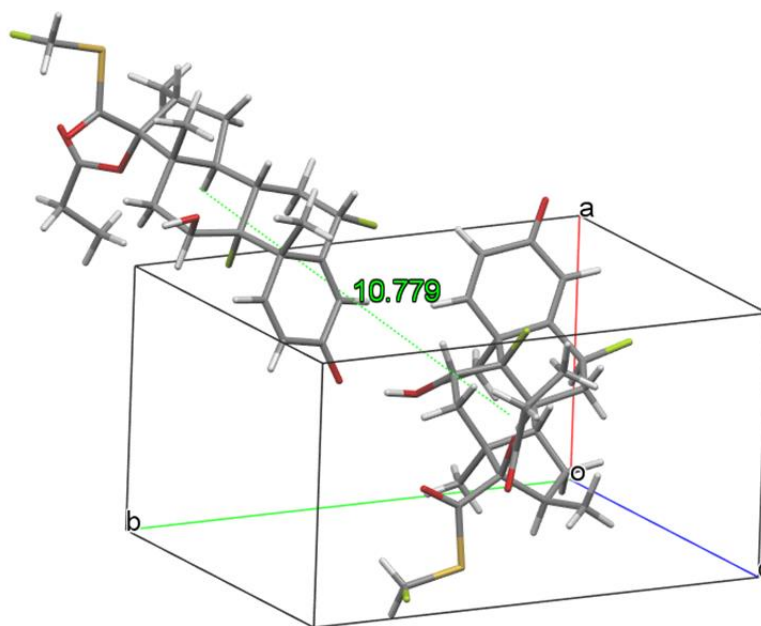


Figure 2-11 Example synthon of fluticasone propionate showing the distance between the centres of geometry. Direction defined with respect to the unit cell.

2.1.3.5 Polymorphism

Polymorphism may occur in crystal structures when the chemical structure is the same, but lattice packing differs (Bernstein, 2002). There are two main types in molecular crystals: conformational and packing polymorphism. The HIV treatment Ritonavir (Bauer et al., 2001) and antidepressant venlafaxine hydrochloride (Effexor) (Roy et al., 2005) are both examples which show conformational polymorphs. The molecules are relatively flexible and show a different conformation in each polymorph, this may be caused by molecules maximising their intermolecular interaction strength, and hence increasing the stability of the overall crystal lattice.

The main difference in Ritonavir's polymorphs is the rotation of the γ segment's bulk phenyl groups, the Figure 2-12 highlights this C-C-C-C torsion angle and shows how the conformation of form I is more compact (Wang et al., 2021). In contrast, packing

polymorphs have identical conformations but the intermolecular packing varies, one example is Aprepriant, the chemotherapy medication (Braun et al., 2008).

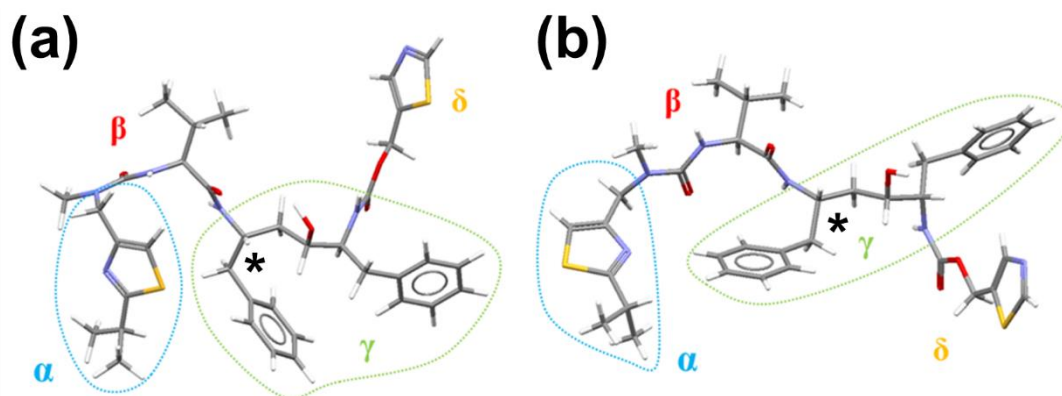


Figure 2-12 Varied molecular conformations in Ritonavir's polymorphs, Form I (a) and Form II (b). The torsional angle change is highlighted by an asterisk (Wang et al., 2021).

2.1.3.6 Miller Indices

One can define a plane within a crystal structure using Miller Indices (hkl). These don't represent just a single plane, rather a collection of parallel planes in a lattice. Each (hkl) expresses where planes intercept the unit cell axes. They can be calculated from the reciprocal of the fractional intercept using Equation 2-9, where a , b , and c are dimensions of the unit cell, X , Y , and Z are where the plane intercepts the cell edge length. Examples of a (100) and (110) plane in a cubic cell are shown below in Figure 2-13. It is also possible to have negative hkl values, i.e. when the plane intercepts an axis in negative position relative to unit cell (Tilley, 2006).

$$h = \frac{a}{X}, \quad k = \frac{b}{Y}, \quad l = \frac{c}{Z}$$

Equation 2-9

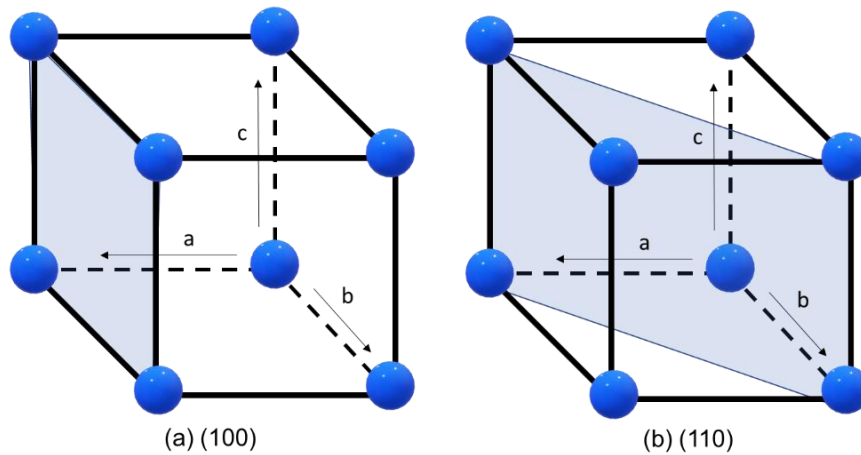


Figure 2-13 Examples of Miller Indices planes relative to a unit cell. (a) shows the (100) plane dissecting the a-axis. (b) Shows the (110) plane dissecting a and b-axis (Tilley, 2006).

Miller indices planes are denoted with curved brackets, different bracket types are used to express other characteristics. For instance, curly brackets, $\{hkl\}$, represent forms of equivalent faces where the same pattern is seen on both. One example is the $\{0\ 0\ 1\}$ form which is equivalent to the (0 0 1) and (0 0 -1) planes. Similarly, square brackets represent a direction vector starting from the origin, such as $[hkl]$, and angle brackets are used to represent a family of equivalent directions, i.e. $\langle hkl \rangle$ (Tilley, 2006).

2.1.3.7 Crystal Habit and Morphology

The macroscopic crystal shape is known as the habit and a wide range are possible, common description terms include prism, needle-like, tomahawk, dendritic and prismatic. Crystals can show different surface and this external morphology described by the (hkl) Miller indices relative to its unit lattice, as shown in Figure 2-14. Crystal habit formation is influenced by the crystallisation conditions, such as supersaturation, growth solvent, and impurities present (Omar and Ulrich, 2006). Certain faces may be morphologically dominant, and it is important to define them so their differences in chemical properties can be understood.

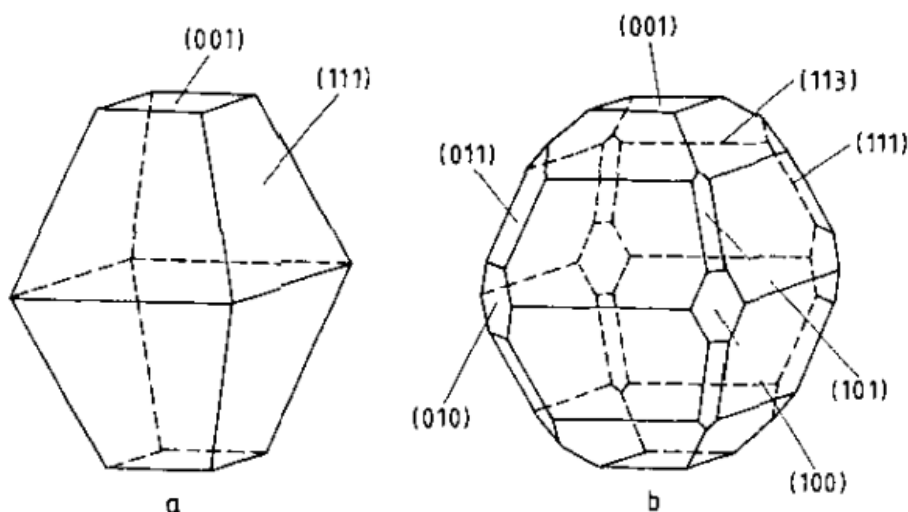


Figure 2-14 Examples of external morphologies with faces defined by Miller Indices (hkl) (Docherty et al., 1991).

The chemical nature of growth solvents can influence their binding at different faces and produce different shaped crystals. For example, Lovastatin produced more elongated, needle habits when recrystallised in polar solvents, and more prismatic habits when formed in non-polar solvents, as seen in Figure 2-15 (a and b), (Turner et al., 2019). Also, rapid cooling of systems or additions of anti-solvents can lead to high levels of supersaturation, which in turn can cause high growth rates of certain faces and form a final habit dominated by slower growing faces. Images of FP produced through anti-solvent crystallisation are shown in Figure 2-15 (c), (Bártová et al., 2022).

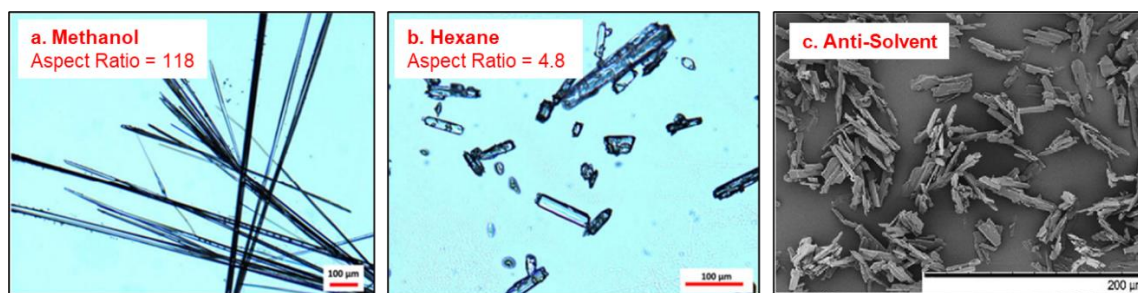


Figure 2-15 Examples of different crystal habits. (a) High aspect ratio needles of Lovastatin crystals produced through cooling crystallisation from methanol, and (b) more prismatic crystals from hexane (Turner et al., 2019). (c) Shows small FP particles crystallised through the addition of an anti-solvent (Bártová et al., 2022).

2.1.4 Morphology Prediction and Molecular Modelling

2.1.4.1 Theories of Morphology Prediction

It was initially proposed by Gibbs that crystals form a 3-D shape with minimum surface energy, in a similar fashion to an isolated droplet of liquid. This theory was developed by Wulff who accounted for the anisotropic nature of a crystal structure. It was suggested by Wulff that the equilibrium crystal habit would be proportional to the specific surface energies of the Miller planes (hkl) of the crystal formed. Each miller plane is a different point which the bulk structure is terminated so its surface chemistry can vary, and therefore also its specific surface energies. This was illustrated by the Wulff plot of Figure 2-16 which defined by the growth directions of Miller planes relative to the nucleation centre.

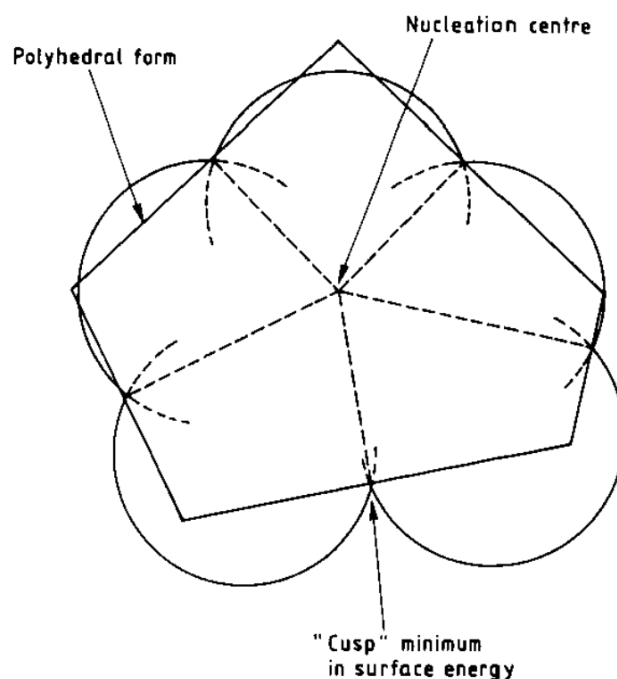


Figure 2-16 Wulff plot illustrating the different growth directions and distances of surfaces relative to the nucleation centre (Docherty et al., 1991).

Surfaces of lowest surface energy were found to have the largest inter-planar spacing, d_{hkl} , which led to the development of by Bravais-Friedel-Donnay-Hakker, BFDH. It states that crystal faces largest surface area, and therefore most important morphologically, will be the ones with largest inter-planar spacing (after considering the reduction of the growth slice thickness from space group symmetry). Therefore, surface growth rate is inversely proportional to inter-planar spacing, d_{hkl} . This was believed to be caused by larger intermolecular distances decreasing the interaction strength between layers and hence slowing growth (Roberts et al., 1993).

As the BFDH method only looks at geometry of the crystal lattice, it does not explicitly consider how the chemical nature of each molecule can impact the strength of interactions involved with crystal growth (Clydesdale et al., 1997b). While the attachment energy model can predict the morphology by predicting atom-atom interaction strengths. This models the crystal lattice as different growth layers and interactions between molecules are viewed as atom pairs relative to a central reference atom. Growth of each face is proportional to its predicted energy of a new layer forming on that face. Hence, faces with the smallest attachment energy are the slowest growing so are the most dominant faces (Hartman and Bennema, 1980).

The interactions are defined as either slice or attachment energy depending whether the secondary atom is located inside or outside the growth layer (Docherty et al., 1991). Figure 2-17 shows a slice of thickness d_{hkl} and illustrates the process of deciding if atoms are either inside or outside the slice. Slice energy (E_{sl}) is equivalent to the energy released when a growth layer forms and is calculated from all atom-atom interactions within a growth layer of d_{hkl} thickness. Attachment energy (E_{att}) is equivalent to the energy released when one of these layers attaches to a growing crystal face and is calculated by summing all the interactions that are outside this layer. The start and end points of a slice can be adjusted relative to a crystal structure to find the most energetically favourable slice position, i.e., with the highest slice energy. Figure 2-17 shows the slice of thickness d_{hkl} and illustrates the process of deciding if atoms are either inside or outside the slice. Take the central atom, A , with the atom under consideration, B , form a vector AB . The program calculates the magnitude of bonding vector normal to the growth slice, AC , using the angle between the vector AB and \hat{n} . If AC falls within $\frac{1}{2} d_{hkl}$ then the interaction contributes to the slice energy. Figure 2-17 shows molecule B is outside the slice, whereas D is inside the slice.

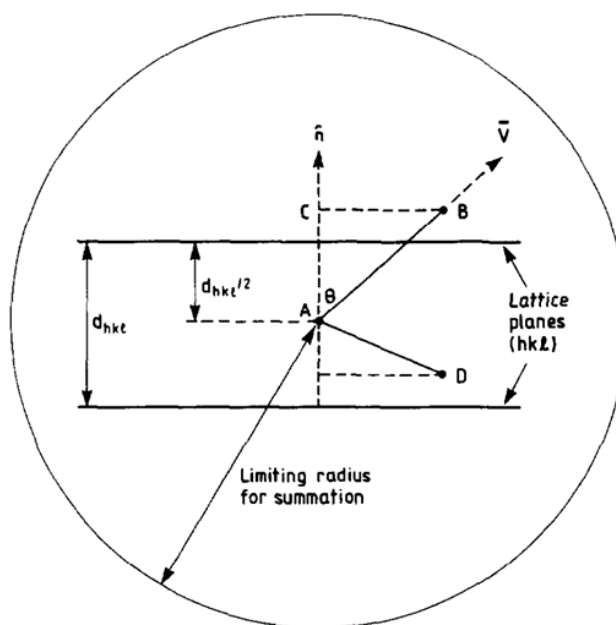


Figure 2-17 Process of deciding if interacting molecule is within the same slice as central molecule, A. e.g., Molecule B is outside the slice and D is within the slice (Clydesdale et al., 1991).

The sum of slice and attachment energy is the total crystal lattice energy (E_{latt}), as shown in Equation 2-10. which is equivalent to the energy released when molecules are brought together into the crystal lattice from infinite space, i.e., a perfect gas.

$$E_{latt} = E_{att}^{hkl} + E_{sl}^{hkl} \quad \text{Equation 2-10}$$

The concept of lattice energy can be related to the experimentally measured sublimation energy (ΔH_{sub}) with a correction factor to account for vibrational energy. As shown with Equation 2-11 below, where R is the ideal gas constant and T is the temperature sublimation was measured (Williams, 1966). The atom-atom approach of calculating lattice energy shows good correlation to experimentally measure sublimation enthalpy for different systems (Clydesdale et al., 1996).

$$E_{latt} = \Delta H_{sub} - 2RT \quad \text{Equation 2-11}$$

Once attachment energy of faces are calculated, a classical Wulff plot is used to predict the morphology by assuming the attachment energy per face is proportional to the centre-to-face distance. Computational techniques can help by predicting the interaction energies crystal structure using the atom-atom approach, one example is

HABIT98 (Clydesdale et al., 1996). These techniques can employ force field potentials to predict the intermolecular interaction energy.

2.1.4.2 Molecular Mechanics: Force Fields

In molecular mechanics, intramolecular forces and the intermolecular interactions described earlier in section 2.1.2 are represented by mathematical functions. Atoms are represented by point masses and molecules are modelled as balls connected by springs. This is possible with the Born-Oppenheimer principle which assumes electrons instantaneously follow nuclei movement due to the large differences in their masses. No electron density or wave function is accounted for which makes it more computationally efficient (Bladon et al., 2012). The expressions shown in section 2.2 are not used directly within force fields. For example, a specific dipole term of a molecule is not included as it is represented by the point charges.

Force field represent the forces experienced by atoms through different functional forms, these forces can be evaluated to calculate a low energy molecular conformation. For example, Equation 2-12 shows how the total potential energy of a molecule is the sum of different energy terms. These are assigned for intra-molecular energy terms, including bond stretch ($E_{Stretch}$), angle bending (E_{Bend}), and torsional angle ($E_{Torsion}$). Non-bonded inter-molecular interaction energy terms are also included for van der Waals (E_{vdW}) and electrostatic interactions (E_{Elec}).

$$E_{total} = \underbrace{\Sigma E_{Stretch} + \Sigma E_{Bend} + \Sigma E_{Torsion} + \Sigma E_{StretchBend}}_{\text{Intramolecular interactions}} + \underbrace{\Sigma E_{vdW} + \Sigma E_{Elec}}_{\text{Non-bonded interactions}} \quad \text{Eq. 2-12}$$

Examples of different functional forms are detailed in Table 2-1. They produce different shaped energy wells characteristic of an equilibrium point which atom properties oscillate around, such as an equilibrium bond length. The shape of these energy wells change depending on the terms, so suitable terms must be chosen to accurately represent different types of molecular movement. Sometimes stretch-bend terms can be included in force fields to describe how a bond lengths equilibrium may vary when the bond angle of a connected atom changes. Additionally, note that the terms featured in Table 2-1 are summated to show the total energy is equal to the sum of all atom types. For example, a molecule can consist of multiple atom types, so the total bond stretch energy is summated from all the atom types and their different constants.

Table 2-1 Typical functional forms of energy terms used in force field potentials. Where, l is bond length. θ is bond-angle. r is non-bonded distance. q is charge. D_e is dissociation energy. n is an integer. α , k , ϵ and σ are parameterised constants for atom types (Young, 2001). Each energy term is summated to represent how the total energy of a particular molecular movement or interaction is equal to the sum of all the different atom types.

Use:	Name:	Energy Term:
Bond Stretch	Harmonic	$\sum k(l - l_0)^2$
Bond Stretch	Morse	$\sum D_e[1 - e^{-\alpha(l-l_0)}]^2$
Angle Bend	Harmonic	$\sum k(\theta - \theta_0)^2$
Torsion Stretch	Cosine	$\sum k[1 + \cos(n\theta)]$
Stretch-bend	Taylor	$\sum k(\theta - \theta_0)^2 [(l_1 - l_{1_0})(l_2 - l_{2_0})]$
van der Waals	Lennard-Jones 6-12	$\sum 4\epsilon_{ij} \left[\left(\frac{\sigma_{ij}}{r_{ij}} \right)^{12} - \left(\frac{\sigma_{ij}}{r_{ij}} \right)^6 \right]$
van der Waals	Lennard-Jones 10-12	$\sum 4\epsilon_{ij} \left[\left(\frac{\sigma_{ij}}{r_{ij}} \right)^{12} - \left(\frac{\sigma_{ij}}{r_{ij}} \right)^{10} \right]$
Electrostatic	Coulomb	$\sum \frac{q_i q_j}{4\pi\epsilon_0 r_{ij}}$

Bond stretch energy ($E_{Stretch}$) is related to the energy between two atoms covalently bonded, so is a function of the distance between two atoms. Harmonic oscillators or Morse potentials usually portray the relationship between energy and bond length, as shown in Table 2-1. The symbol l_0 represents the equilibrium bond length, and the constant k mediates how much it fluctuates. The constant k is also known as a spring constant. Example Harmonic and Morse energy profiles in Figure 2-18 (a) show the energy well position is determined by the equilibrium bond length, and its shape is affected by the spring constant.

Bond angle energy, also known as bending energy, (E_{Bend}) is a term describing how potential energy varies with respect to bond angle measured between three covalently bounded atoms. Harmonic functions are the primary way of describing this relationship, as shown in Table 2-1. The symbol θ_0 represents the equilibrium bond angle. Torsion angle energy ($E_{Torsion}$) term represents the equilibrium point of a bond rotation and Cosine functions are typically used. The angle is defined via four connected atoms, 1-2-3-4, it is between the planes formed by atoms 1-2-3 and 2-3-4. Generally, staggered conformations are more energetically favourable than eclipsed, as shown in the energy profile of Figure 2-18 (b).

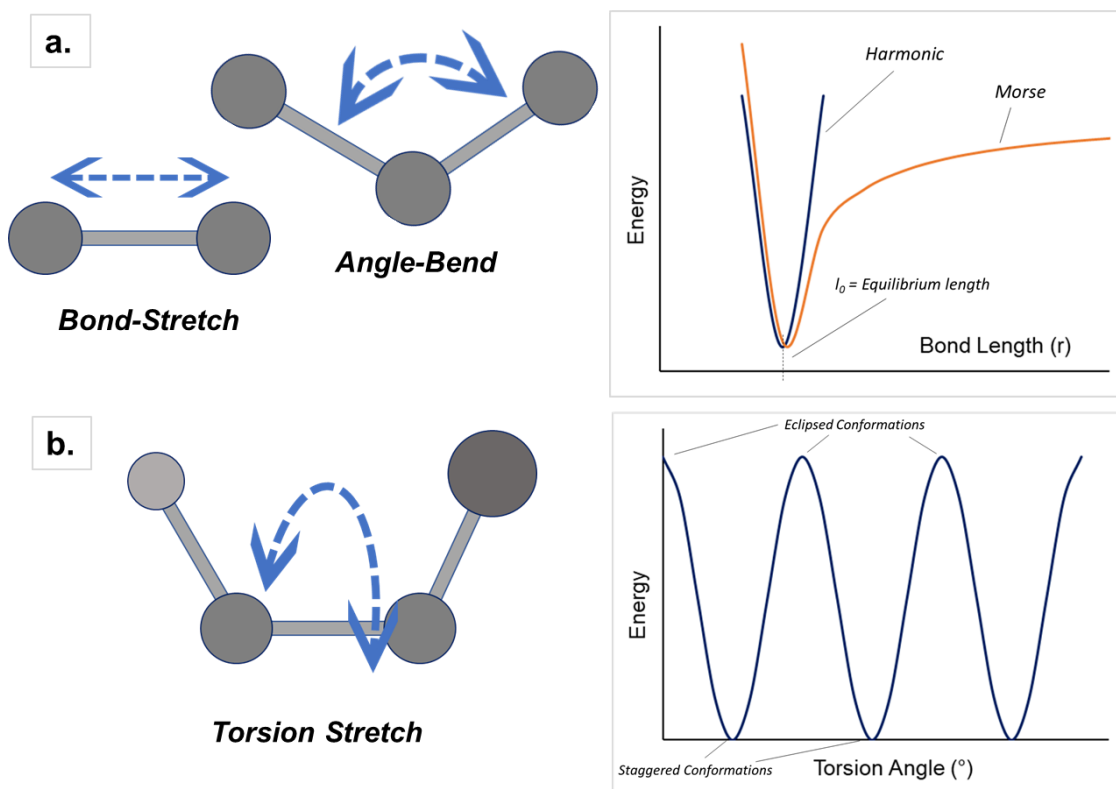


Figure 2-18 (a) Examples of bond-stretch and angle bend mechanisms, with Harmonic and Morse energy profiles as a function of bond length. (b) Example of torsion stretch mechanism, with Cosine energy profile as a function of torsion angle.

Van der Waals (E_{vdW}) and electrostatic interaction (E_{Elec}) energy terms are also included to account for interactions between non-covalently bonded atoms. Such as, intermolecular interactions or even intramolecular between atoms not directly linked atoms, like carbon 1 and 4 in an alkane chain. Van der Waals energy terms represent the three main types of van der Waals interactions, which were all proportional to $1/r^6$. These are represented using the Lennard-Jones interaction, the 12-6 variation has an attractive term also proportional to $1/r^6$. Figure 2-19 (a) shows how the repulsive and attractive terms combine. In this case, the constant, ϵ , defines the depth of the interaction energy well and the constants, σ , defines the distance of the well. Electrostatic charge interactions (E_{Elec}) can be attractive or repulsive and Figure 2-19 (b) shows both examples. Typically, Coulombs law is used to calculate the interaction between point charges which represent the partial charges, assumed to be at the centre of each nuclei. For improved solvation modelling, dielectric constants can be included.

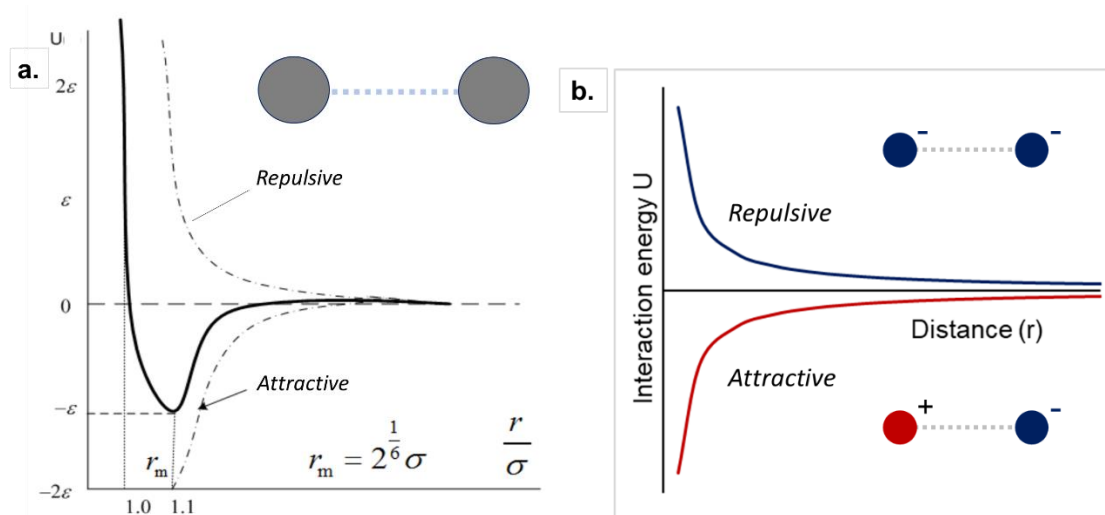


Figure 2-19 (a) Energy profile of 12-6 Lennard-Jones potential, representative of van der Waals interactions between two atoms. Total energy is the sum of attractive and repulsive terms (Maghfiroh et al., 2020). (b) Example of attractive and repulsive coulombic interactions.

Additionally, force field performance is affected by constants used in energy terms, such as the depth of the interaction energy well in the Lennard-Jones potential. These energy terms are usually found through a parameterisation step where constants are adjusted until the force field satisfactorily reproduces a database of values which can come from ab-initio or spectroscopic data. This results in different constant values for different atom types. Some force fields are parameterised for a specific set of molecules or for certain conditions of systems. It is important that the force fields strengths and weaknesses are observed before being used. Some examples include **AMBER**, assisted model building with energy refinement, which is both a force field and molecular mechanics program. It was parametrised for proteins and nucleic acids (Weiner et al., 1986). Another example is **Dreiding** which includes five valence terms, parametrised for a wide range of organic systems. It models non-bonded atom interactions using the LJ 12-6 potential for van der Waals interactions and coulombic potential for electrostatic interactions (Mayo et al., 1990). Also, there is **OPLS**, optimised potentials for liquid simulations (Jorgensen et al., 1996). It uses five valence terms and was fitted to a broader range of organic molecules in the liquid phase with original parameter values based on the AMBER potential. Finally, there is the polymer consistent force field, **PCFF**, which was originally parameterised for polysilanes (Sun, 1995).

2.1.4.3 Charge calculation / Semi-Empirical Methods

Coulombic interaction terms are featured in force field potentials, but methods of predicting atomic charges are not included. Therefore, this must be done separately. The Gasteiger method predicts atom charges using a set of parameters that are based on atoms electronegativity. Alternatively, quantum mechanical methods can predict the

molecular orbitals by solving the wave functions of the Schrodinger equation. There are two main methods, ab-initio and semi-empirical, both aim to find the minimal electron energy. Ab-initio techniques are considered to be more rigorous, with basis sets defining what parameters and variables are used. Semi-empirical methods are faster to compute, they use more approximations and include parameters fitted to experimental heat of formation values (Bladon et al., 2012). The names of these semi-empirical methods reflect their approximations, such as **NDDO**, neglect of diatomic differential overlap, and **MNDO**, modified neglect of differential overlap. These were improved upon with the **AM1**, Austin model 1, with parameters fitted to a larger experimental data set. It was refitted again with more parameters to form **PM3**, parameterisation model 3, which addressed some of the issues AM1 had with certain molecules (Jensen, 2010).

2.1.4.4 Molecular Dynamics

Molecular dynamics (MD) can be used to look at the motion classical many particle systems. Simulations consist of many molecules inside a box and force fields, such as the one in Equation 2-13, are incorporated into Newtonian equations of motion. This shows molecular movement develops over a period time, so it is possible to represent non-equilibrium scenarios (Frenkel and Smit, 2023).

Force fields are used to represent the atom pair interaction forces in a system with N number of particles, i.e., constituent atoms of many molecules. Assuming that the total interaction force on a particle is the sum of all particle pair forces, this means the force experienced by atom i caused by all its interactions (its internal force) is summarised by Equation 2-13 where R is the position coordinates of r_i , and \hat{r}_{ij} is a unit vector pointing from particle i to j going along $r_j - r_i$.

$$F_i(R) = \sum_{j=1,N} F(|r_i - r_j|) \hat{r}_{ij} \quad \text{Equation 2-13}$$

By neglecting forces that would be present experimentally, such as gravitational and boundary interactions, one can incorporate Equation 2-13 into the Newtonian equations of motion. The differential form is shown in by Equation 2-14, where m_i is the mass of particle i , t is time, F is the force, and a is acceleration.

$$\frac{F_i(R)}{m_i} = \frac{d^2 r_i(t)}{dt^2} \quad \text{or} \quad \frac{F_i(R)}{m_i} = a(t) \quad \text{Equation 2-14}$$

The atoms positions must be initially specified, these can come from different sources depending on the system. Sometimes molecules are randomly positioned, or if available, an optimised geometry can be used. Similarly, the initial atom velocities must be specified. This usually comes from a Boltzmann Distribution for a certain temperature but normalised for the system. Now the atoms have momentum, and the

force field potentials can compute the forces on atoms. Following this, new atom positions can be evaluated by numerically solving Equation 2-14. Likewise, new atom velocities and acceleration can be evaluated, this integration procedure is then repeated until the end of the simulation, as represented in Figure 2-20 (Frenkel and Smit, 2023). Thermodynamic properties, such as pressure, are calculated using the evaluated position and velocities. However, values at this microscopic scale will vary from experimental data. So time averages of instantaneous values must be collected for experimental comparisons (Frenkel and Smit, 2023).

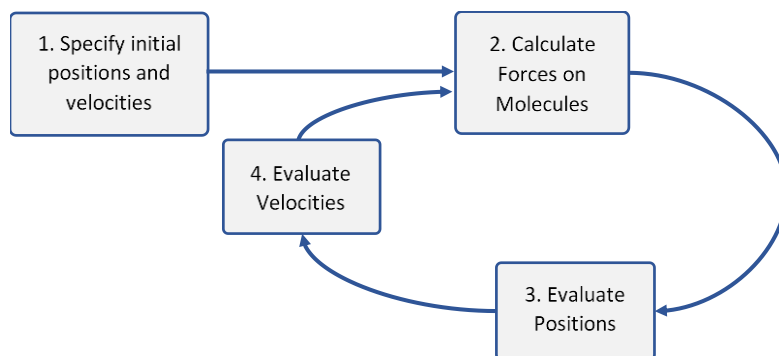


Figure 2-20 Summary of procedure for MD simulations numerically solving the equations of motion. After step 1, simulations cycle through steps 2 through 4.

There are multiple ways to evaluate new atom positions and velocities. The Verlet algorithm is based on the principle that the Taylor expansion of atom coordinates can be used to approximate its new position and hence velocity at the next timestep, Δt . Equation 2-15 shows the basic form of the Verlet algorithm for atom i , this approximation is better with smaller Δt , i.e., smaller increments of time.

$$r_i(t + \Delta t) \approx 2r_i(t) - r_i(t - \Delta t) + \Delta t^2 a(t) \quad \text{Equation 2-15}$$

The Verlet algorithm has drawbacks, it does not explicitly use velocity to calculate the new position. Therefore, the mean value for velocity needs to be calculated from multiple atom positions, which can then lead to errors when calculating the kinetic energy. An alternative method, the leapfrog algorithm, first calculates velocities at half-integer timesteps and then using these velocities, new positions are calculated at the integer timesteps. This algorithm has the downside of not directly calculating total energy from kinetic and potential energy because the velocity is not calculated at the same time as the positions. A different integration method, the velocity Verlet algorithm, uses both position and velocity when evaluating changes with each time step. This helps maintain a constant total energy and, as a result, system temperature remains constant. Velocity Verlet is superior compared to the Verlet method in terms of accuracy and stability (Frenkel and Smit, 2023).

2.2.1 Methods and Materials

This second half of the chapter initially describes the materials and experimental method followed when FP was recrystallised. Then, the molecular modelling approaches are detailed. This includes predicting the strength of intermolecular interactions within a crystal structure, and its external crystal shape (morphology). Following this, details of grid-based search methods are given. Finally, the method followed for MD simulations is described.

2.2.2 Materials for Experiments

These materials were used in the recrystallisation of FP.

2.2.2.1 Chemical Powders

Micronized FP powder was obtained from industrial sponsor Kindeva Drug Delivery.

Table 2-2 Details of micronized FP powder used in recrystallisation experiments.

Material	Purity	Source	Comment
Fluticasone Propionate	99.9 %	Kindeva Drug Delivery	Supplied by projects industrial sponsor

2.2.2.2 Solvents

Solvents listed in Table 2-3 were used to recrystallise FP.

Table 2-3 Details of different solvents used in recrystallisation experiments.

Solvent	Purity	Source	Comment
Methanol	99.9 %	VWR Chemicals	
Ethanol	99.93 %	VWR Chemicals	
IPA (2-Propanol)	≥ 99.9 %	Honeywell	For HPLC
Acetone	≥ 99.5 %	Sigma-Aldrich	

2.2.3 Experimental Method

2.2.3.1 Recrystallization of FP through Slow Evaporation

Separate beakers were prepared containing 30 g of each solvent: ethanol, methanol, isopropyl alcohol (IPA), and acetone. At room temperature, powdered FP was added to each container until fully dissolved and any surplus solid deposited to the bottom. Beakers were placed on magnetic stir plates and stirred for 24 hours at room temperature. Solutions were left to settle with no stirring for 24 hours, any remaining powder fell to the bottom of the container. 5 ml of saturated solution was extracted from

the top of the container and deposited into a different 10 ml vial. The vial was covered with para-film, as detailed in the Figure 2-21 below. Holes were placed in the para-film and the containers were left to stand at room temperature for 4 weeks.

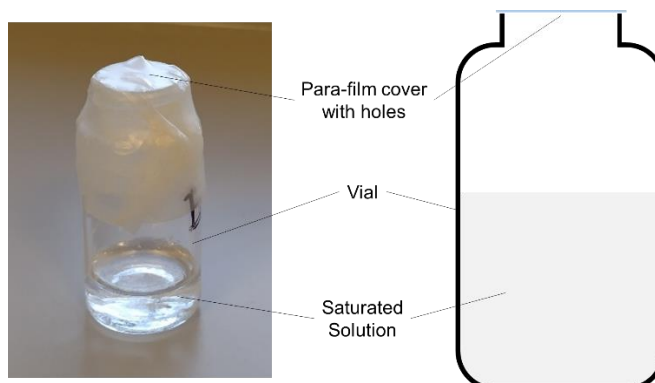


Figure 2-21 An image of the experimental set up and a labelled diagram of vial used for slow evaporation.

2.2.3.2 Visual Identification of Morphology

FP crystals were extracted from the vials and were examined using two different optical microscopes. The Olympus BX51 back lit samples and featured a polarising lens. The Keyence VHX1000 was a top lit optical microscope and could tilt the lens to view samples at different angles. Images of both microscopes are shown in Figure 2-22. Further Analysis of these images were performed using the program ImageJ.

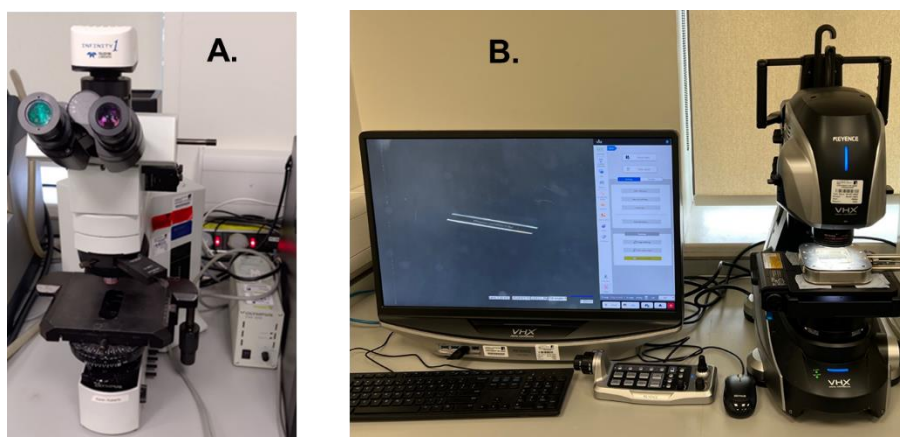


Figure 2-22 (A) Shows the Olympus BX51 Optical Microscope and (B) shows Keyence VHX1000 Optical Microscope when linked to a computer.

2.2.3.3 Characterising Crystal Structure using X-Ray Diffraction

Samples recrystallised from different solvents were prepared into separate crucibles for characterisation through x-ray diffraction (XRD). The Malvern PANalytical Empyrean

XRD machine scanned samples in normal Gonio (Bragg-Brantano) mode over a $2 - 30^\circ$ 2θ range with a 0.013° step size. Each run lasted 30 minutes at 45 kV and 40 mA.

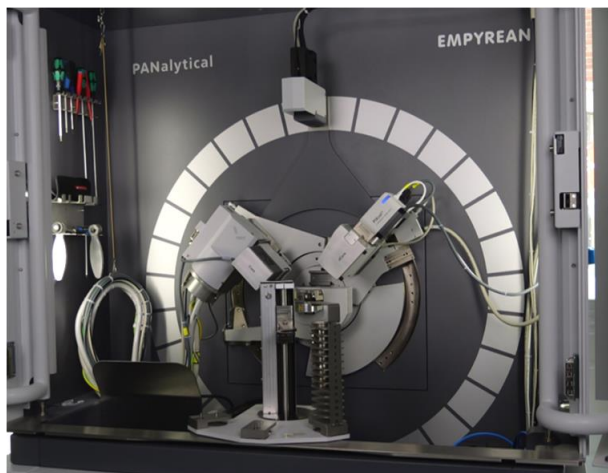


Figure 2-23 Image of the Malvern PANalytical Empyrean XRD machine used to characterise recrystallised FP.

2.2.4 Computational Methods

2.2.4.1 Molecular and Crystal Structure Analysis

2.2.4.1.1 Searching within Cambridge Structural Database

It was possible to search for all deposited polymorphs of a certain compound on the Cambridge Structural Database (CSD) using the browser-based search tool, Web – CSD (Groom et al., 2016). Furthermore, it was also to search for structural features, e.g. benzene ring, in the database using the ConQuest tool (Bruno et al., 2002), and generate a list of deposited crystal structures including said specified feature.

HFA-134a's monoclinic phase had the CSD reference code *VUZQIQ* (Brunelli and Fitch, 2002). Whereas, FP had Form I and II, with CSD reference codes *DAXYUX* (Čejka et al., 2005) and *DAXYUX01* (Kariuki et al., 1999), respectively.

2.2.4.1.2 Crystal Structure Visualisation and Analysis

The CCDC Mercury 2022.2 program (Macrae et al., 2020) visualised crystal structures, different polymorphs were compared through analysis of bond distances and angles. Molecules were shown in different styles, such as ball and stick, capped stick, and space fill. Specified planes of crystal structures, such as (100), were also visualised in the program, which made it possible to inspect molecular projection and d-spacing.

Furthermore, the CSD-Particle feature was used to evaluate surface properties of planes in the crystal structure. This included measuring rugosity, the fluctuation in surface height, and visually assessing surface chemistry from the frequency of H-bond donating and accepting atoms. Topology of the surfaces was also measured using its solvent probe accessible area. Where, a probe of 1.2 Å radius was used with grid spacing of 0.3 Å. Rugosity was equal to the ratio of surface area measured using the probe divided by the projected area of the of that surface.

2.2.4.1.3 Molecular Conformational Relaxation

The molecular conformations were relaxed using the Forcite module in Materials Studio (BIOVIA, 2017). This geometry optimisation used the steepest descent algorithm with the universal force field and Gasteiger partial charges. The conformation potential energy was minimised to a convergence tolerance of 2×10^{-5} kcal/mol. This method removed disorder and relaxed molecules that were used as probes in the grid-search work and FP's different polymorphs.

For example, in the original DAXYUX (form I) .cif structure file from the CSD (Čejka et al., 2005), the high length of OH group had an uncharacteristically high partial charge on the hydrogen atom. Also, the fluoro-methyl group showed disorder and included three atoms with half positions (Čejka et al., 2005). These additional atoms were deleted, and it was assumed the remaining group was the correct position.

The DAXYUX01 (form II) .cif structure file (Kariuki et al., 1999) from the CSD had been determined using powder XRD and solved via genetic algorithm technique where defined structures were mutated until a suitable result was found. This meant the final structure did not show any disorder, such as in the fluoro-methyl group. Also, the final structure did not include hydrogen atom positions because the XRD method struggled to locate them due to their low molecular mass. So, hydrogens needed to be added then were optimised using the Forcite module. The carbon skeleton of the molecule was kept rigid and hydrogen positions were allowed to move.

2.2.4.2 Predicting Strength of Crystal Structure and Morphology

The strength of intermolecular interactions in the crystal structure and its external morphology were predicted by calculating the lattice, slice, and attachment energies, . These calculations were performed under the following assumptions:

- The model was assumed to be at 0 K, so van der Waals and electrostatic interactions can describe the intermolecular interactions between two atoms.

- The charge distribution of an isolated molecule also describes the charge distribution of a molecule in the bulk structure.
- No surface relaxation – so surface terminations and oncoming slices match a similar layer in the bulk.
- The strength of intermolecular bond as a function of (hkl) do not change significantly during crystallisation.

Charge calculation

The semi-empirical AM1 method within MOPAC (Stewart, 1990) was used to predict the partial charges of each atom for all solid-state analysis of HFA-134a and FP, both form I and II. Also, it was used to predict the atomic partial charges of molecules used as probes in the grid-search work.

Habit 98 Input File Format

The molecular modelling program HABIT98 (Clydesdale et al., 1996) applied empirical force fields to predict a crystal structure's lattice energy, intermolecular interaction strength and external morphology. It uses a generic input file which is adapted for different purposes. These input files are generated using *hfile98_new.exe* where a crystal input file in a .cssr format must be specified. Also, the crystal's charge and symmetry file are required.

Lattice Energy Prediction of HFA-134a and FP

HABIT98 (Clydesdale et al., 1996) predicted a crystal structure's lattice energy, when the input file specified LATT mode. The calculation begins with fractional coordinates of an asymmetric unit then uses the space group symmetry operators to complete a unit cell. Subsequently, this is built into a 3-D crystal lattice through repetition along the U, V, and W crystal directions. Then intermolecular interaction energy is calculated using an atom-atom approach, which assumes the interaction energy between a pair of molecules is equivalent to the sum of all constituent atom interactions. Lattice energy is equal to the sum of all atom-atom interactions between a central molecule and all surrounding molecules. The extent of surrounding molecules is determined by the limiting radius, after this point the lattice energy increases by a negligible amount. The input file contains a list of different limiting radii in ascending order and the program goes through each individually using a for loop. With each calculation, bonds are only calculated that fall within the new radius and not the previous. By measuring lattice energy at different limiting radius distances, it capable to see its converged value. If an asymmetric unit consists of more than one molecule, then calculations sum the

interaction energies for each molecule of the asymmetric unit and then find the average interaction energy for all sites.

Electrostatic parameters came from the partial charge prediction specified above, vdW parameters were inherent to the force field potentials and their cutoff distances were set by the limiting radius. This process was performed for FP and HFA-134a. The Dreiding force field (Mayo et al., 1990) was deemed appropriate for calculating the strength of HFA-134a's intermolecular interactions in chapter 5. The predicted lattice energy value was similar to the experimentally measured sublimation enthalpies (Acree and Chickos, 2010). These are discussed further in the results of chapter 5. The Dreiding force field (Mayo et al., 1990) was also deemed most appropriate for FP calculations, the predicted Lattice energy of the stable polymorph, Form I, was stronger than the lattice energy calculated via Tripos 5.2 (Clark M. et al., 1989). Shown in the appendix section A.2. Therefore, the Dreiding force field was used for all the calculations of Form I and Form II in chapter 7. It was also used in grid-based searches shown in chapter 8.

Intermolecular Interaction Strength Prediction

HABIT98 (Clydesdale et al., 1996) also categorised the crystal structure into interactions between molecular pairs and predicted their interaction energies. This meant it could divide the lattice energy into its constituent intermolecular interactions, also known as 'synthons'. Each synthon represented a pair of molecules, their positions and directions were specified with respect to the unit cell. The input file was specified as LATT mode with the DEBUG -1 option and was calculated at different limiting radius distances.

The output of DEBUG -1 divided the total lattice energy into its synthons and categorised each synthon by a number, e.g. *DM 28*, and this was specified as DEBUG 28 in LATT mode. This analysed the constituent atom-atom interaction of each synthon and also created a 3D .cssr, file the molecular pair. The procedures described were followed for both form I FP and HFA-134a's solid-state, results are shown in chapters 7 and 5, respectively.

Morphology Prediction

It was possible to predict the external morphology using HABIT98 (Clydesdale et al., 1996) when the input file specified FULL mode. Initially, this method needed planes with high d-spacing and therefore high likelihood of being present. The program Mercury

Mercury 2022.2 was used to predict the BFDH morphology which identified the planes with largest d-spacing in the crystal structure. These planes were included in the input file so HABIT98 could predict morphology using the attachment energy model.

A single limiting radius is set, such as the radius which lattice energy converged. Then the list of the different identified growth faces is read individually using a for loop. The program identifies the interplanar spacing of the growth faces, identifies the structures bonding network and then calculates the associated interaction energies, using the limiting radius as the cutoff distances of non-bonded interactions. Interactions are assigned to being either slice or attachment energy following the principles discussed in section 2.1.4. Slice energy is equivalent to all atom-atom interactions within a growth layer of d_{hkl} thickness, attachment energy is equivalent to all the interactions that are outside this layer.

A classical Gibbs-Wulff polar plot is used to predict the morphology by using the attachment energy per face and assuming the attachment energy is proportional to the centre-to-face distance. This could then be visualised using the Visual Habit part in the Mercury 2022.2 software (Macrae et al., 2020). A morphology .cif file that was created from the BFDH method was adapted so that instead of d-spacing, each plane had an attachment energy. The synthons previously predicted were related to the growth of each face. Categorised as either external or internal synthons, depending on if they point parallel or perpendicular to the growth direction of a face, respectively. This procedure was performed for form I FP and the results are shown in chapter 6.

2.2.4.3 Grid-Based Search of Molecular Pairs and Crystal Surfaces

Grid based search methods were used to predict intermolecular interactions in different circumstances. Such as, a favourable molecule pair between solute-solute and solute-solvent. Also, favourable binding sites of solutes and solvents on crystal surfaces.

Molecular Pair Searching: Mol-Mol

The mol – mol code (Hammond et al., 2003, Hammond et al., 2006) could calculate the interaction energy between a pair of molecules; target molecule and a probe. This helped understand solute and solvent interactions and to see which sections on the target molecule would have the most attraction. A target molecule remains stationary, while a probe molecule is mobile and moves into different positions, as shown in Figure 2-24 with its spherical coordinates. As probe molecules searched through the grid positions, they would rotate about their axes in order to account for the different molecule orientations and different positions relative to the target molecule.

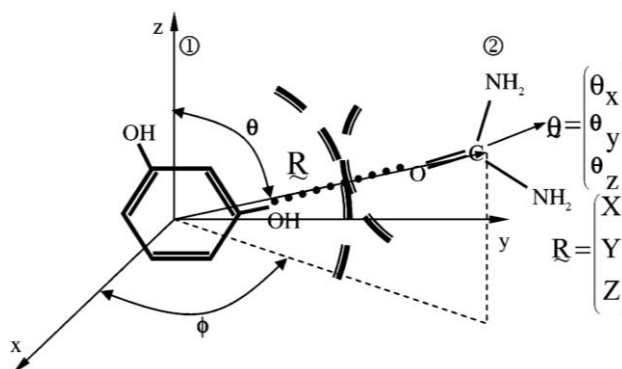


Figure 2-24 Spherical polar coordinates with respect to a stationary target molecule and mobile probe molecule (Hammond et al., 2003).

In the program, the target molecule's coordinates remain frozen, and the mobile probe molecule moves around spherical polar coordinates. The probe molecule is translated through its different positions via a translational magnitude (λ) and the two spherical polar angles, (θ) and (ϕ), that defined a unit vector. Grid positions are at intervals of $\Delta\theta$ and $\Delta\phi$, also the mobile molecules orientation angles are θ_x , θ_y , and θ_z . Leading to Equation 2-16, where x_i , y_i , z_i , and x_i' , y_i' , z_i' , are the atomic coordinates of the starting and final positions post transformation, respectively. M is a rotation matrix (a function of orientation angles), R is a vector defining the central position of the mobile molecule, and λ is a translational magnitude which is minimised with respect to the intermolecular-pair potential energy. Further details can be found via the method's publication (Hammond et al., 2003, Hammond et al., 2006).

$$\begin{pmatrix} x_i' \\ y_i' \\ z_i' \end{pmatrix} = M \begin{pmatrix} x_i \\ y_i \\ z_i \end{pmatrix} + \lambda R \quad \text{Equation 2-16}$$

Interaction energies were calculated using the Dreiding force field potential (Mayo et al., 1990) and it was assumed that the system would be at 0 K, so molecules were rigid. Only single solvent probes were used, which also meant that the liquids intermolecular structuring was assumed to not impact the interactions. In these studies, molecules were relaxed through steepest descent method using the method of section 2.2.4.1.3, all atomic partial charges were predicted using the AM1 method in MOPAC (Stewart, 1990). FP studies used the partial charges predicted for form I and HFA studies used the charges predicted for molecule 1 of its solid-state. Input files were created using the program *SolvationInputMaker.jar*, search specifications were inputted to this graphical user interface. The Dreiding force field potential (Mayo et al., 1990) calculated interaction energies. A 10 x 10 x 10 spherical grid shape with a radius of 15 Å was used, this distance is appropriately larger than the force fields non-bonded interaction cut-off distance. The resulting spherical grid is shown in Figure 2-25 with the stationary target FP molecule in the centre. Although gaps in the grid appear as it expands, this size and

shape was deemed sufficient because it still predicted the strongest interactions at closer distances. The probe molecules were allowed to rotate about their own axes into different orientations, in 30° Euler angle steps. Results of this study are shown in chapter 8.

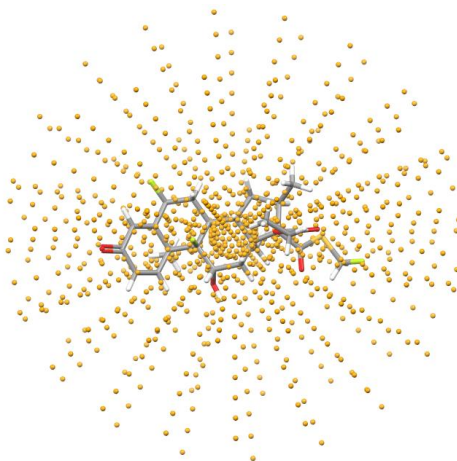


Figure 2-25 Molecule-molecule grid-based search. A probe molecule occupies each of the orange points surrounding the target molecule and interaction energy is measured.

Overall, the mol-mol code predicted the favoured molecular pair positioning for a solute-solute interaction, a stationary FP molecule with another mobile FP solute molecule. Also a solute-solvent interaction of a stationary FP molecule with mobile HFA-134a, ethanol, methanol, and water solvent molecules.

Surface Searching: Syst-Search

The Syst-Search code (Hammond et al., 2007, Ramachandran et al., 2015) is a different grid-based search that performed a systematic grid-based search of a probe molecule over a specified cleaved crystal surface, interaction energy between the two was measured at different positions. This generated a distribution of energies which could compare the different crystal faces, for example, it could help evaluate the favoured surface binding site of a solvent molecule and adsorption with solute molecule.

Syst-Search code is like Mol-mol but has a different grid shape, orthorhombic rather than spherical. The probe molecule rotates about its axis into different orientations, as described above in Equation 2-15 and Figure 2-24, but the stationary target molecule was a slab of a crystal surface. Furthermore, force field potentials were also used to calculate the interaction energy based on an atom-atom summation.

A representation of the grid search over a crystal surface is shown in Figure 2-26. When preparing a study, the (hkl) of a crystal plane must first be specified and the code created a cleaved slab. This was 3 unit cell layers thick in the y and z-axes (horizontal)

to suitably represent the varied surface rugosity. Slabs were 3 unit cell layers thick in the x-axis (vertical) to ensure interaction energies had converged to their maximum and they would not increase if more crystal layers were added. Overall, this resulted in a slab composed of $3 \times 3 \times 3$ unit cells. Also, Some of FP's crystal surfaces have multiple surface terminations. To account for this, the surface terminations which produced the lowest attachment energy were selected.

A three-dimensional orthorhombic grid was placed over the crystal surface, as illustrated in Figure 2-26. A grid size of $10 \times 10 \times 10$ was chosen, the size of this grid in the y and z-axes (horizontal) would vary depending on the slab, whereas vertical spacings in the x-axis were consistently 1.0 \AA . The grid was offset in the x-axis relative to the surface termination so that it produced the highest interaction energy. This meant the grid position accounted for varying degrees of surface rugosity, the offset ensured the lowest probe position would be the closest possible position to the surface. Also, the original slab was encased in a surrounding $3 \times 3 \times 3$ matrix of extra slabs in the model to negate edge effects, as illustrated in Figure 2-26.

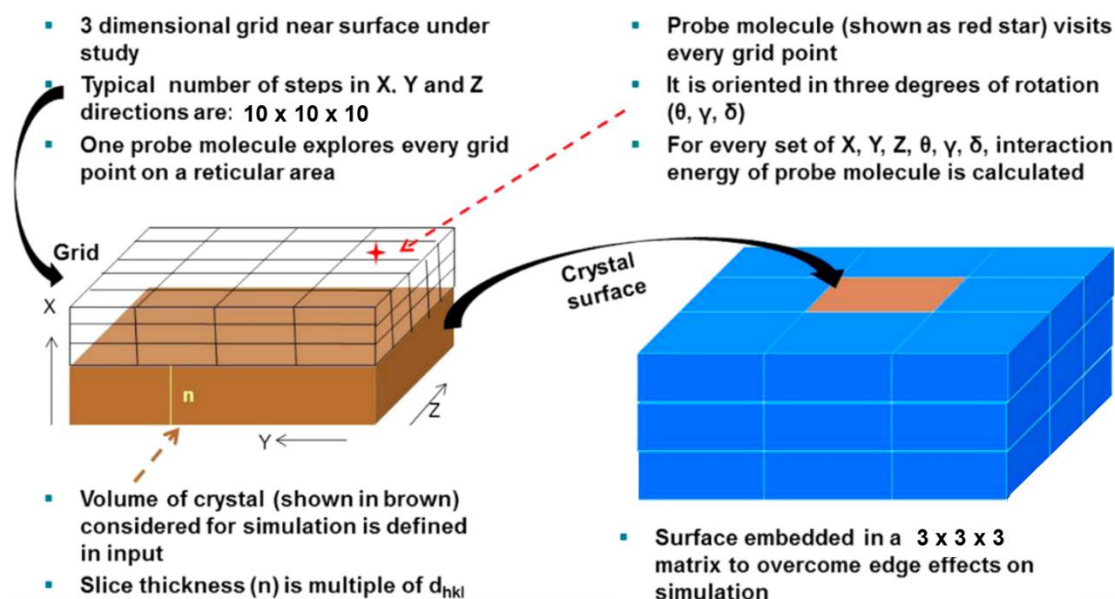


Figure 2-26 Molecule-surface grid-based search. A 3-D grid over crystal surface, probe molecule occupies each cell. Surface embedded in a matrix. Interaction energy between molecule and crystal slab below then predicted (Ramachandran et al., 2015).

Probe molecules would move systematically and occupy each position of the grid, then would rotate about their centres of geometry to represent different molecular orientations. Molecules rotated in 30° Euler angle steps, following Equation 2-15. The model calculated interaction energy between the crystal surface slab and probe molecule using the Dreiding force field (Mayo et al., 1990). The model was assumed to

be at 0 K, so only non-bonded potentials were included. It was also assumed that no surface relaxation takes place. Furthermore, the model only uses a single molecule as a probe. So, for example, if this was a liquid, a single molecule would not account for the intermolecular interactions and structuring of that liquid.

The important morphological faces of FP were probed with FP solute molecules, HFA-134a, ethanol, methanol, and water solvents molecules. Probe molecules were relaxed through steepest descent method, and atomic partial charges were predicted using the MOPAC – AM1 method (Stewart, 1990). The Dreiding force field potential (Mayo et al., 1990) performed calculations. The interaction energy results of this study are shown in chapter 8. They only include the highest value predicted at each grid cell, this removed repeat readings from a molecule rotating about its axis in the same cell.

2.2.4.4 Solvent Influenced Morphology Prediction

The attachment energy morphology prediction was adapted to account for the different solvent interactions with crystal surfaces. In model 1, the growth rate of face was proportional to the ratio of strongest solute and solvent probe interaction on that surface. This is shown in Equation 2-17, where U_{hkl} is the surface growth rate, E_{att} is attachment energy, U_{solute} and $U_{solvent}$ are the solute and solvent probe interaction energy.

$$U_{hkl} = \frac{U_{solute}}{U_{solvent}} \quad \text{Equation 2-17}$$

Model 2 was similar, but also accounted for surface roughness. Growth rate was inversely proportional to the surface's rugosity. Equation 2-18 shows how it divides by the ratio of surface rugosity, R_g , with the lowest surface rugosity, $R_{g\ min}$.

$$U_{hkl} = \frac{U_{solute}}{(U_{solvent} \times \frac{R_g}{R_{g\ min}})} \quad \text{Equation 2-18}$$

Measuring Interaction Energies of Different Particle Morphologies

Systematic search was used to measure particle cohesion and adhesion with propellant. It was performed by probing the surfaces of FP with different molecules, FP represented cohesion and HFA-134 was adhesion. The strongest interaction energy was predicted for each face. This was weighted based by surface area % of each face and used to generate an average interaction energy for each morphology.

2.2.4.5 Molecular Dynamics Simulations

Overview

MD simulations were performed using with DL suite, a combination of packages that would build systems, run the simulations, and analyse the resulting trajectory files. These were all compiled on a Linux operating system. Figure 2-27 overviews how the packages are connected. **DL_FIELD** built the system, creating a box of solvent molecules and assigning each atom force field parameters. **DL_POLY** ran the MD simulations and produced trajectory files. While **DL_ANALYSER** extracted useful information from the trajectory files. Further details of each package are provided in their dedicated sections.

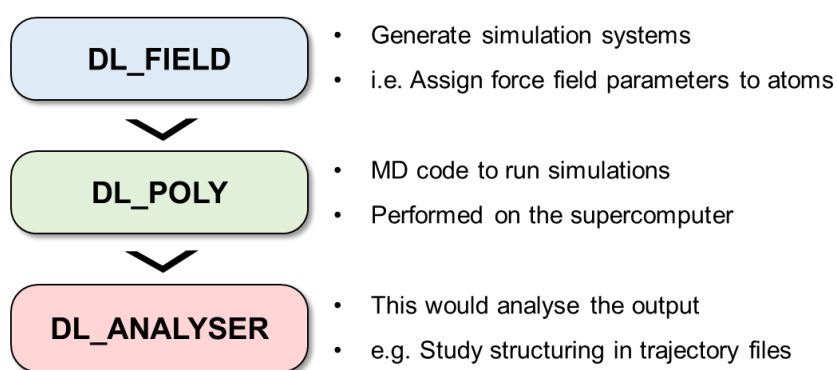


Figure 2-27 Overview of the DL Suite. A series of packages that combined to build, perform, and analyse molecular dynamics simulations.

DL_FIELD: Building Liquid HFA-134a Systems

The *DL_FIELD* (Yong, 2016) package prepared the input files necessary for *DL_POLY* MD simulations. From a user's perspective, details of a desired system were specified within *dl_field.control* file. Then *DL_FIELD* would create two new files, one which specified atom positions, and another which specified force field parameters for each atom.

For this system a molecule file of HFA-134a in the .xyz file format was the initial configuration file, but it was also possible to use a .pdb format. A system consisting of a 53 Å cube containing 1000 molecules was selected. Molecules were randomly distributed, with a minimum 2 Å space between each other. 1000 molecules was deemed a sufficient system size as it was validated by test simulations containing 1500 molecules which reproduced the same overall intermolecular radial distribution functions (RDF), these are shown in the appendix section A.3. Peguin's specialised force field had previously been developed to represent HFA-134a's liquid state (Peguín et al., 2009). Results of a solvent thermal expansion test, in the appendix

section A.3, confirmed that the potential developed by Peguin was the best at reproducing the experimental liquid density when compared against the generic force fields OPLS (Jorgensen et al., 1996) and PCFF (Sun, 1995). Therefore, the Peguin force field was used for all the proceeding simulations, i.e. all the results presented in chapter 6.

It was important that each atom was labelled via the DL_F naming format (Yong, 2016). This provided each atom type with a generic naming convention which remained consistent, regardless of which force field was used. This meant it was possible to use DL_ANALYSER to analyse the trajectory files and it did not matter when different force fields were used. Essentially, the atoms were described in three parts: a letter, a number, a second letter, *e.g.*, *F180C*. The first letter was the element of the first atom. The number referred to the type of bond, was single fluorine atom bonded to a carbon. The second letter was the element of the second atom. A more detailed description of naming nomenclature can be found published elsewhere (Yong, 2016, Rosbottom et al., 2019). However, for ease of understanding, the results shown in chapter 6 do not refer to the DL_F naming format. A more human readable format is used instead. The atoms of HFA-134a are defined by which functional group they belong to. For example, (C)F₃ refers to the carbon in the CF₃ group, and CF(H₂) refers to the hydrogen atoms in the CFH₂ group.

Simulation settings were specified to follow the same method as previously published (Peguín et al., 2009). For example, molecules were rigid apart from rotation around the C-C bond axis, details of bond lengths and angles are provided in the appendix section A.3. Furthermore, atomic partial charges for each atom were provided by the force field and are also detailed in the appendix. A 14 Å cut-off distance for non-bonded interactions between molecules was specified. Overall, DL_FIELD created three new input files necessary for MD simulation FIELD, CONFIG, CONTROL, detailed descriptions of these are provided in next section.

DL_POLY: Simulating MD Systems

The molecular dynamics code DL_POLY 4.10 (Todorov et al., 2006) was used to simulate the liquid structure of HFA-134a. Simulations were performed using ARC 4 at the University of Leeds High Performance Computing (HPC) facilities. Three input files were required: CONFIG, FIELD, and CONTROL. The initial CONFIG file generated by DL_FIELD contained configuration information, where atoms were located. The FIELD file, also generated by DL_FIELD, contained details of which atoms were bonded and their force field parameters. For example, the FIELD file specified that HFA-134a

molecules were rigid apart from rotation around the C-C bond axis, and it assigned the electronic atomic charges that are listed in the appendix. Meanwhile, the CONTROL file detailed simulations settings, such as timestep, length, ensemble, etc. A new CONTROL file generated to perform each simulation step as desired.

At first, atoms in the CONFIG file were randomly positioned and were not equilibrated to temperature. Therefore, the first set of CONTROL steps aimed to gradually introduce energy to reach system equilibration. Runs were first performed in the microcanonical NVE ensemble with a constant number of atoms, volume, and energy. At the very first step a random velocity was introduced to each atom, and to avoid the system expanding uncontrollably from atoms having high repulsion energies, a low starting timestep and temperature was used. Variable timesteps were used so an optimum value was found. The system temperature was incrementally increased in 50 K, starting from 10 K to the target temperatures. Non-bonded cut off distances were set to 14 Å. This was performed for five different target temperatures, ranging from 203 - 323 K.

It typically took a total of 500 pico-seconds (ps) for systems in the NVE ensemble to reach the target temperature and maintain a steady configurational energy. Then, the simulations were equilibrated in the canonical, NVT Berendsen thermostat (Berendsen et al., 1984) for 100 ps with a 0.2 ps constant. To ensure simulated structures were at the correct density, this was followed by the NPT Nose-Hoover (Melchionna, 1993) ensemble simulation with 0.4 ps and 1.0 ps for the thermostat and barostat constants, respectively. A constant target pressure of 20 atm was assigned as this was well above the vapour pressure so it ensured the system would remain in liquid phase, and overall, the process of NPT equilibration lasted 1 nano-second (ns). Simulations returned to the NVT Berendsen thermostat (Berendsen et al., 1984) with a 0.2 ps constant for another 1 ns and then production runs were performed for a total of 5 ns using a fixed time-step of 2 femto-seconds (fs) with the same NVT ensemble. This deemed an acceptable length as it was validated by an example production runs of 100 ns showed the same intermolecular RDF graphs, as seen in the appendix section A.3. Typically, Nose-Hoover is used for production runs as it is better at reproducing the NVT canonical ensemble compared to Berendsen thermostat, which is normally used for minimisation. However, when the force field has been parameterised, such as in this system, then Berendsen is suitable for production runs and is computationally cheaper (Frenkel and Smit, 2023).

After each simulation step, new output files were created. STATIS contained statistical information at each timestep, including box size, temperature, etc. OUTPUT was a summary of both the simulation setting information and statistical data for each step.

The REVCON file contained the atoms new positions post simulation, equivalent to CONFIG. The new trajectory details of each atom after simulation were in REVOLD, equivalent to REVIVE. Before restarting after a new step, the newly formed positional and trajectory information needed to be swapped from the previous step. Therefore, REVCON replaced CONFIG, and REVOLD replaced REVIVE. HISTORY files, also known as the trajectory files, contained atom position at different timestamps of the simulation. These frames were only created during production runs and were written every 2000 timesteps, or 4 ps. Overall, the process of equilibration required many steps, so scripts in bash programming language were developed to automate some of the submission stages.

DL_ANALYSER: Analysing Simulations

The in-house analysis code, *DL_ANALYSER* (Yong and Todorov, 2017), analysed the HISTORY and STATIS files produced by the simulations. The RDF represents system structuring by measuring the probability of finding another atom from that reference atom as a function of spherical radial distance. It is measured within bins divided by varying spherical radius and is equivalent to the ratio between the number of atoms at position r compared to the number of atoms in the bulk density. The term atom can also refer to a point representing the centre of a molecule, e.g., its centre of mass. RDF, $g(r)$ is described by Equation 2-19, where r is the spherical radial distance and dn_r is number of atoms in specified bin, dV_r is the volume of the specified bin, ρ is number density of the bulk liquid.

$$g(r) = \frac{dn_r}{dV_r \cdot \rho} \approx \frac{dn_r}{4\pi r^2 dr \cdot \rho} \quad \text{Equation 2-19}$$

The coordination number is the number of atoms present at a specified distance and is equivalent to the area under the peak in the RDF graph. It was measured by integrating Equation 4-3 using spherical co-ordinates, this produces Equation 2-19 where N is number of molecules, ρ is number density, r is spherical radial distance. Note, the version of Equation 2-20 does not show the spherical coordinates as it has been integrated across all angles. Figure 2-28 shows how the first shell was defined from the start point up to the first trough's mid-point. The second coordination shell was positioned from the first, to the second trough's mid-point.

$$N = 4\pi\rho \int_{r_0}^{r_1} r^2 g(r) dr \quad \text{Equation 2-20}$$

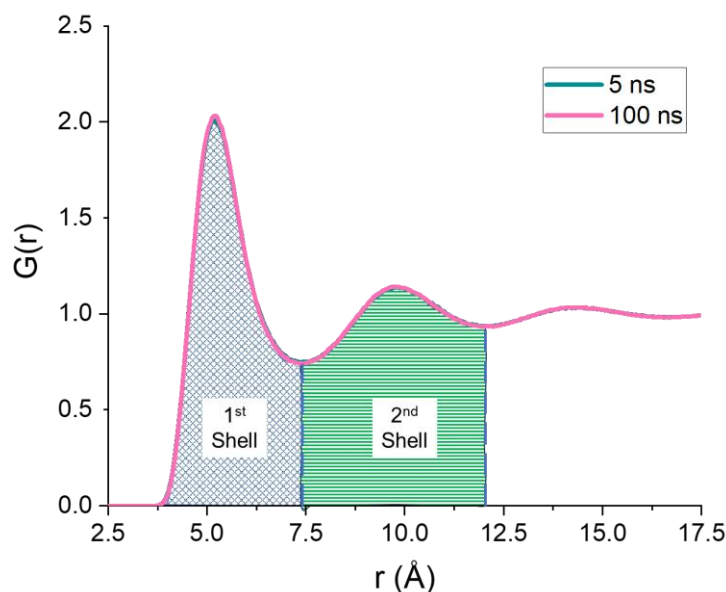


Figure 2-28 Example RDF for a liquid with 1st and 2nd coordination shells highlighted.

DL_ANALYSER could read the trajectory files and calculate the frequency of a specific intermolecular interaction. Hence, it could be used to help understand how HFA-134a molecules arrange and interact. First, HFA-134a was categorised into two groups centred on the two different carbon atoms, CF_3 and CH_2F , also referred to as the tri-fluoroalkane and mono-fluoroalkane groups, respectively. Figure 2-29 illustrates these two groups and atoms within these groups are specified with enclosing brackets, $(\text{C})\text{F}_3$ is referring the carbon of group A and $(\text{C})\text{H}_2\text{F}$ refers the carbon atom of group B.

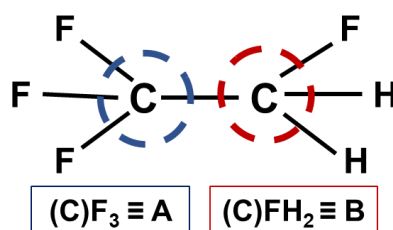


Figure 2-29 HFA-134a molecule categorised into two halves based on its induced dipole. Group A refers to the carbon atom of the tri-fluoroalkane, $(\text{C})\text{F}_3$, and group B refers to the carbon in the mono-fluoroalkane, $(\text{C})\text{H}_2\text{F}$.

DL_ANALYSER searched for occurrences when three groups interacted linearly within a critical distance of 5 Å. This was chosen based on the RDFs to ensure only the first contacts were considered. An example interaction shown in Figure 2-30 where three group A carbon atoms are considered to interact linearly. It shows the three successive groups had to be equal to, or closer than the critical distance of 5 Å, but the first and third groups had to be further than 5 Å. Therefore, the three-point vector angle centred

about the middle group could only adopt a range between 60 – 180°. The interaction was searched for between three group A and B carbon atoms, and other alternate groups (A...B...A and B...A...B). The frequency of interactions was divided by the total number of molecules and averaged over all trajectories.

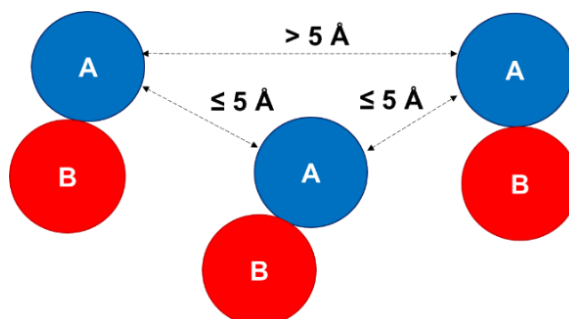


Figure 2-30 Example of a linear interaction with critical distance of 5 Å between three A groups. The 1st and 3rd atoms are further than the critical distance, so it is linear.

It was possible for DL_ANALYSER to analyse the packing of the liquid phase by looking at the arrangement of C-C axes in molecules closest to each other. This was defined by the non-bonded dihedral angle, $d(\varphi)$, and is illustrated in Figure 2-31 where atoms are labelled h, i, j and k. The example shows a dihedral angle between the green and blue planes when viewed along the non-bonded i-j interaction. In other words, the angle represents the twist between bonded axes of h-i and j-k. The distance between atoms i and j were constrained to be a maximum of 7 Å, this ensured angles were recorded when molecules were positioned end to end. The distribution of this angle was investigated using Equation 2-21. Where $n(\varphi)$ is the number of samples with angle φ , divided by the total number of the samples, N .

$$d(\varphi) = \frac{n(\varphi)}{N}$$

Equation 2-21

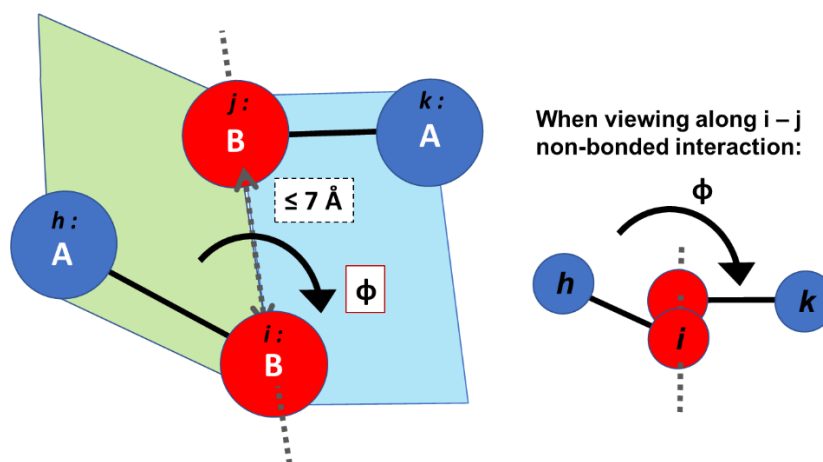


Figure 2-31 Four atoms are defined: h, i, j and k. The non-bonded interaction between atoms i and j have a separation distance ≤ 7 Å. The dihedral angle, φ , is equivalent to the angle between the green and blue planes in the diagram. When viewed along the non-bonded interaction between atoms i and j, the dihedral angle, φ , represents the twist between the bonded axes.

2.2.5 Conclusion

This chapter first equipped the reader with a broad description of scientific theory underpinning the research of this thesis. Following this, the computational and experimental research method for chapters 3 through to 6 was outlined.

Chapter 3: Intermolecular Packing of Hydrofluoroalkane's Solid-State

Summary: This chapter analyses a previously determined solid-state structure of HFA-134a. The strength of its intermolecular interactions is predicted using molecular mechanics techniques. It was identified that a dipole moment, caused by the asymmetric distribution of fluorine atoms, was responsible for the formation of 'weak hydrogen bonds' in the low temperature monoclinic structure. These were the strongest solid-state interactions and were believed to promote structural change from the higher temperature cubic phase.

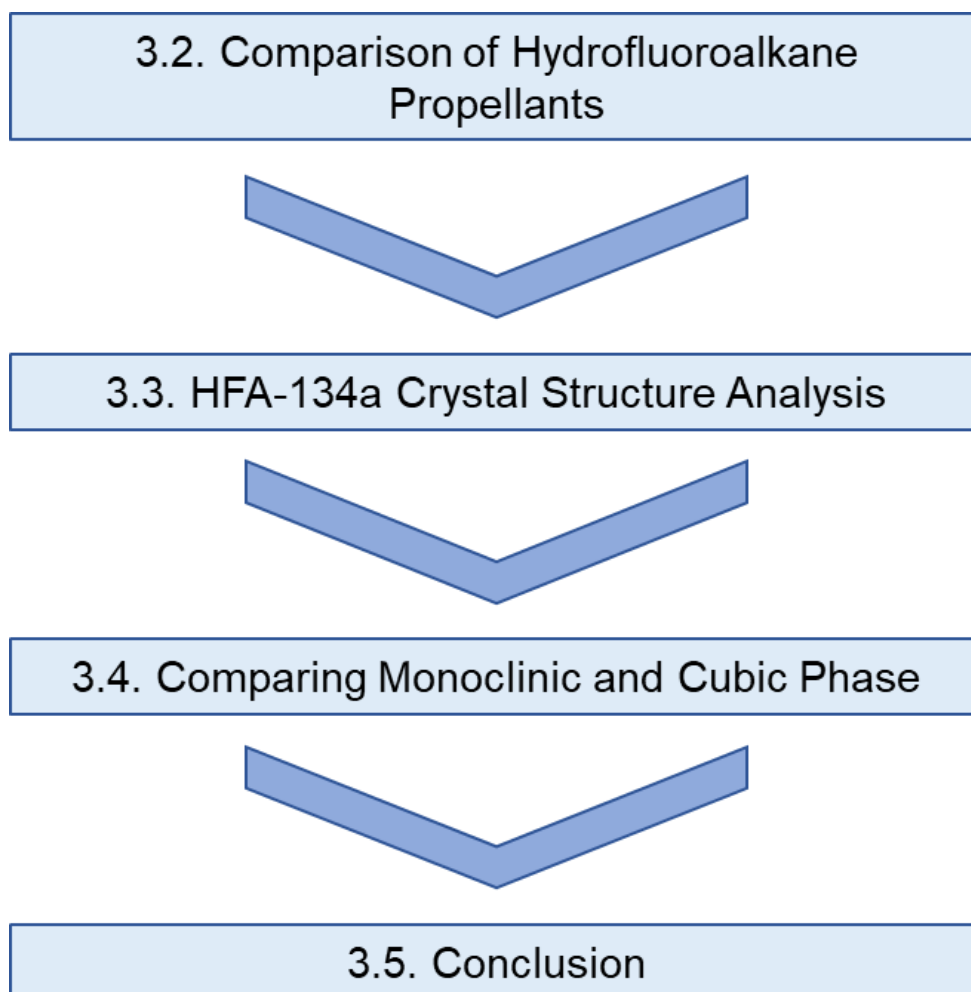
Chapter 3: Intermolecular Packing of Hydrofluoroalkane's Solid-State

3.1 Introduction

Earlier, in section 1.2.2, the physical properties of CFC and HFA propellants were compared. This chapter explores how fundamental molecular properties influence intermolecular interactions, and consequently influence macro scale properties such as melting and boiling point. The solid-state provides an accurate specification of atom positions, so was a useful starting point to analyse favoured intermolecular structuring and potentially identify interactions that are present within liquid phase of MDI formulations. Powder x-ray diffraction was previously used to determine the crystal structure for the propellant of interest, HFA-134a (Brunelli and Fitch, 2002). It has a dynamic structure, showing change between a higher temperature cubic phase and lower temperature, ordered monoclinic phase (Brunelli and Fitch, 2002). It was implied in previous studies that HFA-134a's chain length was too small a to show helical structures, with its preference for the staggered conformations (Do et al., 2010). However, it showed a slight variation from this conformer in the monoclinic phase to maximise intermolecular interaction strength (Brunelli and Fitch, 2002).

A combination of semi-empirical and molecular mechanics methods is used in this chapter, following methods detailed in section 2.2.4.2. First, the polarizability of other fluorinated ethane molecules is assessed to improve one's understanding of why it affects their physical properties. Then the intermolecular structuring of monoclinic HFA-134a is analysed and the strength of interactions are predicted. This helps build a profile of strong interactions between HFA-134a and how they are influenced by molecular properties. Also, comparing the monoclinic and higher temperature cubic phases might reveal a connection, which will help with proposing a structure for the disordered cubic phase. Overall, this fits into the scope of overarching research question by providing the basis of how and why HFA-134a propellant molecules preferably arrange on their own.

Chapter Flowchart Overview

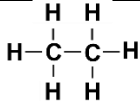
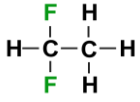
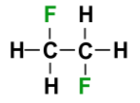
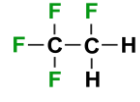
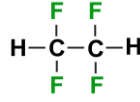
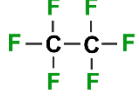


3.2 Hydrofluoroalkane Propellants

3.2.1 Physical Properties

The melting point of fluorinated ethane consistently increases with the number of fluorine atoms, Figure 3-1, and then it plateaus after the inclusion of three fluorine atoms. Boiling point also increases with number of fluorine atoms added and it peaks at the inclusion of three atoms, after that it begins to decrease in value. Figure 3-1 shows molecules with a total of 2, 3, and 4 fluorine atoms each have a pair of melting and boiling points, this is due to the isomers arising from the distribution of fluorine atoms about the ethane skeleton. Values in Table 3-1 shows the boiling points of HFA-152a and 134a are similar despite the differences in molecular mass, 152a's higher dipole moment is believed to compensate for this. The effect of additional fluorine atoms on the molecule's polarizability can be seen in Figure 3-2, with the electronegative fluorine atoms drawing electrons away from their bonded carbons. Note that partial charges were calculated to 4 significant figures using static molecular configurations. i.e., some were taken from available crystal structures and the conformations may not have had an optimised geometry. This resulted in geometric equivalent atoms in Figure 3-2 showing slight differences in partial charges.

Table 3-1 Chemical structures and physical properties of ethane, difluoro, tetrafluoro, and hexafluoro ethanes. ^a (van Nes and Vos, 1978). ^b (Lide, 2005). ^c (Meyer and Morrison, 1991). ^d (Brunelli and Fitch, 2002). ^e (Pace. and Aston., 1948).

Chemical and Commercial name	Structure	Molecular mass (g/mol)	no. of F atoms	Dipole moment (Debye)	Melting point (K)	Boiling point (K)
Ethane		30.07	0	0	90.3 ^a	184.6 ^b
1,1-Difluoroethane (HFA-152a)		66.05	2	2.26 ± 0.01 ^c	156 ^d	248.1 ^b
1,2-Difluoroethane (HFA-152)		66.05	2	0	169	242.3 ^b
1,1,1,2-Tetrafluoroethane (HFA 134a)		102.03	4	2.06 ± 0.01 ^c	172 ^d	247 ^b
1,1,2,2-Tetrafluoroethane (HFA 134)		102.03	4	0	184	253 ^b
Hexafluoroethane		138.01	6	0	173.1 ^e	195.1 ^b

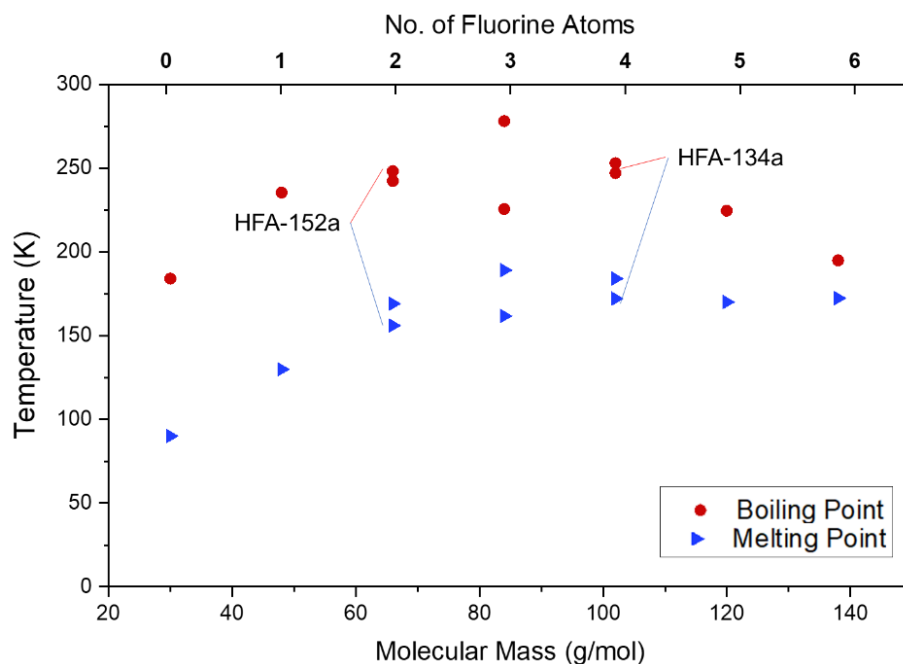


Figure 3-1 Melting and boiling points of fluoro-ethanes; molecules with an ethane skeleton and different numbers of fluorine atoms. Ordered based on molecular mass and varying number of fluorine atoms. (van Nes and Vos, 1978). (Lide, 2005). (Meyer and Morrison, 1991). (Brunelli and Fitch, 2002). (Pace. and Aston., 1948).

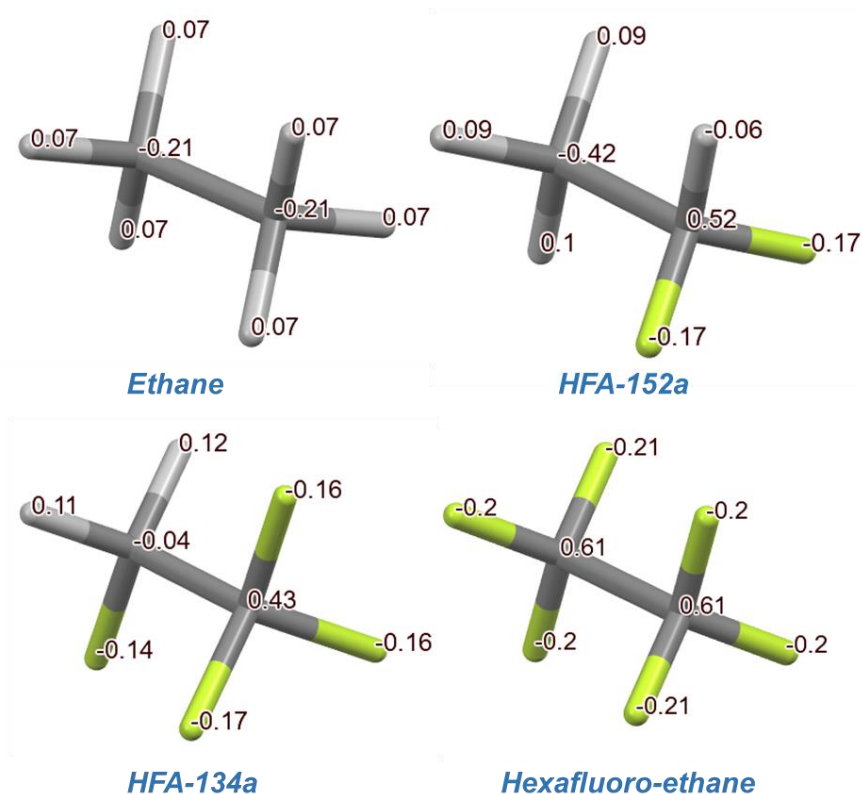


Figure 3-2 Polarizability of different fluorinated ethane molecules. Atomic partial charges showing the effect of additional fluorine atoms.

3.2.2 Lattice Energy Prediction

HFA-134a initially solidifies into a cubic crystal system and then as temperature drops further it transitions to a monoclinic phase. The total lattice energy of this monoclinic phase was predicted using the method described in section 2.2.4.2, it converged to -8.75 kcal/mol at a radial distance of 27 Å, seen in Figure 3-3. An equivalent converged lattice energy for HFA-134a was estimated from an experimentally measured enthalpy of fusion and evaporation (Acree and Chickos, 2010) to be -5.96 kcal/mol with an uncertainty of ± 0.38 kcal/mol. Whilst the predicted value is lower than the experimental one, it is still in the same order of magnitude, therefore values calculated can still be regarded as being useful in terms of comparing the magnitude of the different synthons. The lattice energy of ethane and hexafluoro-ethane were also estimated from experimental sublimation enthalpies (Acree and Chickos, 2010) to be -5.06 and -5.80 kcal/mol, respectively. One would usually expect an increased molecular mass produces a higher polarizability and hence higher lattice energy. Despite having a lower mass, HFA-134a has a similar lattice energy to hexafluoroethane and this is attributed to the dipole moment of 2.06 D increasing the strength of intermolecular interactions.

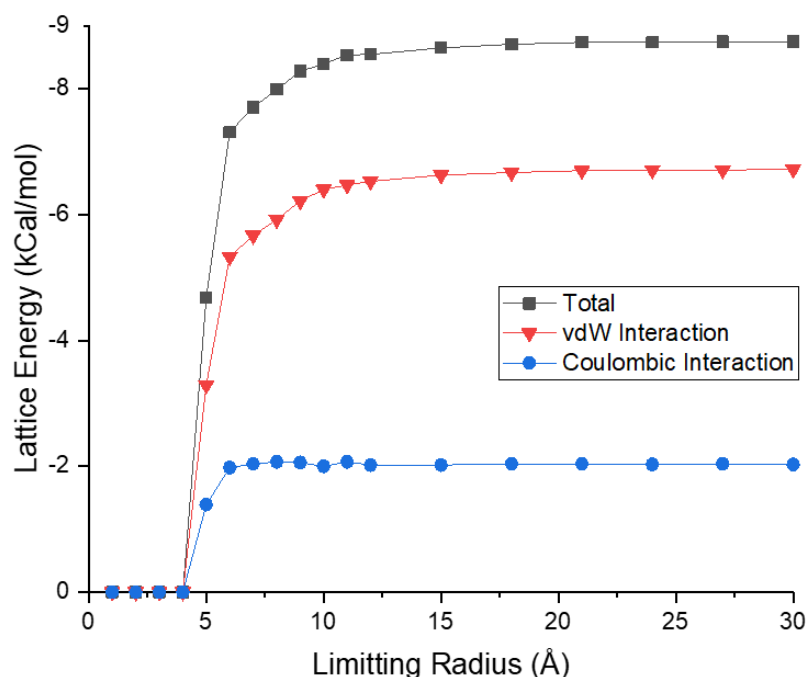


Figure 3-3 Lattice energy of HFA-134a as a function of the limiting radius, predicted using the Dreiding potential. Total lattice energy (black) is broken up into its constituent parts, van der Waals (red) and coulombic (blue).

Figure 3-3 shows that over 50 % of the interactions contributing to the lattice energy were within a 5 Å radius, furthermore, over 80 % of the contribution was within a 6 Å radius. The coulombic interactions converged to -2.03 kcal/mol within a radius of 7 Å. Overall, van der Waals (vdW) interactions make the predominant contribution to the

lattice energy, representing -6.71 kcal/mol. Therefore, vdW and coulombic interactions represented 76.8 % and 23.2 % of the total lattice energy, respectively. This trend was also seen in a previous liquid state study, a Monte Carlo simulation of the liquid state showed vdW interactions represented approximately 70 % of dimer interaction energy (Do et al., 2010). HFA-134a is the propellant of interest so was subjected to further structural analysis.

3.3 HFA-134a Intermolecular Structure Analysis

3.3.1 HFA Crystal Properties

HFA-134a initially crystallises into an orientationally-disordered body centred cubic (BCC) structure below temperatures of 176 K at atmospheric pressure (Brunelli and Fitch, 2002), it further transforms into an ordered monoclinic phase at 110 K (Brunelli and Fitch, 2002). This dynamic behaviour is also seen in ethane (van Nes and Vos, 1978) and other fluoroalkanes, (Brunelli and Fitch, 2002), (Klimenko et al., 2010), with solid to solid phase change from disordered cubic and then ordered monoclinic phase. The temperature-dependant properties of HFA-134a's two solid forms, measured using powder x-ray diffraction, are detailed in Table 3-2. It reveals the density of molecules per set volume doubles when transitioning between phases to ordered from disordered. The BCC phase's space group is yet to be determined so is labelled 'n/a', it is suspected to arrange into the $\text{Im}\bar{3}\text{m}$ space group, which is the same as ethane (van Nes and Vos, 1978) and hexafluoroethane's (Klimenko et al., 2010) cubic phases.

Table 3-2 Summary of the crystal properties of HFA-134a's two solid forms, previously measured using powder x-ray diffraction (Brunelli and Fitch, 2002).

Form:	Monoclinic	BCC
Measurement temperature (K)	80	176
Space group	$\text{P2}_1/\text{c}$	n/a
Z / Z'	2 / 8	1 / 2
α, β, γ (°)	90, 106.48, 90	90, 90, 90
a, b, c (Å)	8.76, 9.35, 9.08	5.76, 5.76, 5.76
Molecular density (n / Å ³)	0.0212	0.0105

Two molecules in the monoclinic phase's asymmetric unit are repeated through symmetry to fill the unit cell with a total of 8 molecules in Figure 3-4 (A), carbons are coloured differently to represent the asymmetric number of bonded fluorine atoms. Viewing the packing of 2x2x2 unit cells in Figure 3-4 (B) makes it clearer to see how the closest neighbouring molecules are orientated in opposite directions. Regardless of the carbon types, it can be seen the C-C axes roughly arrange to point parallel with the b-axis direction.

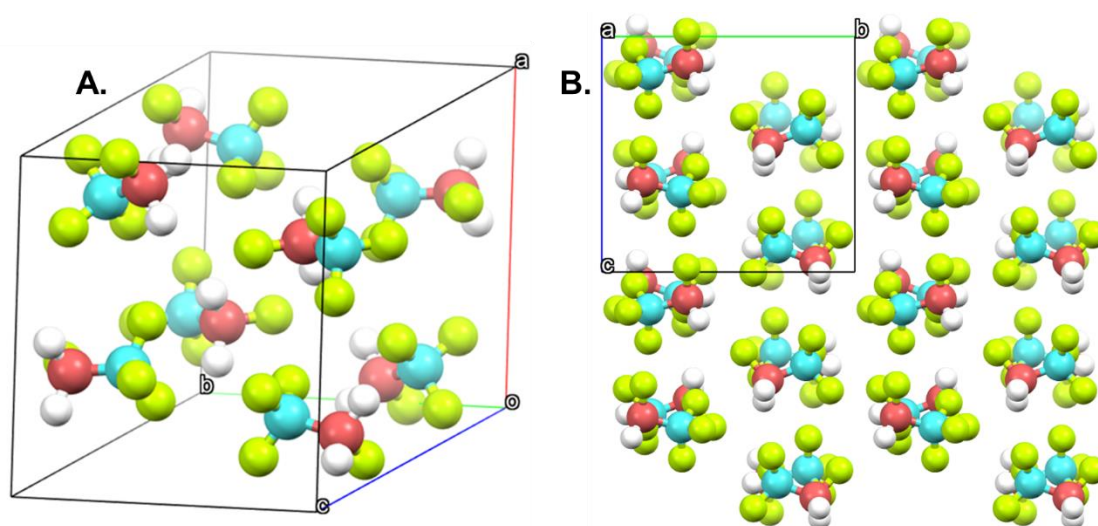


Figure 3-4 (A) Unit cell of monoclinic HFA-134a, the carbon of (C)F₃ is blue whereas the carbon of (C)FH₂ is red. Fluorine atoms are lime green and hydrogen atoms are white. (B) The packing of 2x2x2 unit cells viewed down the a-axis.

3.3.2 Monoclinic Intermolecular Interaction Strength Prediction

The top six strongest individual intermolecular interactions in the solid-state (synthons) are ordered on total intermolecular energy in Table 3-3. Synthons A – F represent pairs of interacting molecules, shown in Figure 3-5, with separation distances measured between the molecular centres of geometry. For synthon A, between molecule 1 and 2 of the asymmetric unit, the H-C-C-F torsion angle changes in a complementary way to allow closer packing. While a staggered conformation, with an angle of 180° has been shown to be the most energetically stable for an isolated molecule (Do et al., 2010), the two molecules in the asymmetric unit are structurally independent with torsion angles of 178° and 182°, enabling them to pack efficiently. Synthon D is also between molecules in the asymmetric unit, but in the opposite direction compared to synthon A. The torsion angle is not complementary and so molecules can't get as close, hence the interaction is not as strong.

Synthons B and C are both between a pair of the first and second asymmetric unit molecules, respectively. They are related by glide plane symmetry, relative to the unit cell, the molecules are reflected in the plane perpendicular to the b-axis and then moved half a cell edge length in the c-direction. The synthons E and F are also between a pair of the first and second asymmetric unit molecules, respectively. They are related via inversion symmetry about the origin of the unit cell.

The P2₁/c space group means the base asymmetric unit is repeated four times throughout the whole unit cell via symmetry operators. For each asymmetric unit there are two examples of synthons A, B, C and D, but only one example of synthons E and

F. Therefore, synthons A – D occur a total of 8 times in the unit cell and have a multiplicity of 8. Whereas, synthons E and F occur 4 times in the unit cell and have a multiplicity of 4.

Table 3-3 Top six strongest synthons are ordered on total interaction strength (Eng), with their van der Waals (vdW) and coulombic (Coul) components included. Multiplicity (Mult) represents frequency per unit cell. Distance (Dist) was measured between centres of geometry. Synthon symmetry was detailed (Symm Op) and which molecule of the asymmetric unit (AU). Also, percentage contribution to lattice energy (Latt %).

Synthon	Mult	Dist (Å)	vdW (kcal/mol)	Coulombic (kcal/mol)	Eng (kcal/mol)	Symm Op	AU ₁	AU ₂	Latt %
A	8	4.2	-0.69	-0.55	-1.24	Identity	2	1	14.2
B	8	4.6	-0.69	-0.42	-1.1	Glide Plane	1	1	12.6
C	8	4.5	-0.6	-0.36	-0.96	Glide Plane	2	2	11.0
D	8	4.6	-0.57	-0.32	-0.9	Identity	1	2	10.3
E	4	5.0	-0.25	-0.45	-0.7	Inversion	1	1	4.0
F	4	5.3	-0.13	-0.48	-0.61	Inversion	2	2	3.5
						Total Top 4 (%):			48.1
						Total Top 6 (%):			55.6

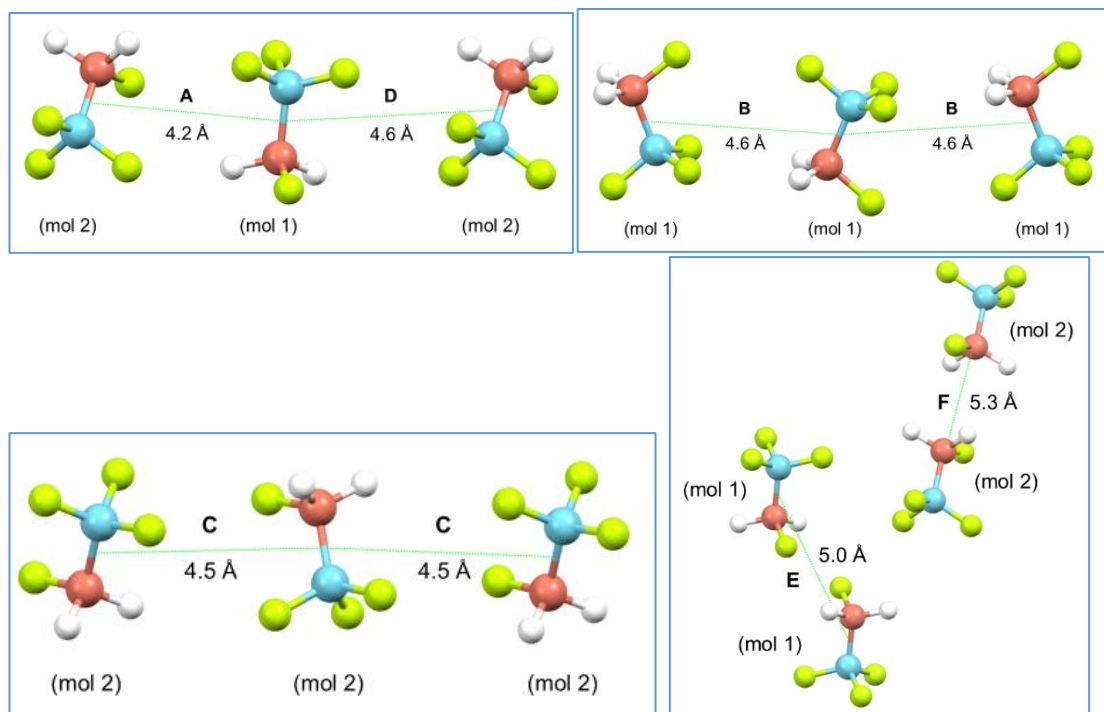


Figure 3-5 Images of synthons A - F with their separation distance labelled and which molecule of the asymmetric unit they belong to. Carbon atoms are coloured based on their group, the carbon of (C)F₃ is blue whereas the carbon of (C)FH₂ is red. Fluorine atoms are lime green and hydrogen atoms are white.

At lower temperatures, for the solid-state, HFA-134a molecules due to their permanent dipoles can be expected to position themselves to attain a greater interaction energy, as shown in Figure 3-5. The top four strongest synthons, A – D, all have molecule separation distances less than 5 Å and contribute 48.1 % of the lattice energy. Furthermore, Figure 3-5 shows these molecule pairs are positioned approximately anti-parallel between their C-C axes, Table 3-4 shows the non-bonded vector angle is in the range of 137-144°. This is the equivalent dot product angle between the two vectors of a C-C axis.

The uneven distribution of electrons in the molecule creates a dipole moment of 2.06 D throughout and anti-parallel alignment of dipole moments produce strong intermolecular interactions and allow for better close packing. In contrast, when the distance between molecules is greater 'in-line' alignments between dipoles (0° angle difference) might be expected to produce a stronger interaction energy (Israelachvili, 2011). The C-F bond in the CF₃ group, seen in Figure 3-2, has the greatest difference in atomic charge with values of +0.43 and -0.17 for carbon and fluorine, respectively. Positioning molecules approximately anti-parallel allows the strongest interatomic interactions to occur between carbon and fluorine atoms, this ranges between -3.3 to -2.2 kcal/mol. Overall, the strongest interactions would be expected to be achieved by arranging the dipole moments closer to 180°, but nonetheless packing efficiency must also be considered as steric repulsions might play a more important role than attractive forces in determining solid-state packing (Israelachvili, 2011). Therefore, this trade-off leads to synthons A, B, C, and D having vector angles in the range of 137-144°.

Table 3-4 Non-bonded vector angles of the different solid-state synthons. This is the equivalent dot product angle between the two vectors of a C-C axis. Group A are the (C)F3 carbon atoms and group B are the (C)H2F carbon atoms.

Ch—Ci — — Cj—Ck				Non-bonded Vector Angle for Each Synthon (°)					
h	i	j	k	A	B	C	D	E	F
B	A	B	A	143.4	137.0	138.1	143.4	180	180
A	B	A	B	143.4	137.0	138.1	143.4	180	180

Synthons E and F were found to have a vector angle between C-C axes of 180°, Table 3-4. Two CF₂H groups are positioned on top of each other in a way that avoids large repulsions and produces attractive inter atomic interactions between carbon and fluorine. Structural analysis in Figure 3-6 (A) shows the directions of the top six strongest synthons relative to each other, with vectors pointing between molecules' centre of geometry. Synthons E and F are pointing roughly perpendicular compared to

the other synthons. When combined with synthon strength prediction, it indicates synthons A, B, C, and D form a layer of strong interactions with closely packed, roughly anti-parallel molecules, and steric repulsions are minimised. These pack on top an equivalent layer which are connected through weaker interactions, synthons E and F. This appears more obviously in space-fill models of the molecules, shown in Figure 3-6 (B), where the foreground has a layer of molecules bonded through dashed black lines and the background shows additional layers.

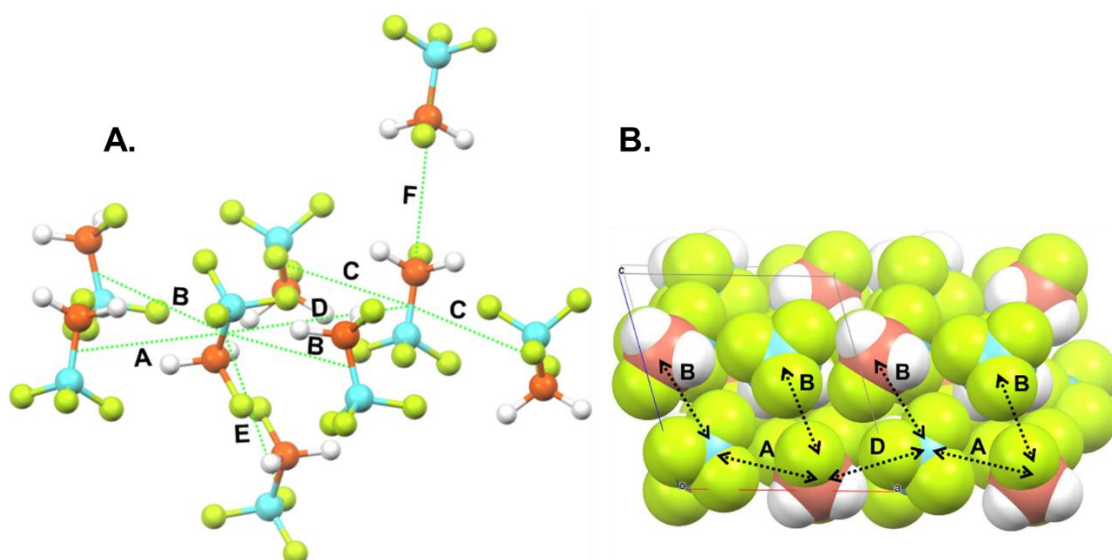


Figure 3-6 (A) Position of the top six strongest synthons relative to each other. The carbon of (C)F₃ is blue and the carbon of (C)FH₂ is red. Fluorine is fluorescent yellow and hydrogen white. (B) Spacefill model of the monoclinic phase. The foreground shows a layer connected by the strong synthons, A, B, C, and D, shown by black lines.

The synthons dihedral angles are shown in Table 3-5 for non-bonded interactions between different carbon atoms. A higher angle favoured, in the range 138-180°, when the non-bonded interaction is between two similar carbon atoms. Conversely, the opposite angle is presented when the non-bonded interaction is between two different carbon atoms, a smaller angle in the range 0-40° is favoured. These values show there is preference in the solid-state for C-C axes to be twisted in opposing directions.

Table 3-5 Non-bonded dihedral angles of the different solid-state synthons. This represents the twist between the two C-C axes in the synthon. Group A are the (C)F₃ carbon atoms and group B are the (C)H₂F carbon atoms.

Ch—Ci — — Cj—Ck				Non-bonded Dihedral Angle for Each Synthon (°)					
h	i	j	k	A	B	C	D	E	F
A	B	B	A	145.3	177.4	140.1	138.7	180	180
B	A	A	B	143.1	177.5	141.3	143.8	180	180
B	A	B	A	32.4	2.7	39.4	36.5	0	0

Hydrogen and fluorine atoms were found to have the closest interatomic distance of all the synthons and HFA-134a's monoclinic phase contains 8 notable examples per unit cell. These are part of synthons A – D, in the distance range of 2.46 to 2.84 Å and have C-H...F bond angles ranging between 160.8° to 111.1° with energies between -1.3 to -1.0 kcal/mol, respectively. These can be classified as 'weak H-bonds' (Desiraju and Steiner, 1999) because the hydrogen atoms are not covalently bonded to an electronegative atom, typically they have a bond energy less than 4 kcal/mol. Conventional H-bonds, where the hydrogen atom is covalently bonded to an electronegative atom, are usually stronger with bond energies ranging between 4 – 15 kcal/mol (Desiraju and Steiner, 1999). Typically, these stronger interactions have bond angles closer to 180° (Desiraju and Steiner, 1999) and this directionality has a larger effect on determining crystal packing (Yadav and Choudhury, 2017). Therefore, Brunelli and Fitch's hypothesis that the presence of C-H...F interactions brings the more ordered monoclinic phase of HFA-134a together appears correct. However, they are relatively weak interactions which don't show strong directionality and so they are perhaps not considered to be very influential in altering the inter-molecular packing structure compared to steric repulsions.

3.4 Relationship between Monoclinic and Cubic Phase

An equivalent pseudo cubic cell was identified within the structure of the lower temperature, ordered monoclinic phase, seen in Figure 3-7 (A). When compared to a standard BCC cell, Figure 3-7 (B), the equivalent cell edge lengths in the monoclinic phase transition from the initial 5.76 Å as molecules have moved into their favoured strong interactions. Figure 3-7 (B) shows the equivalent cell has extended along the c-direction, edge lengths increased to approximately 7.6 Å. Additionally, both equivalent (100) and (010) faces in the monoclinic phase have four corner angles that are close to 90°, whereas the equivalent (001) face resembles a rhombus shape instead with two corners < 90° and two > 90°. Overall, this shows the equivalent cell identified in the monoclinic phase does not retain a cubic shape as the lower temperature shortens one of the body diagonal distances.

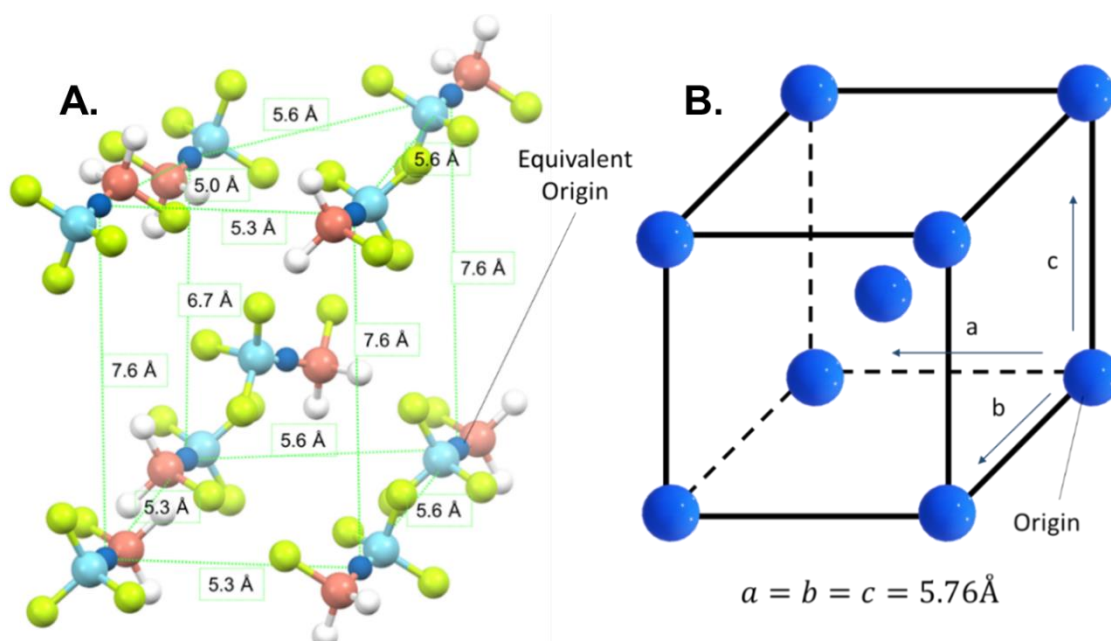


Figure 3-7 (A) Diagram of equivalent pseudo cubic structure within monoclinic structure. Each molecule's central point (centroid) is coloured navy blue, distances are measured between these points. (B) Shows HFA-134a's BCC cell with edge length dimensions.

An alternative view of the transformation can be in the equivalent planes of the two phases. The (040) plane of the monoclinic phase, Figure 3-8 (A), dissects five molecules' central point (centroid), the BCC phase's equivalent (110) plane also dissects the same configuration of centroids, shown in Figure 3-8 (B). The positions of corresponding centroids appear closer in the monoclinic structure compared to the BCC cell, this is attributed to increased intermolecular interaction strengths and denser packing in the lower temperature phase.

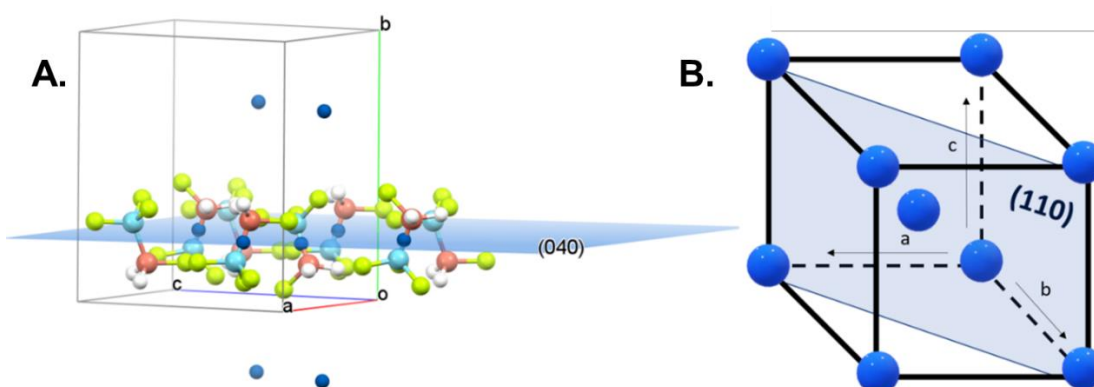


Figure 3-8 (A) The (040) plane in HFA-134a's monoclinic phase unit cell. (B) The BCC phase unit cell with the (110) plane highlighted. These planes are equivalent and dissect the same five centroids, which are represented by navy-coloured spheres.

As temperature is lowered, the disordered cubic lattice contracts and strong interactions begin to dominate due to the reduced thermal vibrations with the molecules “freezing out” into a preferred intermolecular orientation, resulting in a transition from cubic into its monoclinic phase. The strongest synthons in section 3.3 were a compromise between favourable, attractive, dipole positioning and a minimisation of steric repulsions. Figure 3-9 shows Synthons A – D occur from one corner to another of the equivalent pseudo cubic cell in the monoclinic phase, they have a separation distance less than 4.6 Å which is shorter than the BCC phase’s body diagonal length of 5.0 Å. This is the same as the layer of strong synthons shown in Figure 3-6. Furthermore, these strong interactions occur along the (040) plane which can be seen in Figure 3-8 (A). Therefore, the strongest synthons are responsible for distorting the dimensions of the cubic cell to the monoclinic structure and thus sacrificing the structures cubic shape to increase its intermolecular packing density.

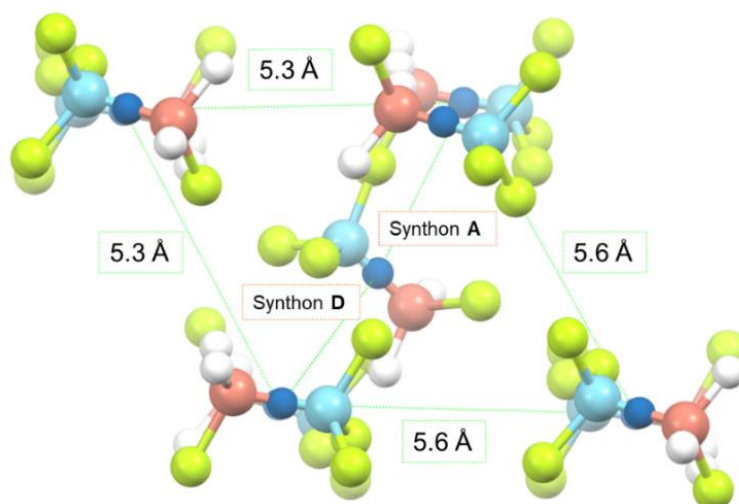


Figure 3-9 Looking down the equivalent (001) face of the pseudo cubic shape in the monoclinic phase. Each molecule’s centre point is coloured navy blue. The closest interactions, synthons A and D, travel diagonally in the equivalent cell.

Cubic phases are typically formed with particles of spherical symmetry, for example, adamantane (McCall and Douglass, 1960) has a comparatively spherical molecular geometry and exhibits rotational disorder. Ethane (van Nes and Vos, 1978) and hexafluoroethane (Klimenko et al., 2010) have also been found to solidify into high temperature cubic phases exhibiting molecular orientational disorder which subsequently order upon cooling into a low temperature monoclinic phase. Therefore, it would suggest HFA-134a’s disordered BCC phase would also follow this pattern, with the molecular centres occupying $Im\bar{3}m$ space group positions and exhibiting different rotational states with respect to their centre of masses. The proposed structure in Figure 3-10 draws upon ethane’s (van Nes and Vos, 1978), where the central point consists of

four molecules which are in-line with different coloured dotted lines at each body diagonal. This illustrates how each molecule would have different rotational states with respect to its own. For ease of visualisation the corner molecules are pointing in a single orientation, these are equally as probable to rotate to the orientations shown in the central point. Overall, this means it obeys symmetry operators compatible with the $Im\bar{3}m$ space group.

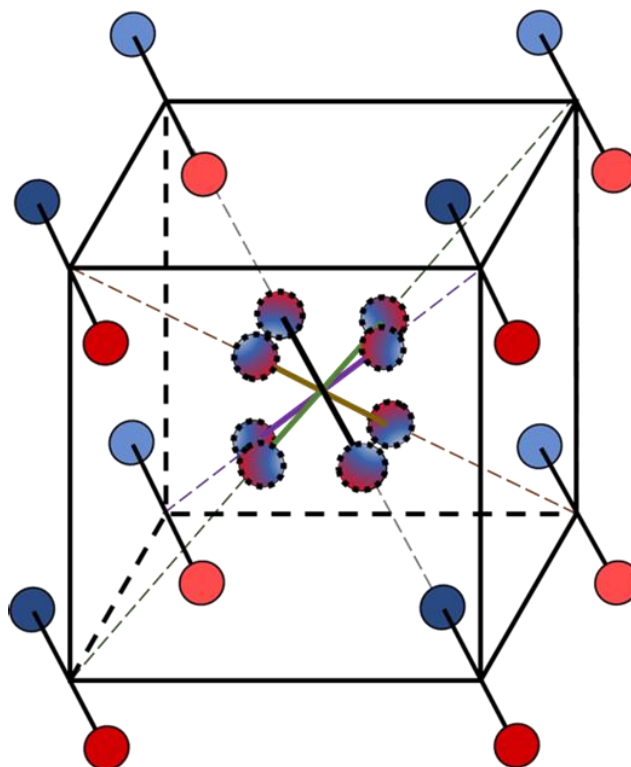


Figure 3-10 A proposed BCC layout for HFA-134a, based on the previously proposed structure of ethane (van Nes and Vos, 1978), where molecules occupy the $Im\bar{3}m$ space group positions. Within each molecule the carbon of $(C)F_3$ is blue and the carbon of $(C)FH_2$ is red. The central point represents the possible orientations as molecules rotate about their centres of mass on each lattice point.

3.5 Conclusion

A monoclinic solid-state structure, previously determined through powder x-ray diffraction, was a valuable record of favoured intermolecular structuring for the propellant of interest, HFA-134a. Use of molecular mechanics techniques helped with understanding how interaction strength was affected by adding fluorine atoms. For example, it was shown how including additional fluorine atoms on an ethane skeleton molecule altered polarizability, particularly if the atoms were asymmetrically distributed. In turn, the subsequent dipole moment enabled the formation of 'weak H-bonds' in the low temperature monoclinic structure as molecules preferably arranged to maximise

the strength of dipole-dipole vdW interactions. The monoclinic structure showed some resemblance to a pseudo cubic structure, like the material's higher temperature BCC phase. Further molecular mechanics analysis showed the strongest synthons in the monoclinic phase were responsible for the transition from disordered cubic to ordered. I have proposed that molecules in the disordered BCC phase would occupy positions of the $Im\bar{3}m$ space group while showing equal preference for different orientations.

Having analysed HFA-134a's strongest solid-state intermolecular interactions in this chapter, it would be interesting to see if they are also present at higher temperatures in the disordered liquid. Therefore, these results will help in the analysis of the following chapter which investigates the liquid states intermolecular structuring at different temperatures.

Chapter 4: Structuring of Pure Liquid Propellant HFA-134a Across Temperature Range

Summary: The liquid phase of HFA-134a is simulated at a range of temperatures using molecular dynamics. Its structuring was compared to interactions seen in the solid-state. As liquid temperature was reduced it caused molecules to be more ordered, and the similarity between the liquid and solid BCC phase's coordination numbers increased. It was shown that steric repulsions were the largest influence on the liquid packing, but weak hydrogen bond interactions also appeared in the liquid.

Chapter 4: Structuring of Pure Liquid Propellant HFA-134a Across Temperature Range

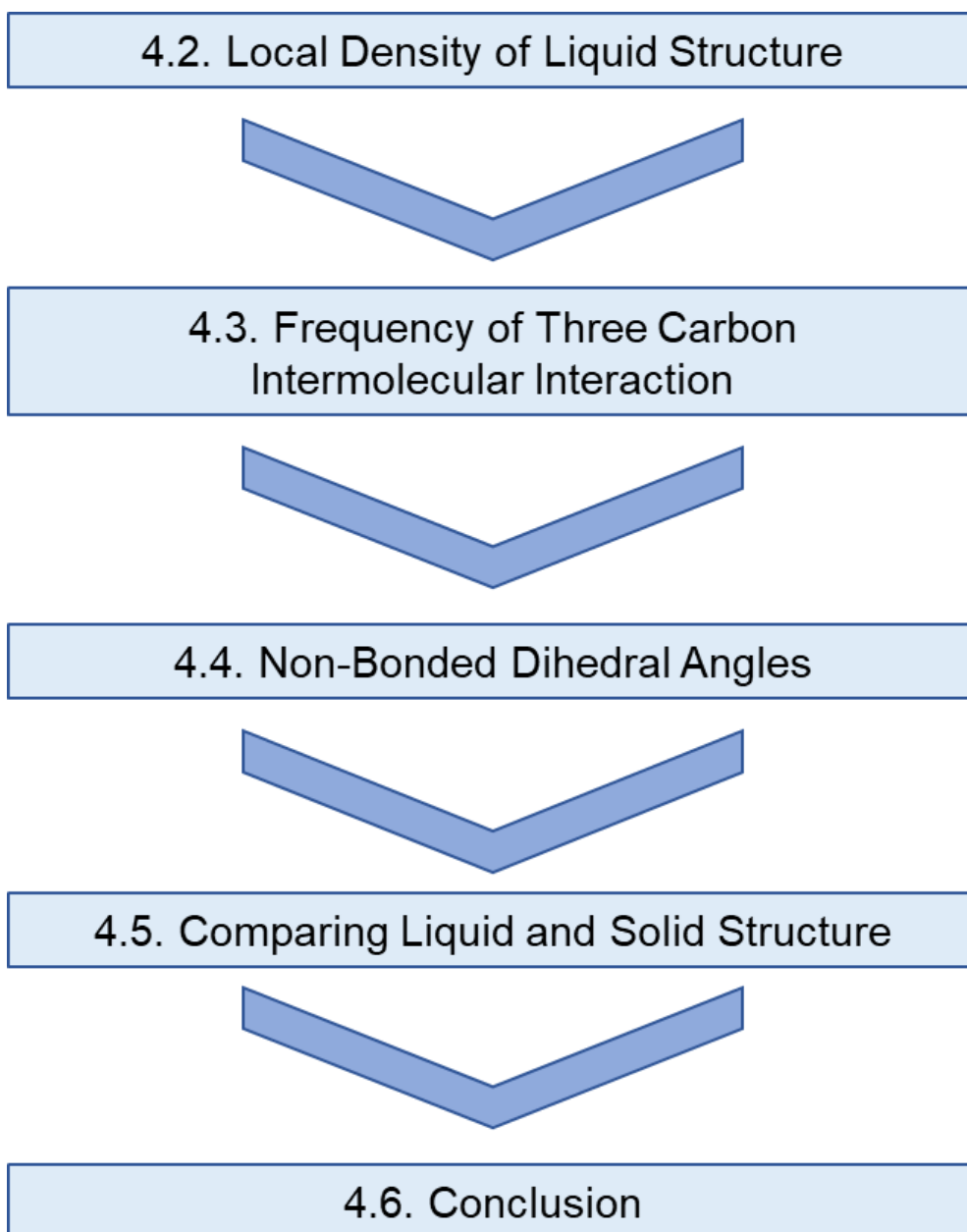
4.1 Introduction

Before molecular modelling can be used as a tool to help MDI formulation development, one must look at the structuring of the two phases: solid and liquid. It is necessary to first understand what complex network of interactions occur within the pure liquid phase. Then, the investigation can be expanded to interactions at the solid to liquid interface and see how this network is disrupted when a second party is included. Such as other formulation materials, including APIs, surfactants, ethanol, or canister coatings.

The last chapter discussed how favoured interactions in HFA-134a's solid-state enabled the formation of weak H-bonds. Previous molecular modelling studies have claimed weak H-bonds were also present in pure liquid (Lísal and Vacek, 1996) (Lísal and Vacek, 1997) (Do et al., 2010), and there was a preference for perpendicular alignment between the C-C axes (Do et al., 2010). Weak H-bonds played an important role in the formulation, separate investigations found their formation can change the dissolution of surfactants into HFA-134a (Wu et al., 2007) (Selvam et al., 2006).

This chapter aims to see if there is a connection in the structuring of the different phases and investigate the effect weak H-bonds have on HFA-134a's liquid phase. The results of MD simulations show the liquid phase's intermolecular structuring across a temperature range. The force field specially developed for HFA-134a was used (Peguin et al., 2009), and more thorough details of computational approaches followed are provided in section 2.2.4.5. Various liquid structural properties will be investigated, including local density (RDF), frequency of specified intermolecular interactions, packing arrangement (dihedrals) and non-bonded vector angle. Finally, the relatively disordered liquid phase will be discussed in relation to the previous chapter's results on the solid-state, which acted as a useful benchmark of favoured interactions.

Chapter Flowchart Overview



4.2 Local Density of Liquid Structure

4.2.1 Molecular Radial Distribution Function

To determine how the molecules interact, the HFA-134a molecule was categorised into two different groups centred on the two carbon atoms, CF_3 and CH_2F , categorised as the tri-fluoroalkane and mono-fluoroalkane groups, respectively. We henceforth refer to CF_3 as group A and CH_2F as group B. Atoms within these groups are specified with enclosing brackets, e.g. $(\text{C})\text{H}_2\text{F}$ refers the carbon atom of group B. We intend to assess the relative tendencies of how these groups interact with one another by identifying the frequency of various modes of contacts among these groups.

A molecular dynamics simulations of 1000 molecules in an initial 53 Å box was simulated over a range of temperatures, with 5 ns production runs in the NVT ensemble. The overall molecular model of HFA-134a's liquid structure is highlighted through the RDF plot for the molecular centres of mass in Figure 4-1. Which reveals three well defined peaks at intermolecular distances of approximately 5, 10 and 14 Å, indicating the extent of intermolecular packing within the liquid structure. These molecular RDF plots match those previously predicted (Lísal and Vacek, 1996, Lísal and Vacek, 1997, Do et al., 2010).

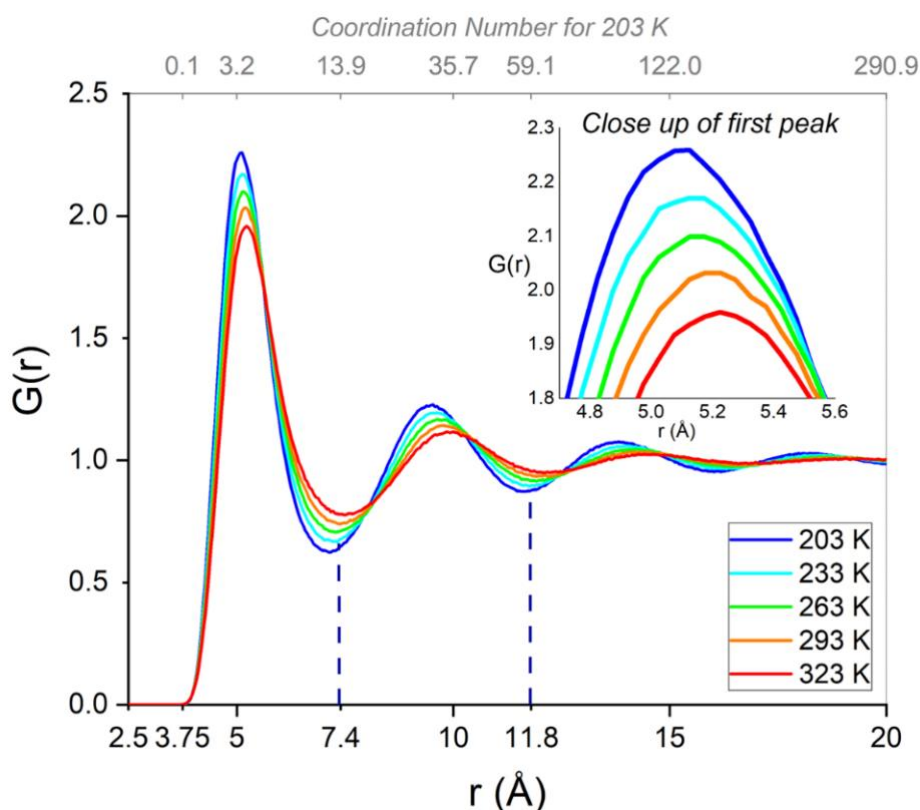


Figure 4-1 Molecular RDF plot for different temperature simulations of liquid HFA-134a. The inset graph shows the first peak. The coordination number of the 203 K simulation is shown in the upper x-axis.

Molecules packed closest together at the lowest temperature, 203 K, as evidenced by its highest initial peak and lowest initial trough. Lower thermal energy reduces molecular movement, so molecules were more likely to occupy positions favouring greater intermolecular interactions. The data reveals higher temperatures caused molecules to be more spread out, decreasing the liquid density. This is represented in Figure 4-2 with peaks in the RDF being positioned further away, lowering in height and troughs becoming shallower. Although, the overall inter-molecular packing behaviour was found to be rather consistent over the range of temperatures examined.

Table 4-1 Number of molecules in the first shell and sum of first and second co-ordination shells at a range of simulation temperatures.

Co-ordination shell:	1st	2nd	Density
Position:	7.4 Å	11.8 Å	(g/cm³)
203 K	13.7	60.0	1.47
233 K	13.1	57.0	1.40
263 K	12.4	53.8	1.32
293 K	11.7	50.4	1.23
323 K	10.8	46.4	1.14

Table 4-1 shows that the number of molecules in the surrounding co-ordination shells decreases when more thermal energy is provided. At the lowest temperature simulation, 203 K, 13.7 molecules are in the first coordination shell with a total number of 60 molecules in the first two shells. Molecule positions in the solid BCC phase were similar, Table 4-2 shows 14 molecules are in the first coordination environment and a total of 58 molecules were present in the first two shells. An RDF plot of both solid and liquid phases alongside each other, Figure 4-2 (A), shows the solid has two distinct initial peaks, representing the 8 closest and 6 next closest, and their positions align with the liquid's first shell. Furthermore, the solid's following peaks align with the liquids second shell. As liquid phase molecules move fluidly between shells, their RDF do not reveal sharp defined peaks as seen in the solid. However, when thermal energy is low enough for the solid to form, the liquid RDF is expected to split into these distinct peaks, as was seen in melt crystallisation of liquid iron into its solid BCC phase (Shibuta and Suzuki, 2008). Overall, this density is consistent with the density of the liquid HFA-134a beginning to resemble the BCC solid phase structure as the temperature reduces.

Table 4-2 Closest contacts in a BCC formation with distance as a function of cell edge and as actual distance for BCC phase of HFA-134a.

Closest contact	1 st	2 nd	3 rd	4 th	5 th	
Closest contact as function of a	$(\sqrt{3}) / 2$	1	$\sqrt{2}$	$(\sqrt{11})/2$	$(\sqrt{3})$	
Distance (Å)	4.99	5.76	8.15	9.55	9.98	
Frequency of molecules	8	6	12	24	8	Total
Total Number of molecules in shells	14		44			58
Equivalent shell [Position]	First Shell [7.4 Å]		Second Shell [11.8 Å]			

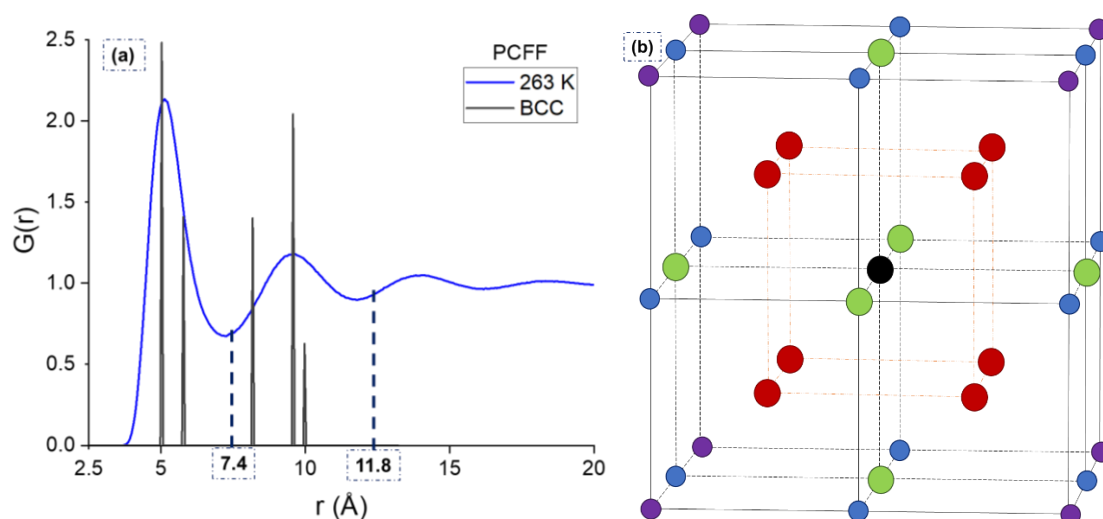


Figure 4-2 (a) Molecular RDF patterns of liquid simulation at 203 K, blue, and BCC solid phase, black. Both were normalised by the same number density. (b) Closest contacts of a BCC solid relative to a central point, black, 8 nearest, red, 6 second nearest, green, 12 third nearest, blue. Fifth nearest, purple.

4.2.2 Intermolecular Atom-Atom Radial Distribution Function

Intramolecular interactions were ignored, and only intermolecular atom-atom interactions were included in this section. Atom pair correlations within RDFs at 203 K are shown in Figure 4-3, showing that interactions involving carbon atoms, C-C, C-H and C-F, exhibit short range order with a relatively high initial peak and lower secondary and tertiary peaks. In contrast, the other atom pairs were found to exhibit little to no ordering at separation distances greater than 7.5 Å. Carbon-carbon interactions had the largest degree of ordering, with defined peaks at 5, 10 and around 14 Å, reflecting the molecular packing up to the third neighbour shells. Peaks were split due to the smaller vdW radius of hydrogen atoms and subsequently the CH_2F (B) groups were asymmetrical. This resulted in the initial peaks involving carbon atoms of the B group

being asymmetrical whereas the peak between carbon atoms of the CF_3 (A) group was symmetrical.

Fluorine to hydrogen was the closest contact, with initial peaks ranging from 2.5 – 3.5 Å, which consisted with the inter-atomic distances where weak H-bonds might be expected to occur (Desiraju and Steiner, 1999). The fluorine-hydrogen RDF between B...B interactions with $\text{CH}_2(\text{F})\text{-C}(\text{H}_2)\text{F}$ showed a clear, defined initial peak and trough whose ordering increased when temperature was reduced, whereas B...A interactions with $\text{C}(\text{H}_2)\text{F-C}(\text{F}_3)$ only showed an initial shoulder. It can be hypothesised from a steric hinderance point of view that A groups may reduce the ease of weak H-bond formation whereas with two B groups, a single F atom can easily form weak H-bonds with one of the two H atoms from the other group. Furthermore, such H-bonds would not be expected to be the strongest as the atomic charge difference between the hydrogen and electronegative fluorine is not as large compared to, say, an electronegative oxygen atom. Nevertheless, the effects of these H-bonds are expressed in the carbon-hydrogen RDF's ordered peaks, in particular the initial peak of the $(\text{C})\text{H}_2\text{F-C}(\text{H}_2)\text{F}$ interaction shows the favourability of two A groups to position themselves together. This is further supported by the long-range order shown in the hydrogen-hydrogen RDF. Figure 4-4 and 4-5 show the atom pair RDFs for simulations at 263 K and 323 K, respectively. They both have similar packing positions to 263 K but with less defined peaks, this highlights how ordering reduces as temperature is increased. Overall, carbon-carbon were the only atom pair RDFs to follow the same sharp peaks as the molecular RDF, indicating strong dipole-dipole interactions were unlikely to be present. Such a packing would allow the functional groups to freely rotate with steric repulsion minimisation likely being the main force directing molecular packing in the liquid state. As carbon atoms were at the centre of these functional groups, it would be expected that they would follow the same structure seen in the molecular RDF.

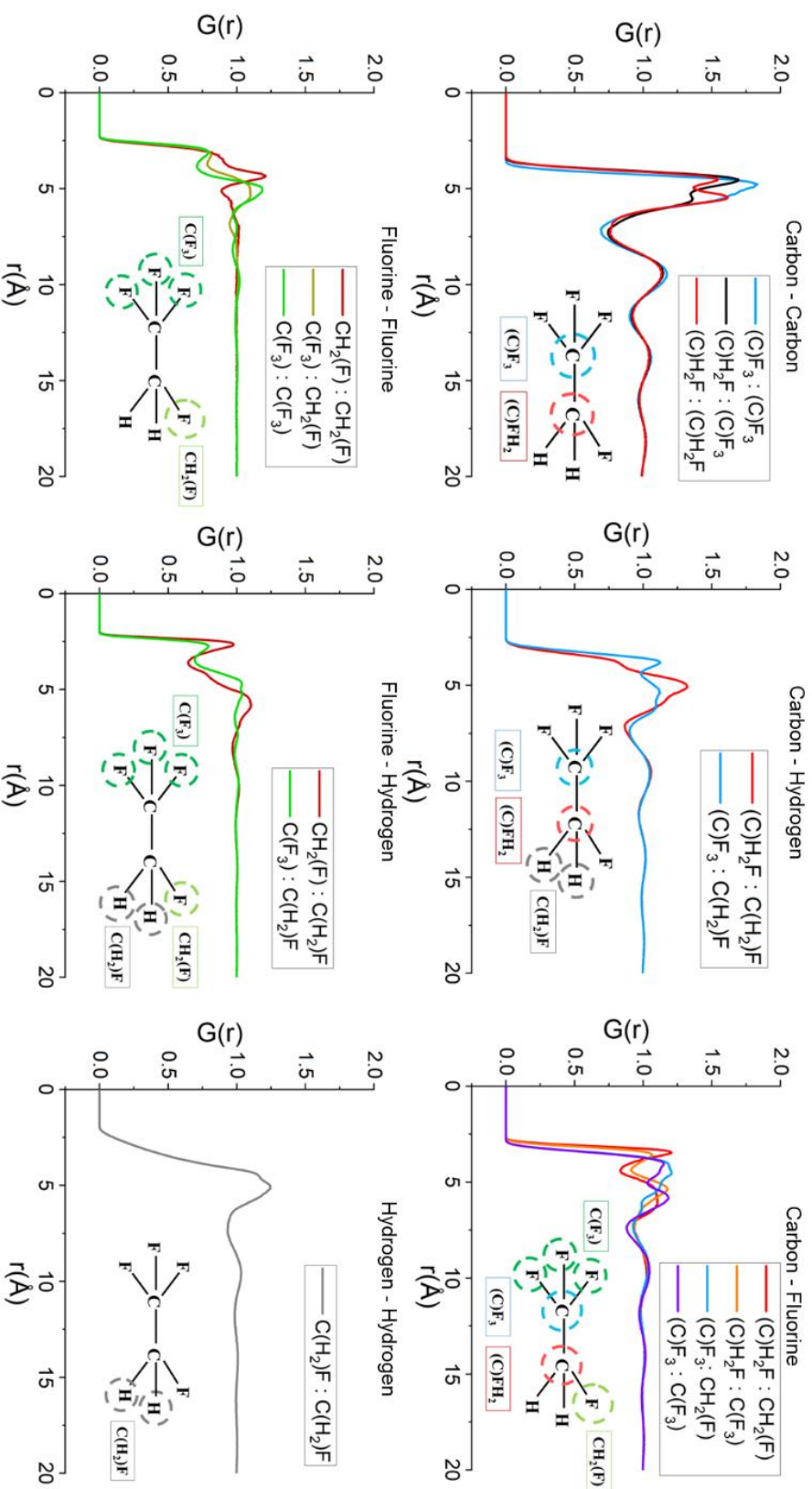


Figure 4-3 Atom pair RDF graphs for simulations at 203 K. These grouped into their different variations: carbon-carbon, carbon-hydrogen, carbon-fluorine, fluorine-fluorine, fluorine-hydrogen, and hydrogen-hydrogen. The notations include atoms in brackets, these represent the atoms involved in the RDF, e.g., $C(H_2)F$ represents the hydrogens of that group.

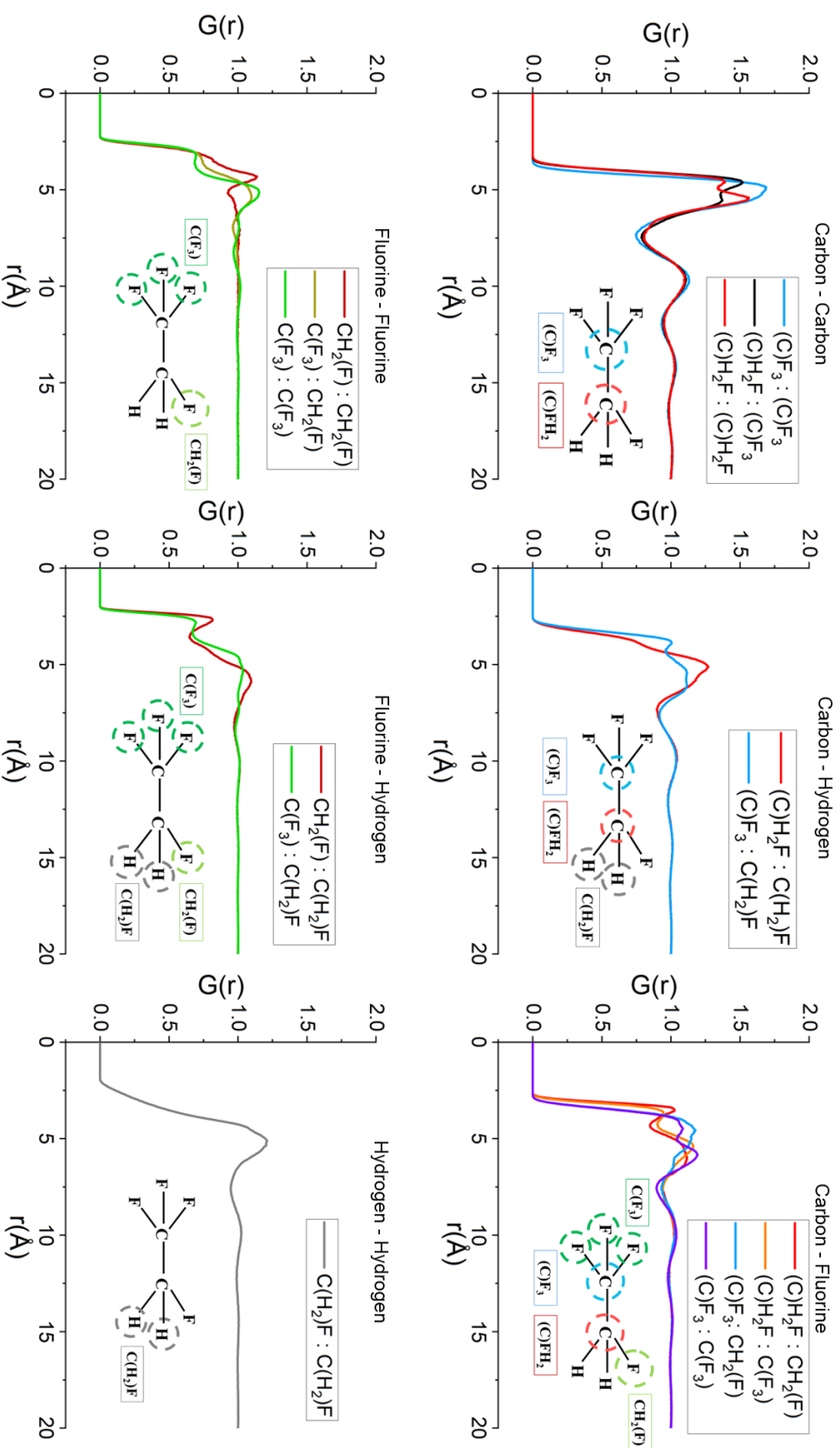


Figure 4-4 Atom pair RDF graphs for simulations at **263 K**. These grouped into their different variations: carbon-carbon, carbon-hydrogen, carbon-fluorine, fluorine-fluorine, fluorine-hydrogen, and hydrogen-hydrogen. The notations include atoms in brackets, these represent the atoms involved in the RDF, e.g. $C(H_2)F$ represents the hydrogens of that group.

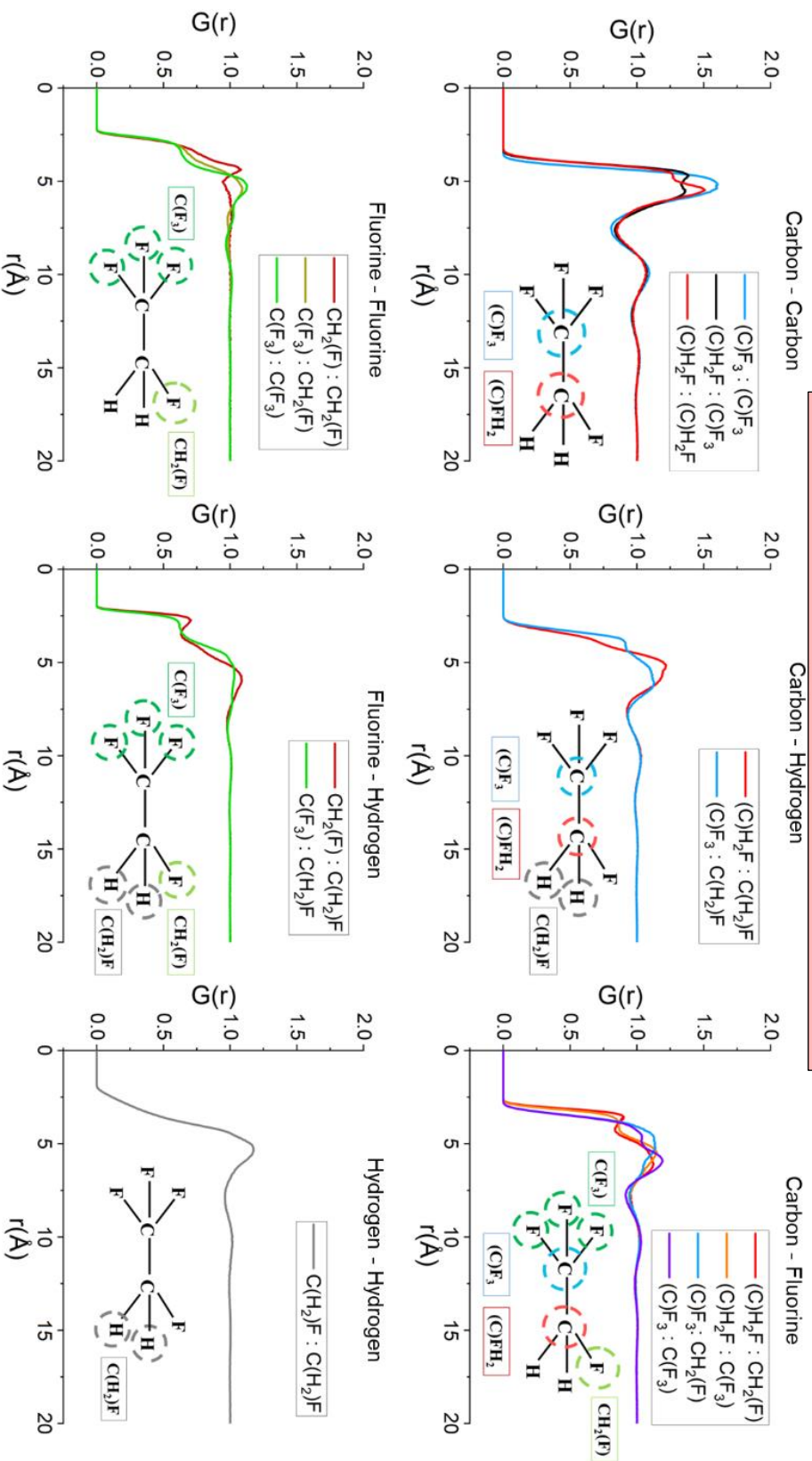


Figure 4-5 Atom pair RDF graphs for simulations at **323 K**. These grouped into their different variations: carbon-carbon, carbon-hydrogen, carbon-fluorine, fluorine-fluorine, fluorine-hydrogen, and hydrogen-hydrogen. The notations include atoms in brackets, these represent the atoms involved in the RDF, e.g., $C(H_2)F$ represents the hydrogens of that group

4.3 Frequency of Three Carbon Intermolecular Interaction

The interaction between three carbon atoms is illustrated in Figure 4-6, group A refers to the carbon belonging to CF_3 , and group B belongs to CFH_2 . A critical distance of 5 Å was chosen based on the RDFs, this ensured only the first contacts were considered. The distance between atoms must be less than 5 Å, the distance between first and third atoms must be over 5 Å. This ensures the interaction is not a ring like structure, rather is closer to 'linear'. Although these interactions are far from straight, an example three-body interaction from a snapshot of the 323 K trajectory in Figure 4-6 shows the angle between atoms is not flat. Two separate interactions are highlighted, and both have angles close to 90°.

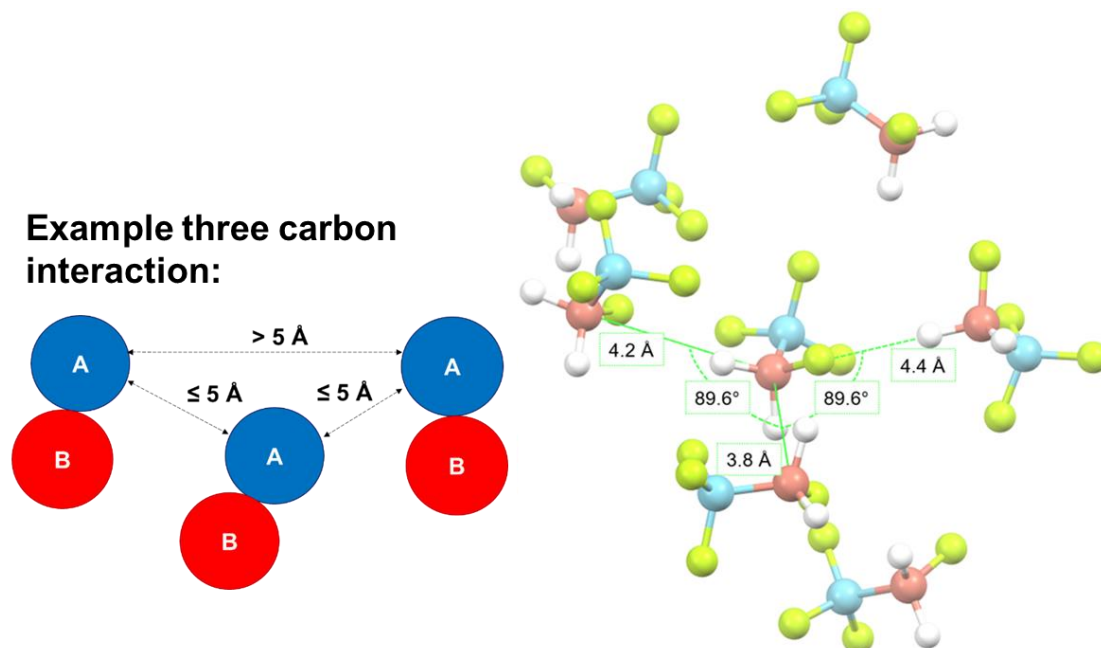


Figure 4-6 Example three carbon interaction with critical distance of 5 Å between three A groups [i.e., the $(\text{C})\text{F}_3$ carbon atoms], the first and third atoms are further than the critical distance, so the interaction is referred to as linear rather than a ring. Snapshot of 323 K trajectory file showing example 'linear interactions'. Distances and angles between three group B, $(\text{C})\text{FH}_2$ carbon atoms, (red) have been labelled. The group B, $(\text{C})\text{F}_3$ atoms, are coloured blue, fluorine is fluorescent yellow, and hydrogen is white.

Overall, the frequency of 3-body intermolecular interactions between the like groups involving three carbon atoms was found to increase when temperature was lowered and hence, density increased. Figure 4-7 shows at the lowest temperature, 203 K, there was a mean average of 3.6 and 3.4 interactions for A...A...A and B...B...B modes, respectively, increasing from 323 K where the average number of interactions was only 1.4 and 1.5, respectively. Generally, the spread of frequency of interactions became wider at the lower temperatures.

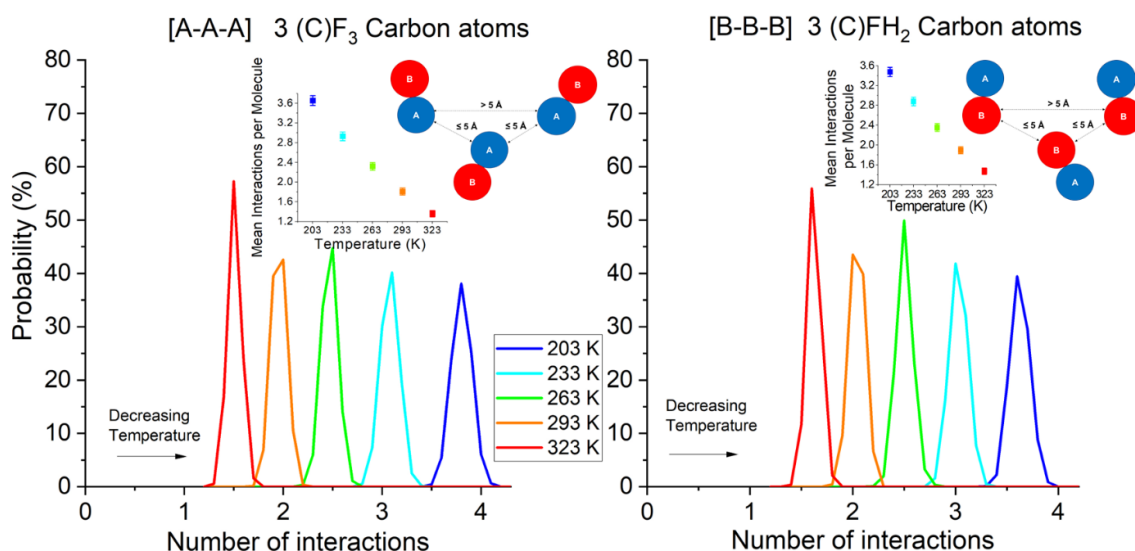


Figure 4-7 Distribution of three-body intermolecular interaction within a critical distance of 5 Å, between three A groups [A-A-A] and three B groups [B-B-B]. Distributions are coloured based on their temperature. Each graph shows an example interaction diagram. The mean number of interactions for each simulation temperature is shown as an inset graph with standard deviation included.

Figure 4-8(A) shows that the angle between A...A...A was far from a flat 180°, with a high probability of 75° and a shoulder around 120°. Also, this structural ordering was found to increase with temperature reduction, as evidenced by a more pronounced peak at 203 K compared to 323 K with the same distribution of angles also being observed for three group B (C)F₃ atoms. A vector angle between HFA-134a molecules centres of geometry in the BCC layout is in a similar range at 70.5°, shown in Figure 4-8(B).

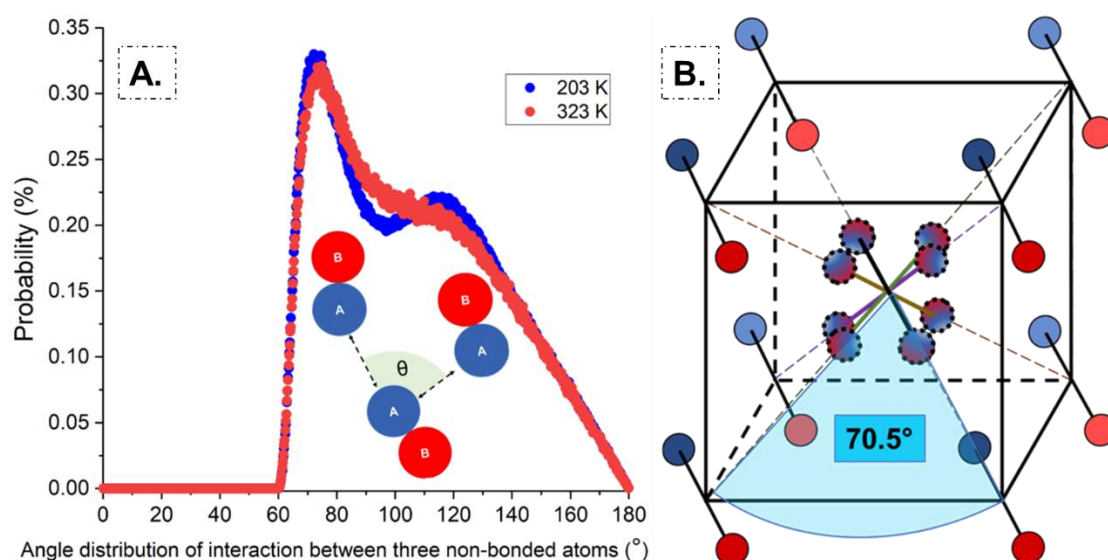


Figure 4-8 (A) Probability of the 1--2--3 vector angle between three A groups, including a diagram highlighting the angle, θ . Two temperatures, 203 K is blue, and 323 K is red. (B) Proposed BCC layout for HFA-134a with a highlighted angle between molecules centres of geometry. Each molecule represented by the two carbons; group A is the blue carbon atom of (C)F₃, whereas group B is the red carbon atom of (C)FH₂.

Figure 4-9 shows 3-body intermolecular interactions between three alternating groups, A...B...A and B...A...B. Both showed similar trends, the mean average number of interactions per molecule was 1.6 at 203 K and this decreased to 0.6 at 323 K. This is a lower frequency compared to Figure 4-8, showing a clear preference for interactions between three like groups. This may reflect the effects of steric hinderance of the A (CF_3) groups which limits the formation of weak H-bonds between alternating groups, whereas B (CFH_2) groups are able to position themselves closely.

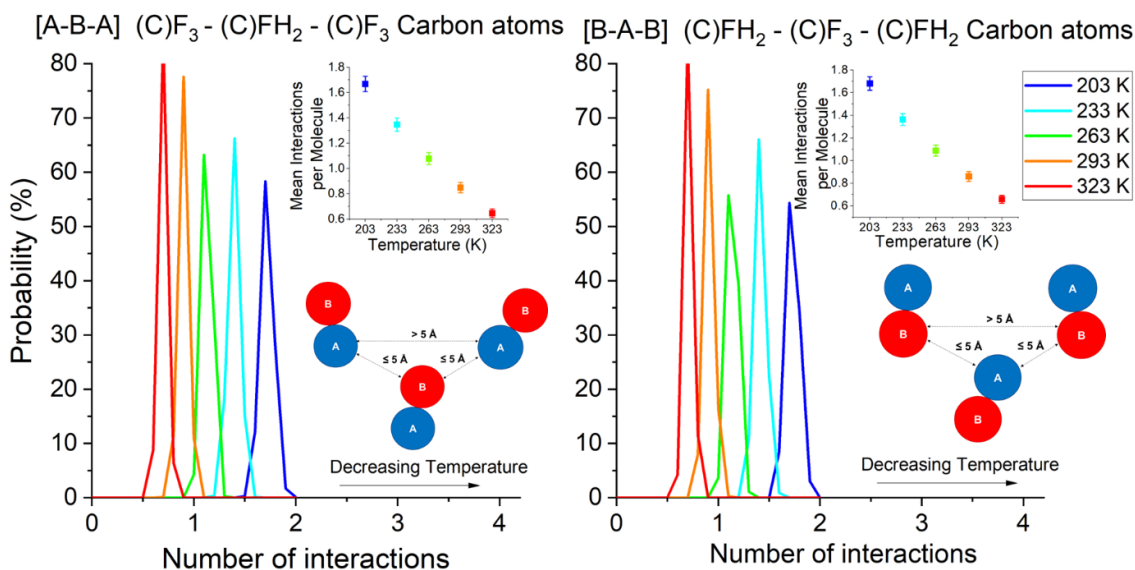


Figure 4-9 Distribution of three-body intermolecular interaction between three alternating carbon atom groups within a critical distance of 5 Å. [A-B-A] Shows the A...B...A interaction and [B-A-B] is the B...A...B interaction. Distributions are coloured based on their temperature. The mean number of interactions for each simulation temperature is also shown with standard deviation included.

4.4 Non-Bonded Dihedral Angle between C-C axes

The non-bonded dihedral angle is defined between four atoms: h, i, j and k. Figure 4-10 shows an example of the dihedral angle between B...B as the angle between the green and blue planes, when viewed along the non-bonded i-j (B...B) interaction. In other words, the angle represents the twist between bonded axes of h-i and j-k. The distance between atoms i and j were constrained to be a maximum of 7 Å, this ensured angles were recorded when molecules were positioned end to end.

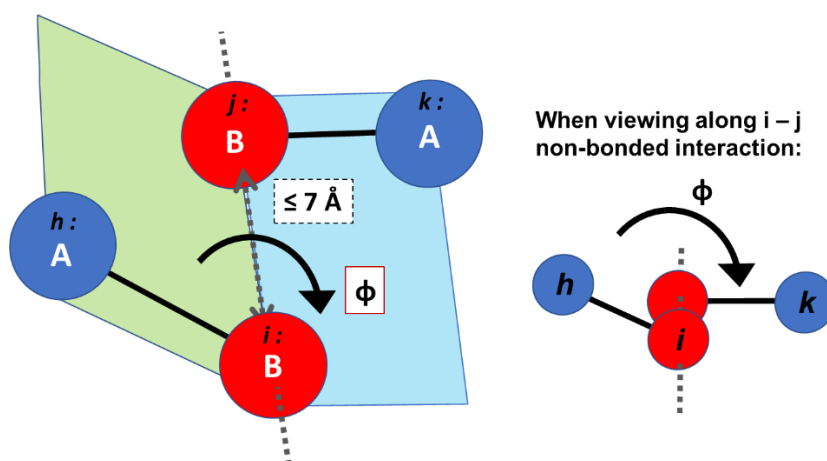


Figure 4-10 The dihedral angle, ϕ , is equivalent to the angle between the green and blue planes. Atoms i and j must have a separation distance ≤ 7 Å. The angle, ϕ , can be seen when viewed along the non-bonded interaction between atoms i and j .

Figure 4-11 shows the dihedral profiles for the non-bonded A...A, B...B and A...B vectors, revealing a preference for a dihedral angle between carbon-carbon axes of 180° when matching groups were close to each other. On the contrary, the inverse dihedral angle was shown about the non-bonded A...B vectors in Figure 4-11. Interestingly, chapter 3 shows that similar dihedral angles were found in the analysis of the monoclinic solid-form structure, matching carbon atoms had angles ranging between 140 – 180° and alternate carbon atoms were between 0 – 40° when close. This may be caused by the ease of weak H-bond formation. As temperature was reduced, both the A...A and B...B dihedral profiles showed a decreased probability for an angle of 180° , rather an increased probability of 0° and 360° . This could be the liquid trying to arrange in a similar way to the cubic solid state, as the proposed $\text{Im}\bar{3}\text{m}$ structure shows the nearest interactions at corners have dihedral angles of 0° .

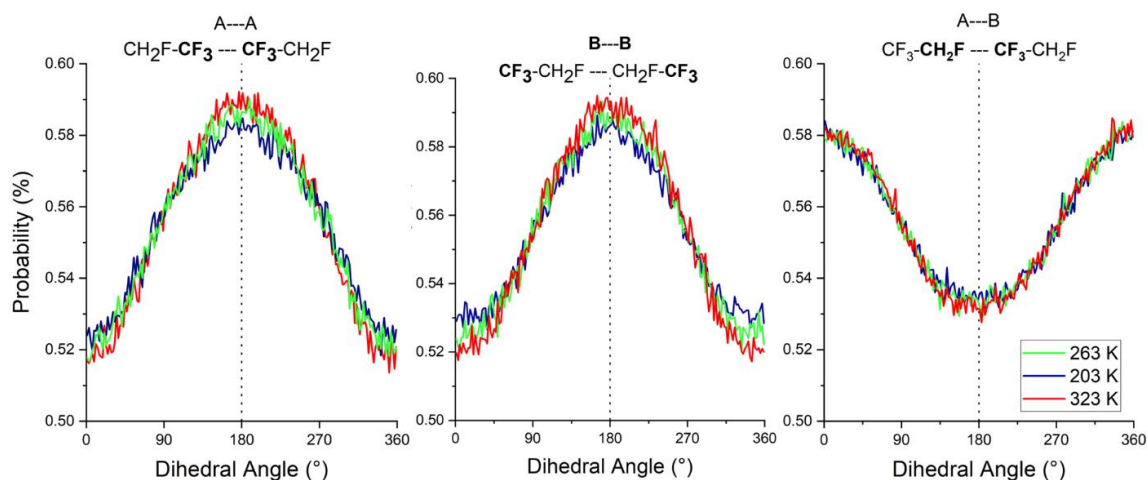


Figure 4-11 Probability of non-bonded dihedral angle distribution between the different carbon-carbon axes. Showing when the two A groups are closest (A...A), two B groups are closest (B...B), and an A and B group are close (A...B). All graphs show three different simulation temperatures, 203 K is blue, 293 K is green, and 323 K is red.

Figure 4-12 shows the non-bonded angular distributions between two close-contact molecules, measured along the C-C axes. These vector angles show a sinusoidal distribution, with a preference for 90° for all cases of close contacts, which is representative of a disordered liquid of randomly orientated molecules and agrees with a previous Monte Carlo simulation at 260 K (Do et al., 2010). In contrast, the non-bonded vector angles observed in the solid monoclinic phase, shown in the previous chapter, were found to range between 140-180°. This difference perhaps reflects vibrational molecular motion in the liquid phase is due to the liquid's thermal energy preventing molecular alignments that might produce attractive interactions. Furthermore, as all vector angle variations showed similar trends, this supports a model whereby molecule directionality rather than attractive interactions directs the packing efficiency.

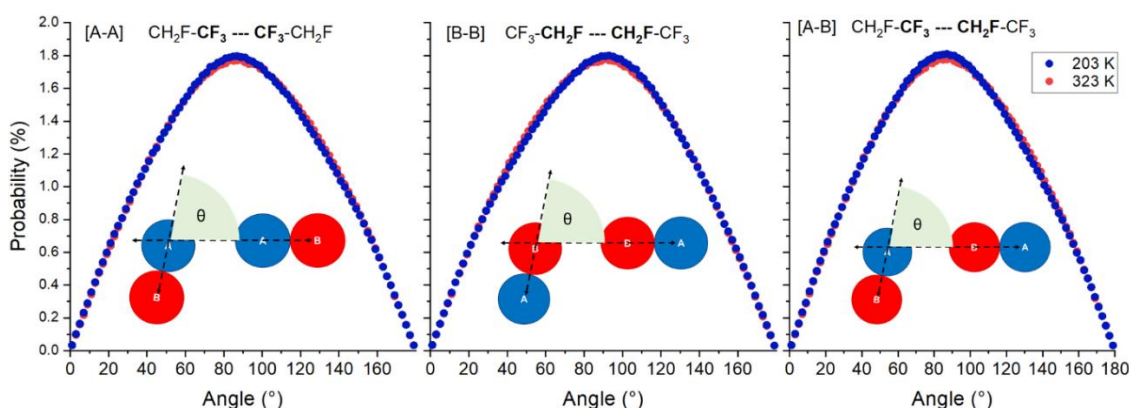


Figure 4-12 Non-bonded vector angle distribution between different carbon-carbon axes, at two different simulation temperatures, 203 K is blue, and 323 K is red. Showing when group A to A [A-A], B to B [B-B], and A to B [A-B].

4.5 Liquid Structure Discussion and Comparison with Solid-State

As the temperature of liquid HFA-134a MD simulations was reduced, density increased, and molecules began to rearrange into structural characteristics resembling the BCC phase. The molecular RDF of the lowest temperature simulation, 203 K, revealed a coordination number of 13.9 molecules occupying the first shell at a 7.4 Å radius, as per Table 4-1. This closely resembled the BCC phase's first shell which had 14 molecules with a 5.76 Å radius, seen in Table 4-2. Additionally, at 203 K, the liquid's initial two solvation shells contained 60 molecules at an 11.8 Å radius which was close to the 58 molecules seen in the BCC phase, within an 11.8 Å radius. Overall, it shows an increased probability of molecules arranging in the BCC lattice when temperature is

reduced. It is expected the RDF peaks would split once the temperature is low enough to crystallise, as observed in the behaviour of liquid iron (Shibuta and Suzuki, 2008).

The highest peaks of all atom pair RDF patterns were seen in carbon-to-carbon interactions, matching a previous Monte Carlo simulation (Do et al., 2010). These carbon interactions approximately followed the same ordering pattern as the molecular RDFs. The effects of steric hinderance were seen in asymmetric initial peaks between the different combinations. Carbon atoms were at the centre of HFA-134a's functional groups, A (CF_3) and B (CFH_2). As they followed the same ordering as molecular RDF pattern, it implies it didn't particularly matter where the outer atoms were positioned, and the liquid structuring was not dominated by a single atom-atom interaction. Which points to the hypothesis that the biggest influence on the packing was minimisation of steric repulsion (Israelachvili, 2011), akin to what was seen in the solid-state.

After carbon-to-carbon, the next highest peak of atom pair RDF patterns was between carbon-to-hydrogen. There was increased probability for interactions between two B groups rather than A-to-B. This might have been due to steric repulsions of the CF_3 group making them less compatible than two CFH_2 groups that can slot into each other. This is even more difficult when the temperature is higher in the liquid, molecules in solid have lower temperature which makes it easier for the A-B interactions to form. A separate investigation into HFA-134a interacting with ionic liquids also speculated that the smaller size of CFH_2 groups meant they could form closer interactions with oxygen atoms compared to CF_3 groups (Lepre et al., 2019).

The strongest interactions identified in solid-state, shown in previous section 5.3, contained C-H---F 'weak H-bonds' in the region 2.5 – 3.0 Å. Liquid phase atom pair RDF patterns of fluorine-to-hydrogen revealed a small peak at approximately 2.7 Å, indicative of typical weak H-bond interaction distances (Desiraju and Steiner, 1999). This peak increased in magnitude when temperature reduced, implying an increased frequency of C-H---F interactions. However, it is not believed the weak H-bonds will have a large influence on the packing and are not as strong as conventional H-bonds. For instance, previous MD studies of fluorinated ethanol looked at a system that could form both weak and conventional H-bonds (Mondal et al., 2017). The predicted RDF patterns showed the peak of the conventional H-bond was far more prominent compared with to the peak belonging to the weak H-bond (Mondal et al., 2017), suggesting molecules packing was not greatly affected by the interaction. Overall, the comparatively higher peaks of carbon-to-carbon RDF patterns indicates steric repulsions were more influential on molecular orientation than the attractive weak H-bonds.

Superior influence of steric repulsions was also believed to be the reason interactions between three like carbon groups occurred more frequently than interactions between alternate carbon groups. It was hypothesised that the larger steric hinderance of CF_3 inhibits the CFH_2 group from positioning itself closely. Further similarity and alignment between the liquid and solid form structures were found when temperature was reduced, three body interactions between corresponding carbon atoms showed an increased preference for an intermolecular vector angle of about 75° , consistent with that likely in the BCC phase at 70.5° . This intermolecular ordering correlates well with the angles expected for the disordered BCC solid-form structure, Figure 4-8(right), in which the 1-2-3 vector angle between corner and centre molecules is 70.5° . Implying that the molecules in the liquid phase preferably pack into these efficient positions when temperature and thus the NPT simulation cell size reduces.

Non-bonded dihedral angles between C-C axes showed a higher probability for 180° when like carbon groups were close e.g., group A-to-A. In contrast, there was a higher probability for an angle of 0° when dissimilar carbon groups were close e.g., group A-to-B. These reflected the dihedral angles of interactions seen in the monoclinic phase with lower attraction strengths. Specifically, synthons E and F shown in section 5.3. These showed a preference for CH_2F groups positioned closely but did not show weak H-bonds. This indicates the interaction seen in the solid and liquid state was driven to maximise packing density rather than due to attractive interactions.

All combinations of non-bonded vector angles showed high probability around 90° , which agreed with a previous investigation in HFA-134a's liquid structure (Do et al., 2010). It is likely that the liquid phases higher thermal energy caused the vector angles to differ from the monoclinic phase. Therefore, it is unlikely that the same types of H-bonds between group A-to-B formed as frequently. This argument was reinforced by the RDF patterns and provided more evidence that steric repulsions were the main influence rather than strong atom-atom attractions.

To summarise, molecules got closer together as temperature was reduced and steric repulsions were the main structural influence, increasing the frequency of molecules occupying positions also seen in the BCC solid.

4.6 Conclusion

This chapter set out to see if there was a connection between structuring of different phases. Results from the previous chapter acted as guidance for analysis of MD simulations of HFA-134a's disordered liquid phase across a range of temperatures. Structural analysis showed the liquid resembled the solid more as temperature was reduced. Molecules had lower vibrational energy and were forced to occupy more space efficient packing.

RDF analysis of local liquid density showed increased probability of molecules occupying coordination shells reminiscent of the BCC packing when the temperature was reduced, shown in Tables 4-1 and 4-2, respectively. Suggesting the liquid structuring would move this way before solidifying. Furthermore, when temperature reduced, the atom-atom interactions showed an increased probability in formation of C-H...F weak H-bonds. Seen in the same 2.5-3 Å region that was identified in the solid-state. These peaks were not as prominent as the conventional H-bonds seen in other, separate liquid simulations. Which implies that these interactions were not as strong and influential on molecule directionality.

Overall, this work provides us with an understanding of how liquid propellant molecules preferably arrange without the influence of additional formulation ingredients. Whilst HFA-134a is polar and weak H-bonds were present in the structure, they were not very influential in directing the structural ordering. The dominant effect of intermolecular packing was believed to be the minimisation of steric repulsions. These results have the potential to help with future investigations into the wetting different crystal surfaces, or dissolution of surfactant molecules.

Chapter 5: Comparing Molecular and Crystal Structure of Form I and II Fluticasone Propionate

Summary: This chapter compares the solid-state packing of fluticasone propionate's two polymorphs. The packing of both are visualised and analysed, empirical force fields are applied to predict their intermolecular interactions strength. There was very little difference between conformations due to the rigidity of the molecule's structure. Similar intermolecular interactions were shown in both crystal structures. However, Form I showed better stability due to its favoured interactions.

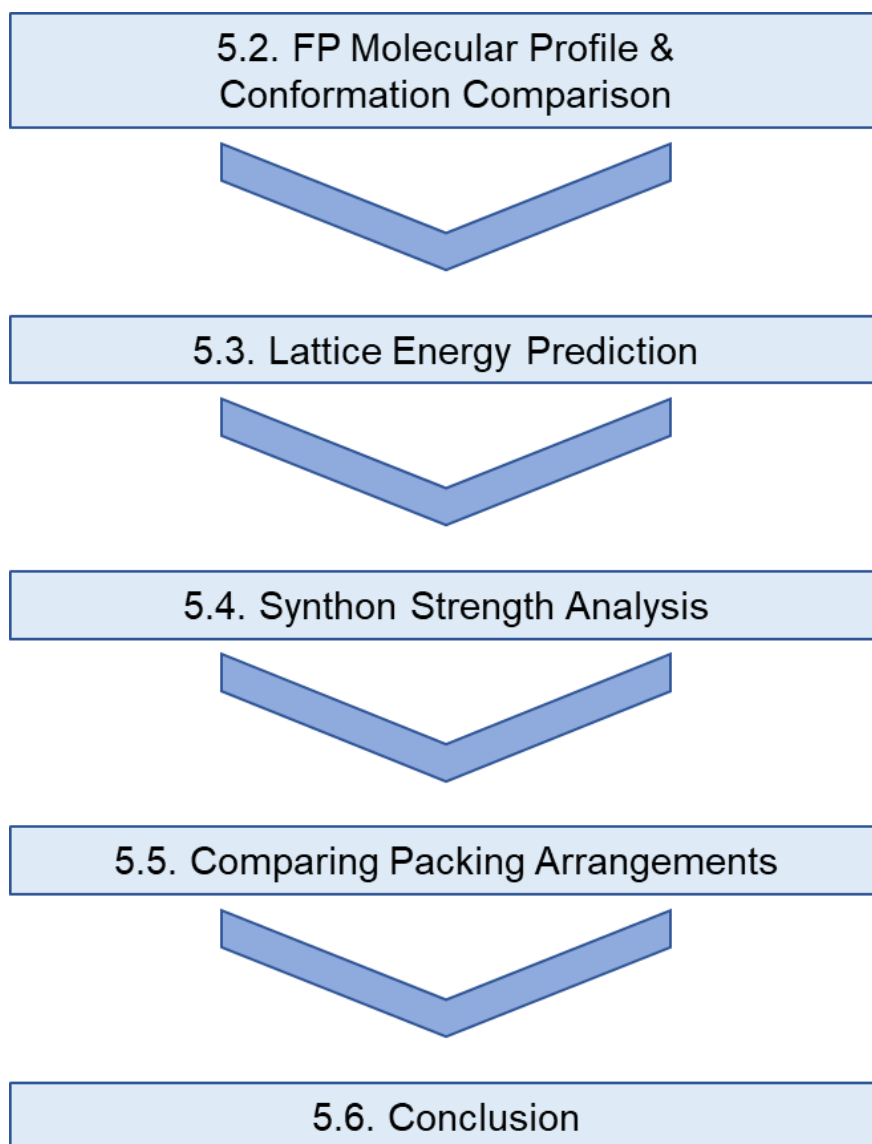
Chapter 5: Comparing Molecular and Crystal Structure of Form I and II Fluticasone Propionate

5.1 Introduction

Drug particles in MDI suspension formulations are typically crystalline, recrystallised through anti-solvent and then micronized. It is generally believed that FP crystallises into its more stable polymorph, form I, through typical crystallisation routes at standard conditions (Čejka et al., 2005, Murnane et al., 2008a, Kubavat et al., 2012). The metastable polymorph, form II, has only been reported to arise when using supercritical fluids (Kariuki et al., 1999, Steckel et al., 1997, Steckel and Müller, 1998) so is therefore unlikely to be present during industrial methods used to manufacture MDI formulations. Nevertheless, the solid-state packing of both polymorphs is compared to help improve one's understanding of form I. It is interesting to see how the same molecular descriptors can lead to two different packing formations.

In this chapter, fluticasone propionate's molecular descriptors are outlined, functional groups and conformations of the two different polymorphs are compared. A molecular modelling approach is used to analyse the molecular orientation in both preferred packing structures and to establish why one polymorph is more stable. A semi-empirical approach, as outlined in section 2.2.4.2, was used to predict their partial atomic charges. Then, molecular mechanics techniques are used to quantify the lattice energy and strength of interactions, detailed methods have been outlined in section 2.2.4.2. These results will provide a foundation for further chapters looking at morphology formation and differences in surface chemistries.

Chapter Flowchart Overview



5.2 Fluticasone Propionate and its Polymorphs

5.2.1 FP Molecular Profile

Fluticasone propionate, $C_{25}H_{31}F_3O_5S$, is based around the corticosteroid structure of three connected cyclic rings and a pentane ring. The chemical structure is shown in Figure 5-1 below, a single hydroxyl group is circled green as the only potential H-bond donator, whereas there are four carbonyl groups and three fluorine atoms that can potentially act as H-bond acceptors, these are circled in red. Fluticasone propionate also has different points of chirality, these are highlighted with S enantiomers presented with orange circles and R enantiomers with purple circles. The molecule has been divided into sub-sections, the first carbonyl group bonded to a cyclic ring is α , the two cyclic and one pentane ring with two fluorine and three methyl groups connected is β , the propionate and fluoro-methyl-sulfanyl-carbonyl group is γ . For ease of understanding, this labelling convention for sub-sections is followed throughout.

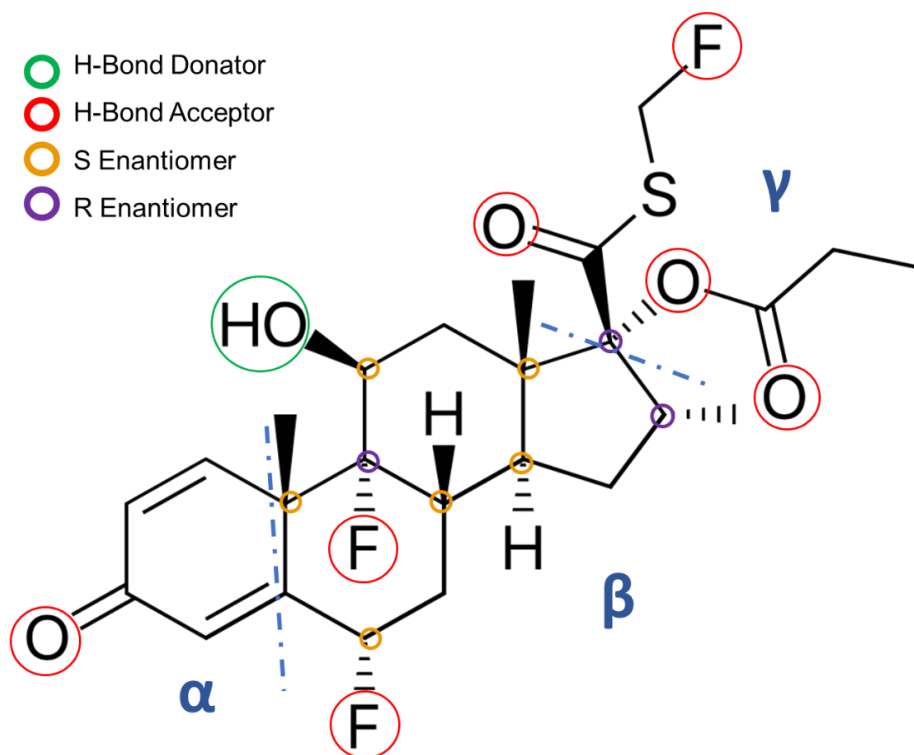


Figure 5-1 Fluticasone Propionate molecule with possible H-bond donator and acceptor atoms labelled green and red, respectively. S and R enantiomers are highlighted orange and purple, respectively. The molecule is divided into three sections: α , β , γ .

5.2.2 Polymorph Comparison

It has two crystal structures registered on the CSD; **DAXYUX**, shown Figure 5-2, is seen more commonly during standard crystallisation methods, such as cooling, anti-solvent and evaporation crystallisation. **DAXYUX01**, shown in Figure 5-3, is the less common polymorph and formed using supercritical fluid anti-solvent crystallisation methods. Structures of DAXYUX and DAXYUX01 were determined with single crystal and powder x-ray diffraction techniques, respectively. Crystal properties and experimental conditions are listed in Table 5-1 below. The $P2_1$ space group of DAXYUX is characteristic of a monoclinic habit and the $P2_12_12_1$ space group of DAXYUX01 is orthorhombic. Both structures have a single molecule per asymmetric unit, this is repeated twice in the DAXYUX structure but the DAXYUX01 structure shows more symmetry with 3 screw-axes and therefore four molecules in total per unit cell. It can also be seen in Table 5-1 that molecules of DAXYUX conform to a smaller volume and overall, this polymorph structure is denser.

Table 5-1 Crystal properties and experimental conditions for fluticasone propionate's two polymorphs. DAXYUX and DAXYUX01 refers to the reference codes used in the structural database for form I and II, respectively.

Refcode .cif	DAXYUX (Form I)	DAXYUX01 (Form II)
Space group: Name	$P2_1$	$P2_12_12_1$
Space group: Number	4	19
Density (g/cm³)	1.418	1.337
Molecular volume	586.006	621.459
Molecules per asymmetric unit	1.0	1.0
Molecules per unit cell	2.0	4.0
Cell dimensions:		
a b c (Å)	7.65 14.14 10.98	23.24 13.98 7.65
α β γ (°)	90.0 99.3 90.0	90.0 90.0 90.0
Habit	Monoclinic	Orthorhombic
Temperature (K)	150	283 – 303
R-Factor (%)	7.51	3.3
Crystallised from	Acetone evaporation	Supercritical fluid membrane with ethanol/acetone
Reference	(Cejka et al., 2005)	(Kariuki et al., 1999)

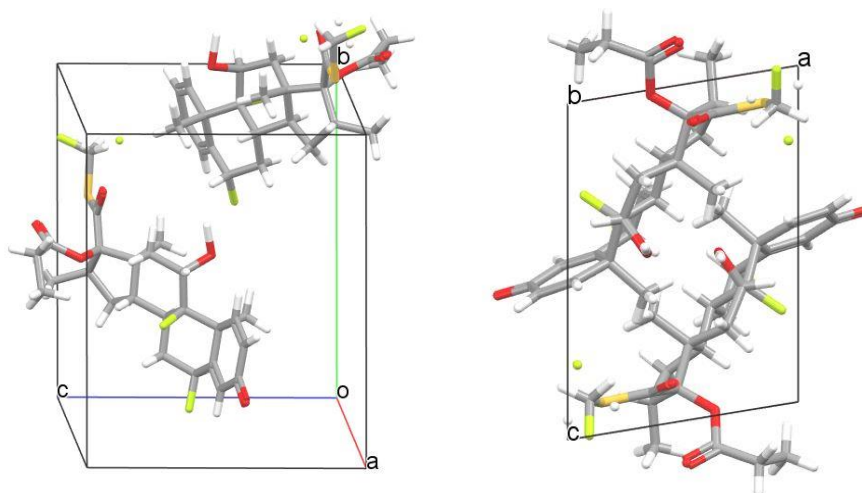


Figure 5-2 Form I, **DAXYUX** unit cell, the right-hand image is viewed down the *b*-axis. This shows the non-90° angle present in the monoclinic unit cell.

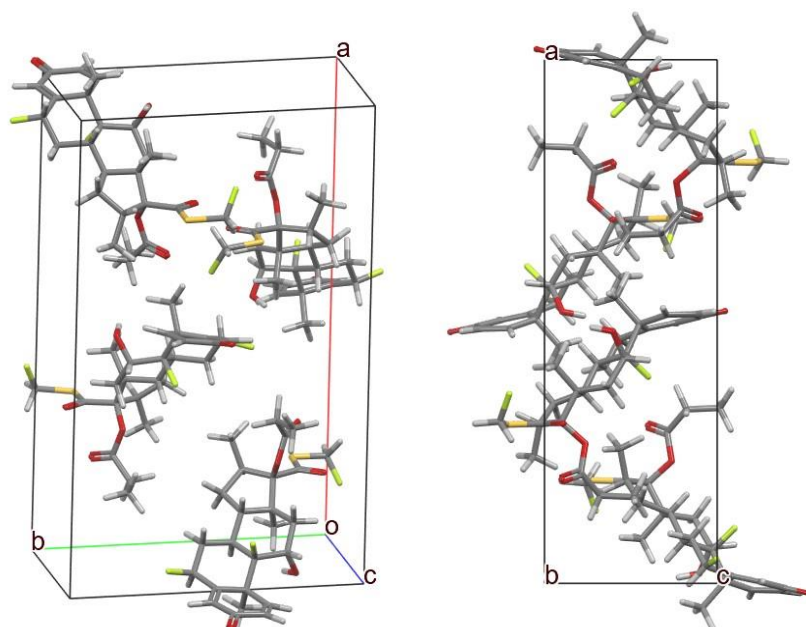


Figure 5-3 Form II, **DAXYUX01** unit cell, the right-hand image is viewed down the *b*-axis. This shows all angles in the orthorhombic unit cell are 90°.

5.2.3 Molecular Conformations

The molecular conformations of both crystal structures are overlaid in Figure 5-4. There is a strong similarity between the corticosteroid skeleton of both conformations, this illustrates the structural rigidity of three connected cyclic rings and a pentane ring. This similarity was also seen in 15 structures on the CSD that shared the corticosteroid skeleton with the two fluorine atoms (Bruno et al., 2002, Čejka et al., 2005). Some slight twisting was shown in the pentane-ring, but their greatest conformational differences came from with flexible side chains. When comparing the DAXYUX and

DAXYUX01 conformations, their largest difference is between the torsion angle of the γ section's propionate and sulphur-fluoro-methyl groups. The positions of the hydroxyl group's hydrogen atoms also differ slightly between conformations.

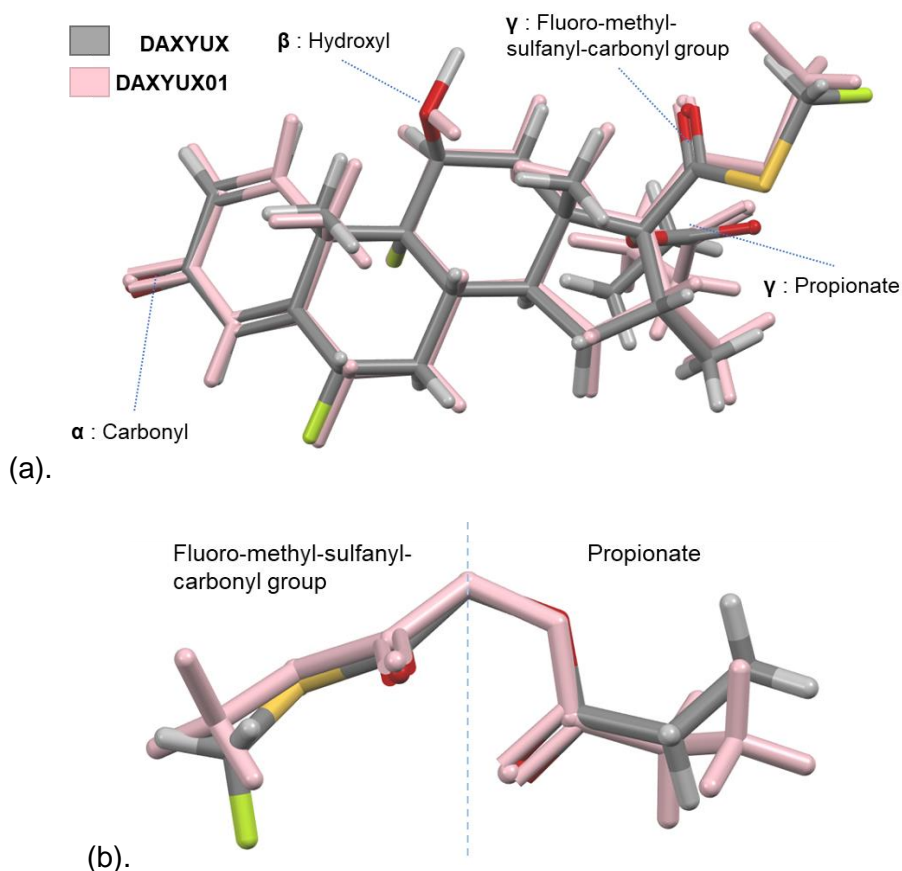


Figure 5-4 (a) Overlay of molecular conformations, DAXYUX structure (Form I) is coloured with grey carbon atoms, and DAXYUX01 (Form II) structure is pink. (b) The γ section's two parts: fluoro-methyl-sulfanyl-carbonyl and propionate.

5.2.4 Polarity of Molecule

The molecule of DAXYUX is coloured based on atomic partial charges in Figure 5-5 below. It shows the highly electronegative atoms, oxygen, and fluorine, have stronger negative charges as they have drawn away electrons from their connected atoms. Subsequently, some carbon atoms have strong positive charges, such as the carbon in the propionate group bonded to two oxygen atoms. The hydrogen atom in the hydroxyl group has the strongest positive charge of approximately +0.2. The γ section's sulphur atom is almost neutral with a charge around +0.01 and has the highest atomic mass of 32, so has high potential for vdW interactions. Polar protic solvents such as methanol and ethanol are likely to bind with the negative fluorine and oxygen atoms. Whereas the negative parts of solvents are likely to be attracted to the positive atoms, such as

the hydroxyls hydrogen and the positive carbons. Dispersive interactions are likely to occur on the sulphur and more neutral carbon atoms.

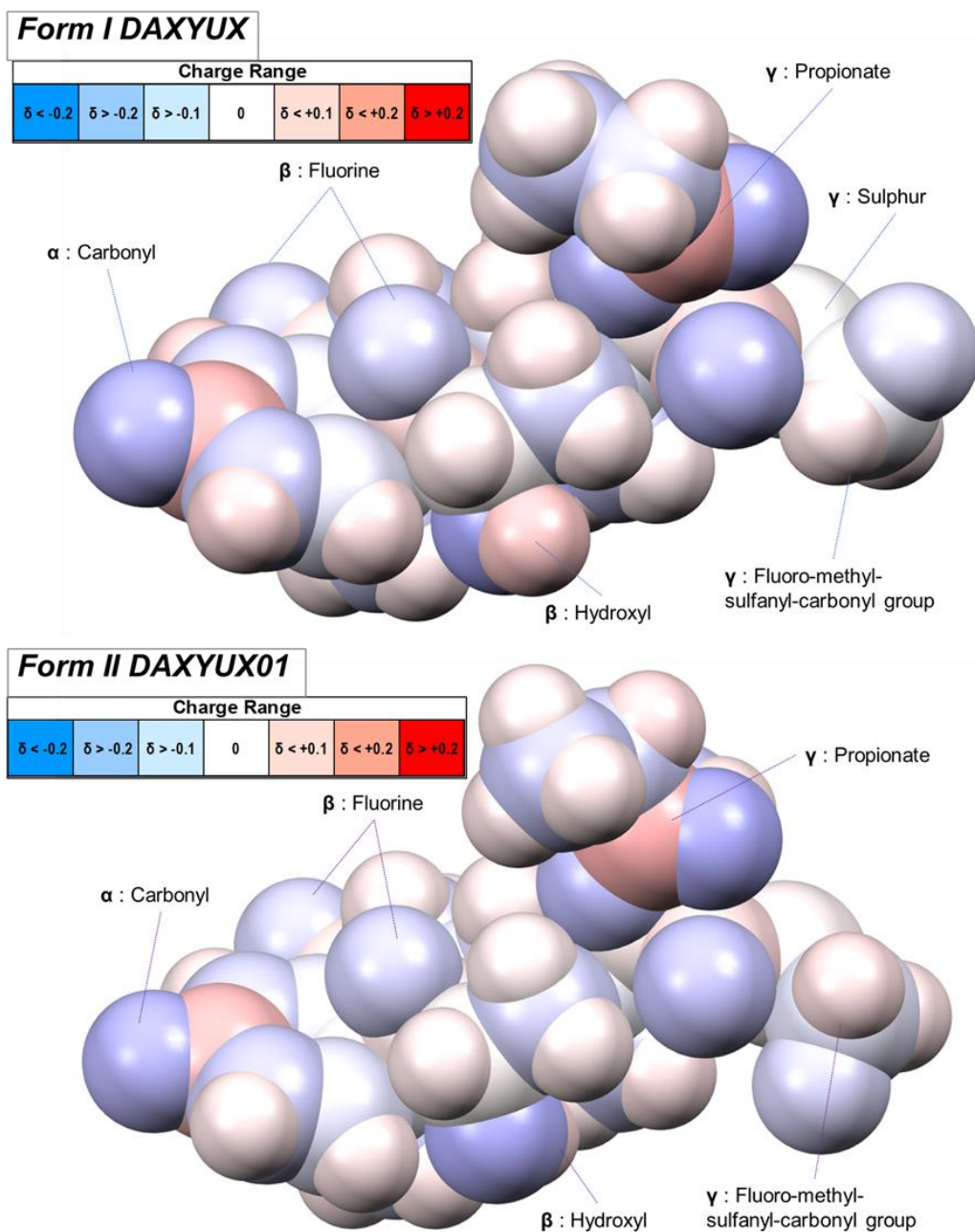


Figure 5-5 Space-fill representation of FP molecule in structures of **Form I DAXYUX** and **Form II DAXYUX01**. Atoms coloured relative to partial charge calculated through MOPAC method. Deeper blue or red coloured atoms represent stronger negative or positive partial charges, respectively, while white atoms are closer to neutral.

The atomic charges of DAXYUX01 illustrated in Figure 5-5 are similar to the DAXYUX structure, this highlights how similar the two conformations are. The most obvious difference compared to DAXYUX is the rotation of the hydroxyl group and this could be due to a different H-bond network changing the bonds directionality. The twist in the γ

section appears to expose the oxygen of the propionate group more so in DAXYUX01 compared to DAXYUX.

5.3 Lattice Energy Calculation

The lattice energy of form I, DAXYUX, calculated using the Dreiding potential following the method in section 2.2.4.2., with cutoff varying at each limiting radius. Figure 5-6 shows it converges at 24 Å to a lattice energy of approximately -43.6 kcal/mol. Around 85% of the total lattice energy contribution occurs within the first 12 Å. The predicted values of form II, DAXYUX01, also converge at 24 Å but to a smaller energy, -29.5 kcal/mol. The DAXYUX01 structure is expected to have a lower magnitude lattice energy compared to DAXYUX due to its lower stability. Similarity is shown with around 85 % of lattice energy occurring within the first 12 Å. Furthermore, both show vdW interactions dominate over electrostatic interactions.

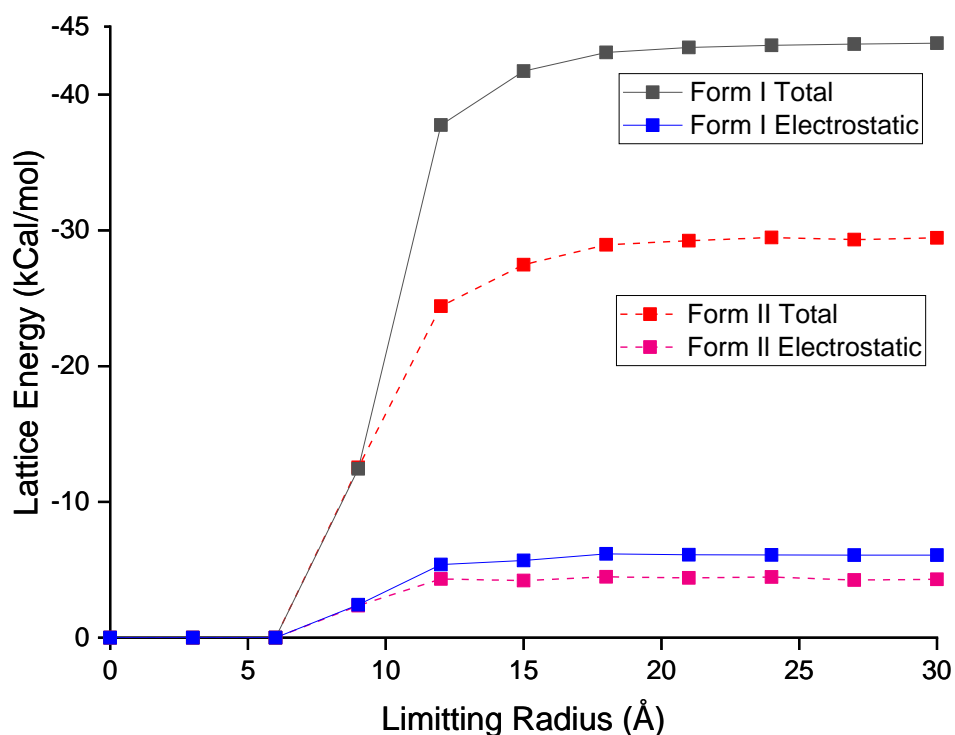


Figure 5-6 Lattice energy of form I and II fluticasone propionate, predicted using the Dreiding force field at different limiting radii. Total lattice energy and its electrostatic contribution are shown.

5.4 Synthons Strength Analysis

5.4.1 Form I - DAXYUX

Table 5-2 lists the predicted strengths of Form I's, DAXYUX. top 5 synthons.

Table 5-2 Attributes of the top five strongest synthons of Form I, DAXYUX. Including: Interaction type, Which molecule of the asymmetric unit, Z, Distance between centres of geometry, Interactions strengths.

Synthon	Interaction Type	Z (mol ID)	Z (mol ID)	Distance (Å)	VdW (kCal / mole)	COUL (kCal / mole)	TOTAL (kCal / mole)
A	vdW	1	1	7.65	-5	-1.21	-6.22
B	vdW	1	2	9.04	-3.62	-0.36	-3.97
C	H-bond	1	2	10.78	-0.78	-1.18	-1.96
D	vdW	1	2	9.21	-3.38	-0.16	-3.54
E	vdW	1	1	10.98	-2.08	0.15	-1.93

Synthon A

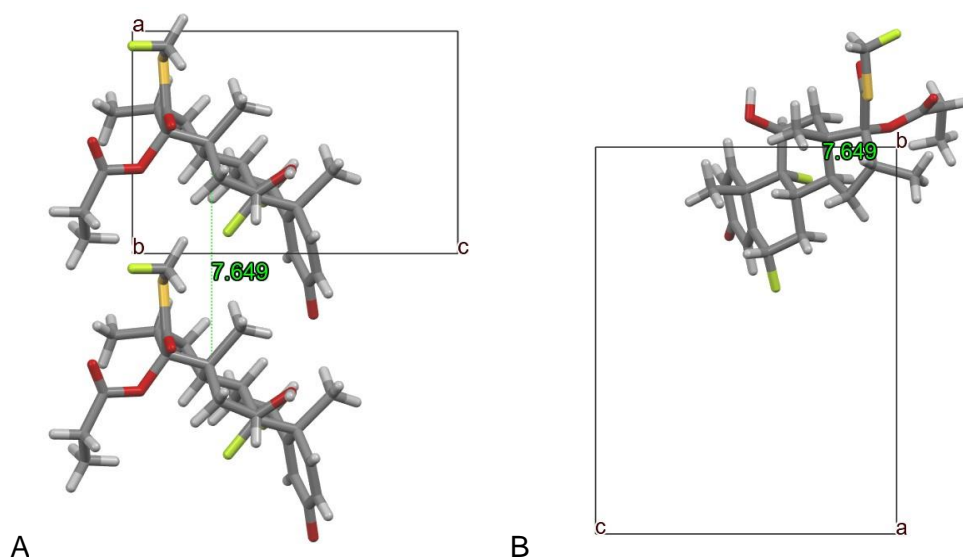


Figure 5-7 Synthon A in the Form I structure relative to the unit cell. (A) is viewed down the b-axis and (B) is viewed down the a-axis. Intermolecular distance between centres of geometry is 7.65 Å.

This interaction is between a pair of the identity molecules from the asymmetric unit and Figure 5-7 (A) shows the molecules stacked upon each other in the [100] direction along the a-axis. When looking down the a-axis in Figure 5-7 (B) the molecules appear to be super-imposed onto one another, as a result there is a large contact area and many atom-atom interactions with short intermolecular distances. This produces high van der Waals (vdW) attraction and repulsions, also fairly high columbic attractions between

atoms with large partial charge differences. Overall, this is the strongest interaction at -6.22 kcal/mol it is approximately 50 % stronger than the next, synthon B, at -3.97 kcal/mol.

Synthon B

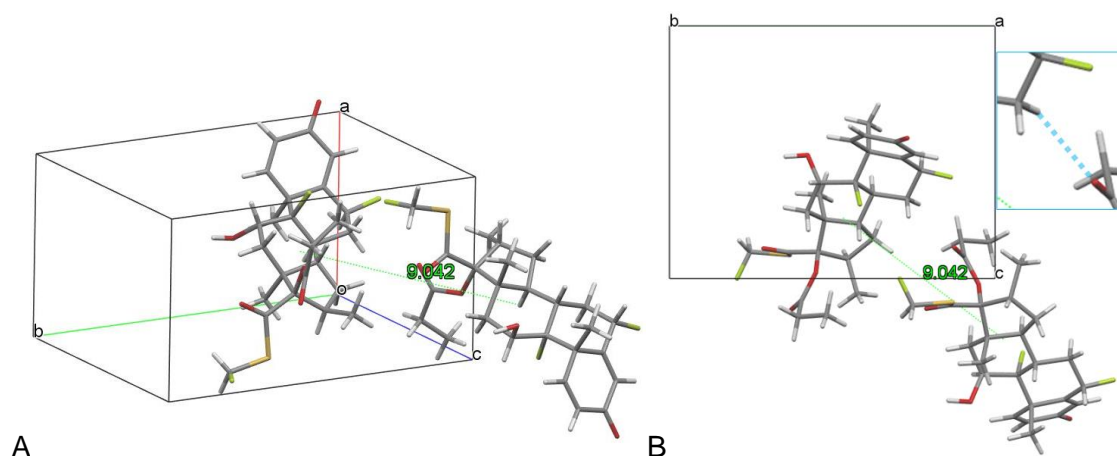


Figure 5-8 Synthon B in the Form I structure, (A) relative to the unit cell, (B) is viewed down the a-axis. Intermolecular distance between centres of geometry is 9.04 Å.

Molecules in synthon B are connected through the screw-axis, so the γ section's propionate and fluoro-methyl-sulfanyl-carbonyl groups are attracted to the β section containing the cyclic and pentane rings. The fluoro-methyl-sulfanyl-carbonyl group does not show a strong directional interaction with the other molecule, this may have affect why that group shows disorder. A close interatomic interaction occurs between the oxygen of the propionate group with hydrogen in the β section. Overall, vdW interactions dominate over coulombic interactions and the chain of molecules following synthon B travel in the [0-11] direction. Coulombic contributions are lower than synthon A but higher than synthon D and E due to the proximity of oppositely charged oxygen and hydrogen atoms.

Synthon C

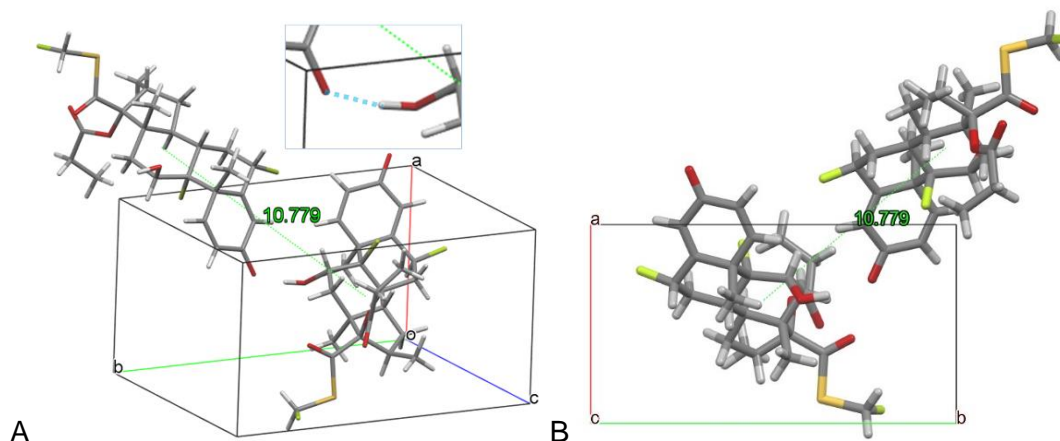


Figure 5-9 Synthon C in the Form I structure, (A) relative to the unit cell, (B) is viewed down the c-axis. Intermolecular distance between centres of geometry is 10.78 Å.

Synthon C is accredited as the only H-bond in DAXYUX structure, the β section's hydroxyl group is the donator to the α section's carbonyl. The O-H---O bond angle is 169° and it forms an H-bond chain connecting molecules in the [010] direction along the b-axis. Additionally, there is a close interatomic distance between two atoms with a large charge difference, the β section's 'upper' fluorine to the α section's hydrogen. This synthon has little molecular overlap and the closest interactions are between atoms with large differences in partial charges, therefore vdW attractions are low and so coulombic interactions dominate.

Synthon D

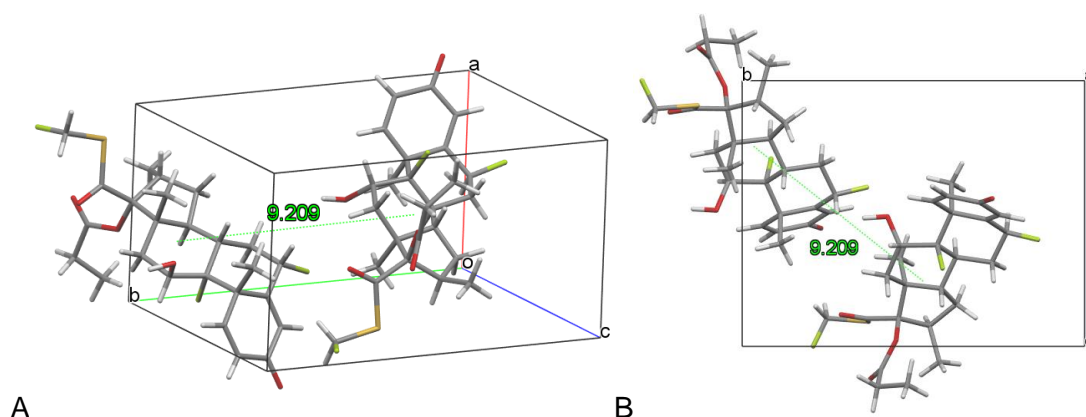


Figure 5-10 Synthon D in the Form I structure, (A) relative to the unit cell, (B) is viewed down the a-axis. Intermolecular distance between centres of geometry is 9.21 Å.

The α section's cyclic ring with carbonyl group is positioned closely to the γ section's fluoro-methyl-sulfanyl-carbonyl group, this might increase propensity for disorder. Despite there being many oppositely charged atom-atom interactions at a short intermolecular distance of 9.2 Å, this synthon is dominated by strong vdW attractions. This was predicted to be the third strongest synthon at -3.54 kcal/mol. Overall, this synthon links a chain of molecules that travel along the [010] direction.

Synthon E

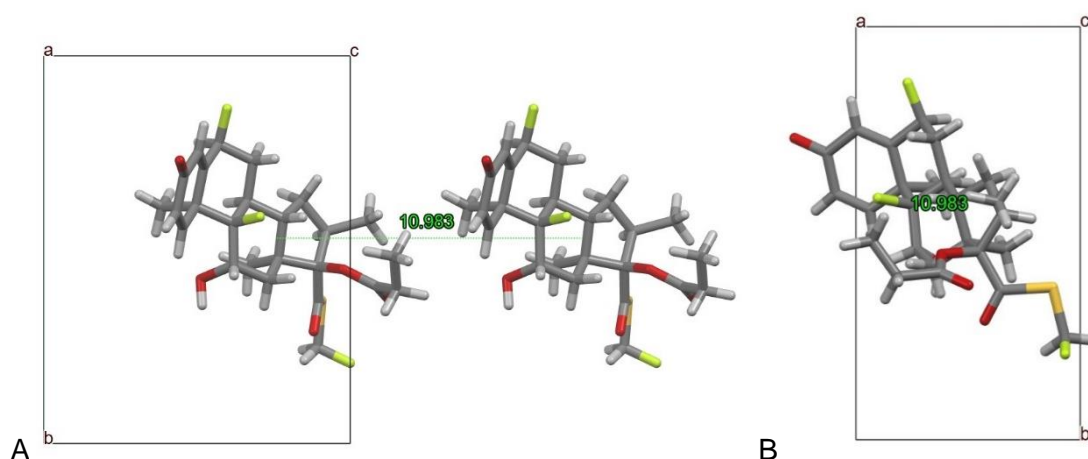


Figure 5-11 Synthon E in the Form I structure, (A) relative to the unit cell. It passes in the direction of the c-axis. (B) is viewed down the c-axis. Intermolecular distance between centres of geometry is 10.98 Å.

Synthon E is between two identity molecules interacting in the [001] direction travelling the c-axis, the closest interaction is between the γ section's propionate group with the α section cyclic ring and methyl group of β . In a similar fashion to Synthon A, the matching molecular profile results in molecules appearing to be super-imposed onto each other when viewed down the c-axis Figure 5-11 (B). Unlike synthon A, there is a smaller contact area, resulting in fewer atom-atom interactions, and the intermolecular distance is further which results in a lower synthon interaction energy. VdW type interactions still dominate, the proximity of hydrogen atoms likely weakens coulombic interactions, and few strongly, oppositely charged atoms are in close contact.

Summary of Form I

In summary, the top 5 strongest synthons, A – E, represent 84 % of the -43.6 kcal/mol converged lattice energy. FP's large molecular mass means interactions are strongly dispersive rather than coulombic. Synthon A is the strongest by far with an energy of -6.22 kcal/mol, over 50 % stronger than the next, synthon B at -3.9 kcal/mol. Synthon A has a strong influence on the crystal packing, it consists of two FP molecules packed

closely with minimal steric repulsion, there is a lot of overlapping so the interaction is highly dispersive. The γ section's fluoro-methyl-sulfanyl-carbonyl group does not show a strong directional interaction in synthon B. This explains why the fluoro-methyl group shows disorder in the DAXYUX structure. Additionally, the fluoro-methyl group is in close proximity between the like charged carbonyl atom in synthon D, so repulsion between these atoms may also contribute to fluoro-methyl disorder. The structures only H-bond, Synthon C, was between the carbonyl and hydroxyl group with an angle of 167° and it points in the direction of the b-axis, [010].

5.4.2 Form II - DAXYUX01

The predicted strengths of Form II's, DAXYUX01, synthons are listed in Table 5-3.

Table 5-3 Attributes of the top five strongest synthons of Form II, DAXYUX01. Including: Interaction type, Which molecule of the asymmetric unit, Z, Distance between centres of geometry, Interactions strengths.

Synthon	Interaction Type	Z (mol ID)	Z (mol ID)	Distance (Å)	VdW (kCal / mole)	Coul (kCal / mole)	Total (kCal / mole)
A	H-Bond	1	3	9.21	-2.79	-0.78	-3.58
B	vdW	1	1	7.65	-2.01	-1.36	-3.37
C	vdW	1	2	8.26	-3.06	0.16	-2.9
D	vdW	1	2	11.57	-1.59	-0.62	-2.22
E	H-Bond	1	3	11.51	-1.34	0.39	-0.96

Synthon A

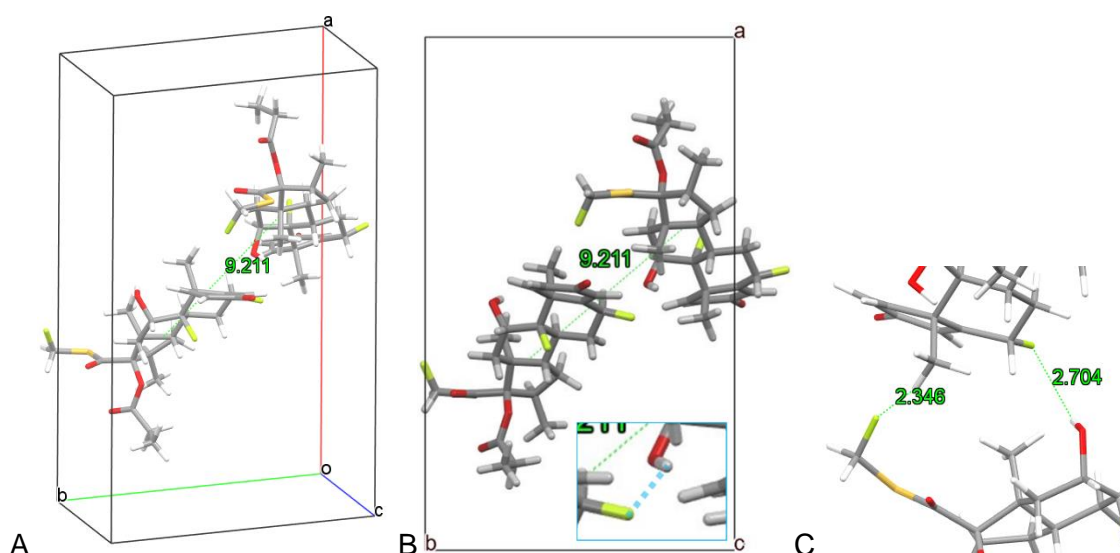


Figure 5-12 Synthon A in the Form II structure, (A) relative to the unit cell, intermolecular distance between centres of geometry is 9.21 Å. (B) is viewed down the c-axis with an inset of F---HC interaction. (C) shows the F---HC and F---HO interactions.

This was predicted to be the strongest at -3.58 kcal/mol. The coulombic interaction is less attractive compared to synthon A. Figure 5-12 A shows the two molecules are related through symmetry via a screw-axis rotation around the b-axis. A H-bond, with an angle of 117° and approximately 2.6 Å in length from hydrogen to fluorine, appears to form between the β section's hydroxyl to the 'lower' fluorine atom of the β section. There is also a close interaction between the fluoro-methyl-sulfanyl-carbonyl group of the γ section interacting with a hydrogen atom on the α section's 'first' methyl group. This atom-atom interaction between oppositely charged fluorine and hydrogen could be classed as a weak H-bond, and it may help prevent the fluoro-methyl group showing disorder in this polymorph.

Synthon B

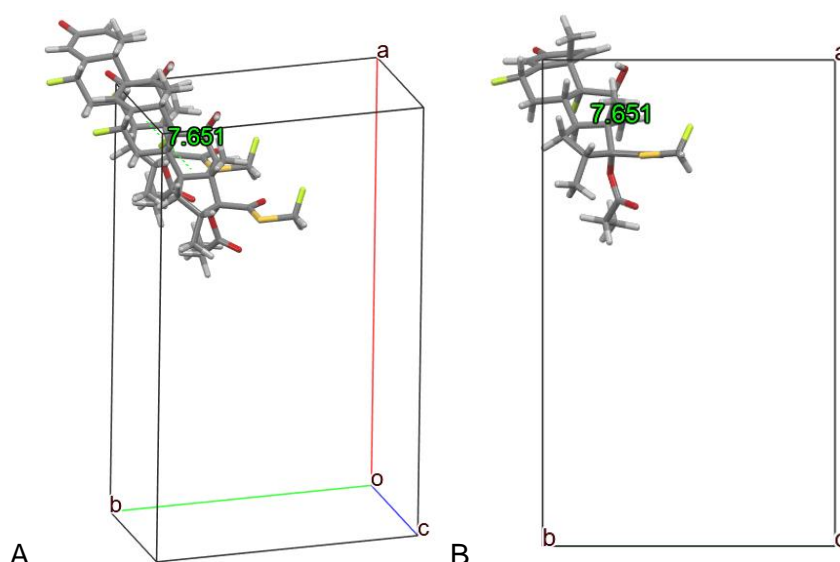


Figure 5-13 Synthon B in the Form II structure, (A) relative to the unit cell, it points in the c-axis direction. (B) is viewed down the c-axis and this shows the molecules are super imposed on top of each other. Intermolecular distance between centres of geometry is 7.65 Å.

Shares a similar molecular arrangement to Synthon A shown in form I, DAXYUX, except it points in the direction of the c-axis. In contrast, it appears that the different conformational torsion angles of the γ section cause this synthon B to have higher repulsion interaction energy. Figure 5-13 (A) above shows the steric repulsion is reduced by the way the molecules slot into each other, this enables the closest intermolecular distance. Molecules appear super imposed upon each other in Figure 5-13 (B) when viewing down the c-axis, showing this synthon points in the [001] direction. It is the most coulombic in nature compared out of DAXYUX01's top five synthons. The

closest interatomic interactions are between the α and the β sections, i.e. the highly negative carbonyl atom of α interacting with the positive hydrogen atoms of β .

Synthon C

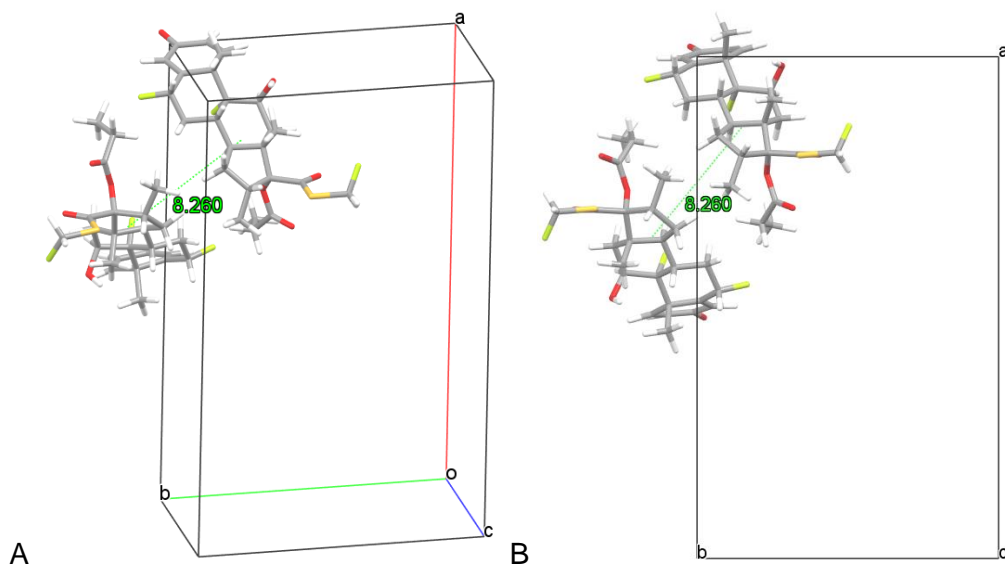


Figure 5-14 Synthon C in the Form II structure, (A) relative to the unit cell, intermolecular distance between centres of geometry is 8.26 Å. (B) is viewed down the c-axis.

The molecules are related through symmetry via a screw-axis rotation around the c-axis. Overall, this synthon is the third strongest of DAXYUX01 but it has a highly repulsive coulombic interaction. Figure 5-14 (A) shows this could be due to the proximity of opposing β section's and subsequent repelling between positive hydrogen atoms. Furthermore, the close interatomic distances between fluorine of the β section with negatively charged atoms of the γ section's propionate group could increase repulsion.

Synthon D

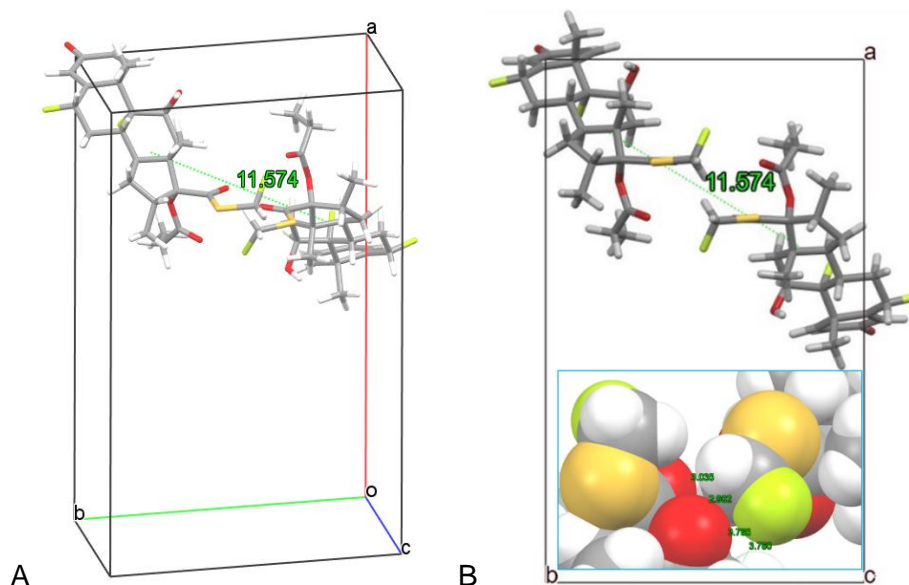


Figure 5-15 Synthon D in the Form II structure, (A) relative to the unit cell, intermolecular distance between centres of geometry is 11.57 Å. (B) is viewed down the c-axis. Inset shows a Space-fill representation of the closest interatomic distances between the two molecules interacting in synthon D.

The molecules are related through symmetry via a screw-axis rotation around the c-axis but in the opposite direction compared to synthon C. This synthon has the lowest vdW contribution of all the top five, due to the minimal molecule overlap. It has a relatively large proportion of attractive coulombic interaction energy thanks to the closest interaction between two γ sections, specifically the fluoro-methyl group interacting with the propionate group.

The space fill image of the fluoro-methyl-sulfanyl-carbonyl group next to the propionate group indicates steric and coulombic repulsions likely plays a role in reducing the rotation of the fluoro-methyl group, as there will be large repulsion energies between the fluorine and oxygen atoms. The DAXYUX01 structure was solved using a machine learning, genetic algorithm method, to match predicted structures to powder x-ray diffraction patterns (Kariuki et al., 1999). Therefore, the fact these predicted structures would do not contain disorder, as seen in the fluoro-methyl group of the DAXYUX structure, is an artefact of the structure solving method. However, this synthon indicates the positioning of molecules help to reduce disorder of the fluoro-methyl group in the DAXYUX01 structure.

Synthon E

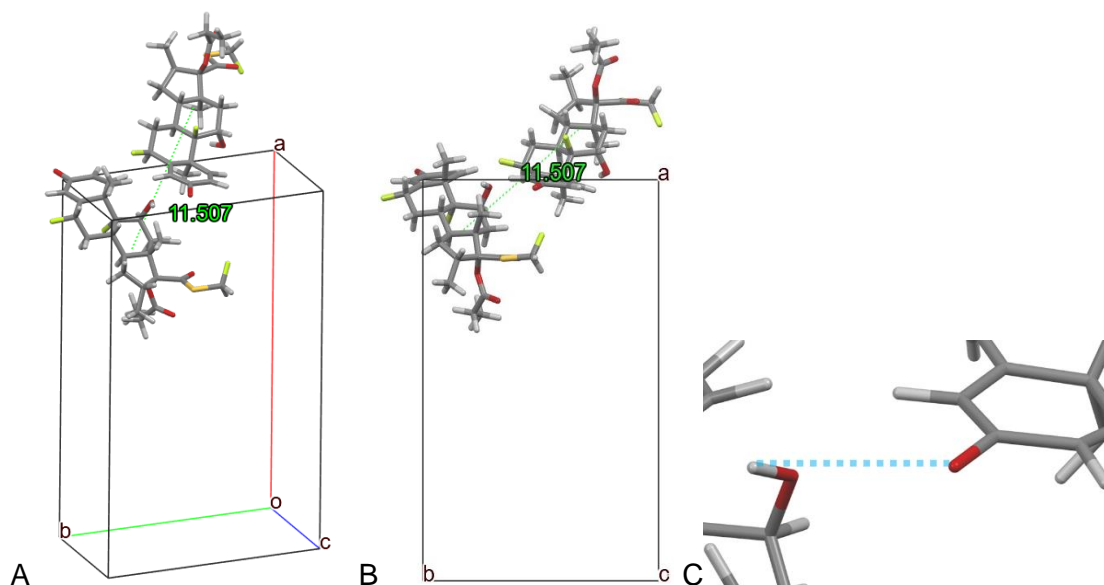


Figure 5-16 Synthon E in Form II structure, (A) relative to the unit cell. (B) Viewed down the c-axis, synthon points in the a-axis direction, with intermolecular distance of 11.5 Å. (C) Shows the H-bond between hydroxyl and carbonyl group.

Synthon E is between two molecules related through screw-axis symmetry by rotation around the b-axis. Overall, the chain of molecules connects in the b-axis direction. This interaction is predicted as the fifth strongest and mostly vdW in nature with a relatively high degree of coulombic repulsion. There is close positioning of α 's carbonyl and β section's hydroxyl which forms a H-bond, with an H---O bond distance of 3.6 Å, and bond angle of 32°. This not very straight and the between oxygen atoms is only 2.8 Å, two close positioned, oppositely charged oxygen atoms likely contribute to the high predicted repulsive interaction. Additionally, there is a close interaction between oppositely charged hydrogen and fluorine atoms of the α and β sections.

Summary of Form II

Synthon A is the strongest at -3.58 kcal/mol, it appears to show a H-bond between the hydroxyl group and the 'lower' fluorine atom of the β section. However, the hydroxyl is not pointing in a direction to make it a straight angle, with an angle of 117° and distance of 2.6 Å. Synthons B is the second strongest, it resembles form I's synthon A and they share the same intermolecular distance. However, it was predicted to have a far higher repulsion interaction, so the total energy was only -3.37 kcal/mol. Synthon C exhibited a large degree of coulombic repulsion, this may have been caused by the proximity of negatively charged atoms. In synthon D, the two molecules are related through a screw-

axis which enables opposing γ section's to accommodate each other. It is theorised this packing increases the ordering of the fluoro-methyl group, which contrasts the disordered fluoro-methyl group shown in the form I, DAXYUX, structure. Synthon E also shows a H-bond, with close positioning of α 's carbonyl with the hydroxyl. However, this bond is not straight, despite the hydrogen atom positions being optimised. It has an angle of 32° and the H---O inter atomic distance was 3.6 Å, hence why it has a low interaction energy.

5.5 Comparing Different Crystal Packing Arrangements

Both polymorph's show vdW dominated lattice energies due to the large molecular mass and fewer H-bond donator groups present. As expected, the more stable polymorph, DAXYUX, had a stronger lattice energy compared to DAYUX01. Molecular conformations were very similar in both polymorphs due to the α and β section's rigidity. Further similarity between both polymorphs was seen in synthon A in Form I and synthon B in Form II, with almost identical orientations and distances between centres of geometry. This synthon was much weaker in DAXYUX01 due to increased dispersive repulsions between hydrogen atoms in opposing β sections. A single H-bond between the hydroxyl and carbonyl groups was present in both polymorphs, travelling in the direction of the b-axis and the two molecules were connected through a 2-fold screw axis. Again, the interaction energy was weaker in DAYUX01. Overall, DAXYUX01's lower interaction energy was attributed to its lower packing density and hence reduced molecular overlap between interactions. The fluoro-methyl group doesn't show strong directional interactions in the DAXYUX structure, and it may repel with the like-charged carbonyl atom. In contrast, the DAXYUX01 structure could reduce fluoro-methyl disorder by steric repulsion minimisation in synthon D's interaction between two γ sections.

5.6 Conclusion

This chapter initially identified the difference between the form I DAXYUX and form II DAXYUX01 polymorphs. The functional groups of an FP molecule were designated into three different sub-sections; α , β and γ . Conformational analysis of the two polymorphs identified the largest difference was the twisting of the γ section, consisting of the propionate and fluoro-methyl-sulfanyl-carbonyl group. High similarities were similar due to the rigidity of the steroid skeleton of cyclic rings. Predicted lattice energy was stronger

in form I, the more common polymorph, and this showed it was more stable. Synthon analysis identified packing orientation relative to unit cell of both polymorphs. Similarity was shown between both polymorphs, Form I's strongest interaction, synthon A, was identical in orientation to Form II's synthon B. Both polymorphs show the same H-bond, between α 's carbonyl and β 's hydroxyl connecting in b-axis direction via screw-axis. Overall, Form II's inferior packing lowers its density and is believed to increase the repulsive interactions, which reduces the cumulative lattice energy.

The next chapter will predict a morphology of Form I and investigate the different chemistries of these surfaces. This will be interesting to see how solvent interactions may change morphology formation and see how particulate surface properties change depending on their surfaces.

Chapter 6: Morphology Prediction of Fluticasone Propionate and Particulate Surface Interactions with Formulation

Summary: Form I fluticasone propionate's external morphology was predicted through the attachment energy model, it partially resembled the needle shaped, experimentally recrystallized samples. The strongest synthon was identified to grow along the length of the crystal and surface analysis showed different functional groups were exposed depending on the directions of intermolecular interactions. A grid-based search tool predicted the interaction energies with probes. It was hypothesised polar solvents preferably adsorbed to the crystal's side faces, which left the non-polar capping faces as a favourable growth environment. Also, particle morphologies with a smaller proportion of capping faces were shown to have lower cohesive energies.

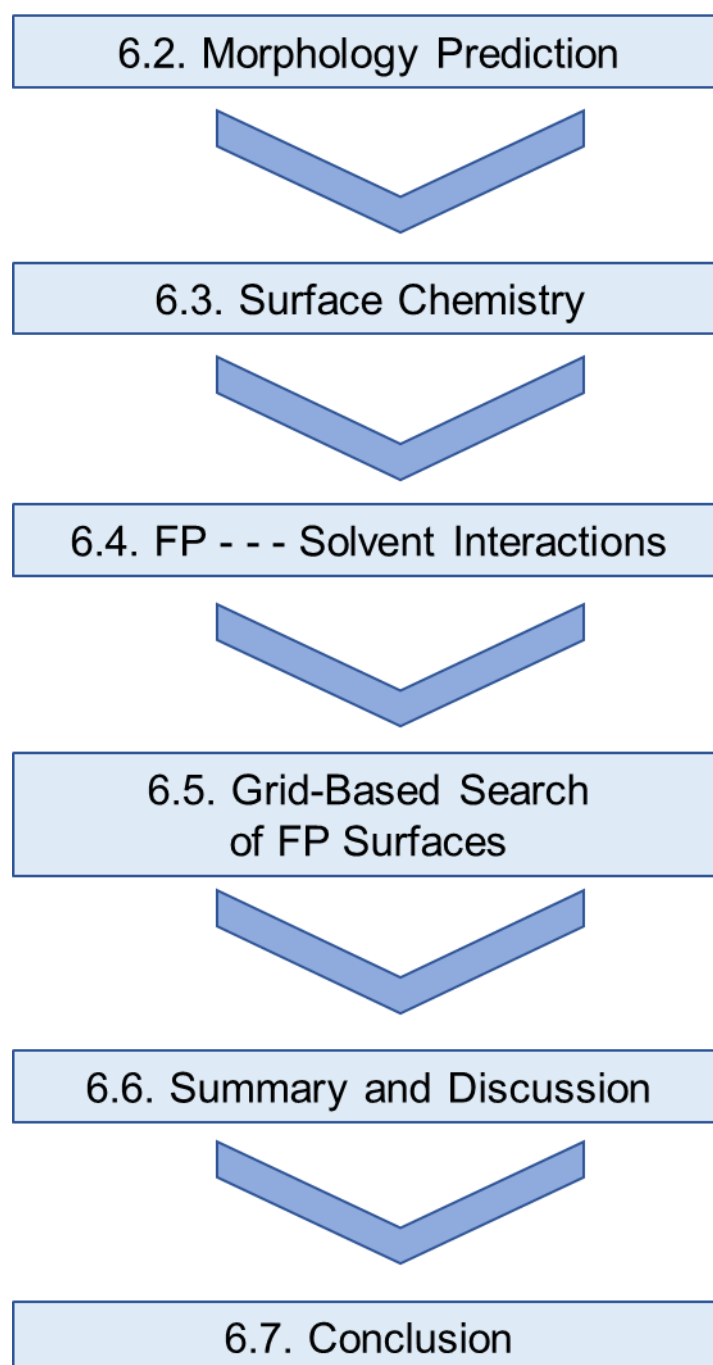
Chapter 6: Morphology Prediction of Fluticasone Propionate and Particulate Surface Interactions with Formulation

6.1 Introduction

Micronized FP tends to agglomerate and has poor flowability (Louey et al., 2004) (Steckel et al., 2003), it is thought to be affected by particle shape and surface properties. Generally, API particles with higher surface polarity were found to show more agglomeration and have poorer aerosol generation performance (Traini et al., 2006a). Before being micronized, FP particles reportedly crystallises into elongated shapes (Čejka et al., 2005) (Murnane et al., 2008a). It would be interesting to investigate particle surfaces at a molecular scale to help hypothesise what may cause FP to aggregate. Molecular modelling techniques can be used to further study the intermolecular interaction previously identified. Predicting drug particle properties from their crystal structure has the potential to complement quality-by-design approaches where MDI performance metrics are related to formulation properties.

In this chapter, the external morphology of Form I FP was predicted using the attachment energy method. Subsequently, grid-based search methods applied force field potentials to predict the interaction energies between probes and crystal surfaces. This made it possible to investigate how solvents influenced growth and how morphology affects particle interactions. Further details of the method followed are given in sections 2.2.4.3 and 2.2.4.4.

Chapter Flowchart Overview



6.2 Morphology Prediction of FP

The crystal morphology of form I was predicted, this was selected as it was likely to be the only polymorph seen in MDIs. Initially, the BFDH method identified the most important crystal faces, those with largest d-spacing. Following this, force field potentials were used to predict the morphology via the attachment energy method. The growth of each face each is determined by the strength of intermolecular interactions. They are assigned as either external or internal synthons depending on their direction, i.e. if they point parallel or perpendicular to the growth direction of a face. These predictions were compared with experimentally recrystallised samples.

6.2.1 BFDH Identified Faces

It can be seen in Table 6-1 below that the surface with the largest d-spacing, {001}, is approximately 25% larger than the next closest. Adjacent to {001} are the two forms with second largest d-spacings, {0-11} and {011}. The surfaces with smallest d-spacing are in the {11-1} and {-111} forms.

Table 6-1 BFDH identified forms belonging to FP, ordered descending from the largest d-spacing. Each form represents two equivalent faces.

Forms:	Face 1	Face 2	D-spacing (Å)
{0 0 1}	(001)	(00-1)	10.8
{0 1 1}	(011)	(01-1)	8.6
{0-1 1}	(0-11)	(0-1-1)	8.6
{1 0 0}	(100)	(-100)	7.6
{0 2 0}	(020)	(0-20)	7.1
{1 1 0}	(110)	(-110)	6.7
{1-1 0}	(1-10)	(-1-10)	6.7
{1 0-1}	(10-1)	(-101)	6.7
{1 1-1}	(11-1)	(-1-11)	6.1
{-1 11}	(-111)	(1-1-1)	6.1

6.2.2 Attachment Energy Model

A symmetrical morphology was predicted using the attachment energy model, Figure 6-1 shows the {10-1}, {1 1-1} and {-111} forms identified in using the BFDH method are not included. The attachment energy values of Table 6-2 show the missing forms have high attachment energy and hence high growth rate, causing them to not be present in the morphology. As outlined in section 2.1.4.1., the attachment energy model predicts an equilibrium morphology where growth rate of each face is proportional to its respective attachment energy. Therefore, faces with smaller absolute attachment

energy would have a slower growth rate, i.e., -17 kcal/mole is considered smaller than -34 kcal/mole. Hence, one would expect a face with the smallest attachment energy to have the slowest growth rate and be the most prominent in the morphology. Table 6-2 shows faces with the top four smallest attachment energies represent the top four largest surface areas. Despite (001) having the smallest attachment energy, it did not have largest surface area. It was found the relationship with surrounding surface growth rates also played an important role. For example, the (100) form represents the largest area, and this is believed to be caused by the comparatively faster growing adjacent forms, (110) and (1-10). Similarly, the high attachment energy form (020) is adjacent to both low attachment energies (011) and (0-11), which results in the latter pair representing the joint second and third largest surface area.

Surface energy was approximated from the attachment energies and D-spacing, Table 6-2 shows that generally faces lower surface energy represent a larger surface area. Overall, this prediction appears to be somewhat elongated, with the side faces; (001), (011), (0-11) and (020), representing ~70% of the surface area. Whereas the capping faces; (110), (1-10) and (100), are less than 30% of the total surface area.

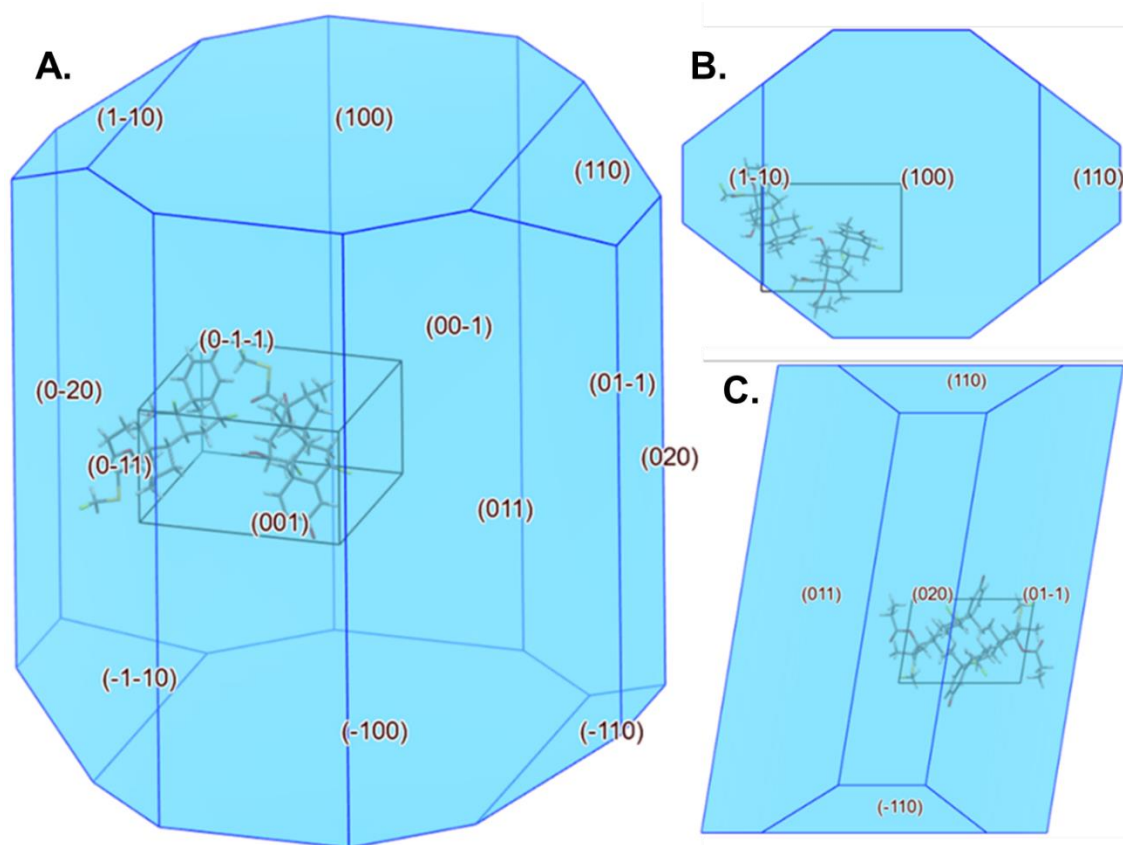


Figure 6-1 (A) Predicted morphology predicted, all faces are labelled. (B) Viewed down the a-axis, and (C) viewed down the b-axis.

Table 6-2 Slice, attachment, and surface energy of each form, predicted at a radius when lattice energy was fully converged. D-spacing and surface area % also listed. Note, labels refer to equivalent morphological faces: (100) represents (100) & (-100).

Faces:	Slice energy (kCal/mole)	Attachment energy (kCal/mole)	Surface Energy (mJ/m ²)	D-Spacing (Å)	Surface Area %
(0 0 1)	-26.07	-17.71	11.38	10.84	17.09
(0 1 1)	-24.89	-18.89	9.63	8.6	22.33
(0-1 1)	-24.89	-18.89	9.63	8.6	22.33
(1 0 0)	-19.59	-24.20	10.83	7.55	23.02
(0 2 0)	-18.66	-25.13	10.53	7.07	7.72
(1 1 0)	-14.96	-28.82	11.38	6.66	3.76
(1-1 0)	-14.96	-28.82	11.38	6.66	3.76
(1 0-1)	-10.39	-33.39	13.32	6.73	0
(1 1-1)	-9.57	-34.21	12.32	6.07	0
(-1 1 1)	-9.57	-34.21	12.32	6.07	0

6.2.3 Synthon Contribution to Growth

It was important to understand how the synthons identified in the previous chapter contributed towards growth of each face and potentially influenced particle shape. Synthons were categorised as either attachment energy or slice energy depending on the direction at different surface terminations. As discussed earlier in section 2.1.4.1., if a synthon pointed outside of a slice, it would help attach a new layer, hence contribute to the attachment energy of that face. Conversely, if the synthon was pointing within a growth slice it would contribute to the slice energy of that face. Growth directions of synthons relative to the important faces of FP are summarised in Table 6-3. The chain of synthon A adds molecules along the [100] direction, therefore it contributes to the attachment of (100), (110) and (1-10) surfaces. The synthons B, C and D form chains of molecules that zig-zig up and down the [001] and [00-1] directions, but overall, travel in the [010] direction, this means they contribute to attachment energy of (001), (011), (110) and (020) surfaces. Molecules in synthon E are connected along the [001] direction, so contribute to the attachment energy of (001) surfaces.

Table 6-3 Growth directions Form I FP synthons relative to morphology faces. If directed outside the growth slice, the interaction was categorised as contributing to face growth via attachment energy (Att), and if it was within the growth slice it contributed to slice energy (Slice).

Synthon	Strength (kCal/mole)	Interaction Type	(100)	(110)	(020)	(001)	(011)
A	-6.22	vdW	Att	Att	Slice	Slice	Slice
B	-3.97	vdW	Slice	Att	Att	Att	Att
C	-1.96	h-bond	Slice	Att	Att	Att	Att
D	-3.54	vdW	Slice	Att	Att	Att	Att
E	-1.93	vdW	Slice	Slice	Slice	Att	Att
Total Attachment Energy (kCal/mole)			-24.2	-28.8	-25.1	-17.7	-18.9

6.2.4 Recrystallisation Experimental Comparison

Methanol

Faster Recrystallisation from methanol produced needle shaped crystals with aspect ratios ranging between 1:20 to 1:40. They appear to have defined facets and Figure 6-2 right highlights a hexagonal profile.

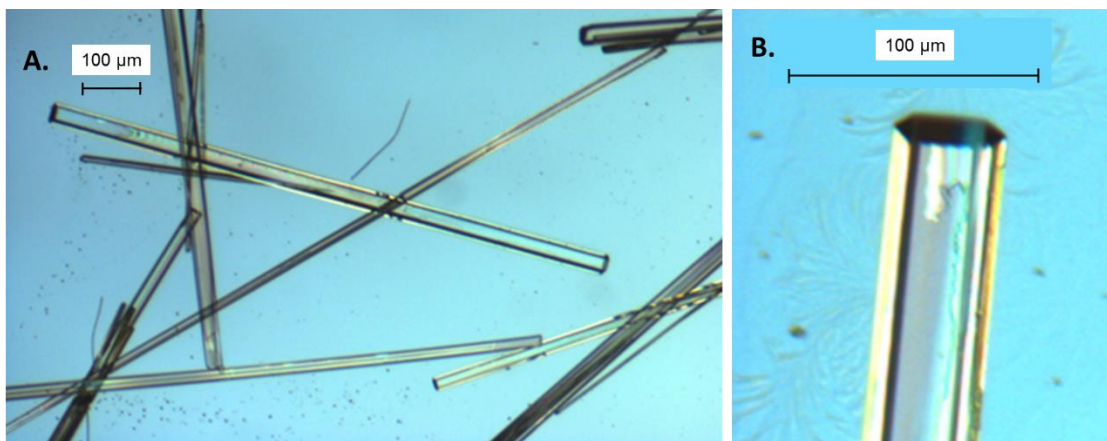


*Figure 6-2 FP recrystallised via slow evaporation from **methanol** over 24 hours. Optical microscope image taken using 5x zoom (A) and taken with 10x zoom (B).*

Slower recrystallisation from methanol produces larger crystals and the same hexagonal profile appears to be present in Figure 6-3. Although, the hexagonal profile is less defined, and it appears wider. A notable difference is the capping faces recrystallised at an angle, it was consistently 28° relative to the perpendicular. This same angle was noted in other crystals formed.

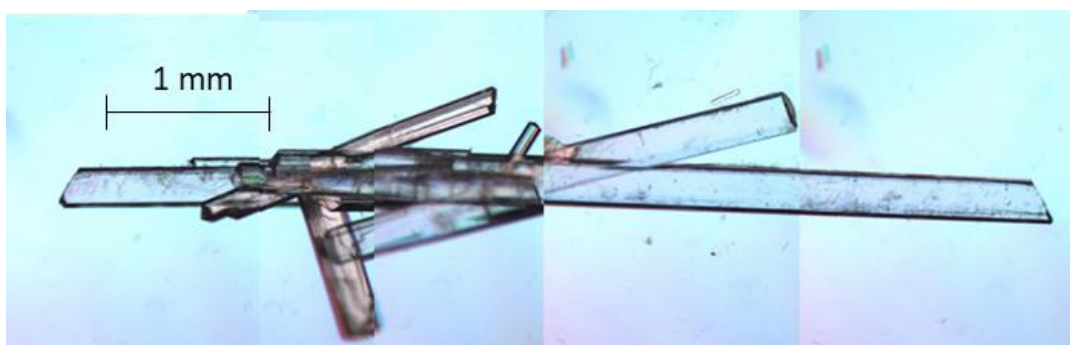


Figure 6-3 FP recrystallised via slow evaporation from **methanol** over 4 weeks. Collection of images captured using an optical microscope with 5x zoom.

The hexagonal profile of the crystal capping face can be made out more clearly when viewed at an angle. This has been outlined in Figure 6-4 and it highlights how it is wider in one of the planes. The image on left shows two secondary crystals that appear to have nucleated on the main needle crystal which shows the preference to grow along the long axis.

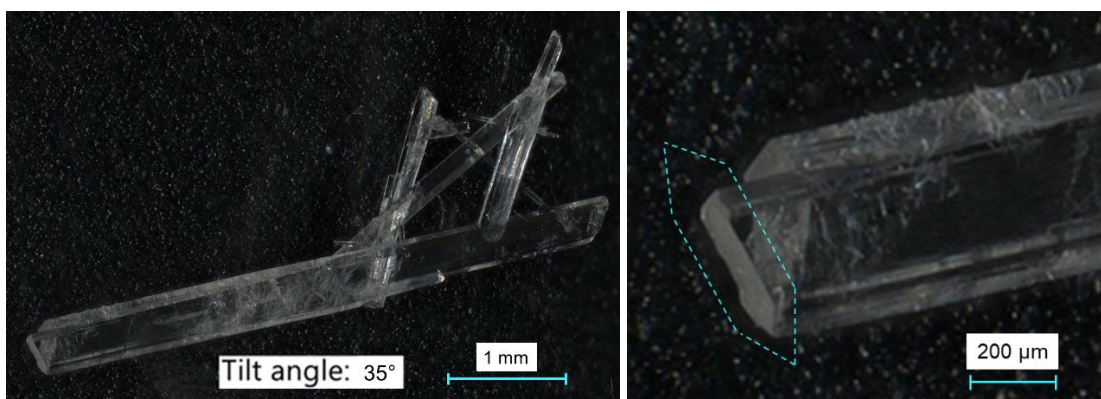


Figure 6-4 FP recrystallized via slow evaporation from **methanol** over 4 weeks. Captured using an optical microscope, the lens was tilted at an angle of 35° relative to the sample.

Ethanol

Recrystallization from pure ethanol formed needle shaped crystals across a wide size range, Figure 6-5 shows aspect ratios varying between 1:10 and 1:50. Overall, visual inspection showed a higher population of crystals with a smaller aspect ratio. An angled capping face is seen on some crystals, but it is hard to identify hexagonal profiles. It is believed the needle shape formed so quickly they are unable to produce clearly defined facets.

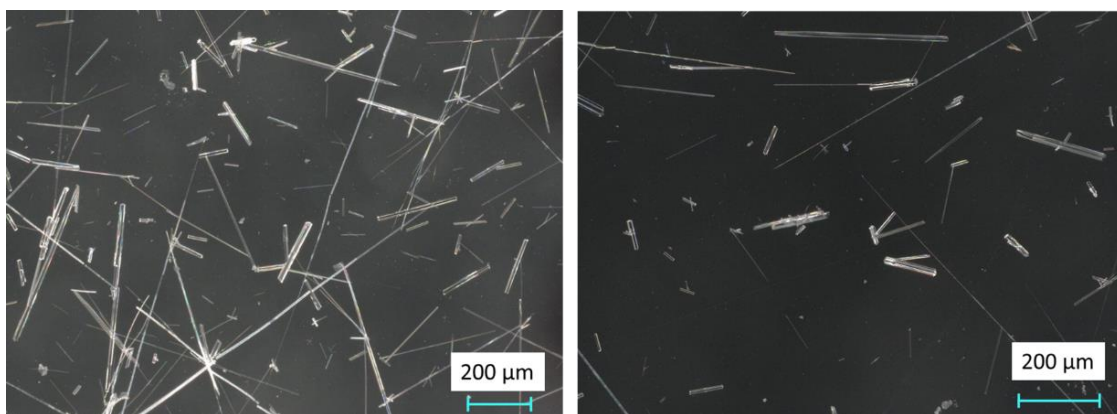


Figure 6-5 FP recrystallized from **ethanol** over 4 weeks. Captured using an optical microscope.

Crystals formed from a solution of ethanol and 10 wt% water, shown in Figure 6-6, also shows the 28° angle on its capping face. The crystals appear stubbier when compared to examples produced in methanol. A wide hexagonal profile appears, similar to when it is slowly formed from methanol.

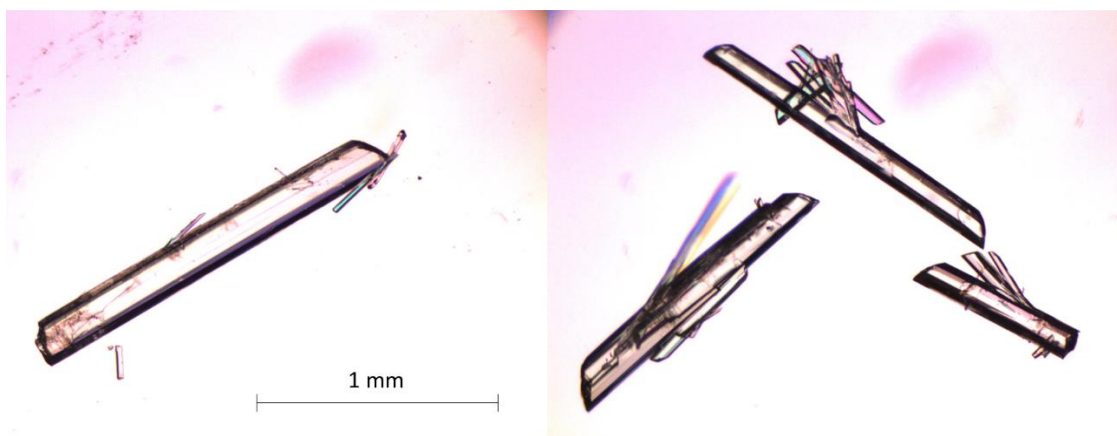


Figure 6-6 FP recrystallised via slow evaporation from **ethanol and 10 wt% water** over 4 weeks. Optical microscope images taken using 5x zoom.

Polymorph Confirmation

Powder XRD patterns of recrystallised samples in Figure 6-7 are compared with reference patterns for form I and II of FP. Key signature peaks in Form I have been found in the other recrystallized samples, these are labelled A – F. Peaks D, E, and F are shown in Form I and the recrystallised samples, but they are not present in Form II. Additionally, the peaks of recrystallized samples have the same spacing as form I but are shifted to the left by $0.1\text{--}0.2^\circ$. They also match the peaks produced from the micronized powder. Overall, this confirms the same polymorph, form 1, has been recrystallised.

The intensities differ, ethanol and methanol samples show a strong preference for certain peaks. This emphasised most in methanol, especially peak D at $\sim 16^\circ$. Their difference in peak heights is due to the elongated morphologies of recrystallised samples and when placed in a sample holder they all align in a way which means more of the needle's side faces are accessed during the scan. In contrast, the particle shape of micronized powder is relatively more uniform, so particles do not tend to have preferred orientation. Also, it is likely to have more amorphous content which would broaden the peaks.

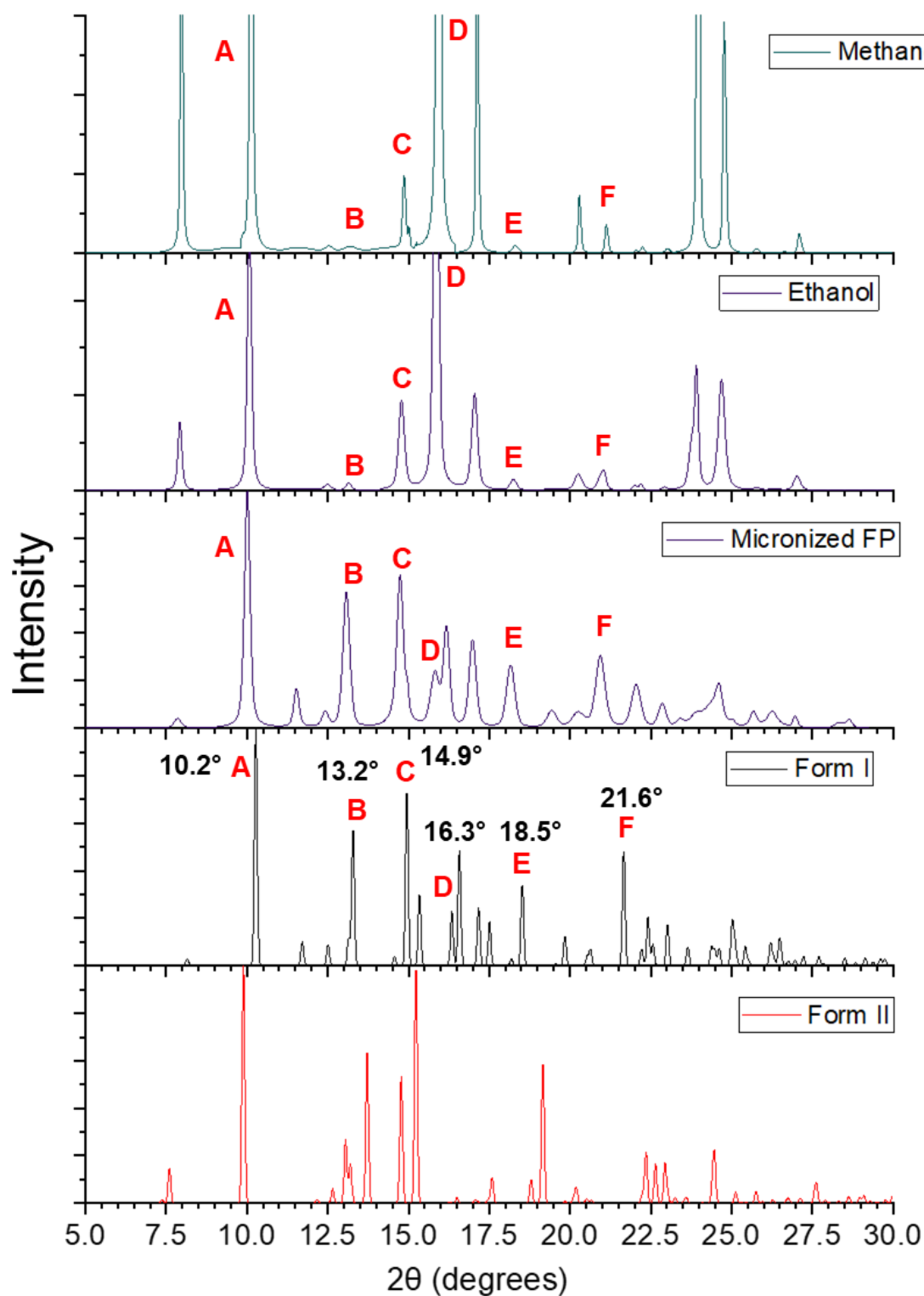


Figure 6-7 PXR D patterns of FP recrystallised from methanol, ethanol, and original micronized sample. Compared with previously measured patterns of Form I (Čejka et al., 2005) and Form II (Kariuki et al., 1999).

6.2.5 Morphology Proposed on Experimental Results

The shape of experimentally recrystallised samples varied compared to the attachment energy morphology as it did not account for solvent effecting growth kinetics. To help understand crystal faces present, the attachment energy prediction was fitted to resemble experimental crystals. Figure 6-8 shows this modified morphology was more elongated, with an increased growth ratio in the $[100]$ direction, likely due to the strongest synthon growing in that direction. The growth rate of (020) and $(0-20)$ faces was higher, which meant this form was not present in the altered morphology. The bottom left of Figure 6-8 shows some experimental crystals featured an angled capping face, measured to be approximately 28° . This matched the angle when either (110) or $(1-10)$ were the capping faces, which complemented the theory of elongation along the $[100]$ direction.

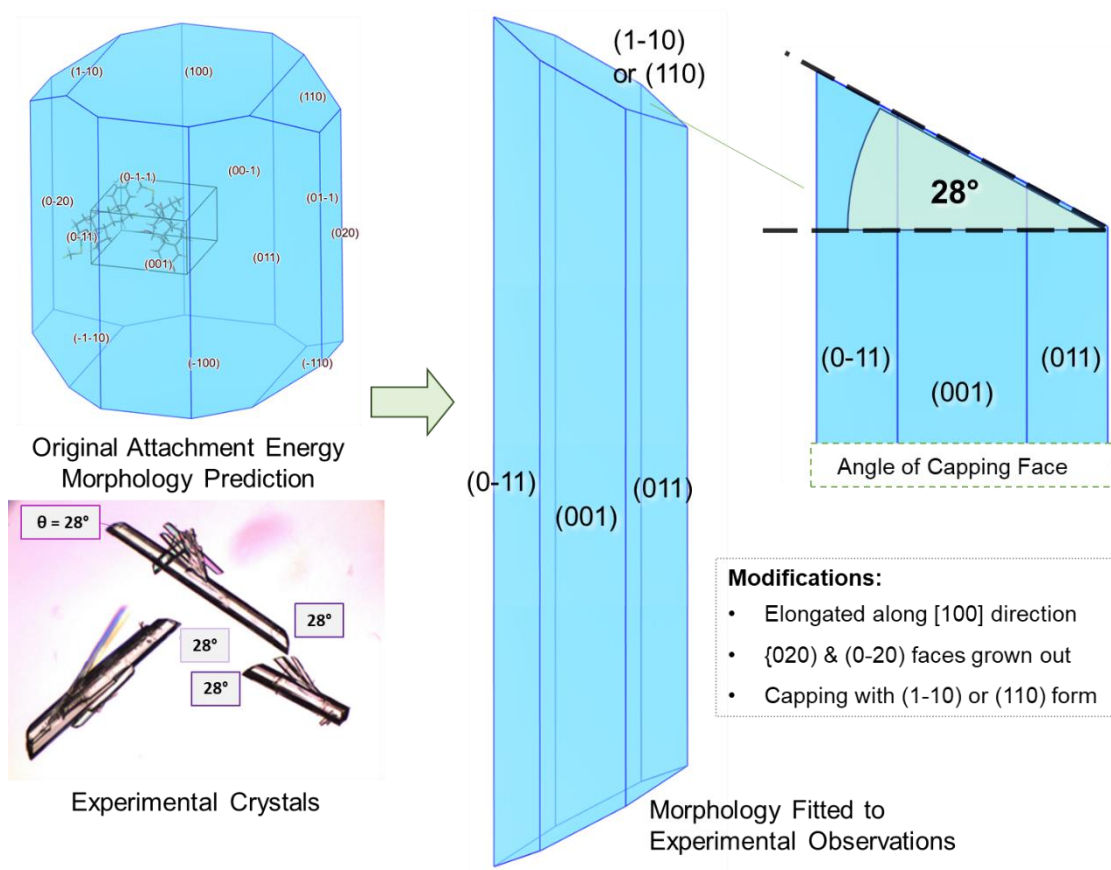


Figure 6-8 Original attachment energy morphology was modified to resemble experimental crystals. New morphology is more elongated and the (020) and $(0-20)$ faces are no longer present. Capping faces have an angle of 28° , matching experimental observations.

6.3 Surface Chemistry

As synthons grow in different directions, extrinsic synthons terminations vary on each surface. This section outlines how at each crystal face, the exposed functional groups of the FP molecule and surface height differs.

6.3.1 (100)

The α and γ section of the FP molecule are revealed at the (100) surface. It can be seen in Figure 6-9 (A) that the main groups at this surface are the carbonyl, the propionate and carbonyl-sulphur-fluoro-methyl. The γ section's carbonyl groups do not appear readily available as they point inwards. Similarly, FP's hydroxyl is near the surface but is pointing laterally. Therefore, this surface is considered non-polar in nature as the only freely accessible H-bond accepting groups are the carbonyl and the fluoro-methyl group, whereas there is a large amount of visible cyclic rings. It is unlikely to be a slip plane with the interlocking shown between layers. It can be seen how molecules stack on top of each other to form synthon A and contribute to the growth of this surface. This strong vdW interaction implies the surface is mostly non-polar in nature. Figure 6-9 (B) and (C) show this surface is relatively flat and surface rugosity was measured to be 1.43, Figure 6-9 (C) highlights pockets in the surface have access to H-bond donor groups.

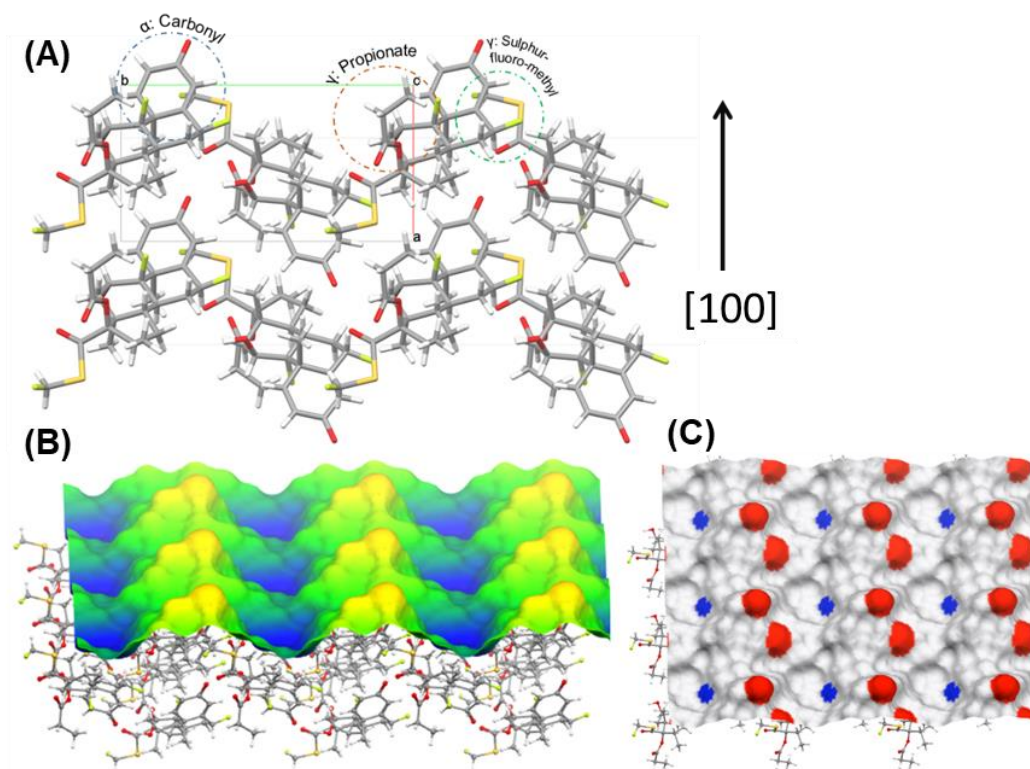


Figure 6-9 (A) Surface chemistry of (100) when viewed down the c -axis, important groups are circled. (B) Topology of (100) surface, coloured by rugosity, higher parts are yellow and lower parts are blue. (C) Coloured by polar interaction proclivity, H-bond acceptor groups are red and donor groups blue.

6.3.2 (110)

The surface topology is smooth apart from the protruding carbonyl-sulphur-fluoro-methyl group belonging to FP's γ section, surface rugosity was measured to be 1.56. The propionate, hydroxyl and α section carbonyl are near the surface. This could be considered a polar surface as the protrusion means the H-bond acceptor groups of the γ section freely available, shown in Figure 6-10 (C). However, H-bond donation may be limited as the hydroxyl is pointing laterally so has restricted accessibility. Less interlocking is shown between layers compared to (100) but more than some of the following surfaces.

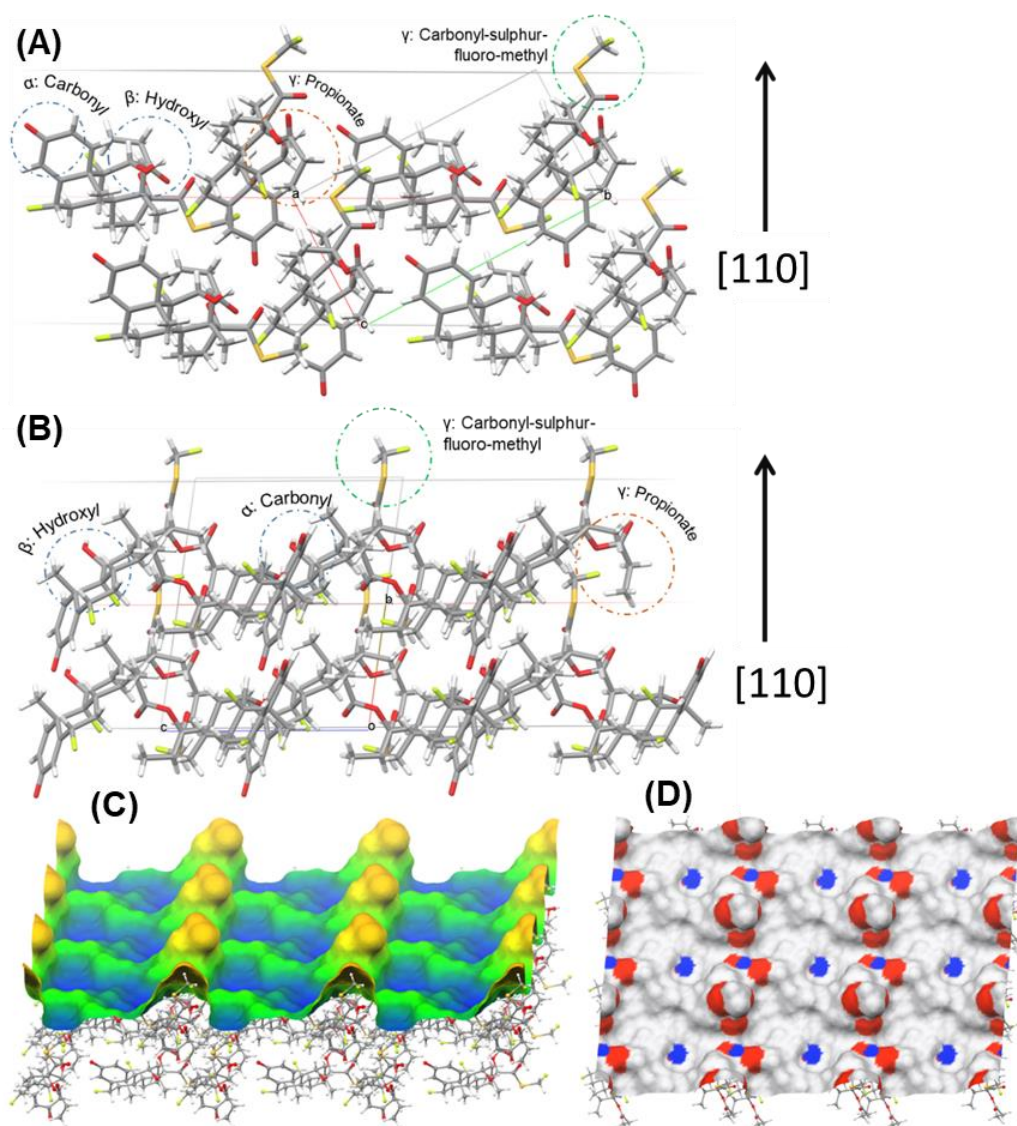


Figure 6-10 Surface chemistry of (110) with important groups circled, (A) is viewed down the c-axis and (B) is perpendicular to that view. (C) Topology of (110), coloured on rugosity, higher parts are yellow and lower parts are blue. (D) Coloured by polar interaction proclivity, H-bond acceptor groups are red and donor groups blue.

6.3.3 (1-10)

This surface appears quite flat but has a rugosity 1.64 due to the deep indentation, shown in Figure 6-11 (B). It has a similar level of interlocking as the (110) surface. The outer surface mostly consists of the cyclic rings of the β section, dispersed throughout are the α section's carbonyl and γ section's carbonyl-sulphur-fluoro-methyl groups. As the cyclic rings dominate, this surface is considered non-polar and it is reflected in Figure 6-11 (C).

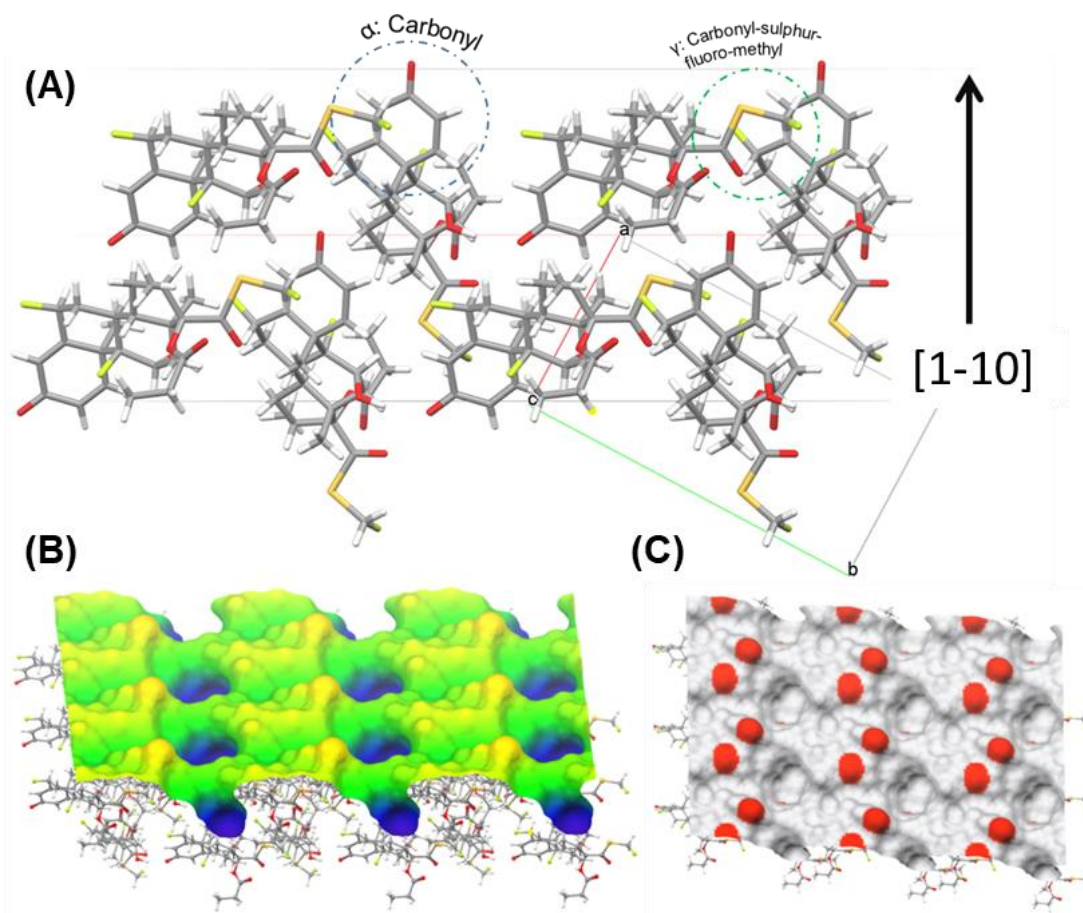


Figure 6-11 (A) Surface chemistry of (1-10) when viewed down the c-axis with unit cell and important groups labelled. Topology of (1-10) surface, (B) colours the surface based on rugosity, higher parts are yellow and lower parts are blue. (C) H-bond acceptor groups are coloured red and donor groups coloured blue.

6.3.4 (020)

The outer surface is relatively flat with a rugosity of 1.49, Figure 6-12 (A) shows hydroxyl group points outwards, the propionate and carbonyl-sulphur-fluoro-methyl groups are exposed, and these are prone to interactions with polar protic solvents. Therefore, this surface appears to be quite polar in nature, Figure 6-12 (C) shows a clear, accessible strip of H-bond acceptor and donor groups on the surface. The H-bond synthon C bonds in the [020] direction.

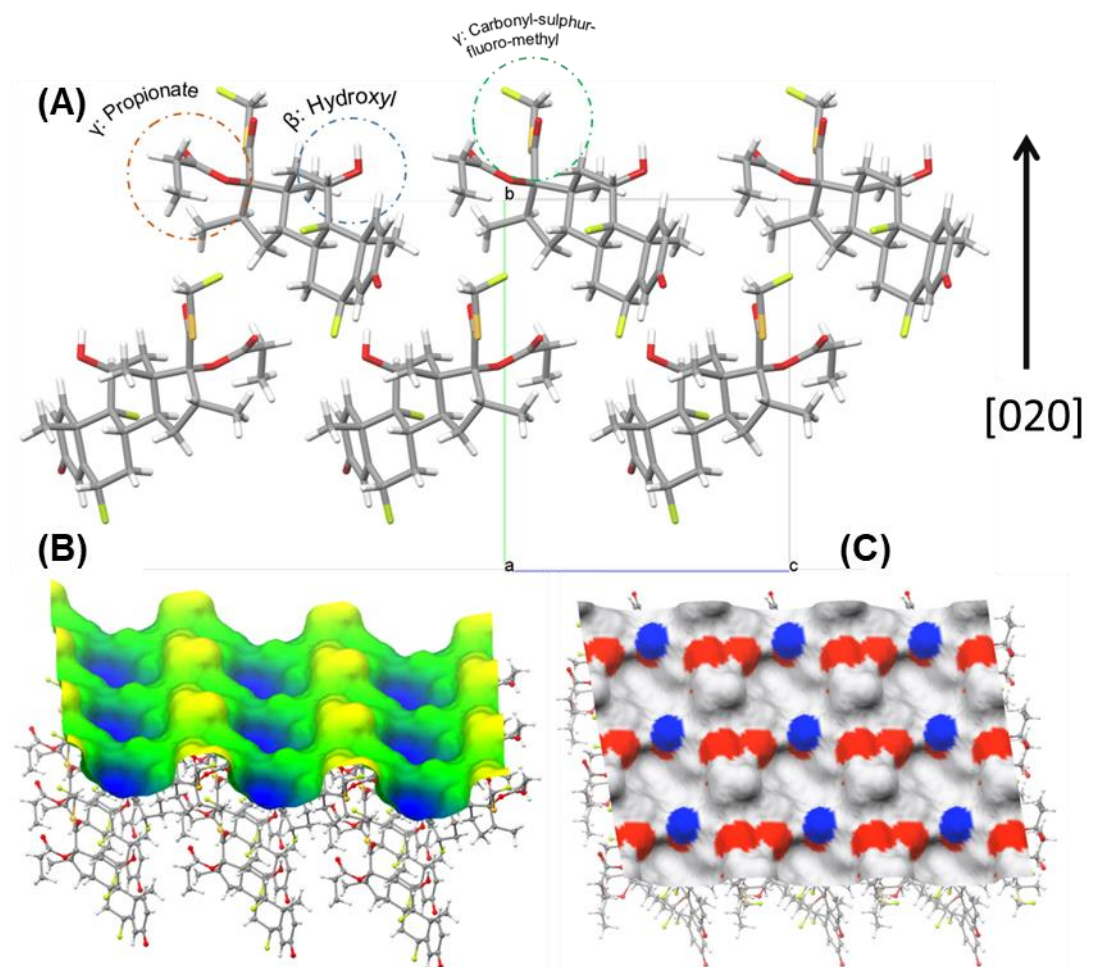


Figure 6-12 (A) Surface chemistry of (020) when viewed down the a-axis with unit cell and important groups labelled. Topology of (020) surface. (B) Colours the surface based on rugosity, higher parts are yellow and lower parts are blue. (C) Shows H-bond acceptor groups are coloured red and donor groups coloured blue.

6.3.5 (0-20)

Due to the screw-axis symmetry of this space group, the FP molecule is connected through symmetry by rotating around the b-axis. This means the opposing faces (020) and (0-20) have differing surface chemistries. It has similar roughness to (020) with a rugosity of 1.53, but fewer H-bond capable groups are available. Figure 6-13 (A) shows the α section's carbonyl and β sections fluorine are freely available for interaction at the highest parts of this surface. Synthon C passes through this surface, so the hydroxyl would form an H-bond with this carbonyl on show. Regardless, this surface appears non-polar in nature, and this is highlighted in Figure 6-13 (C).

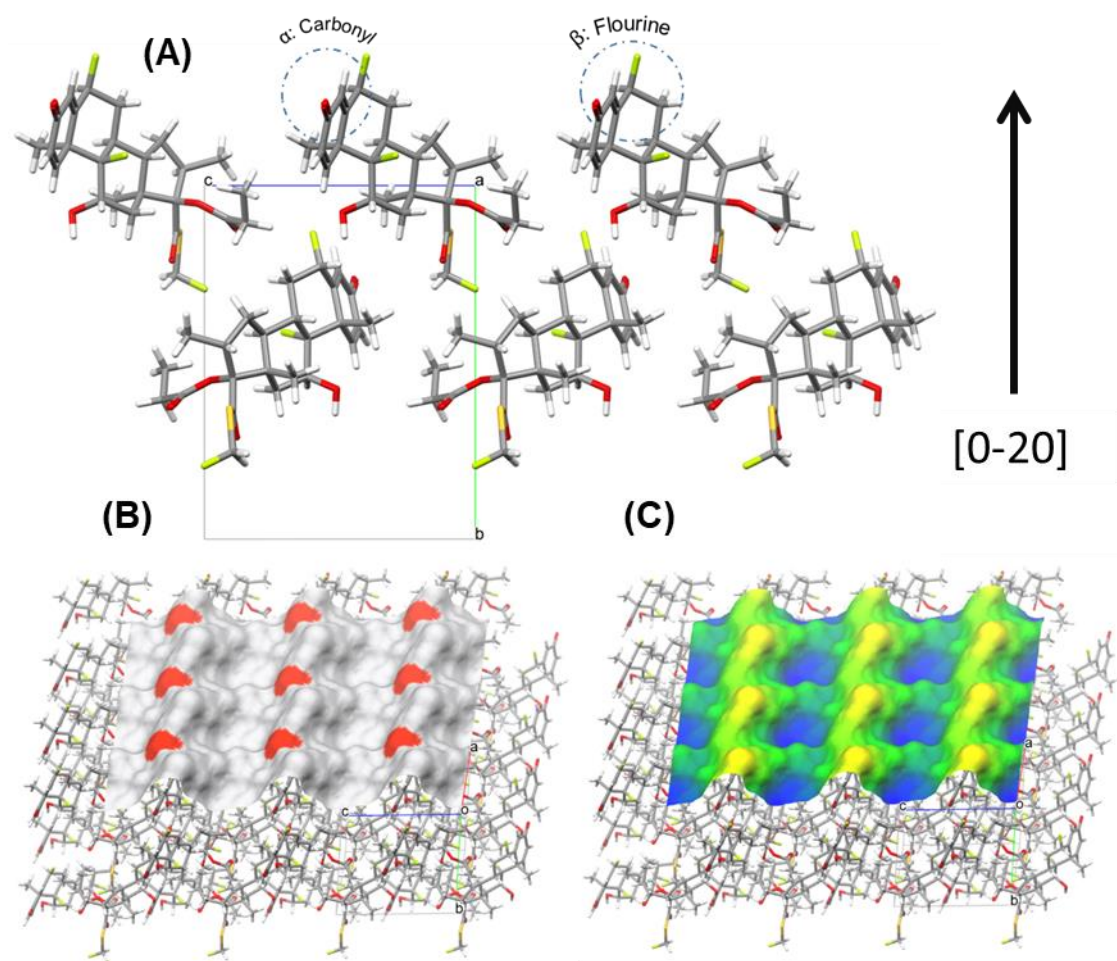


Figure 6-13 (A) Surface chemistry of (0-20) when viewed down the a-axis with unit cell and important groups labelled. Topology of (0-20) surface. (B) Colours the surface based on rugosity, higher parts are yellow and lower parts are blue. (C) Shows H-bond acceptor groups are coloured red and donor groups coloured blue.

6.3.6 (001)

Large undulations are present in the surface topology, the α and β sections of FP protrude out at the top of these peaks while the propionate group sits in the valleys, this is reflected in the high surface rugosity of 1.83. The large valleys are a result of molecular interlocking. Therefore, this surface is unlikely to be a slip plane. Figure 6-14 (C) shows the H-bond capable groups within the valleys. Therefore, polar protic solvents could become trapped in these pockets and be attracted to the H-bond acceptor atoms. Synthon B and E contribute to the growth of this surface which are vdW in nature. However, due to the high rugosity and polar group locations, this surface is considered polar in nature.

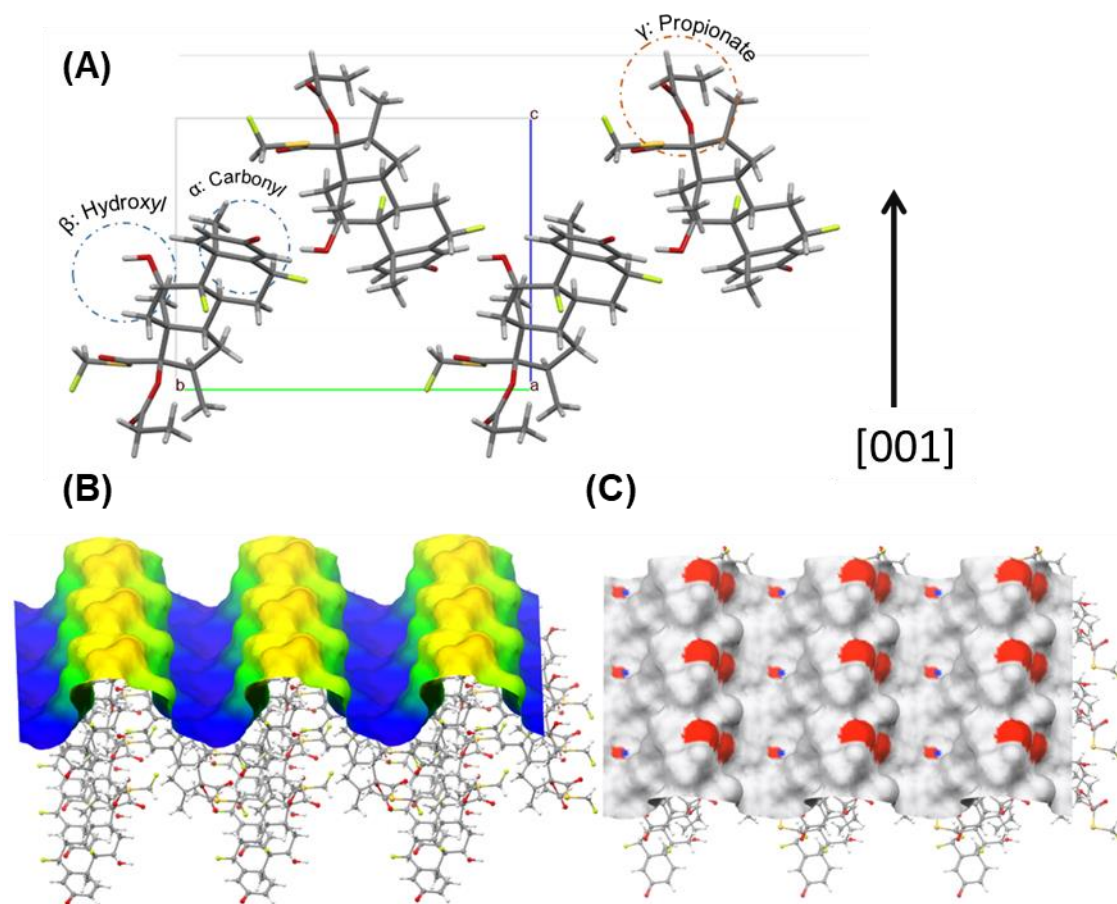


Figure 6-14 (A) Surface chemistry of (001) when viewed down the a-axis with unit cell and important groups labelled. Topology of (001) surface. (B) Colours the surface based on rugosity, higher parts are yellow and lower parts are blue. (C) Shows H-bond acceptor groups are coloured red and donor groups coloured blue.

6.3.7 (011)

Both the hydroxyl group and the γ section, with its multiple H-bond acceptor atoms, are pointing outwards. This surface is flat with a rugosity of 1.33 and shows minimal interlocking between layers, so has the possibility of being a slip planes. The vdW dominated synthons, B, D and E contribute to this face's growth and the H-bonding synthon C contributes. Overall, this surface is more polar in nature as the H-bond acceptor atoms are freely accessible.

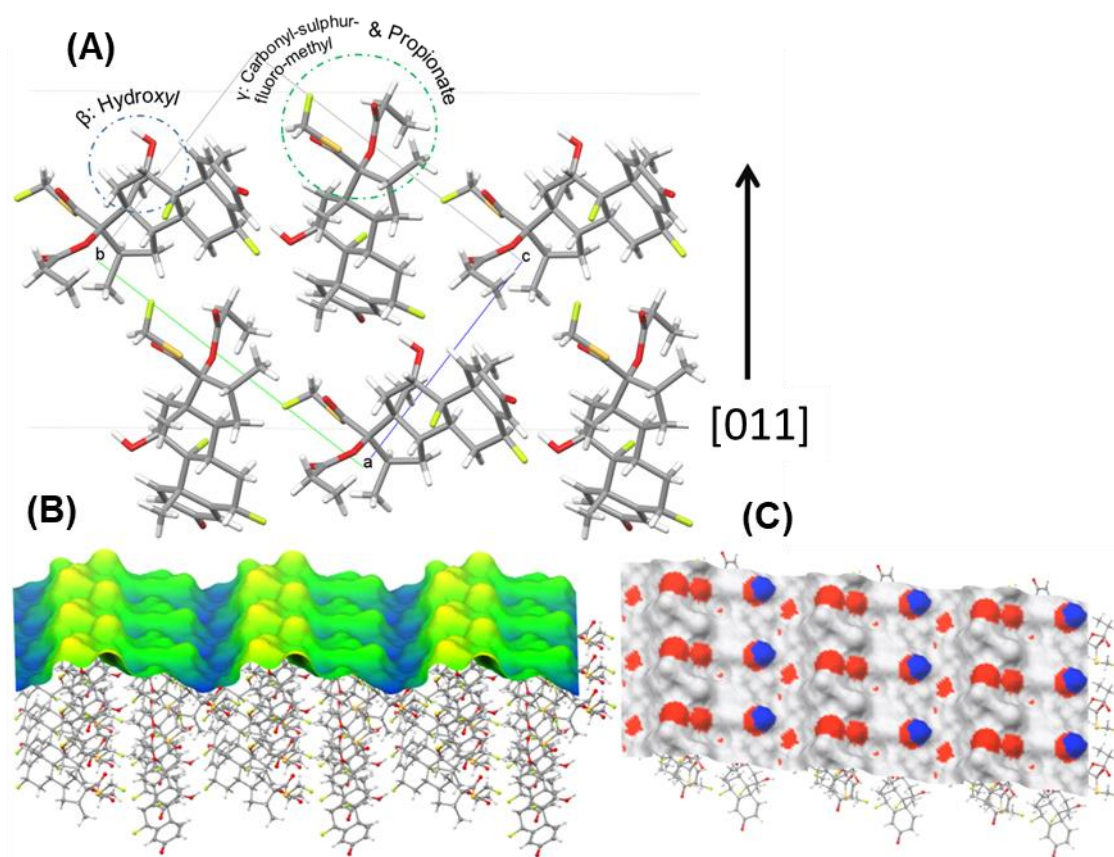


Figure 6-15 (A) Surface chemistry of (011) when viewed down the a-axis with unit cell and important groups labelled. Topology of (011) surface. (B) Colours the surface based on rugosity, higher parts are yellow and lower parts are blue. (C) Shows H-bond acceptor groups are coloured red and donor groups coloured blue.

6.3.8 (0-11)

Similar to (011), this surface is also flat with a rugosity of 1.36 and very little interlocking, so therefore higher likelihood of being a slip plane. The propionate, hydroxyl and α carbonyl are exposed near the outer edge which means the surface appears more polar in nature. The surface appears to be less polar in Figure 6-16 (C) compared to (011) as the hydroxyl group is slightly less accessible. The vdW dominated synthons, B, D, and E contribute to this faces growth and the H-bond synthon C contributes. Overall, this surface could be considered mostly non-polar but still capable of H-bonding.

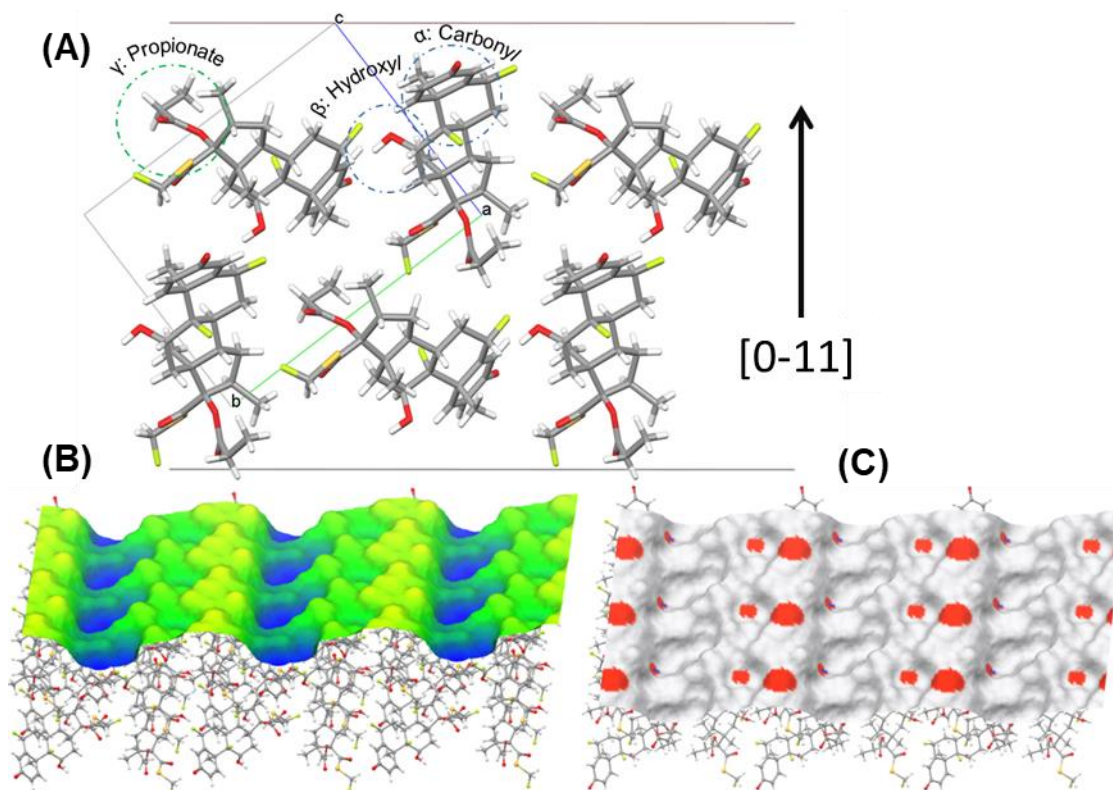


Figure 6-16 (A) Surface chemistry of (0-11) when viewed down the a-axis with unit cell and important groups labelled. Topology of (0-11) surface. (B) Colours the surface based on rugosity, higher parts are yellow and lower parts are blue. (C) Shows H-bond acceptor groups are coloured red and donor groups coloured blue.

6.3.9 Summary and Surfaces Relative to Morphology

It was clear from surface chemistry analysis of (100) how the strongest synthon, A, adds molecules in the [100] direction, which reinforces the argument that this interaction encourages needle shape formation. Large valleys containing H-bond accepting groups were seen on the (001) surfaces, these could potentially act as pockets for solvent molecules. In contrast, the adjacent forms, (011) and (0-11), were the flattest. The summary of surface polarity Figure 6-17 below shows that generally the side faces were deemed more polar in nature and two of the three capping faces were non-polar. The

faces (020) and (0-20) had different surface chemistries due to the unit cells screw-axis symmetry. Although (0-20) had fewer polar groups exposed, it was still deemed polar due to its propensity to form the H-bond synthon, C. Both surfaces in the (020) form showed higher rugosity than their adjacent faces so could be a favourable spot to accept an FP molecule and form a H-bond. So far, interactions between solute FP with different solvents have been speculated. The next sections will go further by investigating the favourable position between solute and solvent molecule interacting with a single FP molecule, and then the different surfaces of FP.

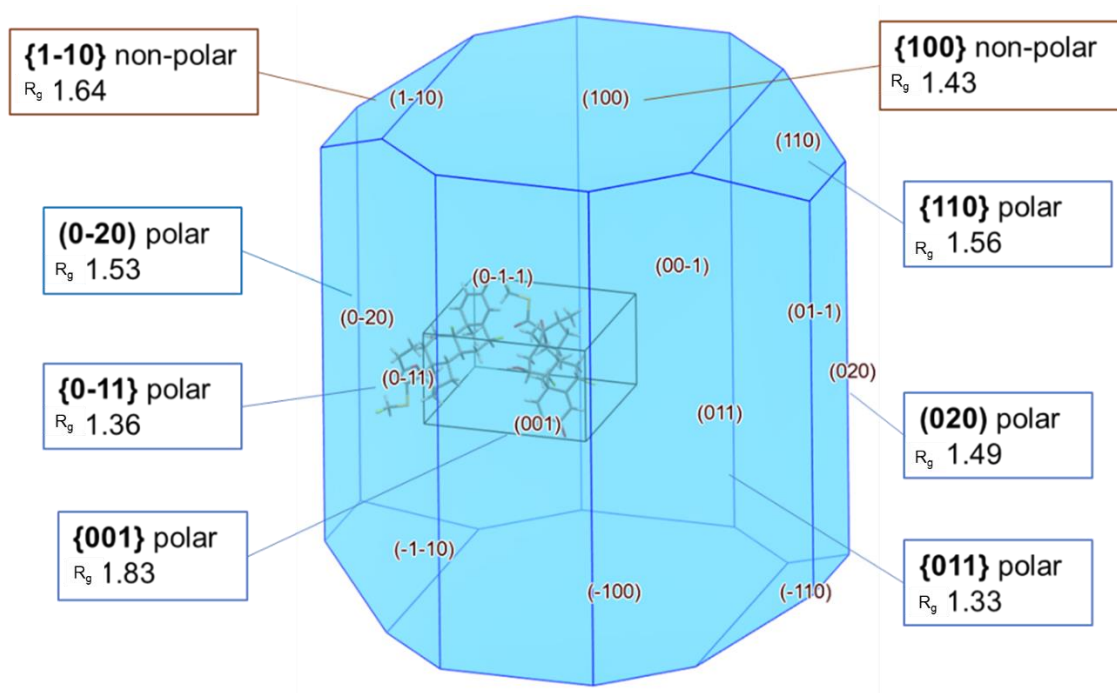


Figure 6-17 Predicted morphology of FP with faces classified as either polar or non-polar based on the observed surface chemistry. The symbol R_g represents surface roughness from measured rugosity. Note some surface properties are labelled by their form, i.e., {100} represents (100) & (-100) as both faces have the same properties. Whereas faces (020) and (0-20) are labelled individually as their properties varied.

6.4 FP Molecule – Solvent Interactions

This section investigates which parts of an FP molecule show the strongest interaction with a secondary molecule, including an FP solute and other solvent molecules.

6.4.1 FP – FP

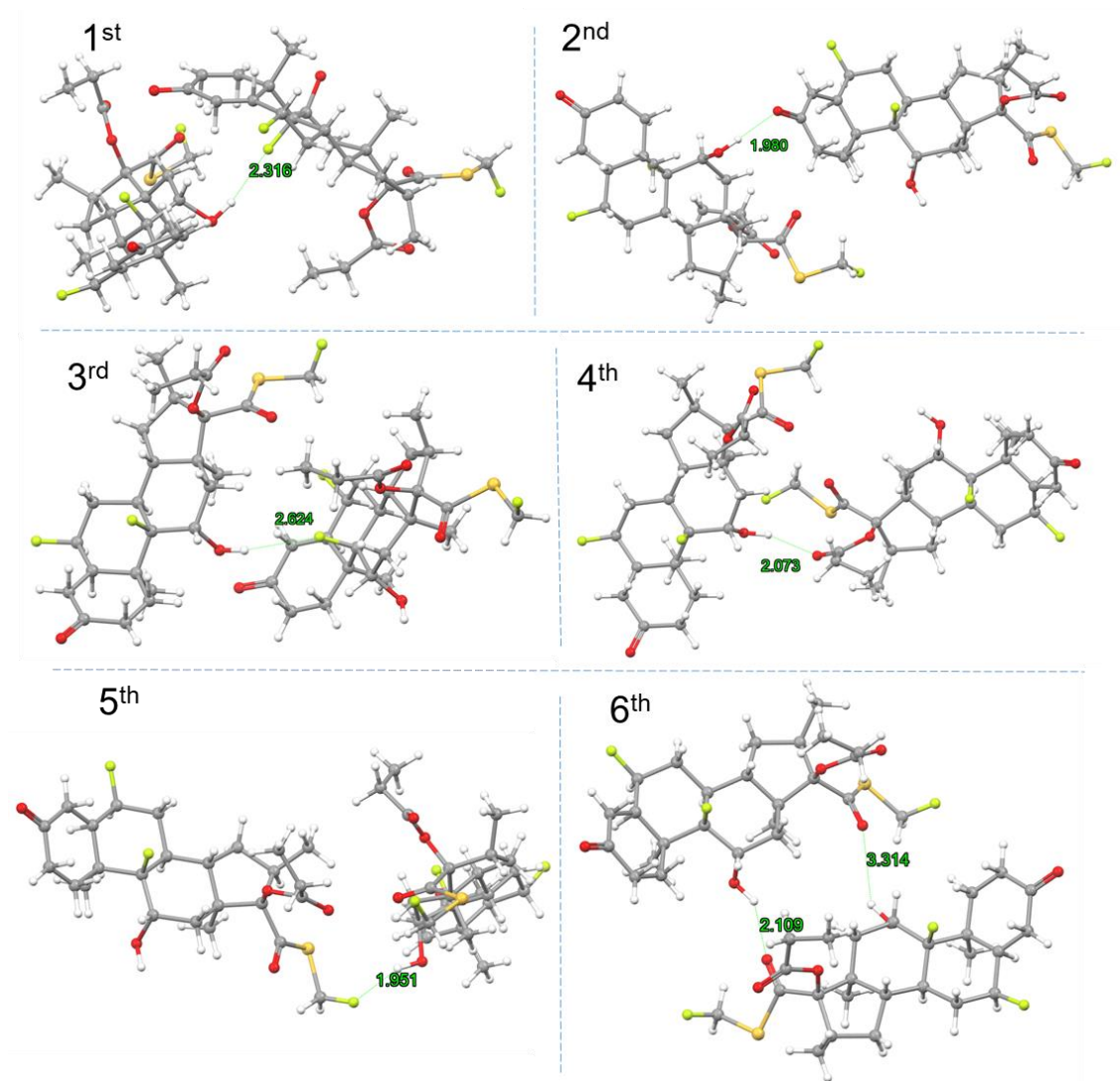


Figure 6-18 Top six strongest interactions of FP interacting with FP. Each interaction is from a unique grid point.

All of the top 5 strongest interactions appear to show H-bonds between two FP molecules, with a distance of <2.6 Å between the hydroxyl's donated hydrogen and the electronegative acceptor. The strongest interaction is between the hydroxyl and the fluorine atom of β section that is near to the hydroxyl group. This is like the H-bond synthon B seen in Form II of FP, except with the different fluorine atom. Interestingly, only the second strongest resembles the same H-bond shown in Form I's crystal lattice, between the hydroxyl and carbonyl of the α section. The third strongest shows an H-bond between the same atom pair as the first, with similar molecule orientations to Form

I's synthon A, there is a large contact area between the two molecules, however the H-bond between the hydroxyl group and fluorine distorts the orientation.

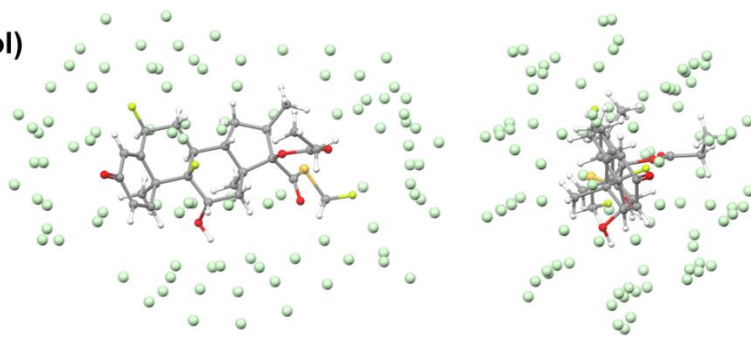
6.4.2 FP – Solvent

The number of unique grid points with interaction energies higher than set values in Table 6-4 highlight how favourable it is for solvent molecules to surround FP. Results reflect FP's poor solubility in water as it has the fewest number of grid points. Water forms strong interactions in localised areas of FP, Figure 6-19 shows it struggles to form interactions with the non-polar section. In contrast, ethanol dissolves FP far better and achieves a greater number of grid points with strong interactions in Table 6-4 and are located more evenly across FP in Figure 6-19. There are fewer interactions between HFA-FP that are stronger than -3 kcal/mol which implies the solubility of FP in HFA is probably lower. It is worth noting the predicted values do not account for structuring of liquids themselves, so the results are best used as a comparative tool.

Table 6-4 Number of unique grid points per solvent with energies greater than the specified values for interactions between FP-solvent.

Interaction Energies (kCal/mol)	No. of Grid Points			
	Methanol	Ethanol	Water	HFA
< -1	74	96	45	93
< -3	6	7	5	4

(Ethanol)



(Water)

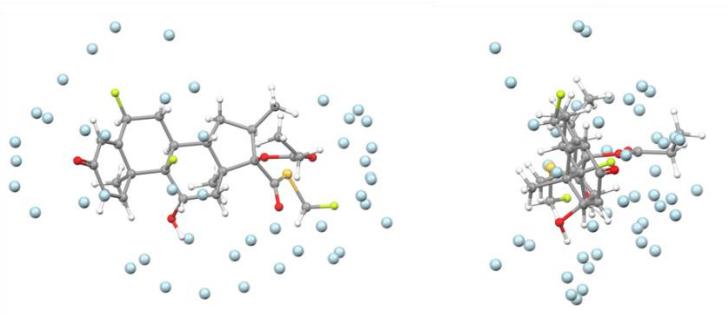


Figure 6-19 Grid point positions with interaction energies greater than -1 kcal/mol, ethanol with green grid points and water with blue grid points.

FP --- Methanol

The hydroxyl group shows a highly electronegative oxygen which draws electrons away from the hydrogen atom, Figure 6-20 (C) shows this creates a negatively charged oxygen and positive hydrogen. The only carbon atom is close to neutral and other hydrogen atoms are positive but not as strongly as the other hydrogen on the hydroxyl. Methanol also interacts as an H-bond donor with the lower fluorine of the β section and prefers H-bond donation to the carbonyl groups of the γ section. Also, it acts as an H-bond acceptor with FP's hydroxyl group.

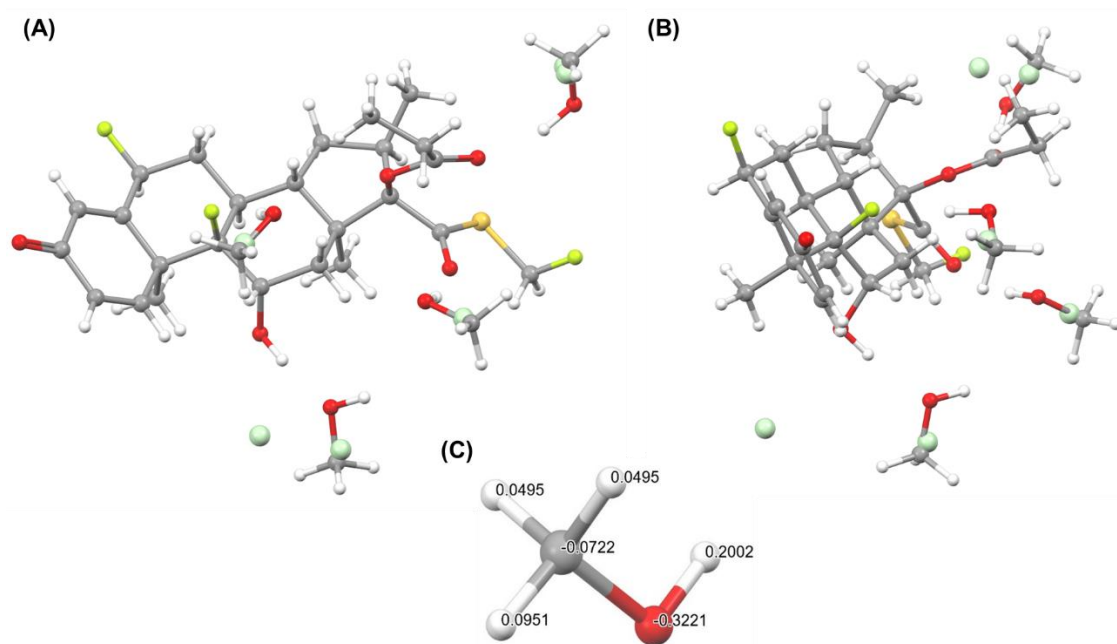


Figure 6-20 (A + B) Two different angles showing examples of the strongest interactions between FP and methanol, grid points of interactions <-3 kcal/mol are also visualised. (C) Partial charges of methanol probe.

FP --- Ethanol

Figure 6-21 (C) shows ethanol's hydroxyl group shows the electronegative oxygen atom draws electrons from the hydrogen, as a result the oxygen has the most negative charge, and the hydrogen atom has the most positive. Dissimilar to methanol, the other hydrogen atoms draw electrons away from their connected carbons, this causes both carbon atoms to have negative charges, especially for the CH_3 carbon. There are 7 grid positions with interaction energies stronger than -3 kcal/mol. H-bond donation occurs with ethanol's hydrogen to the γ section's electronegative carbonyl group and β section's fluorine atom. It can also be seen the oxygen of ethanol accepts FP's hydroxyl hydrogen.

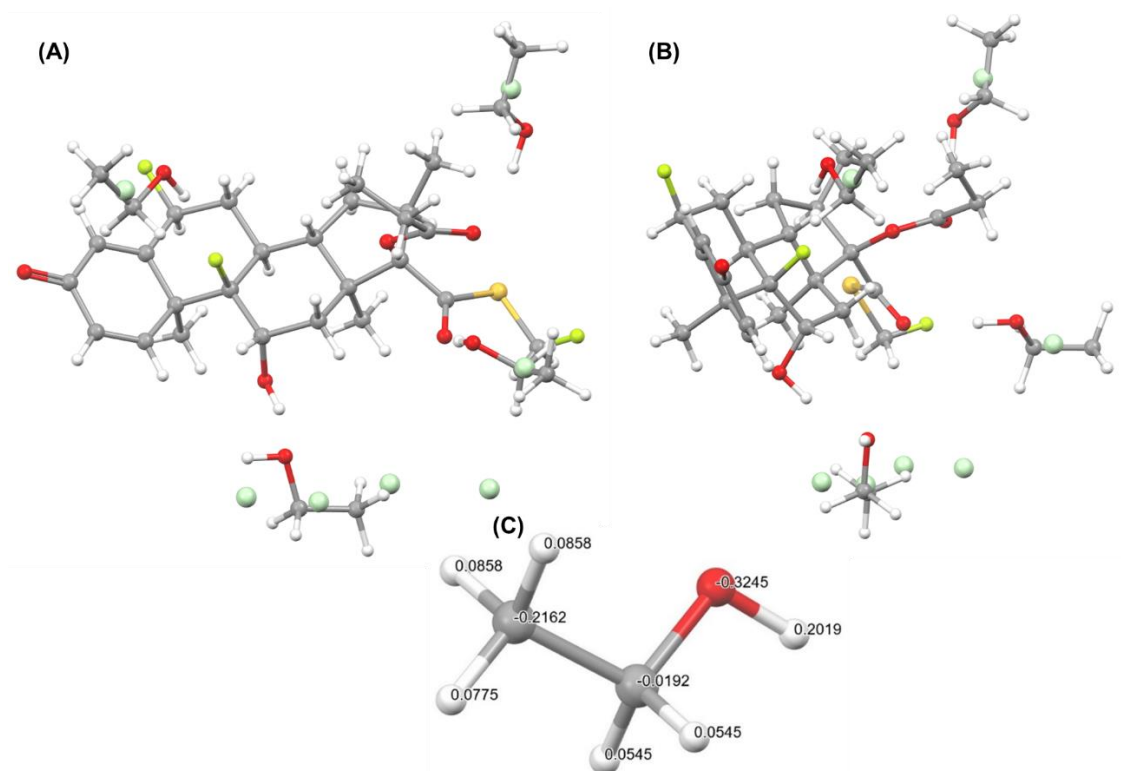


Figure 6-21 (A + B) Two different angles showing examples of the strongest interactions between FP and ethanol, grid points of interactions <-3 kcal/mol are also visualised. (C) Partial charges of ethanol probe.

FP --- Water

The electronegative oxygen has two hydrogens to draw electrons from, causing oxygen to have an even more negative charge compared to the other solvents. Hydrogen atoms have similar level of positive charge as the hydroxyl hydrogens in the ethanol and methanol. The strongest interactions show the positive hydrogen atoms are attracted to the negatively charged carboxyl groups on FP, these are more exposed than the hydroxyl group. Unlike methanol and ethanol, water doesn't show interaction energies stronger than -3 kcal/mol with FP's hydroxyl group.

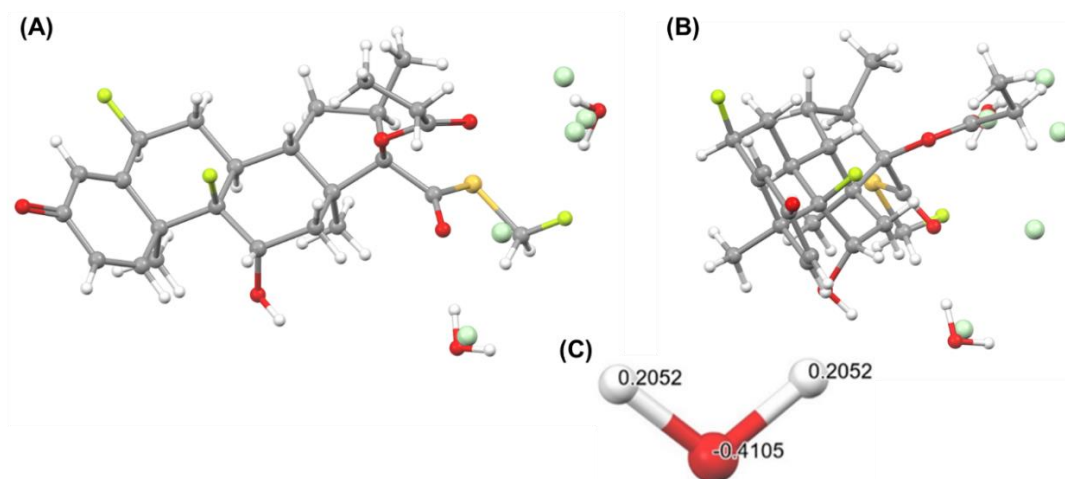


Figure 6-22 (A + B) Two different angles showing examples of the strongest interactions between FP and water, grid points of interactions <-3 kcal/mol are also visualised. (C) Partial charges of water probe.

FP --- HFA-134a

Partial charges of the HFA molecule are shown in Figure 6-23 (C) show fluorine atoms draw away electrons from their bonded atoms, causing them to be negatively charged. The carbon atom in the CF₃ group has a highly positive charge whereas the other carbon is essentially neutral. This polar nature is evident in the top 4 interactions. The positively charged side is attracted to the negatively charged carbonyl groups belonging to FP's α and γ section. HFA's negative side is attracted to FP's positively charged hydroxyl group.

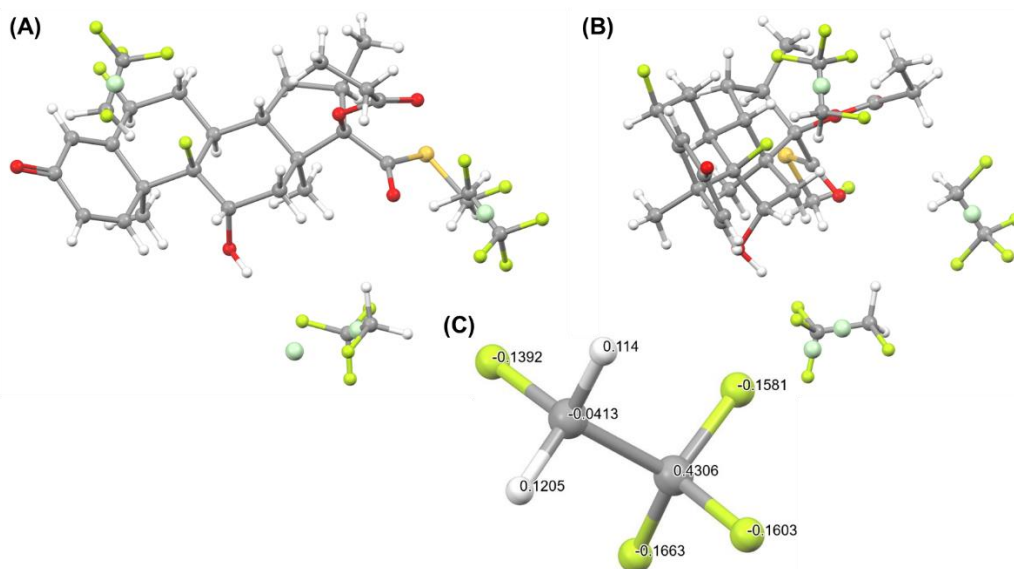


Figure 6-23 (A + B) Two different angles showing examples of the strongest interactions between FP and HFA-134a, grid points of interactions <-3 kcal/mol are also visualised. (C) Partial charges of HFA-134a probe.

6.5 Grid-Based Search of FP Surfaces

Interaction energies were measured between probe molecules and FP's surfaces, this varied depending on exposed functional groups. This investigated how solvent influenced crystal growth and how morphology may affect particle interactions.

6.5.1 Methanol

All faces show a preference for H-bonding, this may be caused by the hydroxyl group representing a large proportion of the methanol molecule. The side faces show stronger a preference for H-bonds over vdW interactions, this difference is clearest in the (011) and (0-11) faces which have a visible gap. The (011) face exposes the hydroxyl and carbonyl-sulphur-fluoro methyl groups, belonging to FP's β and γ sections, respectively. The (0-11) face has the α sections carbonyl group exposed which may form H-bonds. Figure 6-24 shows large undulations in (001) house the methanol molecule for the strongest interaction. An H-bond formed between methanol's hydroxyl and the electronegative fluorine of the γ section of FP, this correlates with the FP-solvent interactions of the previous section.

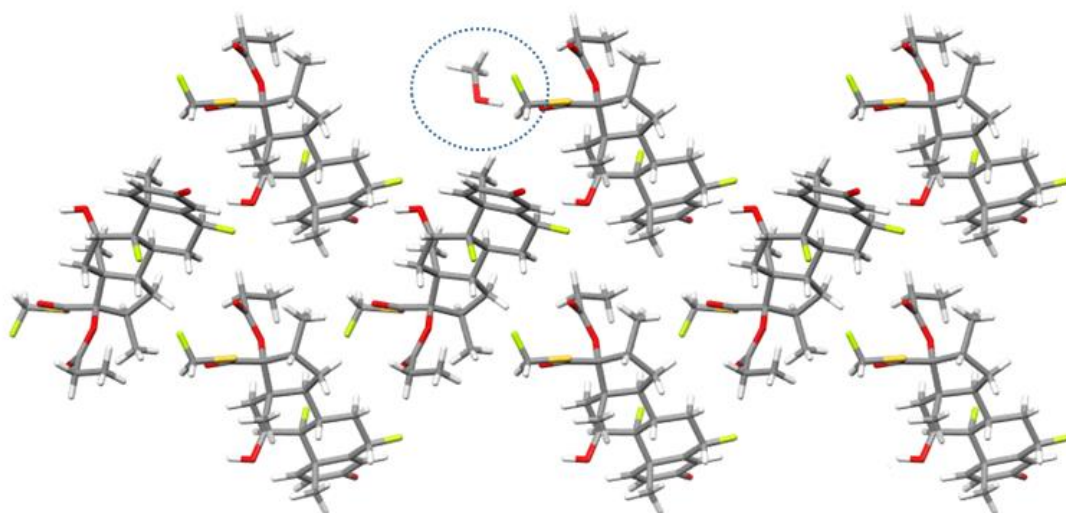


Figure 6-24 Visualisation of the strongest interaction between **methanol** and the (001) surface. The methanol probe has been circled.

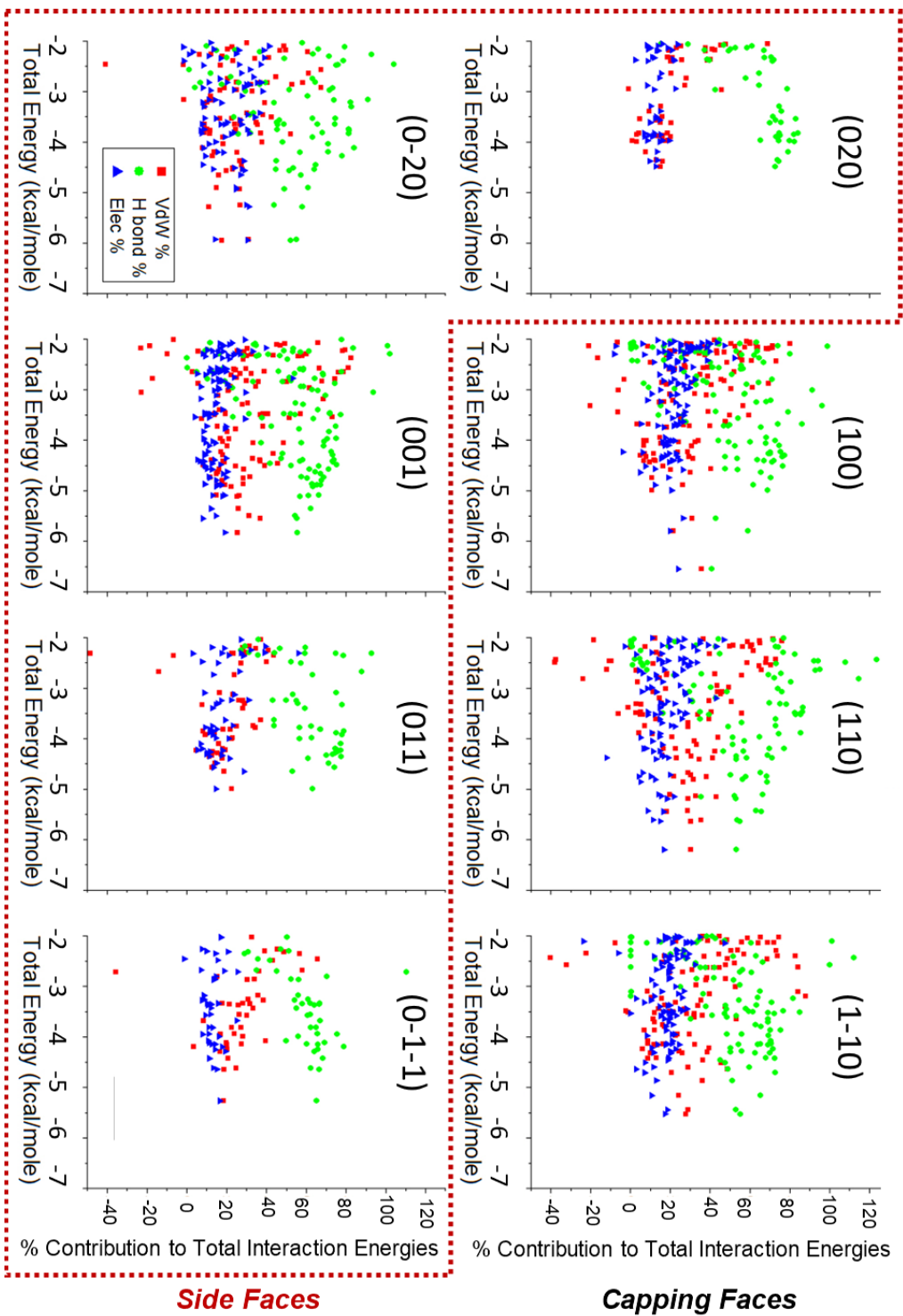


Figure 6-25 Interaction energies of *methanol* probing FP's surfaces with side faces outlined by a dashed line. The x-axis shows total interaction energy and y-axis shows % contribution from different interaction types, shown by red squares for vdW, green circles for H-bonds, blue triangles for electrostatic. Negative % contributions represent repulsive interactions.

6.5.2 Ethanol

It is seen in Figure 6-27 that ethanol's larger molecular mass increases the average interaction energies and van der Waals contribution compared to methanol. The side faces, (011) and (0-11), show a clear distinction for higher H-bond contributions, this was attributed to the increased frequency of exposed polar groups. Visualisation of (011)'s strongest interaction in Figure 6-26 shows an H-bond between the molecule probe and surface's hydroxyl groups.

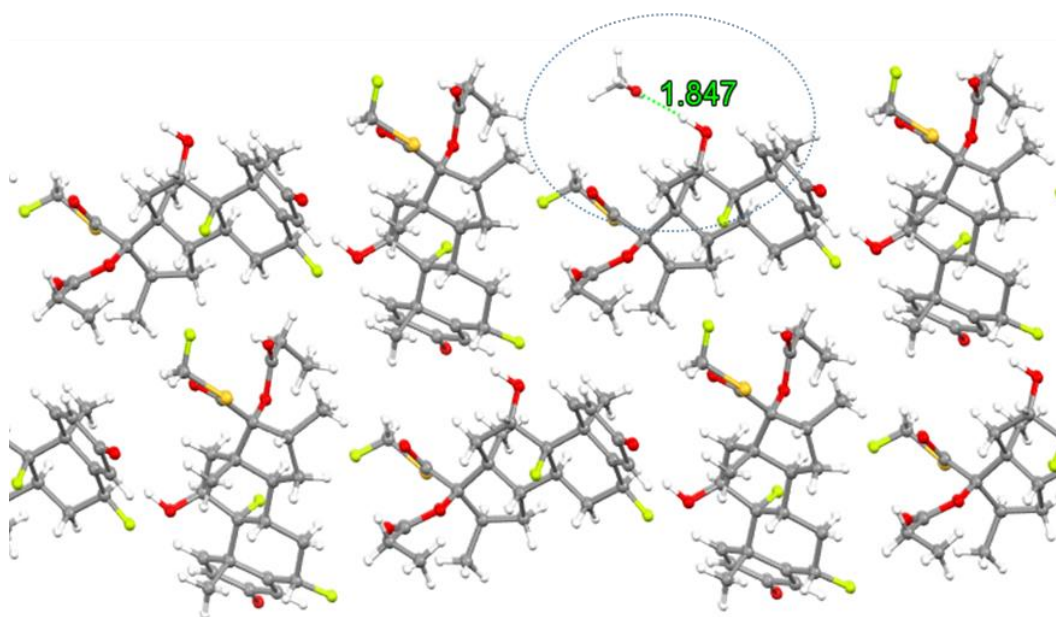


Figure 6-26 Visualisation of the strongest interaction between **ethanol** and the (011) surface. The ethanol probe has been circled.

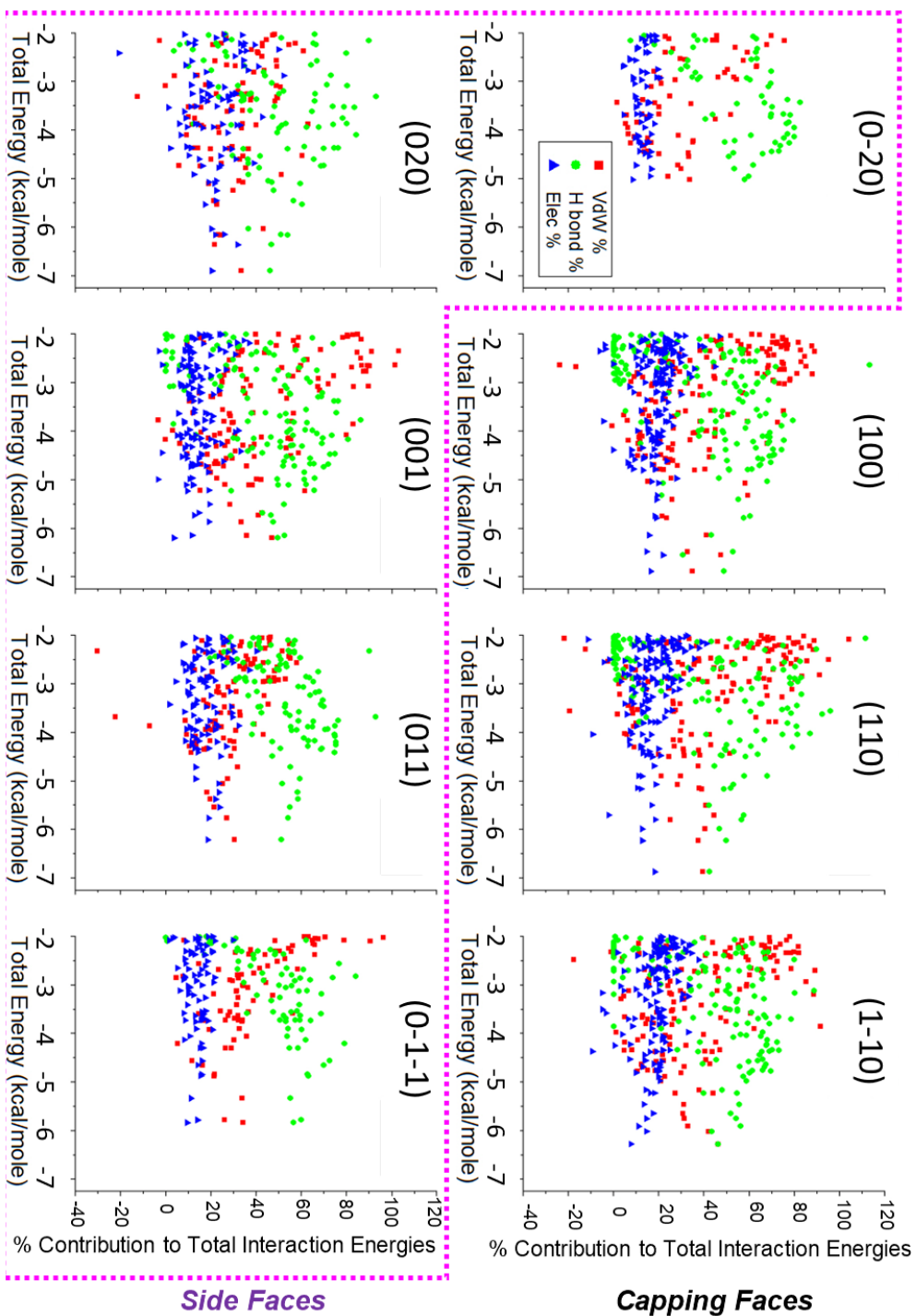
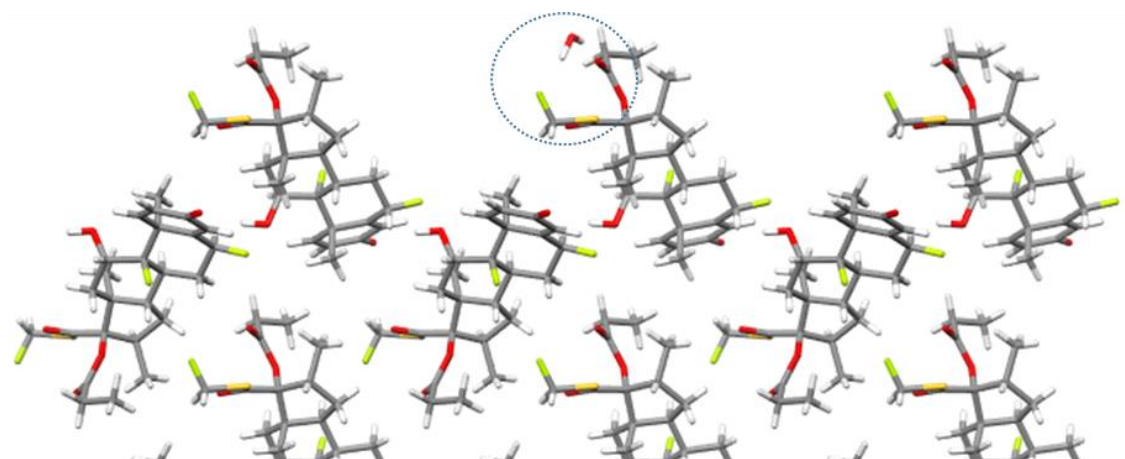


Figure 6-27 Interaction energies of **ethanol** probing FP's surfaces with side faces outlined by a dashed line. The x-axis shows total interaction energy and y-axis shows % contribution from different interaction types, shown by red squares for vdW, green circles for H-bonds, blue triangles for electrostatic. Negative % contributions represent repulsive interactions.

6.5.3 Water

All surfaces in Figure 6-29 show interactions with water are dominated by H-bonding, to such an extent that some vdW contributions are negative due to repulsion between molecules in close proximity. Overall, the face (001) showed the strongest interaction, visualisation in Figure 6-28 showed water would sit in the pockets on the surface and interact with FP's exposed γ section with the carbonyl and fluoro-sulphur-methyl groups. This correlates with the previous section looking showing water preferred to interact with FP's γ section in a molecule-molecule predictions.



*Figure 6-28 Visualisation of the strongest interaction between **water** and the (001) surface. The water probe has been circled.*

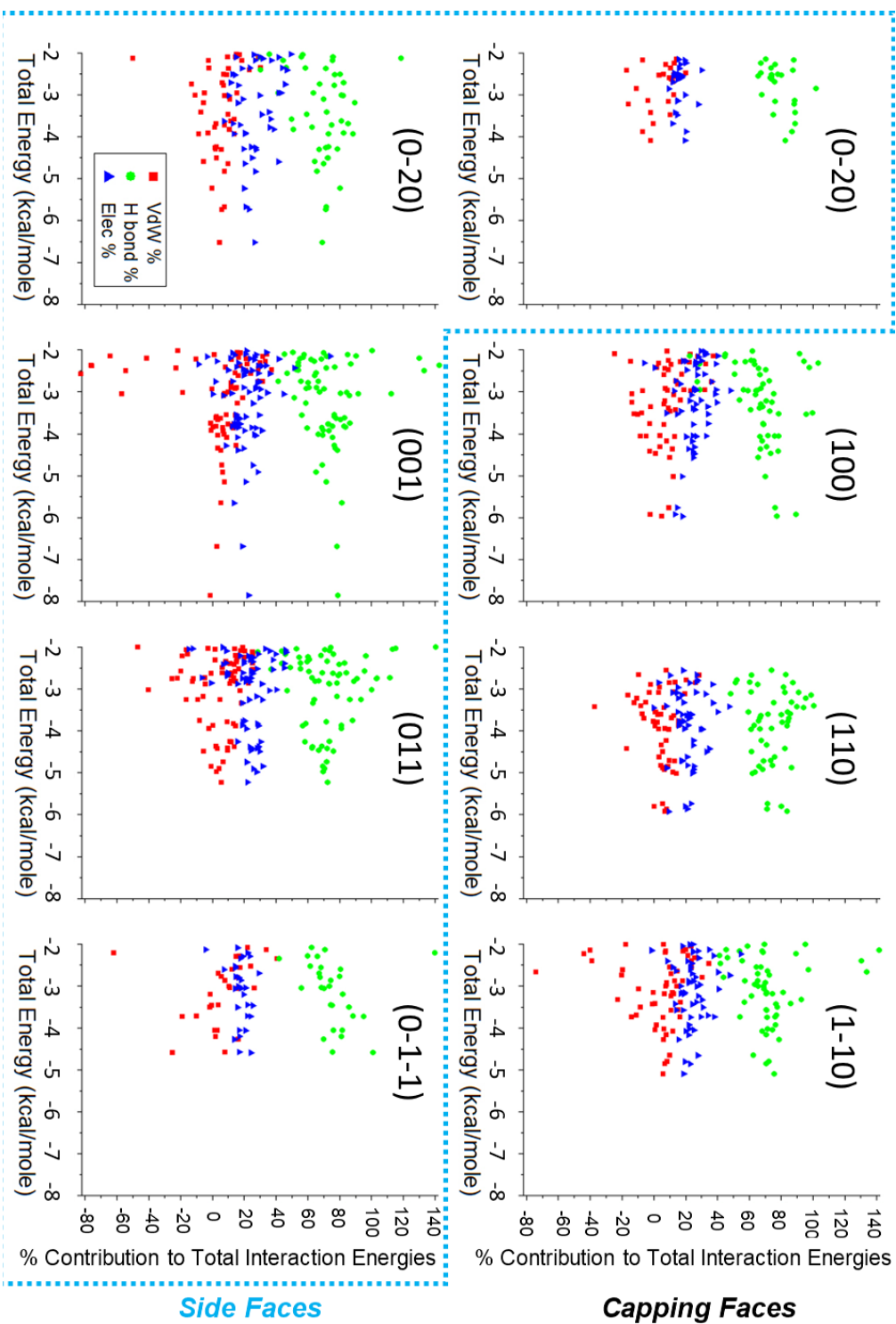


Figure 6-29 Interaction energies of **water** probing FP's surfaces with side faces outlined by a dashed line. The x-axis shows total interaction energy and y-axis shows % contribution from different interaction types, shown by red squares for vdW, green circles for H-bonds, blue triangles for electrostatic. Negative % contributions represent repulsive interactions.

6.5.4 HFA-134a

The average predicted interaction energies shown in Figure 6-31 are stronger than the other solvents due to HFA's larger molecular mass. There is a high contribution of H-bonding with all the surfaces, particularly the (011) face. This is caused by an H-bond interaction between the solvent's CF_3 group and the exposed hydroxyl group, Figure 6-30.

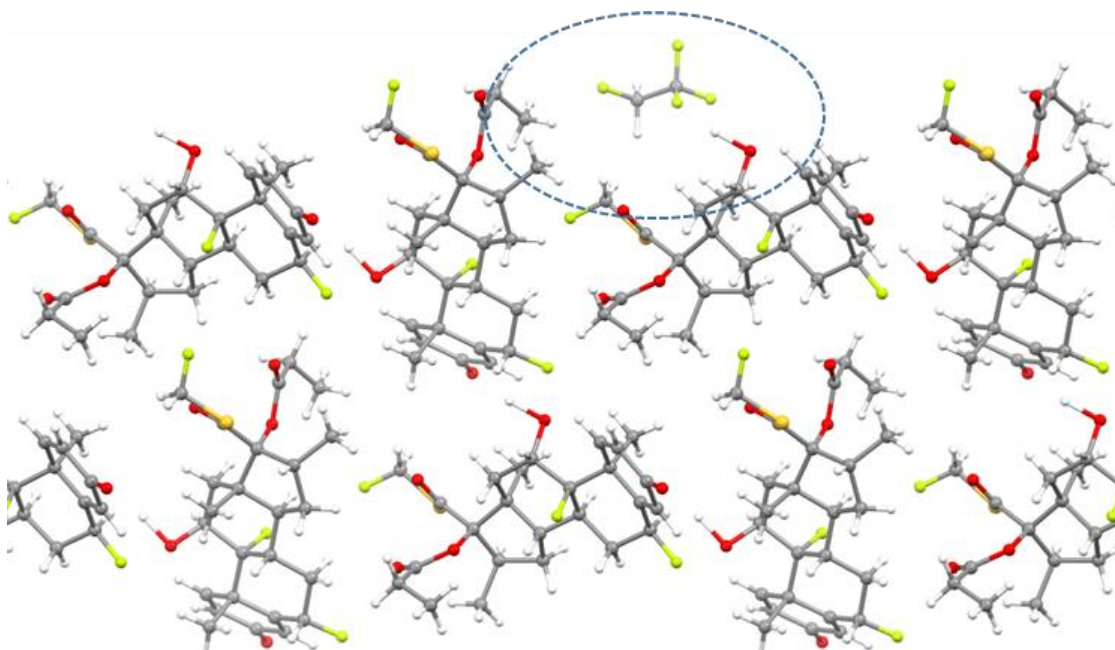


Figure 6-30 Visualisation of strongest interaction between **HFA-134a** and (110) surface. The probe has been circled.

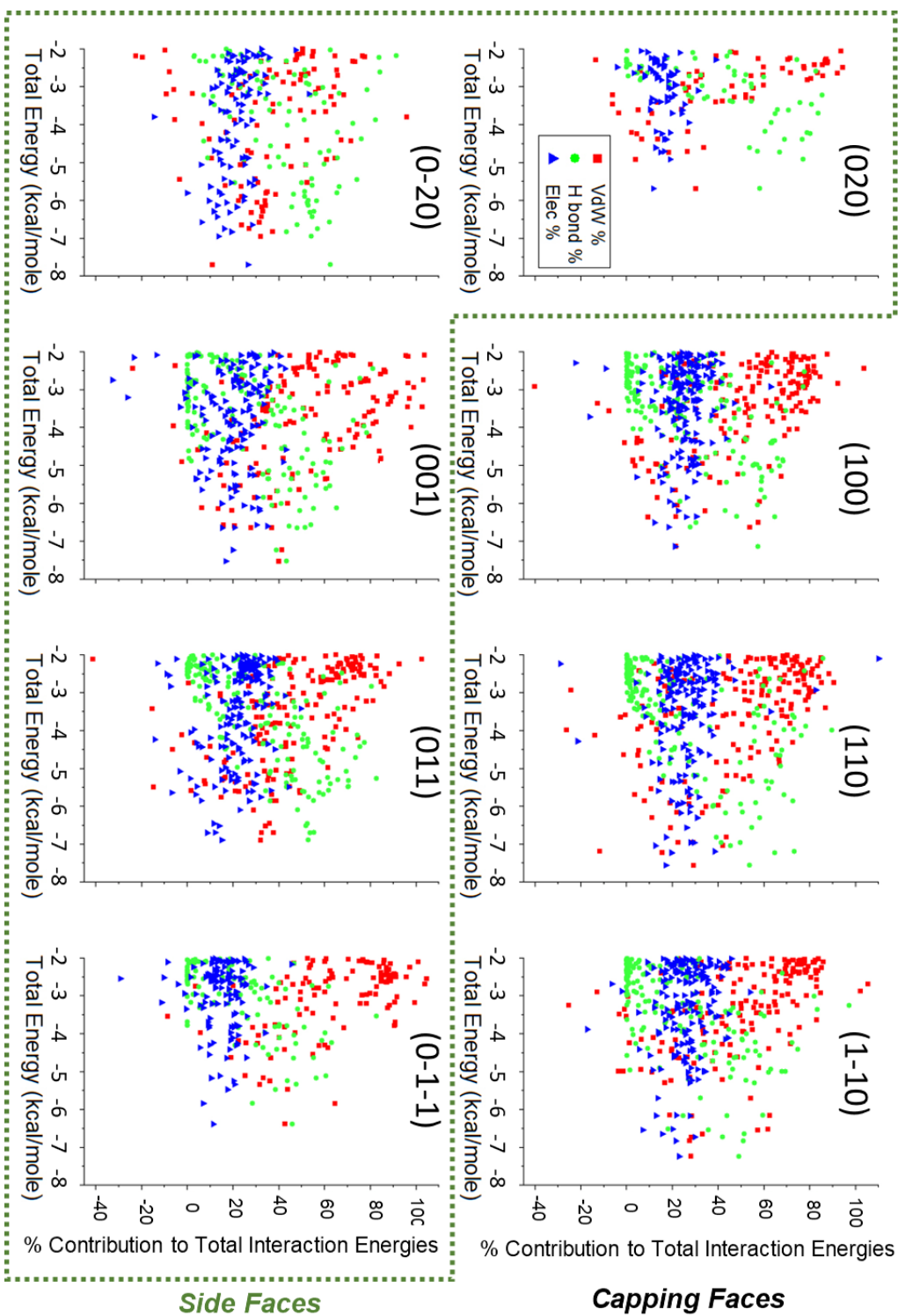
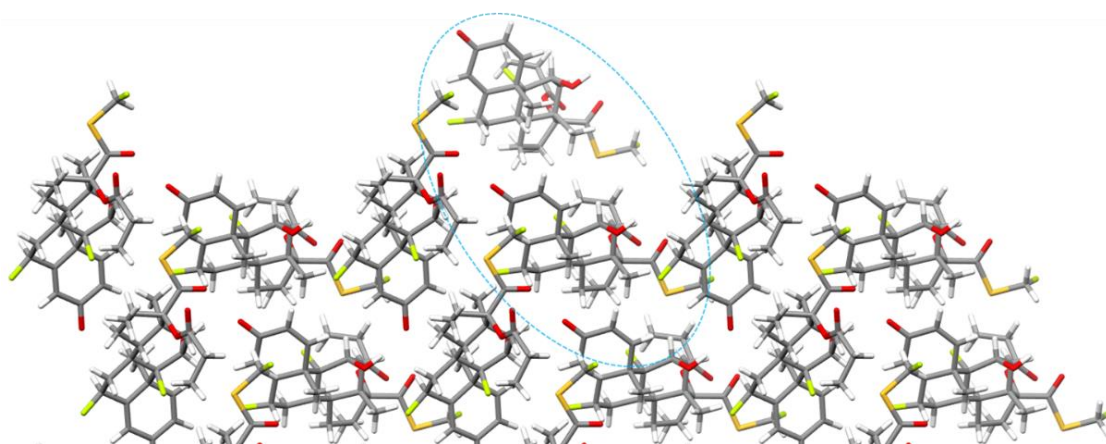


Figure 6-31 Interaction energies of HFA-134a probing FP's surfaces with side faces outlined by a dashed line. The x-axis shows total interaction energy and y-axis shows % contribution from different interaction types, shown by red squares for vdW, green circles for H-bonds, blue triangles for electrostatic. Negative % contributions represent repulsive interactions.

6.5.5 FP Probe

The large molecular mass of FP increases interaction strengths far higher than the solvent probes and causes vdW contributions to dominate for all surfaces. Figure 6-33 shows strongest interactions are far higher on needle capping faces, (100), (110) and (1-10). The α sections carbonyl groups are exposed on these surfaces, and this was shown to produce strong interactions between two FP molecules. Visualisation of face (110) strongest interaction in Figure 6-32 shows the probe molecule matches the orientation of the molecule in the surface beneath. Strong interactions on the capping faces implies they could out compete the rival solvent molecules and promote growth of an elongated morphology. The (011) surface shows a consistently high H-bond percentage which matches the trends shown with the previous solvent probes, this was attributed to the exposed hydroxyl groups. Furthermore, H-bonds also have consistently high percentages for (020) and (0-11), this highlights how synthon C, the H-bond identified in the previous synthon analysis, travels along the [010] direction.



*Figure 6-32 Visualisation of the strongest interaction between **FP** and the (110) surface. The two molecules with similar orientations have been circled.*

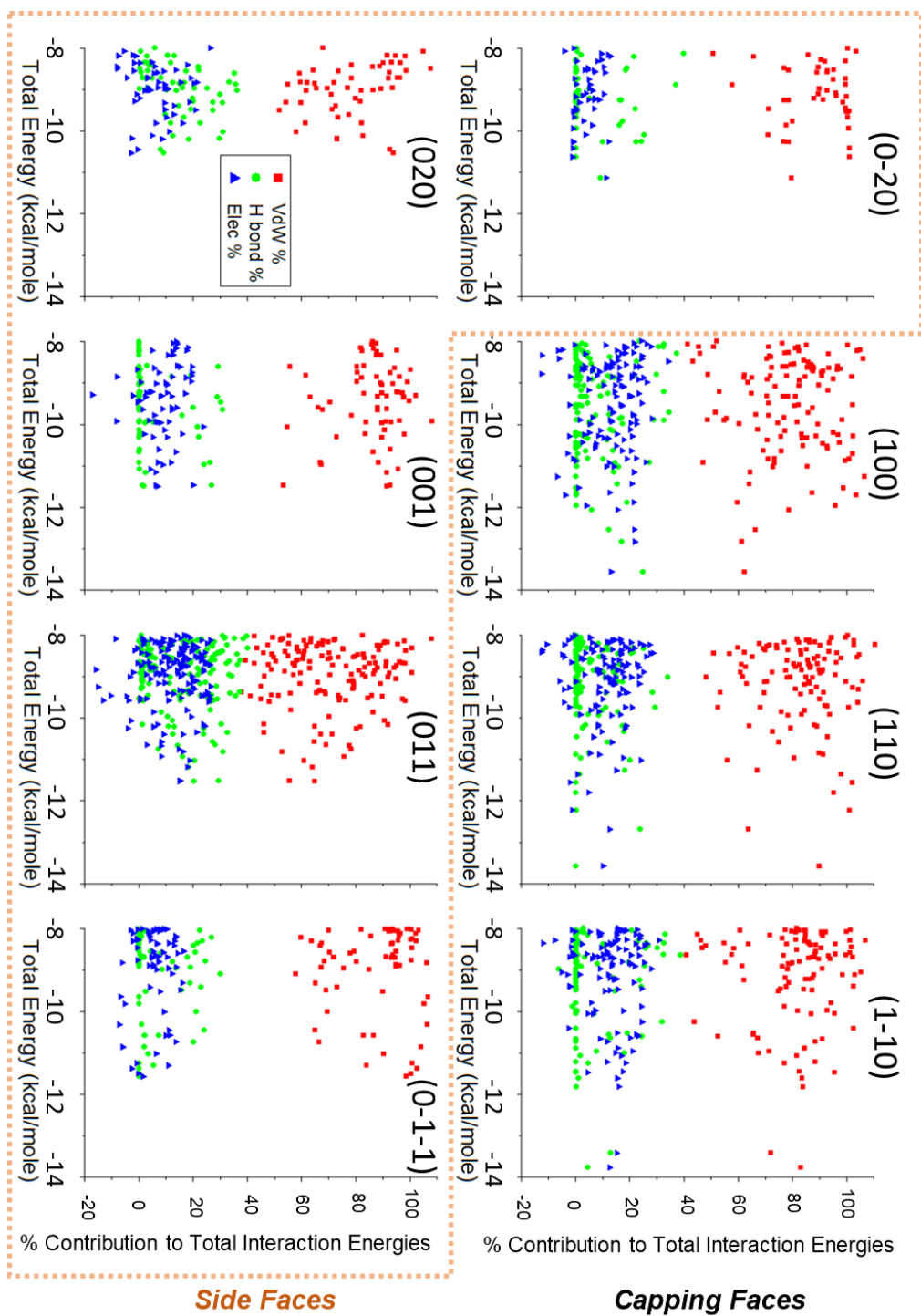


Figure 6-33 Interaction energies of **FP molecule** probing **FP's** surfaces with side faces outlined by a dashed line. The x-axis shows total interaction energy and y-axis shows % contribution from different interaction types, shown by red squares for vdW, green circles for H-bonds, blue triangles for electrostatic. Negative % contributions represent repulsive interactions.

6.5.6 Solvent Influenced Morphology Prediction

The strongest interaction energies of solute and solvent probes on each surface were incorporated into two variations of the attachment energy model. Surface roughness was also accounted for in model 2. Ethanol caused model 1 and 2 to be more elongated like the experimental needle shapes, with a length by height aspect ratio of 1.19. Both model 1 and 2 show (110) is exposed, implying it could be the angled capping face seen experimentally. Also, (001) has a larger surface area, especially in model 2. This was caused by a slower growth rate and suggests these are the wide faces seen in experimental crystals. (020) is larger in both the new models, despite it being thought to have grown out of experimental crystals. This was likely caused the models high growth rate of their adjacent faces, (011) and (0-11).

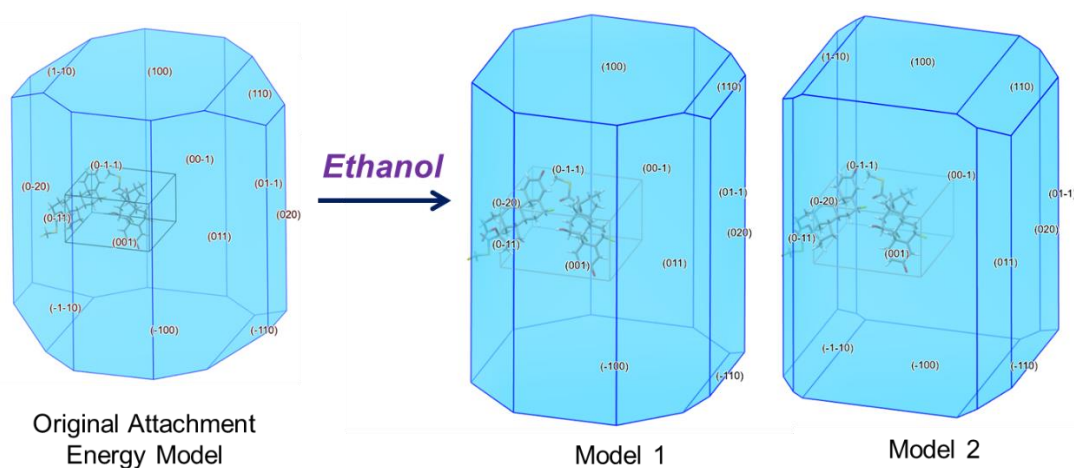


Figure 6-34 Attachment energy morphology modified by incorporating **ethanol** probe interaction energies, Model 1. Model 2 also accounted for surface roughness.

Methanol influenced morphologies show similar faces as the ethanol predictions. For example, the (001) appears to be wider. However, the crystals appear stubbier compared to ethanol with an aspect ratio of 1.11, contrary to what was seen in the experimental work where the methanol crystals had high aspect ratios.

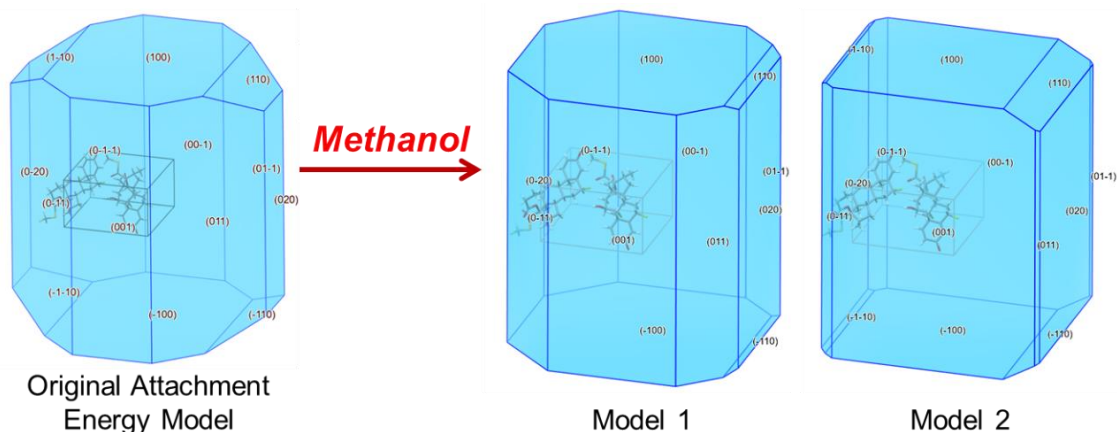


Figure 6-35 Attachment energy morphology modified by incorporating **methanol** probe interaction energies, Model 1. Model 2 also accounted for surface roughness.

FP is highly insoluble in water, so this prediction is more to see how water present may impact morphology formation. Overall, the morphologies appear slightly more elongated with an aspect ratio of 1.18. In Figure 6-36, the (001) and (020) surfaces represent the first and second largest areas, respectively. Which implies water inhibits the growth of these faces. Capping faces show the (110) face is exposed, this matches what is seen experimentally and suggest water leads to the angled capping face. Also, {111} was shown in these morphologies for the first time in the predictions.

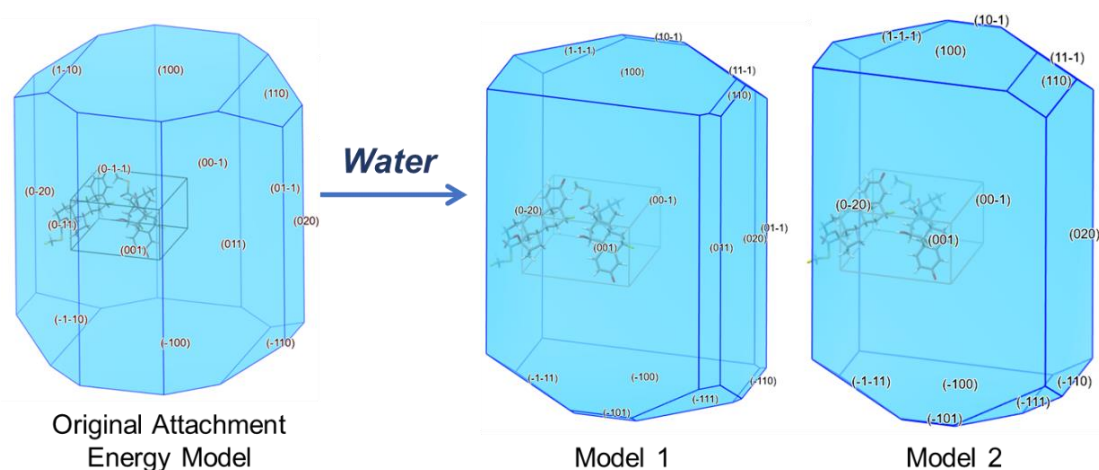


Figure 6-36 Attachment energy morphology modified by incorporating **water** probe interaction energies, Model 1. Model 2 also accounted for surface roughness.

To summarise, the solvent mediated morphology predictions show some resemblance to the experimental crystals. For example, they had a slightly higher aspect ratio compared to the original attachment energy model. But the new shapes were not as elongated because the model did not account for the kinetics of crystal growth, i.e., the

supersaturation. Solvent influenced models showed the (001) face was larger and wider. Its growth rate was lowered due to low energy solute attachment, strong solvent interactions and having the highest rugosity. The (110) surfaces were present on capping faces, like the experimental crystal shapes. Strong solvent interactions on (110) inhibited growth, meanwhile the (1-10) face grew at a comparatively faster rate. Some differences were seen with recrystallised samples, such the (020) surface being larger. Its growth rate was slower due to the low solute interaction energy and high solvent interaction energy, also relatively high rugosity of the surface. As a result, their adjacent faces, (011) and (0-11), had a higher growth rate in the models.

6.5.7 Morphology Effect on Particle Interactions

FP and HFA-134a molecule probes were used to measure the cohesive and wetting interaction energies, respectively. The average energy was predicted for the three different morphologies shown in Figure 6-37. These included the original attachment energy model and the needle morphology fitted to experimental crystals. A platelet morphology was proposed to represent micronized FP particles, these resembled elongated platelets in previous SEM images (Murnane et al., 2008a) which were used as guidance to modify the attachment energy morphology. The (011) face showed minimal molecular overlap and it had the second smallest attachment energy. Layers with smooth molecular overlapping are believed to have higher probabilities of being a slip plane (Ibrahim et al., 2022). It has also been hypothesised that cleavage planes are more likely in planes with lower attachment energy (Roberts et al., 1994). Therefore, (011) appeared to be the most likely slip plane and it dominated the surface area of the proposed platelet morphology in Figure 6-37. It should be noted, this method predicting micronized particles may be limited as it does not account for the high energy surfaces or amorphous content which can be exposed during milling.

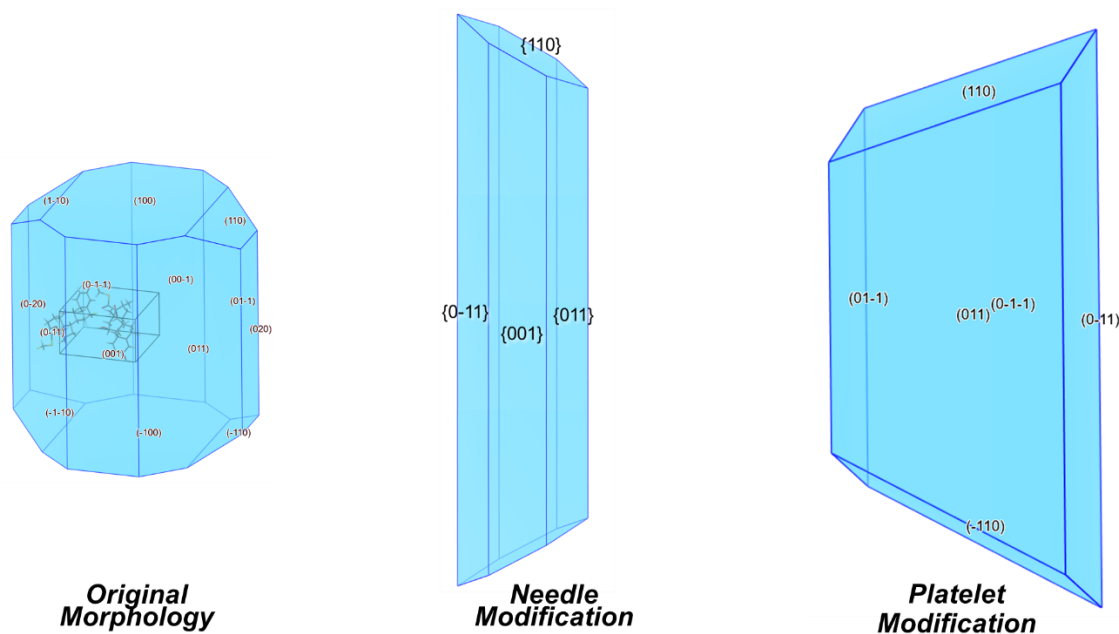


Figure 6-37 Varied surface area % of particle morphologies: Original attachment energy model, experimentally fitted needle shaped modification, and Platelet modification fitted to SEM images of micronized particles.

Interaction energies were weighted based on surface area % of each face and average values of each morphology are listed in Table 6-5. A more detailed version of the table is provided in the appendix section A.4. Both cohesive and wetting interaction types show the original morphology has the highest average energy. The average cohesive interactions of FP show the most variation between morphologies. FP probes formed strongest interactions with the capping faces, (100), (110), (1-10). These represented a smaller portion of total surface area in the needle and platelet morphology. Therefore, average cohesive energies were reduced compared to the original morphology.

Table 6-5 Average interaction energy of FP and HFA-134a probing different FP crystal surfaces. Weighted based on surface area % of different morphologies.

Morphology:	Original	Needle	Platelet
Average Cohesion Interaction Energy - FP Probe (kcal/mol)	-12.10	-11.57	-11.87
Average Wetting Interaction Energy - HFA Probe (kcal/mol)	-6.99	-6.98	-6.86

In contrast to cohesive interactions, the average wetting interactions with HFA-134a were relatively consistent. HFA-134a probe interaction energies were similar for all surfaces of FP, this means average wetting interactions were relatively consistent across the different particle shapes. Overall, this has shown how different proportions of crystal surfaces can change particle interactions with formulation materials.

6.6 Summary and Discussion

First, the external morphology of form I FP was predicted using the attachment energy method. This advantageously applied force field potentials to identify crystal surfaces from their underlying interactions. The prediction did not account for the kinetics of crystallisation, instead it predicted the equilibrium growth rate of each surface. The attachment energy model assumes consistent wetting on all faces, whereas in reality, solvents have different propensity to interact with each face which can change the supersaturation, and hence growth of each face. The predicted morphology proposed was somewhat elongated shape, but far from needle, and had an octagonal profile.

All crystals produced experimentally through slow evaporation were the form I polymorph, but their shapes differed from the attachment energy model. The experimentally formed crystals were needle shaped, with defined facets in the hexagonal profile style, and with a slanted capping face. This corresponded to previous examples showing FP formed needle shaped crystals (Bártová et al., 2022) (Murnane et al., 2008a) (Kubavat et al., 2012). However, it was not clear from the previous SEM images if the morphology had hexagonal profiles or an angled capping face.

By understanding the underlying intermolecular interactions and using grid-based search tools to analyse the surface chemistries, it was possible to speculate how the equilibrium morphology of the attachment energy model was modified to resemble the experimental crystals. It was believed the elongated shape was caused by the non-polar, highly attractive interaction, synthon A, which grew in the [100] direction. Needle crystal shapes from other large APIs have also been dictated by their strongest synthons growing in the needle capping directions (Turner et al., 2019) (Wang et al., 2021).

Surface chemistry analysis concluded that the (1-10) and (100) capping faces were more non-polar in nature, largely due to the dominance of synthon A growing in the [100] direction. The predicted morphology's side faces appeared comparatively polar. As a result, polar protic methanol and ethanol showed higher H-bond interactions on the side faces compared to capping faces. The distinction was more obvious with methanol interactions due to its lower vdW contribution. For example, the (011) and {0-1-1} side surfaces showed exposed polar groups. These produced consistently high H-bond percentage for all solvent probes and the FP solute probe. H-bonding interaction, synthon C, contributes to the growth of these surfaces as it travelled in the [010] direction. Polar protic solvent presence appeared to limit H-bond formation, and therefore promoting morphology elongation by hindering growth of side faces. This

echoes previous investigations into ibuprofen where more polar aprotic solvents were theorised to favourably adsorb onto faces that showed more H-bond extrinsic synthons, and subsequently reduced their growth rates (Nguyen et al., 2017). The results of complementary grid-based search investigations backed up these claims, with more polar solvents showing stronger interactions to faces that grew via H-bonding (Rosbottom et al., 2018).

Other side surfaces, (001) and (020), shared similar interaction energies with all solvents, implying their growth would be affected in the same manner. However, the higher rugosity of (001) meant small solvents, like methanol and water, became lodged within the surface valleys. The trapping of solvent may have interrupted solute molecules from attaching and resulted in an unfavourable growth environment. This was also theorised to limit the growth for one of lovastatin's crystal surfaces (Turner et al., 2019). Furthermore, it was also believed the solvent trapping caused growth along the [010] direction to be relatively higher than (001). As a result, the (020) face seen in the original equilibrium prediction had grown out and left the hexagonal profile seen in experimental crystals.

Experimental crystals were measured to have angled capping faces of 28° , this was the same angle when the morphology's capping face was (110) or (1-10). Despite having the same d-spacing and attachment energy values, the two forms showed different surface chemistries. The (110) surface was the more polar of the pair, showing stronger interaction energies with polar protic solvents. Therefore, it was proposed that polar protic solvents preferably adsorbed to (110) surfaces and inhibited their growth, meanwhile the (1-10) face grew at a relatively faster rate.

The solvent probe to surface interaction energies were incorporated into morphology predictions to help include solvent effects on crystallisation kinetics. This accentuated some of the faces which were believed to appear larger in some experimental crystals. For example, morphologies became slightly more elongated due to the favoured interactions on the side faces inhibiting growth. Likewise, the (001) surface was larger and wider due to stronger solvent interactions. These modified predictions also showed slanted capping surface (110) represented a larger surface area than (1-10). However, the (020) surface became larger due to high solvent interaction energy. This shows the limitations of these solvent modified predictions as they did not account for experimental supersaturation.

The cohesion and wetting of different shaped particles were measured using the grid-based search tool. Average cohesion interaction energies were lowered when particle shaped had a smaller proportion of capping faces. The average wetting interaction

energies did not differ much with variations particle shape. However, these models did not account for the amorphous content or surfaces not present in the morphology prediction that may arise after milling.

6.7 Conclusion

The predicted external morphology of Form I FP partially resembled the experimentally recrystallized elongated samples. Experimental crystals also showed an angled capping face which correlated to the identified (110) face. The attachment energy prediction was an equilibrium model that did not account for growth kinetics. The influence of growth solvent was investigated with grid-based search tools which showed polar solvents preferably adsorbed to the crystal's side faces. Solvent probes appeared to sit in valleys of the (001) surface, which may have inhibited solute attachment and thus growth in that direction. Solvent probes were comparatively less attracted to the non-polar capping faces, which were left as a favourable growth environment for the strongest intermolecular interaction, synthon A, to attach.

The attachment energy model was modified to a new needle and platelet morphology, this made it possible investigate the effect of particle shape on formulation interactions. Particles with a smaller portion of capping faces were found to have lower cohesive interaction energies with FP probes. While, varying the particle shape did not cause big changes in wetting with HFA-134a probes.

Chapter 7: Conclusions and Future Work

Summary: The main findings from this thesis are concluded with respect to the original research objectives. Also, a future workflow is suggested that can build upon the results of this study.

Chapter 7: Conclusions and Future Work

7.1 Introduction

This final chapter concludes the main findings from investigating inter particulate interactions in suspension MDI formulations using molecular modelling techniques. In this report, the propellant HFA-134 and API fluticasone propionate were studied separately, before bringing them together to investigate interactions within a suspension MDI formulation. The main conclusions of each section are summarised, then, the final outcomes of this report are reviewed with respect to the original research question, additionally, suggestions for future work were also made.

7.2 Conclusions of this study

7.2.1 Propellant HFA-134a

Both chapters 3 and 4 studied HFA-134a's intermolecular structuring using molecular modelling and showed a link between phases at different temperatures. The presence of hydrogen atoms in HFA propellants caused them to have a higher polarity compared to CFC predecessors. It was possible to see how this dipole affected the crystal structure of HFA-134a's low temperature, monoclinic phase, which had been previously determined through powder x-ray diffraction. For example, calculations using force field potentials showed molecules in the strongest interactions were arranged to maximise their dipole-dipole attractions. This resulted in the formation of C-H---F 'weak' H-bonds. The higher temperature, cubic polymorph was proposed to be the $Im\bar{3}m$ space group, and it was believed that weak H-bonds facilitated the transition to the lower temperature monoclinic phase.

7.2.2 Solid Drug Fluticasone Propionate

Chapters 5 and 6 are referred to in this sub-section, they both investigated FP using molecular modelling. Initially, a crystal profile of the API understood why form I of FP was more stable than the meta-stable form II. Their crystal structures had previously been determined, and the molecular conformations were similar in both forms, largely due to the relatively inflexible corticosteroid skeleton. Empirical force fields predicted form I had a stronger lattice energy compared to form II, at -40 and -25 kcal/mol, respectively. Despite sharing similar conformations, form II's density was lower than form I due to a different packing arrangement. Form II was believed to have weaker interactions due to its lower density, which increased the intermolecular distance. Synthon A was the strongest intermolecular interaction in form I. It was 50 % stronger

than the second most attractive and consisted of one FP molecule packing on top of another.

The morphology of form I FP was predicted via the attachment energy method. This model did not account for the kinetics of crystallisation, rather each surface had an equilibrium growth rate. In comparison, experimental crystals were more elongated as solvents influenced growth kinetics. Nevertheless, this method was a valuable way of investigating FP's crystal surfaces. From the morphological analysis, synthon A was identified as contributing to growth along the length of the needle. Grid-based search method was used to measure the interaction energies between molecules probing the different crystal surfaces of FP. It was observed that polar protic solvents favourably adsorbed to side faces, which may hinder solute dissolution and growth. Meanwhile, the non-polar synthon A interactions could attach to the capping faces more easily, and hence lead to more elongated morphology.

7.2.3 Suspension Formulation Interactions

This investigation aimed to see how different particulate shapes may have affected interactions with other FP particulates or wetting with the propellant HFA-134a. The predicted morphology was adapted to correlate with experimental crystals, showing a more elongated shape, hexagonal profile and slanted capping face. Also, a micronized platelet morphology was proposed, it was assumed the crystal would slip along the plane with minimal molecular overlap. Interaction energies between molecule probes and the particle surfaces were predicted using the grid-based search method. These were weighted to the surface area % and produced an average interaction energy value per particle shape. Elongated showed minimal cohesive interactions due to capping faces representing a smaller proportion. Results of HFA-134a wetting was similar for all particle shapes, implying the shape did not matter.

7.3 Review of Original Research Objectives

Research Question:

How can molecular modelling techniques investigate inter-particulate interactions between MDI suspension ingredients, such as those affecting the structure of propellants and those which determine drug particulate morphology?

Research Objectives:

Investigate the type and strength of intermolecular interactions in pure propellant. Evaluate how they change across a temperature range.

Solid-state analysis of HFA-134a showed molecules arranged efficiently to minimise steric repulsions, they also formed weak H-bonds between polar parts. MD simulations of the liquid showed its structure had increased probability of arranging in a similar manner to the solid when temperature was reduced. Both the liquid and solid showed favoured compatibility of two CFH₂ groups. There was an increased formation of weak H-bonds when the liquid temperature was reduced, although they were not believed to be strong enough to affect molecule directionality. Having learnt about the intermolecular structuring of pure HFA-134a, it would be interesting to see how the structure changes when other ingredients are included.

From a first principles approach, produce a solid-state profile of an inhalation drug. Identify molecular descriptors and determine the strength of intermolecular interactions in its crystal structure.

A thorough analysis of fluticasone propionate's two known polymorphs, Form I and II, was achieved. The molecular conformations were similar in both forms. This meant both crystal structures shared an equivalent strongest intermolecular interaction, it showed two molecules stacking on top of each other. This interaction was mostly vdW in nature and was by far the strongest interaction within Form I.

Predict the drug's external morphology. Hypothesise which crystal faces will be present in particles within MDI suspensions.

The morphology of Form I fluticasone propionate was predicted, the identified surfaces correlated with crystals formed experimentally. The elongation of experimental crystals was attributed to the strongest synthon seen in the solid-state profile. Morphologies were modified based on experimentally recrystallised and micronized samples. Surface analysis helped with these proposals.

Investigate wetting of particle surfaces with liquid propellant and determine how the propellants structuring is affected by different chemistries of crystal faces.

A grid-search tool helped analyse the difference in crystal faces and quantify the tendency for a molecule to interact. The morphology's side faces appeared to be more polar in nature and they showed higher interaction energies when probed with polar solvents. Results also identified surfaces containing 'valleys' would act as pockets for solvent molecule probes. It was suggested that these favourable solvent interactions promoted the growth of elongated crystals. These simulations only probed surfaces with a single molecule, it would be interesting to perform similar solid-liquid interface investigations using MD. By also investigating the liquid phase structure above a crystal surface, it could be compared to the earlier investigations into liquid structuring of a pure propellant.

Develop a workflow for investigating the effect formulation ingredients and device materials have on particle interactions, including cohesion and adhesion.

The grid-search method showcased an initial way of comparing how particle shape affects wetting with HFA-134a and cohesive interactions with FP. There is scope for development with more advanced investigations. For example, performing the simulations using MD would account for liquid structuring and would enable multiple molecules to probe a surface. The complexity could also be increased by including surfactants, device materials, and representing the surfaces that are present after particles are micronized. Analysis could refer back to the previous investigation of the pure propellant by investigating if the additives form weak H-bonds with HFA-134a.

7.4 Suggestions for Future Work

7.4.1 Future Impact

Generally, new APIs are patented by pharmaceutical companies for a limited time, so it is important that safer drugs are delivered to market faster to maximise their financial revenue. Before it can be distributed, a suitable formulation must be generated. An oral delivery route is the most popular but requires extensive development due to the complexity associated with passing through a digestive tract. Formulations delivered through intravenous injections are faster to develop, although these are less convenient for patients. This promotes selection of the inhalation route as a viable method, it is easier to intake compared to injections or suppositories. Additionally, unlike the oral route, it does not need to pass through the digestion tract which is especially useful for protein-based APIs. The performance of inhalation devices largely depends on the combination of formulation ingredients and the device materials selected. However, no

single formulation fits all due to the different molecular characteristics of each API, so they must be treated case by case. The sheer number of experiments required during development can be very time and resource consuming. Therefore, it is desirable to find ways of speeding up this process, taking advantage of in-silico approaches can help reduce the number of experiments required.

Computational fluid dynamics (CFD) has already established itself as a useful tool for developing inhalation devices, it can model the flow of aerosol out of actuator which helps with designing orifice size and shape. In a similar manner, molecular modelling can also help with development by representing formulation ingredients from a first principles approach and improving one's understanding of a drug's physical properties. However, this encounters a new challenge because there is no universal model that has been developed to investigate MDI problems or comparing suitability of ingredients. Systems are usually designed to investigate specific questions, such as phase separation, particle aggregation, leaching of device materials, and these need to be validated experimentally. Based on the research outcomes of this thesis and the identified potential for development, a workflow has been proposed on how molecular modelling can improve inhalation device development.

7.4.2 Proposed Workflow

The first step is to build a solid-state profile of a new API molecule by evaluating its polarizability, preferred molecular conformation, investigating its intermolecular interactions, and predict its crystal morphology. Following this, interactions between APIs and combinations of ingredients are investigated via a two-stage process, with increasing computational complexity. Initially, a grid-based search method measures the interaction energies between probes around a target molecule or target crystal surface. This stage will identify hotspots of where molecules preferably arrange to maximise intermolecular interactions. Subsequently, the interactions between ingredients will be studied using a relatively computationally more expensive atomistic modelling method, such as MD. This will be capable of investigating the intermolecular structuring of a liquid phase on top of a solid surface. Previous results from the grid search will act as a useful guide for comparing interactions. For example, previous grid-search work looking at para-amino-benzoic acid molecules clustering (Rosbottom et al., 2020) and this aided the analysis of an MD investigation of solute molecules interacting when in a liquid (Rosbottom et al., 2022). An overview of this workflow is illustrated in Figure 7-1.

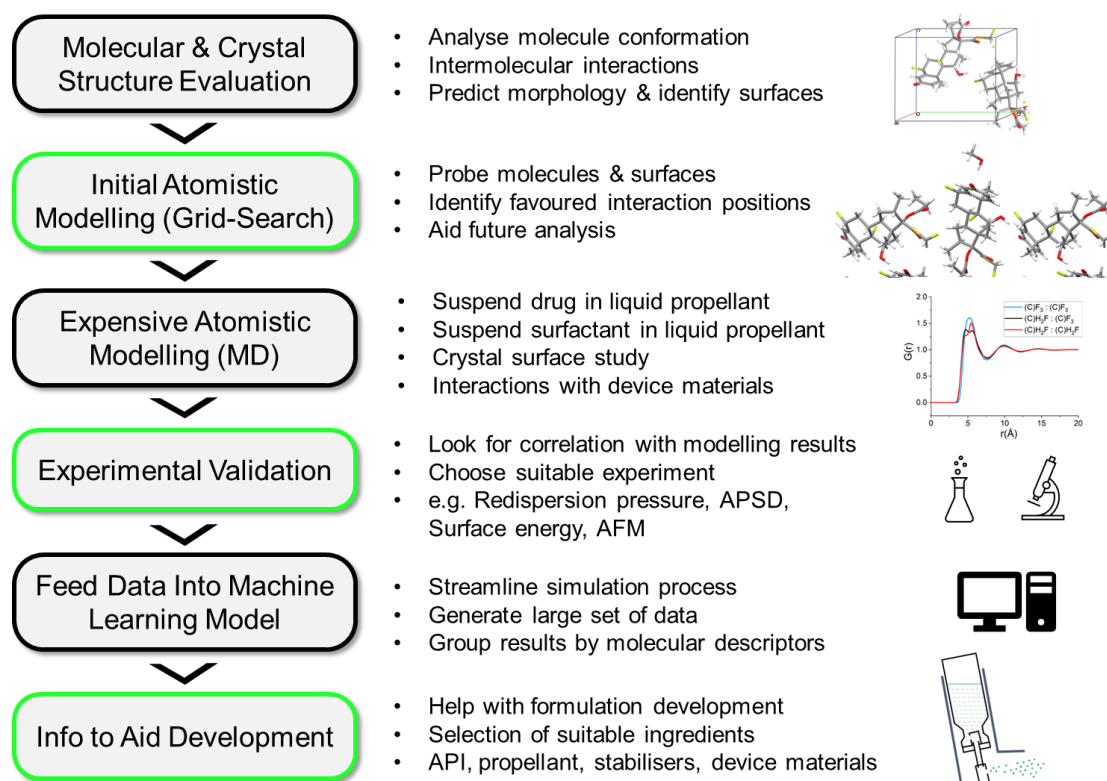


Figure 7-1 Proposed workflow on how to continue from this thesis and implement molecular modelling into the development of inhalation devices.

MD simulations must use representative force fields, this encounters new challenges when looking at multiple phases. Either a single force field potential can represent all phases, or multiple specialised force fields can be combined. For instance, a previous investigation into the wetting of ibuprofen crystal surfaces successfully used the latter approach (Marinova et al., 2019). This thesis has proven the specialised HFA-134a force field is appropriate for a liquid propellant, and the suitability of others can be judged by their ability to reproduce density. For instance, the force field selected for solid-state must be capable of simulating the lattice parameters.

Potential expensive atomistic modelling investigation routes include:

- **Suspending Drug in Liquid Propellant:** A simulation of liquid (e.g., propellant) containing an API molecule. This can investigate how the API molecule conformation changes in different liquids. Also, can investigate the probabilities of finding other solvent molecules near certain atoms of the FP molecule. Results can help analyse how different APIs influence the aerosolised particle size distribution.
- **Suspending Surfactant in Liquid Propellant:** Simulate a surfactant molecule or micelle with and without co-solvent in a liquid propellant. Can look at the surfactant

conformation, propensity for it to form micelles. This may help understand the differences in surfactants used as stabilising agents.

- **Crystal Surface Study:** Simulate APIs crystal surface slab and include solvent on top (e.g., propellant). Surfactants or API molecules could also be included in the liquid phase. This can compare different faces, helping to investigate the free energy of wetting, surfactant binding, and particle cohesion.
- **Interactions with Device Materials:** Simulate formulation interactions with the MDI device materials, such as cannister wall coatings or elastomer seals. Surfaces tend to be amorphous, long chain polymers. Liquid propellants can be included on top, also containing APIs and surfactants. Depending on the size of polymer, coarse grain modelling can represent some of the long chains and reduce computational costs. These simulations can help with evaluating material suitability.

It is important to establish a useful method of analysing the MD simulations which can be validated experimentally. This may be an iterative process of tweaking the design of a particular model to represent an experiment, or vice versa. Previously, ab-initio investigations of surfactant solubility in HFA propellants showed agreement with an AFM experiment. These tested adhesion of drug particle interacting with a cannister surface when both are submerged in a model propellant liquid containing surfactants (Wu et al., 2007). Also, a separate grid search investigation into particle cohesion correlated with experimental investigations into the formulations ease of redispersion (Ramachandran et al., 2015). Ideally, once a correlation of a certain parameter has been shown, then the simulation procedure can be repeated for a wide range of APIs, propellants, or other ingredients. The results have potential to be used as a tool to help experimentalists with formulation development.

To generate the large data set required for machine learning, the process of performing MD simulations must be streamlined by automating as many steps as possible. Therefore, scripts would need to be developed that build and run simulations using a standardised set of conditions. Additionally, once a useful parameter and way of analysing has been identified, then all analysis steps can also be automated with scripts that extract information from trajectory files and generate graphs. For example, an MD simulation of an API suspended in a propellant could be re-produced with several hundred different APIs. Analysis of the RDF and coordination number could evaluate the number of interactions between solute and solvents, such as weak H-bonds. Once this process has formed a large enough data set, the results can be fed into clustering machine learning methods which organise them based on simulation results. It may

group the results by molecular descriptors, such as number of H-bond donors, so it can help predict certain behaviours when new APIs are introduced and therefore aid with the development of MDI formulations with faster predictions.

7.5 Closing Remarks

In this study, molecular modelling was applied to identify intermolecular interactions that affect the structuring of liquid and solid phases in suspension MDI formulations. A broader understanding of liquid propellant HFA-134a's intermolecular structuring was developed. Furthermore, the morphology of API fluticasone propionate was predicted from its inherent interactions. A new workflow was proposed to meet some of the original objectives that were incomplete. Results of this thesis can be progressed with further investigations into the solid-liquid phase interface, complemented with suitable experimental studies. In turn, this has potential to be a valuable tool for understanding the causes of MDI formulation issues and could contribute to a digital drug design approach.

Appendix Chapter

Appendix Chapter

A.1 Predicted Partial Charges

Fluticasone Propionate: Form I & II

Partial charges assigned to FP's different atoms for both of its polymorphs. Charges were calculated using AM1 method in MOPAC. The naming convention for each atom follows the Figure A-1 below. Predicted partial charge values for Form I DAXYUX and Form II DAXYUX01 are given in Table A-1 and A-2, respectively.

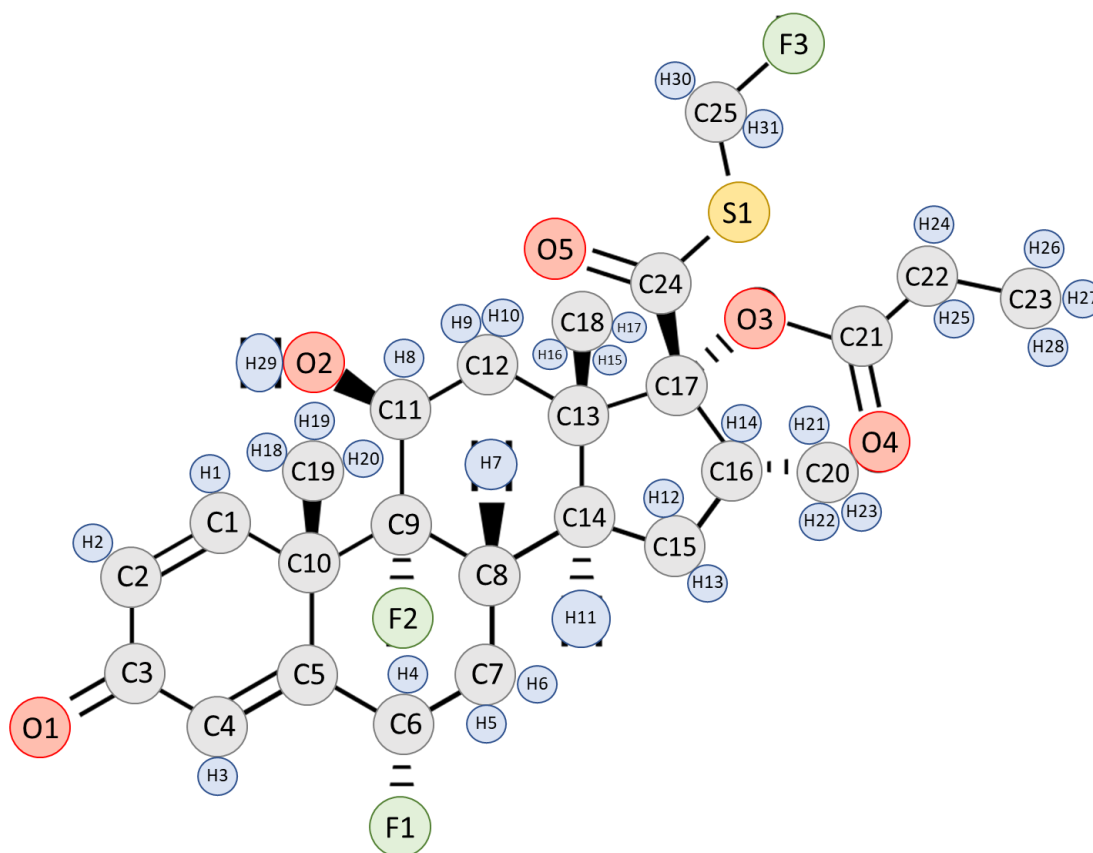


Figure A-1 Labelled atoms of fluticasone propionate. First, letter corresponds to its element, second, the number is the repetition of that element.

Table A-1 Atomic partial charges for **DAXYUX** Form I, calculated using semi empirical AM1 method within MOPAC

Atom	Charge	Atom	Charge	Charge Range	Colour Key
F1	-0.1655	S1	0.0153	< -0.2	
F2	-0.1735	H1	0.126	-0.2 < -0.1	
F3	-0.126	H2	0.144	-0.1 < 0	
O1	-0.2836	H3	0.1549	0	
O2	-0.3276	H4	0.0953	0 > +0.1	
O3	-0.2672	H5	0.1075	+0.1 > +0.2	
O4	-0.3138	H6	0.0966	> +0.2	
O5	-0.2544	H7	0.102		
C1	-0.0847	H8	0.0825		
C2	-0.1966	H9	0.1081		
C3	0.2761	H10	0.0925		
C4	-0.1672	H11	0.1088		
C5	-0.0963	H12	0.0899		
C6	0.1082	H13	0.0829		
C7	-0.1657	H14	0.104		
C8	-0.0973	H15	0.0783		
C9	0.1415	H16	0.0747		
C10	-0.0245	H17	0.0931		
C11	0.0278	H18	0.0726		
C12	-0.1569	H19	0.0825		
C13	-0.0455	H20	0.0972		
C14	-0.1013	H21	0.0926		
C15	-0.1364	H22	0.0722		
C16	-0.1071	H23	0.0788		
C17	0.0621	H24	0.1052		
C18	-0.1904	H25	0.1084		
C19	-0.1671	H26	0.0784		
C20	-0.1837	H27	0.0743		
C21	0.3193	H28	0.0843		
C22	-0.1529	H29	0.2104		
C23	-0.1856	H30	0.0924		
C24	0.1609	H31	0.0905		
C25	-0.0215				

Table A-2 Atomic partial charges for **DAXYUX01** Form II, calculated using semi empirical AM1 method within MOPAC

Atom	Charge	Atom	Charge	Charge Range	Colour Key
F1	-0.1759	S1	0.0422	< -0.2	
F2	-0.1737	H1	0.1473	-0.2 < -0.1	
F3	-0.1511	H2	0.1559	-0.1 < 0	
O1	-0.2979	H3	0.1665	0	
O2	-0.3348	H4	0.0878	0 > +0.1	
O3	-0.2613	H5	0.127	+0.1 > +0.2	
O4	-0.3302	H6	0.0877	> +0.2	
O5	-0.233	H7	0.1245		
C1	-0.1066	H8	0.0837		
C2	-0.1924	H9	0.1163		
C3	0.2689	H10	0.0921		
C4	-0.175	H11	0.1195		
C5	-0.0762	H12	0.0807		
C6	0.0981	H13	0.0874		
C7	-0.1836	H14	0.0988		
C8	-0.1026	H15	0.095		
C9	0.0961	H16	0.1059		
C10	-0.0084	H17	0.0768		
C11	0.0377	H18	0.0985		
C12	-0.1706	H19	0.0713		
C13	-0.0263	H20	0.0849		
C14	-0.1166	H21	0.0883		
C15	-0.1496	H22	0.0959		
C16	-0.1132	H23	0.1148		
C17	0.0812	H24	0.1079		
C18	-0.2231	H25	0.1352		
C19	-0.2147	H26	0.1022		
C20	-0.2159	H27	0.1232		
C21	0.3284	H28	0.0845		
C22	-0.1793	H29	0.2089		
C23	-0.2006	H30	0.1159		
C24	0.1468	H31	0.1218		
C25	-0.0933				

Solid-State HFA-134a

The two molecules in the asymmetric unit of HFA-134a's crystal structure VUZQIQ were assigned charges using the semi-empirical MOPAC AM1 method.

Table A-3 Atomic charges for solid-state HFA-134a assigned using the MOPAC method. The VUZQIQ structure contains two molecules in the asymmetric unit.

Molecule 1 Atoms	Partial Charge	Molecule 2 Atoms	Partial Charge
C1 @ CF₃	0.4306	C3 @ CF₃	0.4336
C2 @ CFH₂	-0.0413	C4 @ CFH₂	-0.0488
F1	-0.1663	F5	-0.1581
F2	-0.1581	F6	-0.1609
F3	-0.1603	F7	-0.1602
F4	-0.1392	F8	-0.1458
H1	0.1205	H3	0.1168
H2	0.114	H4	0.1233

Ethanol Probe

Table A-4 Atomic charges for relaxed ethanol probe assigned using the MOPAC method.

Molecule 1 Atoms	Partial Charge
C @ CH₃	-0.216
H	-0.019
H	0.077
H	0.085
C @ CH₂OH	0.085
O	-0.324
H	0.054
H	0.054
H	0.201

Methanol Probe

Table A-5 Atomic charges for relaxed methanol probe assigned using the MOPAC method.

Molecule 1 Atoms	Partial Charge
C	-00.072
O	-00.322
H	00.049
H	00.095
H	00.049

Water Probe

Table A-6 Atomic charges for relaxed water probe assigned using the MOPAC method.

Molecule 1 Atoms	Partial Charge
O	-00.410
H	00.205
H	00.205

A.2 Force Field Comparison: Lattice Energy of FP

The lattice energy of Form I fluticasone propionate, the more stable polymorph, was predicted with the Dreiding and Tripos 5.2 force field potentials, using the same charges detailed in section A.1. The lattice energy predicted by Dreiding was stronger than Tripos 5.2 and this is cleared in the inset of Figure A-2.

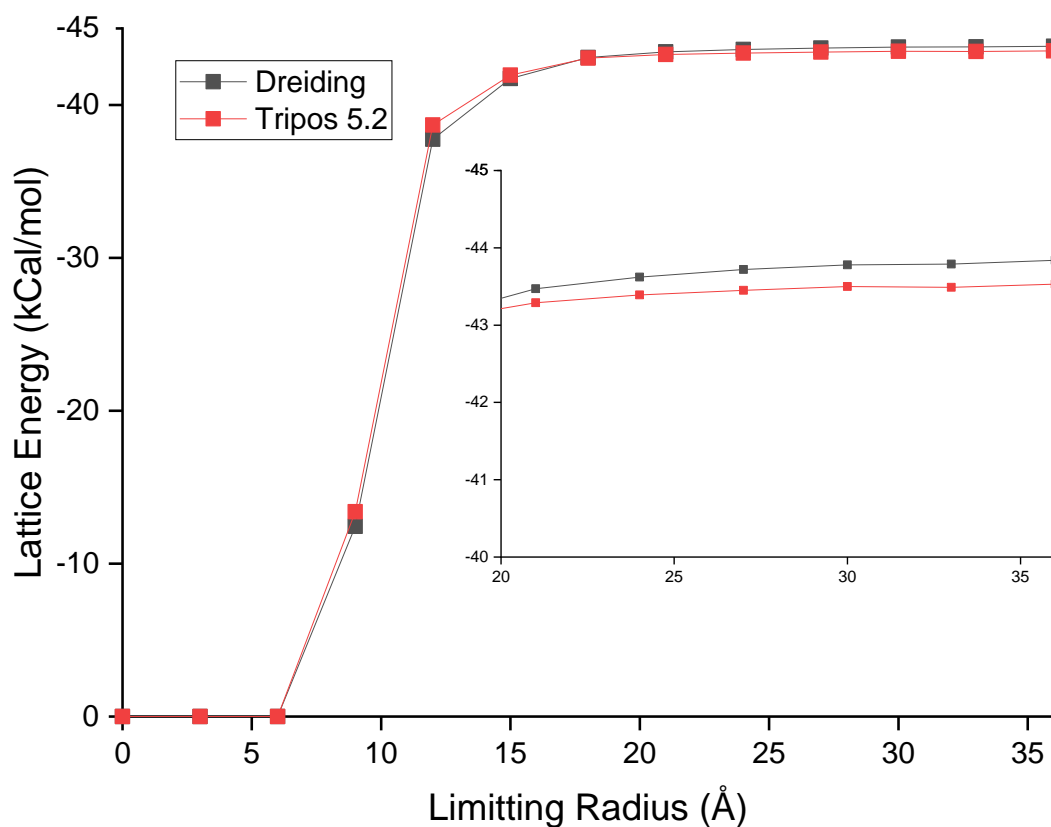


Figure A-2 Predicted lattice energy of Form I fluticasone propionate, DAXYUX. Predicted using the Dreiding and Tripos 5.2 force field potentials with identical charges.

A.3 MD Simulation Settings: Liquid HFA-134a

Simulation Size Test

The PCFF potential was used to compare the liquid structuring as a function of number of molecules in the system. These simulations were performed at 293 K, at 6 atm pressure in the NPT Berendsen barostat (Berendsen et al., 1984) with 0.1 and 2.0 ps thermostat and barostat, respectively. Production runs lasted 1 ns. Figure A-3 shows the results of systems containing 200, 1000 and 1500 HFA-134a molecules. A comparable RDF was predicted using 1000 and 1500 molecules, hence why 1000 molecule systems were used in further simulations.

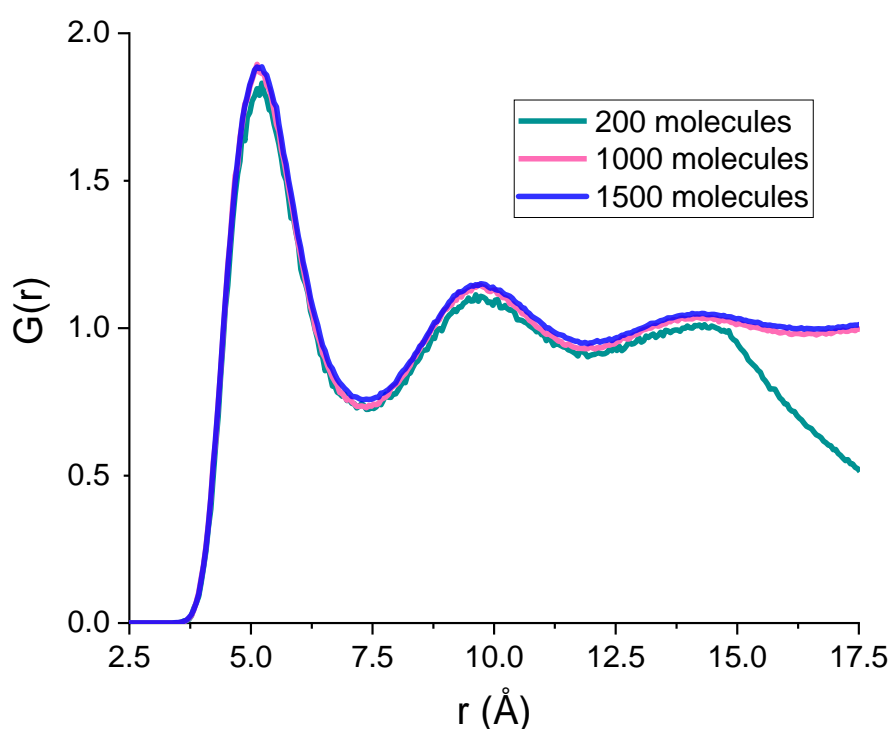


Figure A-3 Molecular RDF for simulation size test. A cubic box filled with different number of HFA-134a molecules was simulated using the PCFF potential, for 1 ns at 293 K, at 20 atm pressure in the NPT ensemble.

Peguin Force Field - Parameters

The force field potential developed by (Peguin et al., 2009) was based on OPLS (Jorgensen et al., 1996) with the LJ parameters for fluorine atoms being optimised to reproduce VLE properties obtained from Monte Carlo simulations. Bond lengths were kept constant and torsion was only permitted along the C-C axis. More details can be found in the force field's publication (Peguin et al., 2009).

Table A-7 Intramolecular parameters for HFA-134a for Peguin force field

	Bond length b_0 (Å)	Angle Θ_0 (°)	K_1 (K/ mole.° ²)	V_1 (kcal / mole.°)	V_2 (kcal / mole.°)	V_3 (kcal / mole.°)
CC	1.529					
CF	1.360					
CH	1.09					
CCH		110.7	18889.4			
CCF		109.5	25185.8			
HCH		107.8	16622.6			
HCF		107.0	20148.7			
FCF		109.1	38786.2			
FCCF				44.492	-49.0	2140.36
FCCH				-93.238	19.92	2129.3

Non-bonded atom interactions were measured using the LJ 12-6 potential for van der Waals interactions and Coulombic potential for electrostatic interactions. Charges were calculated by CHELPG in Gaussian 03 with MP2, values are listed in Table A-8.

Table A-8 Partial charges for HFA-134a assigned by Peguin's optimised force field

Atom	Partial Charge
C belonging to CF ₃	0.534
F	0.1915
F	0.1915
F	0.1915
C belonging to CFH ₂	0.002
F	0.1915
H	0.115
H	0.115

Comparing Force Field Suitability

Systems followed the same method as described in section 2.2.4.5 with the force field developed by Peguin being compared against generic force fields of OPLS (Jorgensen et al., 1996 and PCFF (Sun, 1995). The average simulated system density at respective temperature was compared with experimentally measured density values, which were extrapolated so they were equivalent to the simulation pressure of 20 atm. Figure A-4 shows the physical values of liquid HFA-134a's thermal expansion follows a linear trend between 200 K to 300 K, (Padua et al., 1996) measurements by Padua et al had an accuracy of 0.05 % so the error bars are too small to see on the graph. Simulated values include an error bar of one standard deviation. The force field developed by Peguin et al., is by far the best at reproducing the experimental densities. Hence, confirming its suitability for further simulations.

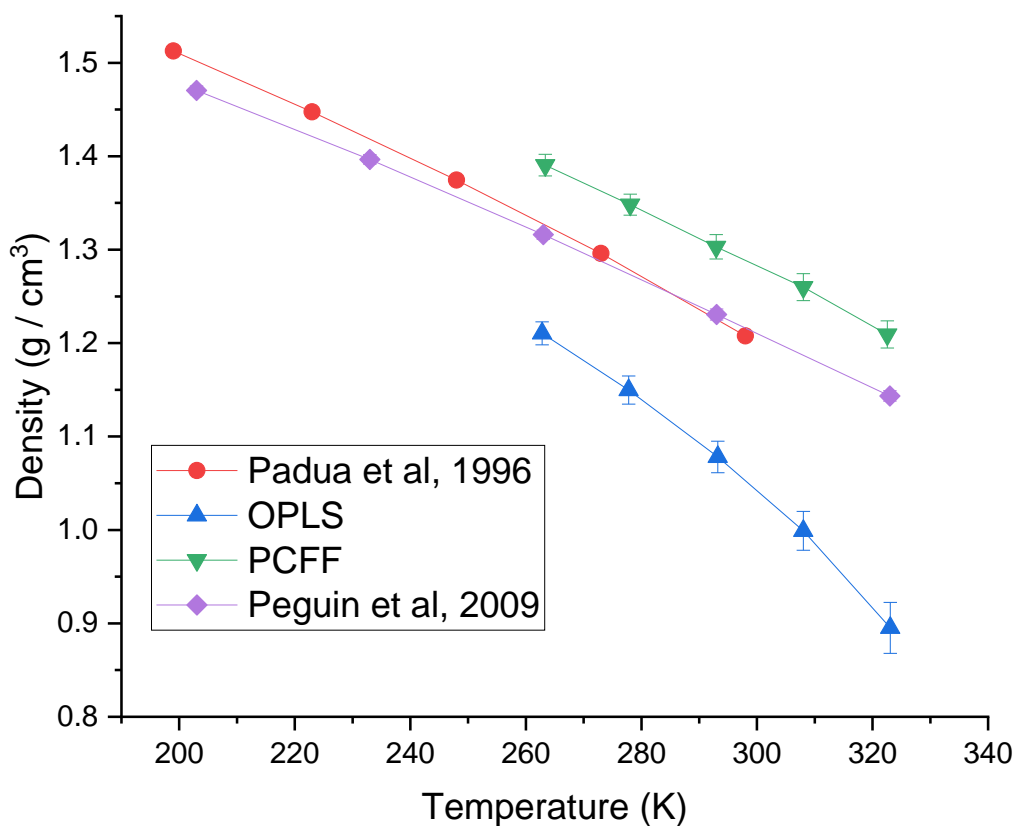


Figure A-4 Thermal expansion of HFA-134a, average density from molecular dynamics simulations using different force fields is compared to physical measurements by Padua et al, 1996, illustrated by red points.

Length of Production Run

Systems were simulated using the same method described in section 2.2.4.5 using the Peguin force field. Production runs lasted 5 and 100 ns, for systems consisting of 1000 HFA-134a molecules in the NVT Berendsen thermostat (Berendsen et al., 1984) with a 0.2 ps constant. The aim was to evaluate differences with production run lengths. Results of Figure A-5 show the molecular RDF is comparable for 5 and 100 ns production runs, with both following the same pattern. Hence, this is why further productions runs lasted 5 ns.

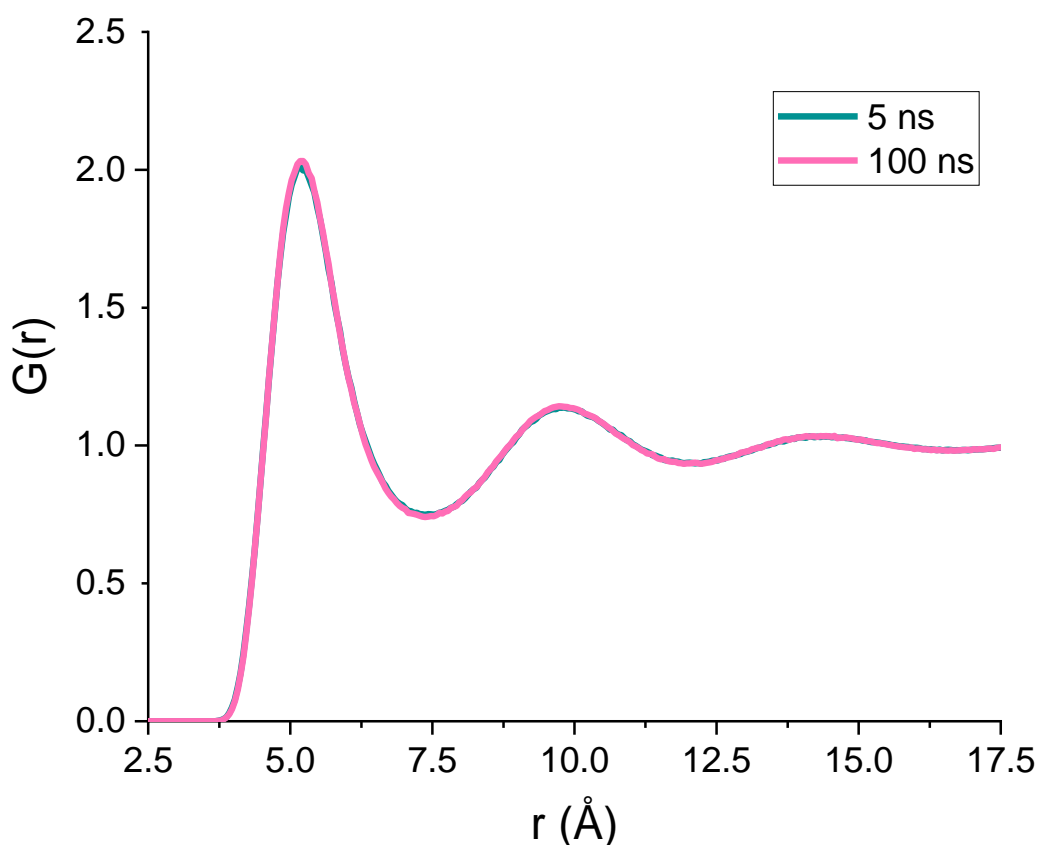


Figure A-5 Molecular RDF of simulations testing production run length. A cubic box filled with 1000 HFA-134a molecules simulated using the Peguin potential, for 5 and 100 ns. At 293 K 20 atm pressure in the NVT ensemble.

A.4 Morphology Effect on Particle Interactions

This section accompanies chapter 8, it shows detailed tables of the surface area percentage and weighted interaction energy of each morphology.

Table A-9 Average cohesion interaction energy of FP probing different FP crystal surfaces. Weighted based on surface area % of different morphologies.

FP Forms / Faces	Cohesion (FP)	ORIGINAL		NEEDLE		PLATELET	
		Surface area %	Weighted Interaction	Surface area %	Weighted Interaction	Surface area %	Weighted Interaction
{100}	-13.55	23.02	-3.12		0.00		0.00
{110}	-13.57	3.76	-0.51	2.23	-0.30	15.69	-2.13
{1-10}	-13.76	3.76	-0.52		0.00		0.00
{001}	-11.49	17.09	-1.96	39.22	-4.51		0.00
(011)	-11.53	22.33	-2.57	21.00	-2.42	26.79	-3.09
(01-1)	-11.53		0.00		0.00	10.10	-1.16
(0-11)	-11.57	22.33	-2.58	37.55	-4.34	15.17	-1.75
(0-1-1)	-11.57		0.00		0.00	32.25	-3.73
(020)	-10.53	3.86	-0.41		0.00		0.00
(0-20)	-11.13	3.86	-0.43				
		Average (kcal/mol)	-12.10	Average (kcal/mol)	-11.57	Average (kcal/mol)	-11.87

Table A-10 Average wetting interaction energy of HFA-134a probing different FP crystal surfaces. Weighted based on surface area % of different morphologies.

FP Forms / Faces	Wetting (HFA)	ORIGINAL		NEEDLE		PLATELET	
		Surface area %	Weighted Interaction	Surface area %	Weighted Interaction	Surface area %	Weighted Interaction
{100}	-7.13	23.02	-1.64		0.00		0.00
{110}	-8.24	3.76	-0.31	2.23	-0.18	15.69	-1.29
{1-10}	-7.23	3.76	-0.27		0.00		0.00
{001}	-7.53	17.09	-1.29	39.22	-2.95		0.00
(011)	-6.89	22.33	-1.54	21.00	-1.45	26.79	-1.85
(01-1)	-6.89		0.00		0.00	10.10	-0.70
(0-11)	-6.38	22.33	-1.43	37.55	-2.40	15.17	-0.97
(0-1-1)	-6.38		0.00		0.00	32.25	-2.06
(020)	-7.70	3.86	-0.30		0.00		0.00
(0-20)	-5.70	3.86	-0.22				
		Average (kcal/mol)	-6.99	Average (kcal/mol)	-6.98	Average (kcal/mol)	-6.86

References

- ACREE, W. & CHICKOS, J. S. 2010. Phase Transition Enthalpy Measurements of Organic and Organometallic Compounds. Sublimation, Vaporization and Fusion Enthalpies From 1880 to 2010. *Journal of Physical and Chemical Reference Data*, 39.
- ADI, S., ADI, H., CHAN, H.-K., FINLAY, W. H., TONG, Z., YANG, R. & YU, A. 2011. Agglomerate strength and dispersion of pharmaceutical powders. *Journal of aerosol science*, 42, 285-294.
- AFREZZA. 2022. *AFREZZA INHALED INSULIN* [Online]. Available: <https://afrezza.com/> [Accessed 2022].
- ALI, M. 2010. CHAPTER 9 - Pulmonary Drug Delivery. In: KULKARNI, V. S. (ed.) *Handbook of Non-Invasive Drug Delivery Systems*. Amsterdam, Netherlands: Elsevier.
- ALONSO, J. L., ANTOLÍNEZ, S., BLANCO, S., LESARRI, A., LÓPEZ, J. C. & CAMINATI, W. 2004. Weak C–H ... O and C–H ... F–C Hydrogen Bonds in the Oxirane– Trifluoromethane Dimer. *Journal of the American Chemical Society*, 126, 3244-3249.
- ASTHMAUK. 2022. *Asthma data visualisations* [Online]. Asthma and Lung UK. Available: <https://asthma.org.uk/support-us/campaigns/data-visualisations> [Accessed 2022].
- BARPAGA, D., NGUYEN, V. T., MEDASANI, B. K., CHATTERJEE, S., MCGRIL, B. P., MOTKURI, R. K. & DANG, L. X. 2019. Insight into Fluorocarbon Adsorption in Metal-Organic Frameworks via Experiments and Molecular Simulations. *Sci Rep*, 9, 10289.
- BÁRTOVÁ, A., GABRIEL, R., PRUDILOVÁ, B. B., OTYEPKOVÁ, E., MALINA, L. & OTYEPKA, M. 2022. Controlled nucleation of crystallization process as an efficient tool to tune the properties of corticosteroid API. *Powder Technology*, 402.
- BAUER, J., SPANTON, S., HENRY, R., QUICK, J., DZIKI, W., PORTER, W. & MORRIS, J. 2001. Ritonavir: an extraordinary example of conformational polymorphism. *Pharmaceutical research*, 18, 859-866.
- BERENDSEN, H. J. C., POSTMA, J. P. M., VAN GUNSTEREN, W. F., DINOLA, A. & HAAK, J. R. 1984. Molecular Dynamics with Coupling to an External Bath. *The Journal of Chemical Physics*, 81, 3684-3690.
- BERNSTEIN, J. 2002. *Polymorphism in Molecular Crystals*, Oxford, Oxford University Press.
- BIOVIA, D. S. 2017. BIOVIA Materials Studio Forcite. San Diego: Dassault Systèmes.
- BLADON, P., GORTON, J. & HAMMOND, R. B. 2012. *Molecular Modelling: Computational Chemistry Demystified*, Cambridge, UK., RSC Publishing.
- BLONDINO, F. E. & BYRON, P. R. 1998. Surfactant dissolution and water solubilization in chlorine-free liquified gas propellants. *Drug Development and Industrial Pharmacy*, 24, 935-945.
- BRAUN, D. E., GELBRICH, T., KAHLENBERG, V., LAUS, G., WIESER, J. & GRIESSER, U. J. 2008. Packing polymorphism of a conformationally flexible molecule (aprepitant). *New Journal of Chemistry*, 32, 1677-1685.
- BRUNELLI, M. & FITCH, A. N. 2002. Crystal Structures of Hydrofluorocarbons from Powder X-ray Diffraction Data: HFC-134a and HFC-152a. *Zeitschrift Fur Kristallographie*, 217, 395-400.
- BRUNO, I. J., COLE, J. C., EDGINGTON, P. R., KESSLER, M., MACRAE, C. F., MCCABE, P., PEARSON, J. & TAYLOR, R. 2002. New software for searching the Cambridge Structural Database and visualizing crystal structures. *Acta Crystallogr., Sect. B: Struct. Sci*, 58, 389-397.
- BUDINSKÝ, R., VACEK, V. & LÍŠAL, M. 2004. Vapor–Liquid Equilibria of Alternative Refrigerants and Their Binaries By Molecular Simulations Employing the

- Reaction Gibbs Ensemble Monte Carlo Method. *Fluid Phase Equilibria*, 222-223, 213-220.
- CARVALHO, T. C., PETERS, J. I. & WILLIAMS III, R. O. 2011. Influence of particle size on regional lung deposition – What evidence is there? . *International Journal of Pharmaceutics*, 406, 1-10.
- ČEJKA, J., KRATOCHVIL, B. & JEGOROV, A. 2005. Crystal structure of fluticasone propionate, C₂₅H₃₁F₃O₅S. *Zeitschrift für Kristallographie-New Crystal Structures*, 220, 153-154.
- CLARK, A. R. 1995. Medical Aerosol Inhalers: Past, Present, and Future. *Aerosol Science and Technology*, 22, 374-391.
- CLARK M., CRAMER R. D. & VAN OPDENBOSCH N. 1989. Validation of the General Purpose Tripos 5.2 Force Field. 10, 982-1012.
- CLEGG, W. 1998. *Crystal Structure Determination*, Oxford, Oxford University Press.
- CLINICALC. 2023. *The Top 300 of 2020* [Online]. ClinCalc.com. Available: clincalc.com/DrugStats/Top300Drugs.aspx [Accessed 30th January 2023].
- CLYDESDALE, G., DOCHERTY, R. & ROBERTS, K. J. 1991. HABIT - a program for predicting the morphology of molecular crystals. *Computer Physics Communications*, 64, 311-328.
- CLYDESDALE, G., ROBERTS, K. & WALKER, E. 1997a. The crystal habit of molecular materials: A structural perspective. *Molecular solid state syntheses, structure, reactions, applications. Volume 2 Chapter7 Theoretical aspects and computer modelling*. Ed. A Gavezzotti.
- CLYDESDALE, G., ROBERTS, K. J. & DOCHERTY, R. 1996. HABIT95 - A Program for Predicting the Morphology of Molecular Crystals as a Function of the Growth Environment. *Journal of Crystal Growth*, 166, 78-83.
- CLYDESDALE, G., ROBERTS, K. J., TELFER, G. B. & GRANT, D. J. 1997b. Modeling the crystal morphology of α -lactose monohydrate. *Journal of pharmaceutical sciences*, 86, 135-141.
- DALEY-YATES, P. T., MEHTA, R., CHAN, R. H., DESPA, S. X. & LOUEY, M. D. 2014. Pharmacokinetics and pharmacodynamics of fluticasone propionate and salmeterol delivered as a combination dry powder from a capsule-based inhaler and a multidose inhaler in asthma and COPD patients. *Journal of aerosol medicine and pulmonary drug delivery*, 27, 279-289.
- DAVIES, N. M. & FEDDAH, M. R. 2003. A novel method for assessing dissolution of aerosol inhaler products. *International journal of pharmaceutics*, 255, 175-187.
- DE BOER, A., GJALTEMA, D., HAGEDOORN, P. & FRIJLINK, H. 2002. Characterization of inhalation aerosols: a critical evaluation of cascade impactor analysis and laser diffraction technique. *International journal of pharmaceutics*, 249, 219-231.
- DERHOVANESSIAN, A., DOYON, J. B., JAIN, A., RABLEN, P. R. & SAPSE, A.-M. 1999. Models of F-H Contacts Relevant to the Binding of Fluoroaromatic Inhibitors to Carbonic Anhydrase II. *Organic Letters*, 1, 1359-1362.
- DERJAGUIN, B. V. 1941. Theory of the stability of strongly charged lyophobic sol and of the adhesion of strongly charged particles in solutions of electrolytes. *Acta phys. chim. URSS*, 14, 633.
- DESIRAJU, G., R. & STEINER, T. 1999. *The Weak Hydrogen Bond: In Structural Chemistry and Biology*, Oxford, UK, Oxford University Press,.
- DESIRAJU, G., VITTAL, J. J. & RAMANAN, A. 1989. *Crystal Engineering: The Design of Organic Solids*, Elsevier.
- DO, H., WHEATLEY, R. J. & HIRST, J. D. 2010. Microscopic Structure of Liquid 1-1-1-2-Tetrafluoroethane (R134a) from Monte Carlo simulation. *Phys Chem Chem Phys*, 12, 13266-72.
- DOCHERTY, R., CLYDESDALE, G., ROBERTS, K. & BENNEMA, P. 1991. Application of Bravais-Friedel-Donnay-Harker, attachment energy and Ising models to predicting and understanding the morphology of molecular crystals. *Journal of Physics D: Applied Physics*, 24, 89.

- DOLOVICH, M. B., AHRENS, R. C., HESS, D. R., ANDERSON, P., DHAND, R., RAU, J. L., SMALDONE, G. C. & GUYATT, G. 2005. Device Selection and Outcomes of Aerosol Therapy: Evidence-Based Guidelines: American College of Chest Physicians/American College of Asthma, Allergy, and Immunology. *Chest*, 127, 335-371.
- DUNITZ, J. D. & TAYLOR, R. 1997. Organic Fluorine Hardly Ever Accepts Hydrogen Bonds. *Chemistry A European Journal* 3, 89-98.
- EL-GENDY, N., PORNPUTTAPITAK, W. & BERKLAND, C. 2011. Nanoparticle agglomerates of fluticasone propionate in combination with albuterol sulfate as dry powder aerosols. *European Journal of Pharmaceutical Sciences*, 44, 522-533.
- EPA. 2022. *Ban for Nonessential Products Containing Ozone-depleting Substances* [Online]. Available: <https://www.epa.gov/ozone-layer-protection/ban-nonessential-products-containing-ozone-depleting-substances> [Accessed 2022].
- FERMEGLIA, M., FERRONE, M. & PRICL, S. 2003. Development of an All-Atoms Force Field from Ab Initio Calculations for Alternative Refrigerants. *Fluid Phase Equilibria*, 210, 105-116.
- FRENKEL, D. & SMIT, B. 2023. *Understanding molecular simulation: from algorithms to applications*, Elsevier.
- GROOM, C., BRUNO, I., LIGHTFOOT, M. & WARD, S. 2016. Acta Crystallogr., Sect. B: Struct. Sci., Cryst. Eng. Mater, 72, 171.
- HAMMOND, R., PENCHEVA, K., RAMACHANDRAN, V. & ROBERTS, K. 2007. Application of grid-based molecular methods for modeling solvent-dependent crystal growth morphology: Aspirin crystallized from aqueous ethanolic solution. *Crystal growth & design*, 7, 1571-1574.
- HAMMOND, R. B., HASHIM, R. S., MA, C. & ROBERTS, K. J. 2006. Grid-based molecular modeling for pharmaceutical salt screening: Case example of 3, 4, 6, 7, 8, 9-hexahydro-2H-pyrimido (1, 2-a) pyrimidinium acetate. *Journal of pharmaceutical sciences*, 95, 2361-2372.
- HAMMOND, R. B., MA, C., ROBERTS, K. J., GHI, P. Y. & HARRIS, R. K. 2003. Application of Systematic Search Methods to Studies of the Structures of Urea-Dihydroxy Benzene Cocrystals. *The Journal of Physical Chemistry B*, 107, 11820-11826.
- HARTMAN, P. & BENNEMA, P. 1980. The attachment energy as a habit controlling factor: I. Theoretical considerations. *Journal of Crystal Growth*, 49, 145-156.
- HOYE, W. L., MOGALIAN, E. M. & MYRDAL, P. B. 2005. Effects of extreme temperatures on drug delivery of albuterol sulfate hydrofluoroalkane inhalation aerosols. *American journal of health-system pharmacy*, 62, 2271-2277.
- IBRAHIM, S. F., PICKERING, J., RAMACHANDRAN, V. & ROBERTS, K. J. 2022. Prediction of the Mechanical Deformation Properties of Organic Crystals Based upon their Crystallographic Structures: Case Studies of Pentaerythritol and Pentaerythritol Tetranitrate. *Pharm Res*, 39, 3063-3078.
- IQIVA 2020. IQVIA Unit Sales: October 2019-September 2020.
- ISRAELACHVILI, J. N. 2011. *Intermolecular and Surface Forces*, MA, USA, Academic Press.
- JAMES, J., CREAN, B., DAVIES, M., TOON, R., JINKS, P. & ROBERTS, C. J. 2008. The surface characterisation and comparison of two potential sub-micron, sugar bulking excipients for use in low-dose, suspension formulations in metered dose inhalers. *International journal of pharmaceuticals*, 361, 209-221.
- JANG, S. S., BLANCO, M., GODDARD, W. A., CALDWELL, G. & ROSS, R. B. 2003. The source of helicity in perfluorinated N-alkanes. *Macromolecules*, 36, 5331-5341.
- JENSEN, J. H. 2010. *Molecular Modelling Basics*, Boca Raton, CRC Press.
- JORGENSEN, W. L., MAXWELL, D. S. & TIRADORIVES, J. 1996. Development and Testing of the OPLS All-Atom Force Field on Conformational Energetics and

- Properties of Organic Liquids. *Journal of the American Chemical Society*, 118, 11225-11236.
- KAMIYA, A., SAKAGAMI, M., HINDLE, M. & BYRON, P. R. 2004. Aerodynamic sizing of metered dose inhalers: An evaluation of the andersen and next generation pharmaceutical impactors and their USP methods. *Journal of Pharmaceutical Sciences*, 93, 1828-1837.
- KARIUKI, B. M., PSALLIDAS, K., HARRIS, K. D., JOHNSTON, R. L., LANCASTER, R. W., STANIFORTH, S. E. & COOPER, S. M. 1999. Structure determination of a steroid directly from powder diffraction data. *Chemical Communications*, 1677-1678.
- KASKIEWICZ, P. L., ROSBOTTOM, I., CORZO, D. M. C., HAMMOND, R. B., DOWNIE, R., DOWDING, P. J., GEORGE, N. & ROBERTS, K. J. 2021. Influence of solution chemistry on the solubility, crystallisability and nucleation behaviour of eicosane in toluene: acetone mixed-solvents. *CrystEngComm*, 23, 3109-3125.
- KINDEVADRUGDELIVERY 2015. MDI Images.
- KLIMENKO, N. A., GAL'TSOV, N. N. & PROKHAVILOV, A. I. 2010. Structure of the Low-Temperature Phase of Hexafluoroethane. *Low Temperature Physics*, 36, 189-195.
- KUBAVAT, H. A., SHUR, J., RUECROFT, G., HIPKISS, D. & PRICE, R. 2012. Investigation into the influence of primary crystallization conditions on the mechanical properties and secondary processing behaviour of fluticasone propionate for carrier based dry powder inhaler formulations. *Pharm Res*, 29, 994-1006.
- LEPRE, L. F., ANDRE, D., DENIS-QUANQUIN, S., GAUTIER, A., PÁDUA, A. A. H. & COSTA GOMES, M. 2019. Ionic Liquids Can Enable the Recycling of Fluorinated Greenhouse Gases. *ACS Sustainable Chemistry & Engineering*, 7, 16900-16906.
- LEVINE, I. N. 2009. *Physical Chemistry*, New York, McGraw-Hill.
- LEVY, M. L., HARDWELL, A., MCKNIGHT, E. & HOLMES, J. 2013. Asthma patients' inability to use a pressurised metered-dose inhaler (pMDI) correctly correlates with poor asthma control as defined by the global initiative for asthma (GINA) strategy: a retrospective analysis. *Prim Care Respir J*, 22, 406-11.
- LI, H., SUN, J. & WANG, M. 2006. Construction of oriented thin film via C-F... H-C intermolecular interaction. *Materials Letters*, 60, 2379-2382.
- LIDE, D. R. (ed.) 2005. *CRC Handbook of Chemistry and Physics, 85th Edition*, Boca Raton, FL: CRC Press, .
- LISAL, M., BUDINSKY, R., VACEK, V. & AIM, K. 1999. Vapor-Liquid Equilibria of Alternative Refrigerants by Molecular Dynamics Simulations. *International Journal of Thermophysics*, 20, 163-174.
- LISAL, M. & VACEK, V. 1997. Effective Potentials for Liquid Simulation of the Alternative Refrigerants HFC-134a (CF₃CH₂F) and HFC- 125 (CF₃CHF₂). *Fluid Phase Equilibria*, 127, 83-102.
- LÍSAL, M. & VACEK, V. 1996. Molecular Dynamics Aimulations of Fluorinated Ethanes. *Molecular Physics*, 87, 167-187.
- LIU, P., GODDARD, J., ARSENAULT, G., GU, J., MCALEES, A., MCCRINDLE, R. & ROBERTSON, V. 2007. Theoretical studies of the conformations and 19F NMR spectra of linear and a branched perfluorooctanesulfonamide (PFOSAmide). *Chemosphere*, 69, 1213-1220.
- LOUEY, M. D., VAN OORT, M. & HICKEY, A. J. 2004. Aerosol dispersion of respirable particles in narrow size distributions produced by jet-milling and spray-drying techniques. *Pharm Res*, 7, 1207-1213.
- MACRAE, C. F., SOVAGO, I., COTTRELL, S. J., GALEK, P. T. A., MCCABE, P., PIDCOCK, E., PLATINGS, M., SHIELDS, G. P., STEVENS, J. S., TOWLER, M. & WOOD, P. A. 2020. Mercury 4.0: from Visualization to Analysis, Design and Prediction. *J Appl Crystallogr*, 53, 226-235.

- MAGEE, G. A., FRENCH, J., GIBBON, B. & LUSCOMBE, C. 2003. Bile salt/lecithin mixed micelles optimized for the solubilization of a poorly soluble steroid molecule using statistical experimental design. *Drug development and industrial pharmacy*, 29, 441-450.
- MAGHFIROH, C., ARKUNDATO, A. & MAULINA, W. Parameters (σ , ϵ) of Lennard-Jones for Fe, Ni, Pb for Potential and Cr based on Melting Point Values Using the Molecular Dynamics Method of the Lammmps Program. *Journal of Physics Conference Series*, 2020. 012022.
- MARINOVA, V., WOOD, G. P. F., MARZIANO, I. & SALVALAGLIO, M. 2019. Solvent Dynamics and Thermodynamics at the Crystal–Solution Interface of Ibuprofen. *Crystal Growth & Design*, 19, 6534-6541.
- MAYO, S. L., OLAFSON, B. D. & GODDARD, W. A. 1990. DREIDING - A Generic Force-Field for Molecular Simulations. *Journal of Physical Chemistry*, 94, 8897-8909.
- MCCALL, D. W. & DOUGLASS, D. C. 1960. Nuclear Magnetic Resonance in Solid Adamantane. *The Journal of Chemical Physics*, 33, 777-778.
- MCMURRY, J. 1992. *Organic Chemistry*, Pacific Grove, California, USA, Brooks/Cole Publishing Company.
- MELCHIONNA, S., CICCOTTI, G. AND HOLIAN, B.L. 1993. Hoover NPT Dynamics for Systems Varying in Shape and Size. *Molecular Physics*, 78, 533-544.
- MEYER, C. W. & MORRISON, G. 1991. Dipole Moments of Seven Partially Halogenated Ethane Refrigerants. *The Journal of Physical Chemistry*, 95, 3860-3866.
- MOLDOVAN, A. A., ROSBOTTOM, I., RAMACHANDRAN, V., PASK, C. M., OLOMUKHORO, O. & ROBERTS, K. J. 2017. Crystallographic structure, intermolecular packing energetics, crystal morphology and surface chemistry of salmeterol xinafoate (form I). *Journal of Pharmaceutical Sciences*, 106, 882-891.
- MONDAL, S., BISWAS, B., SARKAR, S. & SINGH, P. C. 2017. A combined molecular dynamics simulation, atoms in molecule analysis and IR study on the biologically important bulk fluorinated ethanols to understand the role of weak interactions in their cluster formation and hydrogen bond network. *Journal of Molecular Liquids*, 240, 708-716.
- MOURA, C., NEVES, F. & COSTA, E. 2016. Impact of jet-milling and wet-polishing size reduction technologies on inhalation API particle properties. *Powder Technology*, 298, 90-98.
- MULLIN, J. W. 2001. *Crystallization*, Amsterdam, Elsevier.
- MURNANE, D., MARRIOTT, C. & MARTIN, G. P. 2008a. Crystallization and crystallinity of fluticasone propionate. *Crystal Growth and Design*, 8, 2753-2764.
- MURNANE, D., MARTIN, G. P. & MARRIOTT, C. 2008b. Investigations into the formulation of metered dose inhalers of salmeterol xinafoate and fluticasone propionate microcrystals. *Pharmaceutical research*, 25, 2283-2291.
- MYRDAL, P. B., SHETH, P. & STEIN, S. W. 2014. Advances in Metered Dose Inhaler Technology: Formulation Development. *AAPS PharmSciTech*, 15, 434-55.
- NEWMAN, S. P. 2005. Principles of Metered-Dose Inhaler Design. *Respiratory Care*, 50, 1177 - 1190.
- NGUYEN, T. T. H., ROSBOTTOM, I., MARZIANO, I., HAMMOND, R. B. & ROBERTS, K. J. 2017. Crystal Morphology and Interfacial Stability of RS-Ibuprofen in Relation to Its Molecular and Synthonic Structure. *Crystal Growth & Design*, 17, 3088-3099.
- NICE. 2021. *Asthma: diagnosis, monitoring and chronic asthma management* [Online]. National institute for health and care excellence. Available: <https://www.nice.org.uk/guidance/ng80> [Accessed 2022].
- O'DONNELL, K. P. & WILLIAMS, R. O., 3RD 2013. Pulmonary Dispersion Formulations: The Impact of Dispersed Powder Properties on Pressurized Metered Dose Inhaler Stability. *Drug Dev Ind Pharm*, 39, 413-24.

- OMAR, W. & ULRICH, J. 2006. Effect of the addition of alcoholic miscible co-solvents on the properties of ascorbic acid in its supersaturated aqueous solution. *Crystal Research and Technology: Journal of Experimental and Industrial Crystallography*, 41, 431-436.
- PACE., E. L. & ASTON., J. G. 1948. The Thermodynamics of Hexafluoroethane from Calorimetric and Spectroscopic Data. *J. Am. Chem. Soc.*, 70, 566-570.
- PADUA, A. A. H., FARELEIRA, J. M. N. A. & CALADO, J. C. G. 1996. Density and Viscosity Measurements of 1,1,1,2-Tetrafluoroethane (HFC-134a) from 199 K to 298 K and up to 100 MPa. *J. Chem. Eng. Data*, 41, 731-735.
- PEGUIN, R. P. S. & DA ROCHA, S. R. P. 2008. Solvent-Solute Interactions in Hydrofluoroalkane Propellants. *J. Phys. Chem. B*, 112, 8084–8094.
- PEGUIN, R. P. S., KAMATH, G., POTOFF, J. J. & DA ROCHA, S. R. P. 2009. All-Atom Force Field for the Prediction of Vapor-Liquid Equilibria and Interfacial Properties of HFA134a. *J. Phys. Chem. B*, 113, 178–187.
- PEGUIN, R. P. S., SELVAM, P. & DA ROCHA, S. R. P. 2006. Microscopic and Thermodynamic Properties of the HFA134a-Water Interface: Atomistic Computer Simulations and Tensiometry under Pressure. *Langmuir*, 22, 8826-8830.
- PEGUIN, R. P. S., WU, L. & DA ROCHA, S. R. P. 2007. The Ester Group: How Hydrofluoroalkane-philic Is It? *Langmuir*, 8291-8294.
- PRIMARYCARESUPPLIES 2022. Medix Turboneb Nebuliser.
- PRITCHARD, J. N. 2020. The Climate is Changing for Metered-Dose Inhalers and Action is Needed. *Drug Des Devel Ther*, 14, 3043-3055.
- PU, Y., KLINE, L. C., KHAWAJA, N., VAN LIEW, M. & BERRY, J. 2015. Comparison of optical particle sizing and cascade impaction for measuring the particle size of a suspension metered dose inhaler. *Drug Development and Industrial Pharmacy*, 41, 737-743.
- RAMACHANDRAN, V., MURNANE, D., HAMMOND, R. B., PICKERING, J., ROBERTS, K. J., SOUFIAN, M., FORBES, B., JAFFARI, S., MARTIN, G. P., COLLINS, E. & PENCHEVA, K. 2015. Formulation Pre-screening of Inhalation Powders Using Computational Atom–Atom Systematic Search Method. *Molecular Pharmaceutics*, 12, 18 - 33.
- ROBERTS, K., DOCHERTY, R., BENNEMA, P. & JETTEN, L. 1993. The importance of considering growth-induced conformational change in predicting the morphology of benzophenone. *Journal of Physics D: Applied Physics*, 26, B7.
- ROBERTS, R., ROWE, R. & YORK, P. 1994. The relationship between indentation hardness of organic solids and their molecular structure. *Journal of materials science*, 29, 2289-2296.
- ROSBOTTOM, I., MA, C. Y., TURNER, T. D., O'CONNELL, R. A., LOUGHREY, J., SADIQ, G., DAVEY, R. J. & ROBERTS, K. J. 2017. Influence of Solvent Composition on the Crystal Morphology and Structure of p-Aminobenzoic Acid Crystallized from Mixed Ethanol and Nitromethane Solutions. *Crystal Growth & Design*, 17, 4151-4161.
- ROSBOTTOM, I., PICKERING, J., ETBON, B., HAMMOND, R. & ROBERTS, K. 2018. Examination of inequivalent wetting on the crystal habit surfaces of RS-ibuprofen using grid-based molecular modelling. *Physical Chemistry Chemical Physics*, 20, 11622-11633.
- ROSBOTTOM, I., PICKERING, J. H., HAMMOND, R. B. & ROBERTS, K. J. 2020. A Digital Workflow Supporting the Selection of Solvents for Optimizing the Crystallizability of p-Aminobenzoic Acid. *Organic Process Research & Development*, 24, 500-507.
- ROSBOTTOM, I., ROBERTS, K. & DOCHERTY, R. 2015. The solid state, surface and morphological properties of p-aminobenzoic acid in terms of the strength and directionality of its intermolecular synthons. *CrystEngComm*, 17, 5768-5788.
- ROSBOTTOM, I., TURNER, T. D., MA, C. Y., HAMMOND, R. B., ROBERTS, K. J., YONG, C. W. & TODOROV, I. T. 2022. The structural pathway from its solvated

- molecular state to the solution crystallisation of the alpha- and beta-polymorphic forms of para amino benzoic acid. *Faraday Discuss*, 235, 467-489.
- ROSBOTTOM, I., YONG, C. W., GEATCHES, D. L., HAMMOND, R. B., TODOROV, I. T. & ROBERTS, K. J. 2019. The Integrated DL_POLY/DL_FIELD/DL_ANALYSER Software Platform for Molecular Dynamics Simulations for Exploration of The Synthonic Interactions in Saturated Benzoic Acid/Hexane Solutions. *Molecular Simulation*, 1-16.
- ROWLAND, M., CAVECCHI, A., THIELMANN, F., KULON, J., SHUR, J. & PRICE, R. 2018. Measuring The Bipolar Charge Distributions of Fine Particle Aerosol Clouds of Commercial PMDI Suspensions Using a Bipolar Next Generation Impactor (bp-NGI). *Pharm Res*, 36, 15.
- ROY, S., AITIPAMULA, S. & NANGIA, A. 2005. Thermochemical analysis of venlafaxine hydrochloride polymorphs 1– 5. *Crystal growth & design*, 5, 2268-2276.
- SALEEM, I. Y. & SMYTH, H. D. 2013. Tuning aerosol particle size distribution of metered dose inhalers using cosolvents and surfactants. *BioMed research international*, 2013.
- SANGWAL, K. 2007. *Additives and Crystallisation Processes*, New York, John Wiley and Sons.
- SELVAM, P., PEGUIN, R. P. S., CHOKSHI, U. & DA ROCHA, S. R. P. 2006. Surfactant Design for the 1,1,1,2-Tetrafluoroethane-Water Interface: ab initio Calculations and in situ High-Pressure Tensiometry. *Langmuir*, 22, 8675-8683.
- SHETH, P., SANDELL, D., CONTI, D. S., HOLT, J. T., HICKEY, A. J. & SALUJA, B. 2017. Influence of Formulation Factors on the Aerosol Performance of Suspension and Solution Metered Dose Inhalers: A Systematic Approach. *Aaps Journal*, 19, 1396-1410.
- SHIBUTA, Y. & SUZUKI, T. 2008. A Molecular Dynamics Study of The Phase Transition In BCC Metal Nanoparticles. *J Chem Phys*, 129, 144102.
- SHOYELE, S. A. & CAWTHORNE, S. 2006. Particle engineering techniques for inhaled biopharmaceuticals. *Adv Drug Deliv Rev*, 58, 1009-29.
- SHUTTERSTOCK 2022. Purple Asthma powder inhaler on white background.
- SICARD, A. J. & BAKER, R. T. 2020. Fluorocarbon Refrigerants and their Syntheses: Past to Present. *Chem Rev*, 120, 9164-9303.
- SINGLA, L., YADAV, H. R. & ROY CHOUDHURY, A. 2020. Evaluation of fluorine-mediated intermolecular interactions in tetrafluorinated tetrahydroisoquinoline derivatives: synthesis and computational studies. *Acta Crystallogr B Struct Sci Cryst Eng Mater*, 76, 604-617.
- SMYTH, H. D. C. 2003. The Influence of Formulation Variables on The Performance of Alternative Propellant-Driven Metered Dose Inhalers. *Advanced Drug Delivery Reviews*, 55, 807-828.
- SOSNOWSKI, T. R. 2018. Powder Particles and Technologies for Medicine Delivery to the Respiratory System: Challenges and Opportunities. *KONA Powder and Particle Journal*, 35, 122-138.
- STECKEL, H. & MÜLLER, B. 1998. Metered-dose inhaler formulation of fluticasone-17-propionate micronized with supercritical carbon dioxide using the alternative propellant HFA-227. *International Journal of Pharmaceutics*, 173, 25-33.
- STECKEL, H., RASENACK, N., VILLAX, P. & MULLER, B. W. 2003. In vitro characterization of jet-milled and in-situ-micronized fluticasone-17-propionate. *Int J Pharm*, 258, 65-75.
- STECKEL, H., THIES, J. & MÜLLER, B. 1997. Micronizing of steroids for pulmonary delivery by supercritical carbon dioxide. *International journal of pharmaceutics*, 152, 99-110.
- STEIN, S. W., SHETH, P., HODSON, P. D. & MYRDAL, P. B. 2014. Advances in metered dose inhaler technology: hardware development. *AAPS PharmSciTech*, 15, 326-38.

- STEIN, S. W., SHETH, P., YOUNIS, U. S., MOGALIAN, E. & MYRDAL, P. B. 2015. Modeling and Understanding Combination pMDI Formulations with Both Dissolved and Suspended Drugs. *Mol Pharm*, 12, 3455-67.
- STEWART, J. J. P. 1990. Special Issue - MOPAC - A Semiempirical Molecular-Orbital Program. *Journal of Computer-Aided Molecular Design*, 4, 1-45.
- STOLL, J., VRABEC, J. & HASSE, H. 2003. A Set of Molecular Models for Carbon Monoxide and Halogenated Hydrocarbons. *The Journal of Chemical Physics*, 119, 11396-11407.
- SUN, H. 1995. Ab-Initio Calculations and Force-Field Development for Computer-Simulation of Polysilanes. *Macromolecules*, 28, 701-712.
- TAGUCHI, K., GARSIDE, J. & TAVARE, N. S. 1996. Nucleation and growth kinetics of barium sulphate in batch precipitation. *Journal of crystal growth*, 163, 318-328.
- TAULELLE, P., SITJA, G., PÉPE, G., GARCIA, E., HOFF, C. & VEESLER, S. P. 2009. Measuring enthalpy of sublimation for active pharmaceutical ingredients: Validate crystal energy and predict crystal habit. *Crystal growth & design*, 9, 4706-4709.
- THALLADI, V. R., WEISS, H.-C., BLÄSER, D., BOESE, R., NANGIA, A. & DESIRAJU, G. R. 1998. C-H...F Interactions in the crystal structures of some fluorobenzenes. *Journal of the American Chemical Society*, 120, 8702-8710.
- TILLEY, R. 2006. *Crystals and crystal structures*, New York, John Wiley and Sons.
- TODOROV, I. T., SMITH, W., TRACHENKO, K. & DOVE, M. T. 2006. DL_POLY_3: New Dimensions in Molecular Dynamics Simulations Via Massive Parallelism. *Journal of Materials Chemistry*, 16, 1911-1918.
- TRAINI, D., ROGUEDA, P., YOUNG, P. & PRICE, R. 2005. Surface Energy and Interparticle Force Correlation in Model pMDI Formulations. *Pharm Res*, 22, 816-25.
- TRAINI, D., YOUNG, P. M., ROGUEDA, P. & PRICE, R. 2006a. In Vitro Investigation of Drug Particulates Interactions and Aerosol Performance of Pressurised Metered Dose Inhalers. *Pharmaceutical Research*, 24, 125-135.
- TRAINI, D., YOUNG, P. M., ROGUEDA, P. & PRICE, R. 2006b. Investigation Into the Influence of Polymeric Stabilizing Excipients On Inter-Particulate Forces In Pressurised Metered Dose Inhalers. *International Journal of Pharmaceutics*, 320, 58-63.
- TRAINI, D., YOUNG, P. M., ROGUEDA, P. & PRICE, R. 2006c. The Use of AFM and Surface Energy Measurements to Investigate Drug-Canister Material Interactions in a Model Pressurized Metered Dose Inhaler Formulation. *Aerosol Science and Technology*, 40, 227-236.
- TSUZUKI, S., UCHIMARU, T., MIKAMI, M. & URATA, S. 2003. Ab Initio calculations of intermolecular interaction of CHF₃ dimer: origin of attraction and magnitude of CH/F interaction. *The Journal of Physical Chemistry A*, 107, 7962-7968.
- TURNER, T. D., HATCHER, L. E., WILSON, C. C. & ROBERTS, K. J. 2019. Habit modification of the active pharmaceutical ingredient lovastatin through a predictive solvent selection approach. *Journal of Pharmaceutical Sciences*, 108, 1779-1787.
- VAN NES, G. J. H. & VOS, A. 1978. Single-Crystal Structures and Electron Density Distributions of Ethane, Ethylene and Acetylene. *Acta Crystallographica Section B-Structural Science*, 34, 1947-1956.
- VATANARA, A., ROUHOLAMINI NAJAFABADI, A., GILANI, K., ASGHARIAN, R., DARABI, M. & RAFIEE-TEHRANI, M. 2009. Precipitation of fluticasone propionate microparticles using supercritical antisolvent. *DARU*, 17, 6-12.
- VERVAET, C. & BYRON, P. R. 1999. Drug-Surfactant-Propellant Interactions in HFA-Formulations. *International Journal of Pharmaceutics*, 186, 13-30.
- VERWEY, E. J. W. 1947. Theory of the stability of lyophobic colloids. *The Journal of Physical Chemistry*, 51, 631-636.
- WANG, C., ROSBOTTOM, I., TURNER, T. D., LAING, S., MALONEY, A. G., SHEIKH, A. Y., DOCHERTY, R., YIN, Q. & ROBERTS, K. J. 2021. Molecular, solid-state

- and surface structures of the conformational polymorphic forms of ritonavir in relation to their physicochemical properties. *Pharmaceutical Research*, 38, 971-990.
- WEINER, S. J., KOLLMAN, P. A., NGUYEN, D. T. & CASE, D. A. 1986. An All Atom Force Field for Simulations of Proteins and Nucleic Acids. *Journal of Computational Chemistry*, 7, 230-252.
- WESTMEIER, R. & STECKEL, H. 2008. Combination particles containing salmeterol xinafoate and fluticasone propionate: Formulation and aerodynamic assessment. *J Pharm Sci*, 97, 2299-310.
- WILLIAMS, D. E. 1966. Nonbonded potential parameters derived from crystalline aromatic hydrocarbons. *The Journal of Chemical Physics*, 45, 3770-3778.
- WILLIAMS III, R. & LIU, J. 1999. Formulation of a protein with propellant HFA 134a for aerosol delivery. *European journal of pharmaceutical sciences*, 7, 137-144.
- WILSON, A. F., MUKAI, D. S. & AHDOUT, J. J. 1991. Effect of Canister Temperature on Performance of Metered-Dose mhalers'. *Am Rev Respir Dis*, 143, 1034-1037.
- WU, L. B., PEGUIN, R. P. S. & DA ROCHA, S. R. P. 2007. Understanding Solvation in Hydrofluoroalkanes: Ab Initio Calculations and Chemical Force Microscopy. *Journal of Physical Chemistry B*, 111, 8096-8104.
- YADAV, H. R. & CHOUDHURY, A. R. 2017. Can C H...F C Hydrogen Bonds Alter Crystal Packing Features in the Presence of N H...O C Hydrogen Bond? *Journal of Molecular Structure*, 1150, 469-480.
- YANG, T., SIEPMANN, J. I. & WU, J. 2020. Phase Equilibria of Difluoromethane (R32), 1,1,1,2-Tetrafluoroethane (R134a), and trans-1,3,3,3-Tetrafluoro-1-propene (R1234ze(E)) Probed by Experimental Measurements and Monte Carlo Simulations. *Industrial & Engineering Chemistry Research*, 60, 739-752.
- YONG, C. W. 2016. Descriptions and Implementations of DL_F Notation: A Natural Chemical Expression System of Atom Types for Molecular Simulations. *J Chem Inf Model*, 56, 1405-9.
- YONG, C. W. & TODOROV, I. T. 2017. DL_ANALYSER Notation for Atomic Interactions (DANAI): A Natural Annotation System for Molecular Interactions, Using Ethanoic Acid Liquid as a Test Case. *Molecules*, 23.
- YOUNG, D. C. 2001. *Computational Chemistry*, New York, John Wiley and Sons.
- YOUNG, P. M., PRICE, R., LEWIS, D., EDGE, S. & TRAINI, D. 2003. Under Pressure: Predicting Pressurized Metered Dose Inhaler Interactions Using the Atomic Force Microscope. *Journal of Colloid and Interface Science*, 262, 298-302.
- ZHANG, X. & LERNER, M. M. 1999. Structural refinement of the perfluorooctanesulfonate anion and its graphite intercalation compounds. *Physical Chemistry Chemical Physics*, 1, 5065-5069.
- ZHU, B., TRAINI, D., LEWIS, D. A. & YOUNG, P. 2014. The solid-state and morphological characteristics of particles generated from solution-based metered dose inhalers: Influence of ethanol concentration and intrinsic drug properties. *Colloids and Surfaces A: Physicochemical and Engineering Aspects*, 443, 345-355.